On Board Cone Beam CT for Treatment Planning in Image Guided Radiotherapy

By

Fouad Abdulaziz Abolaban

A thesis submitted to the University of Surrey for the award of the degree of Doctor of Philosophy.

Supervisors:

Professor Andrew Nisbet and Professor Nicholas Spyrou

Department of Physics
School of Electronic and Physical Sciences
University of Surrey
Guildford, GU2 7XH

March 2011

Contents

Abstract IV
Acknowledgments VII
List of Figures VIII
List of Tables XIV
Structure of the thesis XVI
1 1
Chapter 1
1 Background 1
1.1 Introduction and Problem Definition 1
1.2 Cone Beam Computed Tomography 5
1.2.1 CBCT technology 6
1.2.2 Current usage of CBCT 12
1.3 Literature review of the scope of CBCT 14
1.3.1 CBCT doses 14
1.3.2 Cone Beam CT based treatment planning 20
1.4 Why this research and what does it contribute to the field of IGRT radiotherapy? 23
2 24
Chapter 24
2 CBCT dose measurements 24
2.1 Phantoms used in this study 25
2.1.1 RANDO phantom 25
2.1.2 Computerized Imaging Reference System CIRS-062A 26
2.1.3 Water phantoms 29
2.2 TLD preparation and calibration 31
2.2.1 TLD Calibration using the PANTAK DXT300 31
2.2.2 Discussions of TLD calibration 34
2.3 RANDO Phantom dose measurements 35
2.4 Water phantom dose measurements 37
2.4.1 Standard dose head mode 37

2.4.2 Pelvis mode 38
2.5 2D mathematical approach to CBCT dose measurement on water phantoms 41
2.5.1 Methods 41
2.5.2 Results 43
2.5.3 Discussion and Conclusions 45
2.6 Risk assessment of CBCT dose 47
2.7 CBCT doses: Discussion and Conclusions 51
3 61
Chapter 61
3 Monte Carlo simulation of CBCT 61
3.1 MCNP-4C simulation of the CBCT dose 61
3.1.1 Method 62
3.1.2 Results 63
3.1.3 Discussion 66
3.2 BEAMnrc and DOSXYZnrc MC simulation 69
3.2.1 BEAM CBCT Monte Carlo component modules 70
3.2.2 Results of the MC BEAM simulation 76
3.2.3 The Effect of beam hardening methods and bow-tie filter on the CBCT beam 80
3.2.4 Percentage Depth Dose (PDD) of the MC simulations 81
3.2.5 MC DOSXYZnrc, CBCT dose measurement on water cylindrical phantoms 84
3.3 BEAM simulation: Discussion and conclusions 89
4 101
Chapter 101
4 Hounsfield number to electron density relationship 101
4.1 Methodology 102
4.1.1 CIRS-062A phantom configuration 102
4.1.2 3D image acquisitions 103
4.2 HU-to-ED Calibration curve results 105
4.3 HU-to-ED calibration curves: Discussion and Conclusions 110
4.4 Suggestions and conclusions on suitable mode 119
5 120

Chapter 120
5 Treatment planning based on CBCT at Royal Surrey County Hospital 120
5.1 Methodology 120
5.1.1 CBCT Calibration curves 120
5.1.2 Contouring 125
5.1.3 Single beam profile comparison 126
5.1.4 The Intensity Modulated Radiation Therapy plan comparison 127
5.2 Dose calculation results 132
5.2.1 Single beam results 132
5.2.2 IMRT plan results 138
5.3 CBCT based treatment planning: Discussion and Conclusions 141
6 149
Chapter 149
6 Conclusions and future work. 149
6.1 Conclusions 149
6.2 Suggested treatment plan based on the CBCT data set 152
6.2.1 Quality assurance: 152
6.2.2 Dose measurement 153
6.2.3 Calibration 154
6.2.4 Dose verification 154
6.3 Future work 155
References 156
Appendix 1 Monte Carlo simulation codes 162
MCNP-4c 162
BEAM 165
DOSXYSnrc 188
Appendix 2 Matlab program 196
Presentation arising from this work 199

Abstract

***Background*:** Movement of tumours between or during radiotherapy treatment fractions poses a risk to surrounding healthy tissues and potentially lowers the treatment dose to the intended area. To increase the efficacy of radiotherapy, radiation oncologists utilise image-guided radiotherapy (IGRT) to enhance the delivery of radiation to cancerous tumours. Concern about concomitant radiation doses and poor quality images have previously limited the use of such technology when developing treatment plans for adaptive radiotherapy. Recent improvements to the On-board Imager (OBI; Varian version 1.4) including expansion of the number of acquiring modes from four to six, have rejuvenated efforts to use Cone Beam Computed Tomography (CBCT) with OBI as a radiotherapy treatment planning tool.

***Aim*:** This research aimed to investigate the possibility of using the new version of the Varian On-Board CBCT imager V1.4, for adaptive radiotherapy. This work has led to the development of a methodology on how to initiate and implement CBCT scans for the purpose of increasing the accuracy of radiotherapy treatments using adaptive radiotherapy.

***Methods*:** The adaptation of radiotherapy plans using CBCT scan images involved three stages. CBCT concommitant doses were determined in the first stage by measuring the dose received by three types of phantom; the RANDO anthropomorphic phantom, the computer-imaging reference system phantom (CIRS) and cylindrical water phantoms of varying diameter. Two- and three-dimensional simulations were also obtained for CBCT using EXCEL, and Monte Carlo codes (BEAMnrc and DOSXYZnrc). The manufacturer's schematic diagram of the head was used to simulate a detailed CBCT dose simulation with the effect of beam output and bow-tie filter included as dose-modifiers. Based on these dose measurements, relationships between CBCT concomitant dose and patient size were found. In addition, estimations of secondary induced cancer were modelled based on these doses. In the second stage, CBCT scan calibrations were conducted. The relationship

between the Hounsfield Unit (HU) and electron density (ED) of CBCT scans were described mathematically for each CIRS-062A phantom configuration. Later, these CBCT HU-to-ED calibrations were benchmarked against the CT HU-to-ED relationship of GE lightspeed CT employed in treatment planning. Finally, in the third stage, the obtained HU-to-ED calibrations were applied to treatment plans calculated on CIRS and RANDO phantoms using single-beam and IMRT configurations. Dose calculations derived from the OBI CBCT were compared with those from the GE Lightspeed CT.

Results: Using a female RANDO phantom, doses were lowered by factors of 36, 8, 22 and 16, at the eyes, oesophagus, thyroid and brain, respectively, when using the new version of Varian CBCT v1.4. In both the standard dose head mode and pelvis mode, the concomitant dose at all positions decreases as the phantom size increases. The concomitant dose measured on the smallest cylindrical water phantoms (10cm in diameter) resulted in a theoretical risk of secondary skin cancer of 0.005% in the standard dose mode and 0.05% in the pelvis mode, assuming a 30-fraction course of treatment with CBCT images acquired on a daily basis. Importantly, these doses are approximately 10 times greater than those measured for the largest phantom. The risk of secondary cancer for this phantom size at the oesophagus, thyroid, and brain sites are 0.0443, 0.0106 and 0.0439 % respectively for 30 daily images of head and neck treatment.

Dose calculations on both the CIRS and RANDO phantoms showed that for the single beam treatment, only 1% difference in the mean dose values are delivered to the majority of insertions when using the original CT or CBCT images and respective calibration curves. The only exception was for dense bone, which exhibited a 2% difference. For the IMRT treatment plan results showed that when the CT scan image is used the mean doses were less than 1.1%.

Conclusion: CBCT doses from the OBI version 1.4 are significantly lower than doses from version 1.3, making it possible to use CBCT to assist with adaptive radiotherapy on a daily basis, without a significantly increased secondary cancer risk. This technology is a useful tool to aid patient positioning for radiotherapy and to allow

daily adaptive IGRT. Radiation dose varies significantly with both patient size and tumour position in relation to scanning mode. It is therefore recommended that patient-specific imaging protocols be considered, especially with regard to paediatric patients who can be expected to receive a higher dose. The single beam and the IMRT comparisons showed that the CBCT images and calibration curves can be used in treatment planning.

Acknowledgments

I would like to take this opportunity to express my sincere gratitude to all those who have supported me to complete this thesis; First of all, I am deeply indebted and thankful to my supervisors Professor Andrew Nisbet and Professor Nicholas Spyrou for their help, guidance and encouragement during my three years of research at the University of Surrey. It has been my great fortune to have them as academic supervisors. Words would not be enough to express my feelings for their tremendous help and support.

I also would like to gratefully acknowledge the useful discussions with Mr Tom Jordan, Head of Radiotherapy Physics at the Royal Surrey County Hospital. These discussions with Mr Jordan were always challenging for me; and resolved many puzzles during my research.

I am grateful to Mohamad Hussien and James Earley, who are in the radiotherapy department at the Royal Surrey County Hospital, for their significant support in facilitating accessibility to the Linear accelerator and working the treatment planning system at the hospital.

Some of my work would not be completed without the help of my colleague and PhD researcher Mukhtar Al-Shangity who has always been giving me research gifts regarding how the data should be presented.

Finally, to the number one person in my life, to my Mam Ebtisam, after whom I have named my daughter, for her deep moral support throughout all my overseas studies. I just want to be in-between her arms all my life. It is to her I dedicate this work.

List of Figures

Figure 1: Schematic diagram showing the sequence of adaptive radiotherapy treatment. 2

Figure 2: Conventional geometry of Cone-beam CT (Murphy et al, 2007) 3

Figure 3: Varian's CBCT system. 1- x-ray source and 2- flat panel detector, (Varian, 2008) 4

Figure 4: Clinical LINAC with OBI, Varian medical system, (Varian, 2008). 6

Figure 5: Top view of the OBI system. 1- kV detector, 2- Forearm, 3- Upper arm, 4- Wrist, 5- Elbow joint, 6- Shoulder joint and 7- kV source, (Varian, 2008). 7

Figure 6: CBCT detector. (Varian, 2008). 7

Figure 7: Full and half bow-tie filter used in the Varian OBI v1.4 (Ding et. al., 2007). 8

Figure 8: Full fan and bow-tie filter. Head scan, left. Half fan and half bow-tie filter, Body scan, right. 9

Figure 9: Standard dose mode as an example of CBCT 204^{o} rotation around the CIRS-062A (left). The arrows show the direction of rotation of the X-ray source. Pelvis mode as an example of 364^{o} rotation around the CIRS-062A is shown on the right. 12

Figure 10: The ART female head phantom. The image on the right shows the top slice without a TLD insertion. 25

Figure 11: Side view of the ART female phantom slice. Top right and left images are slice numbers 4 and 7 respectively. Bottom right and left images are slices 9 and 11 respectively. 26

Figure 12: CIRS-062A phantom representation of the human body. Full phantom with insertions and slices (top). Cross sectional view of the slice, which contains the insertion positions (bottom). 27

Figure 13: Possible configurations of the CIRS phantom 28

Figure 14: Manufactured phantoms at RSCH. 29

Figure 15: Positions of the TLDs on/in the water phantom. 30

Figure 16: Illustration of TLD placement with the Ion-chamber on the surface of the medium density fiber bord (MDF). 31

Figure 17: The percentage difference in the TLD calibration factor in both measurements 33

Figure 18: TLD positions in slices numbered 2, 3, 4, 7 and 8 of the RANDO head phantom. 35

Figure 19: Relationship between phantom size and CBCT v 1.4 concomitant dose using the standard dose head mode. L = left, P = posterior, R = right, C = centre and A = anterior. 38

Figure 20: Relationship between phantom size and CBCT v1.4 dose using the Pelvis mode. L = left, P = posterior, R = right, C = centre and A = anterior. 39

Figure 21: Illustration diagram to show the 2D mathematical approach to determine the CBCT dose. 41

Figure 22: CBCT doses using 2D mathematical model (black) and hospital measurement (red) of the standard dose head mode. L = left, P = posterior, R = right, C = centre and A = anterior. 44

Figure 23: CBCT doses using 2D mathematical model (black) and hospital measurement (red) of the pelvis mode. L = left, P = posterior, R = right, C = centre and A = anterior. 45

Figure 24: Illustration of the dose–response relationship for radiation induced carcinogenesis in humans. The atomic-bomb data represents the "gold standard," that is, the best quantitative data over a dose range from about 0.1 to 2.5 Gy, (Hall, 2006). 47

Figure 25: The dose response relationship for radiation-induced carcinogenesis for 3 types of cancer, for which data are available over a wide range of doses. The low-dose data are from the atomic bomb survivors, and the high-dose data are from radiotherapy patients. The figure was compiled by Dr. Elaine Ron, National Cancer Institute (Hall, 2006). 48

Figure 26: Illustration of the cone beam coverage at the phantom surface. 57

Figure 27: Illustration of the scattering radiation from the adjacent phantom slices to the calculated point. 59

Figure 28: Illustration of the MCNP-4c simulation of the CBCT dose as the point source rotates around the cylindrical phantom. 61

Figure 29:2D illustration of the MCNP-4c source position and accumulation of the final result. 62

Figure 30: X-ray spectrum generated by Ding et al., (2008), which was used in the MCNP-4c simulation. 63

Figure 31: Dose at each source position for a 2 cm water phantom. 64

Figure 32: Dose at each source position for 20 cm water phantom. 65

Figure 33: MCNP-4c simulation of the CBCT dose received at all positions by water phantoms of different radii in the standard dose mode. 66

Figure 35: Steps required in BEAMnrc to perform a simulation of a radiotherapy system (Rogers et. al., 2011). 69

Figure 36: A detailed schematic diagram of the X-ray tube from Varian. 71

Figure 37: Schematic diagram of the simulated Varian G242 CBCT X-ray tube with full bow-tie filter. 1-XTUBE as target source; 2-CONESTAK as exit window; 3-SLABS as pre-filter; 4-BLOCK as pre-collimator; 5-JAWS as upper blades; 6-SLABS as filter support; 7-SLABS as glass; 8-PYRAMIDS as bow-tie filter. The axes are in centimetre measurement. . 73

Figure 38: Varian OBI X-ray tube geometries for each full-fan mode and half-fan mode. Full-fan mode uses full-bowtie filter and half-bowtie is used for half-fan mode (Kim, et al., 2010). 74

Figure 39: Schematics of the geometry of the OBI device used for Monte Carlo simulation. As shown, the x-axis is parallel to the line joining the centres of the anode and cathode. The y-axis is perpendicular to the x-axis and the beam central ray. Thus, the y-axis is perpendicular to the plane of the diagram and the x–y plane is parallel to the detector plane, (Ding, et al., 2007)..... 75

Figure 40: Phase-space files positions in the MC BEAM simulation. . The axes are in centimetre measurement. 77

Figure 41: X-ray spectrum of 100 kVp electron beam on source target. 78

Figure 42: x-ray spectrums of the target source using 100, 110 and 125 kVp electron beam 79

Figure 43: X-ray spectra for the three phase space files of the 100keV electron beam. 80

Figure 44: X-ray spectra of the 100kVp electron beam before and after the bow-tie filter. 81

Figure 45: X-ray spectrums of the 100kVp, 110kVp, and 125kVp electron beam before and after the full bow-tie filter 82

Figure 46: PDD of the photon in the water phantom for the 100kVp electron beam. . 82

Figure 47: PDD of the MC/BEAMnrc beam on a water phantom. 83

Figure 48: Geometry of the DOSXYZnrc MC code for calculating the dose distribution in the water cylindrical phantom. 84

Figure 49: 2D Dose distribution at the centre transverse views of a 4, 8, 12, and 16 cm radius water cylindrical phantom (top-right, top-left, bottom-right and

bottom-left) from the standard dose head mode of CBCT using the DOZXYZnrc code. Note that the colour scale is in units of as percentage of the maximum dose. 85

Figure 50: 2D Dose distribution at the centre sagittal view of a 4, 8, 12, and 16 cm radius water cylindrical phantom (top-right, top-left, bottom-right and bottom-left) from the standard dose head mode of CBCT using the DOZXYZnrc code. Note that colour scale is in units of percentage of the maximum dose. 86

Figure 51: 2D Dose distribution at the centre transvers view of a 4, 8, 12, and 16 cm radius water cylindrical phantom (top-right, top-left, bottom-right and bottom-left) from the pelvis mode of CBCT using the DOZXYZnrc code. Note that colour scale is in units of percentage of the maximum dose. 87

Figure 52: 2D Dose distribution at the centre sagittal view of a 4, 8, 12, and 16 cm radius water cylindrical phantom (top-right, top-left, bottom-right and bottom-left) from the pelvis mode of CBCT using the DOZXYZnrc code. Note that colour scale is in units of percentage of the maximum dose. 88

Figure 53: (A), (B), (C) and (D) show the photon energy spectra for 60 kVp, 80 kVp, 100 kVp and 120 kVp beams, respectively. (E) Photon energy spectra for a CBCT 125 kVp beam with and without bow tie filters (Ding, et al., 2007). 90

Figure 54: Energy spectra profiles of selected collimator inserts for the F1 bowtie filter (Downes, et al., 2009)..... 91

Figure 55: Spectra distributions for the radiation beams defined by a selected number of XVI collimator cassettes (Spezi, et al., 2009)..... 91

Figure 56: Beam profile on the X off-axis for the 100kVp electron beam before and after the full bow-tie filter. 93

Figure 57: 2D representation of the Bow-tie filter used in the CBCT simulation. 93

Figure 58: Beam profile on the Y off-axis for the 100kVp electron beam before and after the full bow-tie filter. 94

Figure 59: Beam profile on the Y off-axis for the 125kVp electron beams before and after the full bow-tie filter. 95

Figure 60: MC BEAM result for the X off axis versus beam flounce for the half bow-tie filter in the 125kVp electron beam. 95

Figure 61: Central axis depth-dose distribution for different quality photon beams (Khan, 2003)..... 96

Figure 62: MC result of PDD at different phantoms for 100kVp. 98

Figure 63: Visualization of the 2D dose distribution for each new CBCT scan protocol: a) Head, b) pelvis, c) pelvis spot light, and d) low-dose thorax scans. The start and end points for the partial-angle scan was marked (a). Note that the colour scale is in the unit of mGy (Kim, et al., 2010). 100

Figure 64: Insertion positions in the CIRS-062 phantom. 102

Figure 64: CIRS-062A phantom configuration during the scan and calibration of the CBCT HU-to-ED.....104

Figure 65: HU-to- Electron density relationship for the CT scans when using different phantom configurations.....105

Figure 66: HU-to-Electron density relationship for head insertions in the head slice scan at position A and different modes. 107

Figure 67: HU-to-Electron density relationship for head insertions for the body phantom at position A. 107

Figure 68: HU-to-Electron density relationship for head insertions in the body phantom at position B. 108

Figure 69: HU-to- Electron density relationship for the body insertions in the body phantom scan at position A 109

Figure 70: HU-to- Electron density relationship for the body insertions in the body phantom scan at position B 109

Figure 71: HU comparison between central and offset positions of the body insertions. 115

Figure 72: (A) Standard dose head mode calibration for the offset positions of the insertions and full body scan. (B) Low dose head mode for centeral positions of the insertions and full body scan. 116

Figure 73: CT versus CBCT modes. (A) Standard dose head mode (B) Low dose head (C) High quality head (D) Pelvis (E) Pelvis spot light and (F) low dose thorax.....117

Figure 74: HU values of the head insertions using the standard head, low dose head and high quality head modes at the central position. 118

Figure 75: Head slice contouring at the RSCH.....125

Figure 76: Body phantom contouring at the RSCH.....126

Figure 77: Summary of the steps followed in the single beam treatment plans. 127

Figure 78: (A) Illustration of the five fields of the IMRT head and neck treatment plan on a RANDO phantom. (B) Calculated dose distribution from head and neck IMRT treatment plan using CBCT calibration curve (M1-A-HS). .128

Figure 79: (A) Illustration of five fields of the IMRT prostate treatment plan on a RANDO phantom. (B, D, and E) Calculated dose distribution for the IMRT prostate treatment plan using CBCT calibration curve (M4-A-HS). 130

Figure 80: Summary of the steps followed in the IMRT treatment plans. 131

Figure 81: DVH of the CBCT image (M1-A-HS) using the CT calibration curve. ..133

Figure 82: DVH values for a single beam directed on a CIRS phantom. Scan (M1-A-HS) using the CT(solid line) and M1-A-HS(dash line) calibration curves. 134

Figure 83: DVH values for a single beam directed on a CIRS phantom. Scan (M1-A-HS) using the CT(solid line) and M4-A-HS(dash line) calibration curves. 135

Figure 84: DVH values for a single beam directed on a CIRS phantom. Scan (M1-A-HS) using the CT(solid line) and M6-A-HS(dash line) calibration curves. 136

Figure 85: DVH values for the head(H) and body (B) insertions of the CIRS phantom using CT (solid) and M4-A-HS (dash) calibration curves. 137

Figure 86: DVH values of the IMRT head and neck plan on CT and CBCT head scan mode using CT and M1-A-HS calibration curves.....139

Figure 87: DVH values of the IMRT prostate plan on CT and CBCT head scan mode using CT and M4-A-HS calibration curves. 140

Figure 88: Insertion positions with respect to the incoming AP beam. 141

Figure 89: Distribution of the mean dose to a CIRS phantom using a 6MV single beam and different calibrations. 143

Figure 90: The mean dose differences in the head and neck IMRT plan using different calibration curves. 145

Figure 91: Error displayed when using the pelvis mode calibration curve in the T-BOX computer. 147

Figure 92: Suggested plan for treatment planning based on CBCT. 152

List of Tables

Table 1: Parameters and the correlation between versions 1.3 and 1.4) of the CBCT modes 10

Table 2: Comparison between old and new CBCT dose. 17

Table 3: Physical and electron density of CIRS-062A phantom insertions (Varian, 2008)..... 28

Table 4: Setup parameters and results for the PANTAK-300 measurements. 32

Table 5: CBCT doses on RANDO phantom at organs with TLDs slice numbers..... 36

Table 6: Factor a and b values from the fitted exponential curve equation 40

Table 7: ICRP 103 risk coefficients (%/Sv). 49

Table 8: The risk of secondary skin cancer for the different modes and phantom radii as a percentage for 30 fractions. 50

Table 9: Single fraction CBCT dose measurement studies using version 1.3 of Varian system, units are in cGy. 53

Table 10: Comparison between old and new CBCT applied doses. All data are TLD measurement except Ding et. al. (simulation)..... 55

Table 11: Standard dimensions of the head and pelvis for infants, children, and adults (Yarn Standards, 2011). 55

Table 12: Source positions used in the MCNP-4c simulation. 65

Table 13: The simulated and expected photon peaks using the 100kVp electron beam on the 95% W and 5% Rh source target..... 78

Table 14: PDD values at different depths for different x-ray tube voltages. 97

Table 15: Symbol names used to refer to scanned images 103

Table 16: Examples of image codes and their descriptions 104

Table 17: The average HU number of all the CT scans. (Reference HU numbers) .. 106

Table 18: The differences in HU for different phantom configurations. 111

Table 19: Calibration curves for the standard dose head mode used in treatment planning at the RSCH. 122

Table 20: Calibration curves for the pelvis mode, used for treatment planning at the RSCH 123

Table 21: Calibration curves for the low dose thorax mode used for treatment planning at the RSCH.....124

Table 22: IMRT treatment plan field details for the head and neck on a RANDO phantom.....128

Table 23: IMRT TP field details for the prostate plan on a RANDO phantom.....129

Table 24: The difference in relative dose at 60% volume of all insertions using different calibration curves.....142

Table 25: Mean dose to a CIRS phantom insertion using a single 6MV beam and two different calibrations. 143

Table 26: The mean doses of the dense bone insertion during the pelvis mode scan and single beam treatment.....144

Table 27: The mean dose differences in the head and neck IMRT plan using different calibration curves. 146

Table 28: The mean dose differences in the pelvis IMRT plan using different calibration curves 146

Table 29: Suggested organs in the body for dose measurement. 153

Structure of the thesis

There are six chapters in this thesis. The author intended to investigate the feasibility of using the Cone Beam CT (CBCT) directly in treatment planning and adaptive radiotherapy. Therefore, these chapters have been arranged in such a manner to give the reader a journey covering an introduction to CBCT technology; the CBCT concomitant image dose, the relationship between the images and the electron density/HU calibration, treatment planning based on CBCT and; last but not least, a suggested plan on how to initiate the use of CBCT directly for treatment planning.

Chapter one, provides an introduction to image guided radiotherapy and addresses in some detail the technology of CBCT. A review of the literature describes the scope of CBCT usage to date. This includes a summary of work on concomitant doses as well as CBCT based treatment planning. The problem definition and the aim of this research are both embedded within this chapter.

Chapter two, explains and discusses the methodology and results of the dose measurements of the new version of Varian CBCT v1.4 experimentally and theoretically. Dose measurements were carried out on three types of phantoms; RANDO-phantom, Computer Imaging Reference System phantom CIRS, and cylindrical water phantoms. Two- and three-dimensional simulations were obtained for the CBCT, using EXCEL and Monte Carlo simulation respectively. In the mathematical approach to calculate the CBCT dose a 2D plan was used. This means that if the water phantom is sliced into 1 mm sections that are then separated from each other, the effect of the neighbouring slices is not considered. The aim of this 2D mathematical model is to see the effect of the cone beam on the dose, since the simulation is carried out using a point source moving around a 2D water disk of 1mm only, without considering the neighbouring slices.

Chapter three, describes the simulation of the CBCT using the Monte Carlo codes MCNP-4C, BEAMnrc and DOSXYZnrc. The Monte Carlo simulation of the CBCT was initially attempted by using a static code simulation, MCNP-4c. The author found that the MCNP-4c is not sufficient to simulate the dynamic movement of the imaging device and recommends the use of BEAMnrc/DOSXYZnrc instead. In this chapter a detailed CBCT x-ray head is simulated using the manufacturer schematic diagram. Discussions on the beam outputs and bow-tie effect on the beam are added. The CBCT doses on the cylindrical water phantoms are also included.

Chapter four, describes the Hounsfield Unit (HU) to Electron Density (ED) relationships (HU-to-ED) where a comprehensive study on HU number changes within the CIRS-062A phantom is addressed in detail. In addition, the HU-to-ED relationships for all the CIRS-062A phantom configurations using the CBCT modes is obtained and benched marked against the GE Lightspeed CT HU-to-ED calibration curve at the Royal Surrey County Hospital (RSCH). Then selections of the best mode which can be used for each treatment plan site are carefully chosen and tested in chapter five.

Chapter five is the final stage of this research. The final test of the CBCT HU-to-ED relationships is carried out by applying these obtained calibrations on CIRS-062A and RANDO phantoms with single beam plan and complex IMRT plans respectively. The results have been compared against the CT calibration curve.

Chapter six, provides conclusions and suggestion for future work. This chapter starts by summarising the results found during the research; then provides a suggested adaptive treatment plan procedure using the CBCT scan images. At the end, this chapter closes by suggesting future plan that the author intends to do in the near future.

1 Background

1.1 Introduction and Problem Definition

Cancer has a profound influence on the lives of every member of the family concerned and it is one of the leading causes of death in the developed world (Neville, 1995). There are a number of treatment modalities available to treat cancer, either as stand-alone treatments or as synergistic combinations. However, the three main treatments are surgery, radiation therapy and chemotherapy (Khan, 2003). The main concern of this thesis is radiotherapy and its applications.

Treatment using radiotherapy should follow a sequence of steps where the initiation of each step depends upon the successful completion of the former (Figure 1). Following diagnosis and determination of the tumour stage, the extent and geometric position of the tumour and organs at risk are determined. This is achieved by using one or more of the available imaging modalities, such as computed tomography (CT), magnetic resonance imaging (MRI), ultrasound (US) and/or positron emission tomography (PET). CT is the primary imaging mode for the planning of radiotherapy treatment since it displays soft tissue structures well enough for organ delineation, reveals the bony landmarks used for patient setup, allows for the generation of digitally reconstructed radiographs (DRRs) for patient positioning, and directly measures the electron densities needed for dose computation during the planning process (Murphy, et al., 2007). However, the dose received by the patient undergoing CT should be monitored, because it represents by far the largest contribution to the

total radiation exposure from diagnostic medical sources. This is still of concern for patients undergoing radiotherapy (Nisbet & Cocker, 2004).

The accuracy of radiotherapy treatment depends on many factors, including the technology used in the treatment process, such as the imaging modality and treatment planning system. A published report (IPEM report no 81) entitled "Physics Aspects of Quality Control in Radiotherapy" covers each stage of the radiotherapy planning and treatment process (Mayles, et al., 2000).

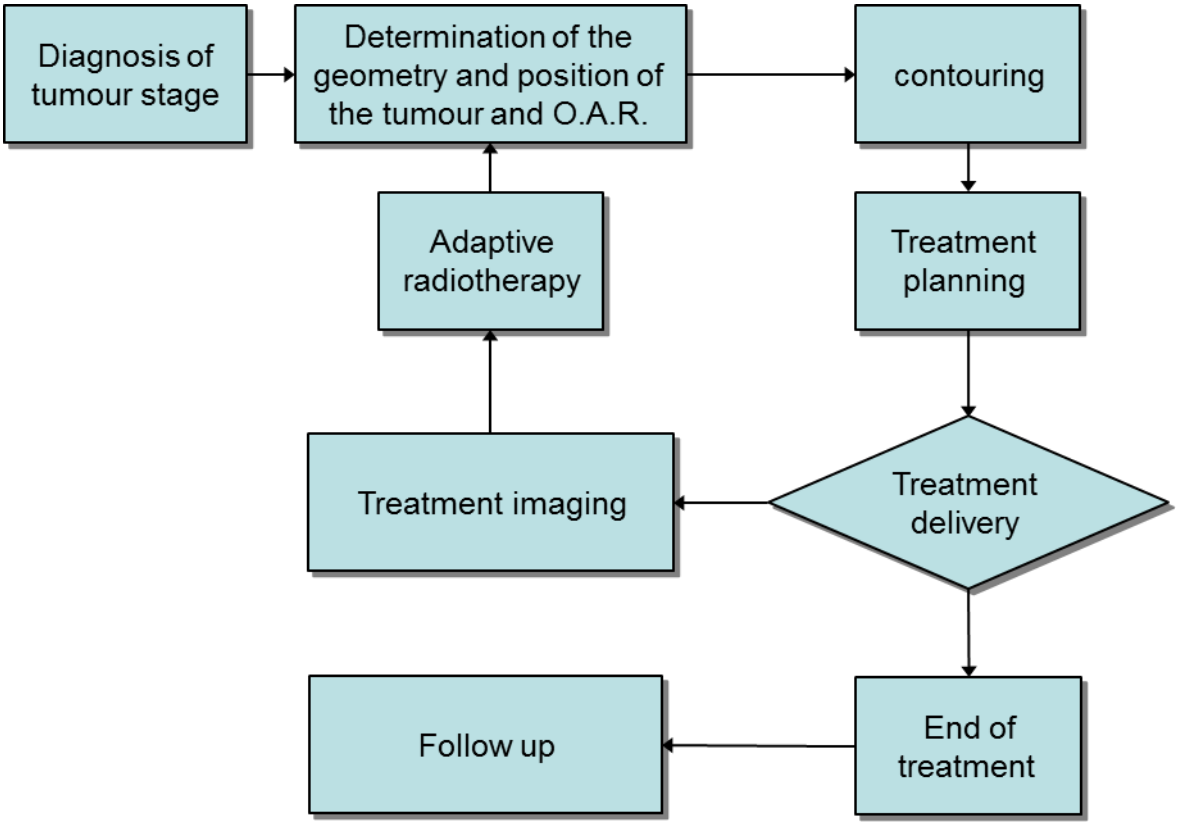

Figure 1: Schematic diagram showing the sequence of adaptive radiotherapy treatment.

Several sources of treatment uncertainty are being addressed and reduced with the use of Image-Guided Radiotherapy (IGRT). IGRT is the process of frequent two- or three-dimensional (3D) imaging utilising the imaging coordinates of the actual radiation treatment plan to direct radiation beams during a course of radiation treatment (Murphy, et al., 2007). In other words, IGRT is a technique used to help ensure the treatment plan made for the patient is accurate, by checking and matching the position

of the patient and/or the organs at risk (OAR) during delivery of treatment. However, organ movement during the treatment fraction and deformation of the tumour itself between fractions may still reduce the accuracy of the radiotherapy.

The concept of Adaptive Radiation Therapy (ART) appears to overcome the problem of tumour deformation between fractions, as the treatment plan is delivered whilst monitoring the tumour response to the radiation in real-time. In this way, the treatment plan can be adapted to match the deformation of the tumour. The ART concept can only be achieved if complete representations, deformations, and records of the tumour position are registered for each treatment fraction. There are many imaging modalities that record the tumour movement for the purpose of ART, one of them is Cone Beam Computed Tomography (CBCT). This form of imaging gives a complete 3D representation of the imaging site. On Board Imager (OBI), such as an X-ray CT source and a flat panel detector can be attached to the treatment gantry (Figure 2 and Figure 3) to generate the 3D view (L'etourneau, et al., 2005; Ding & Coffey, 2009).

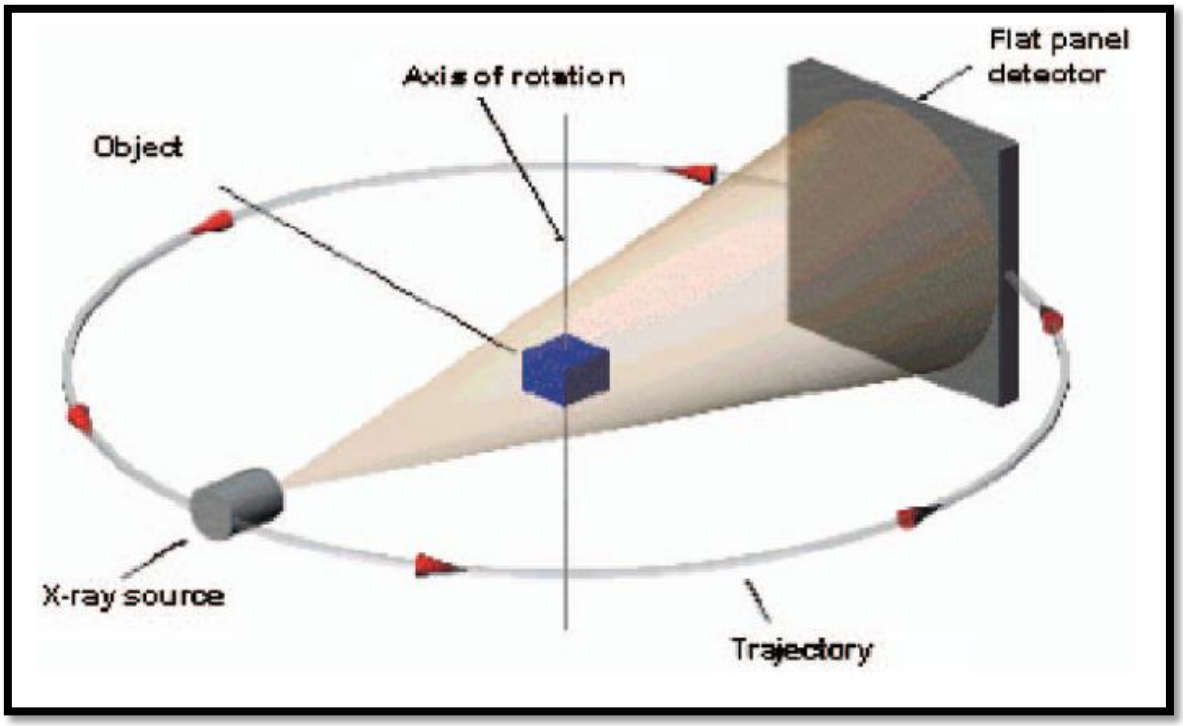

Figure 2: Conventional geometry of Cone-beam CT (Murphy et al, 2007)

Adaptive radiotherapy has the potential to reduce the radiation dose received by normal cells and facilitate dose escalation to the target. Re-planning of the original treatment based on CBCT images may help to accommodate changes to tumour position and configuration, on a daily basis, or whenever the treatment is given. For CBCT images to be used in the treatment planning, several prior investigations and measurements, such as determining the actual CBCT image doses, need to be performed. The radiation dose received from CBCT imaging is possibly the main concern of using the technology on a daily basis. The decision to use CBCT on a daily basis or not can be made based on the amount of radiation delivered per investigation/scan. Following the decision, the correct CBCT mode setting must be chosen based on the specific site of the human body under treatment.

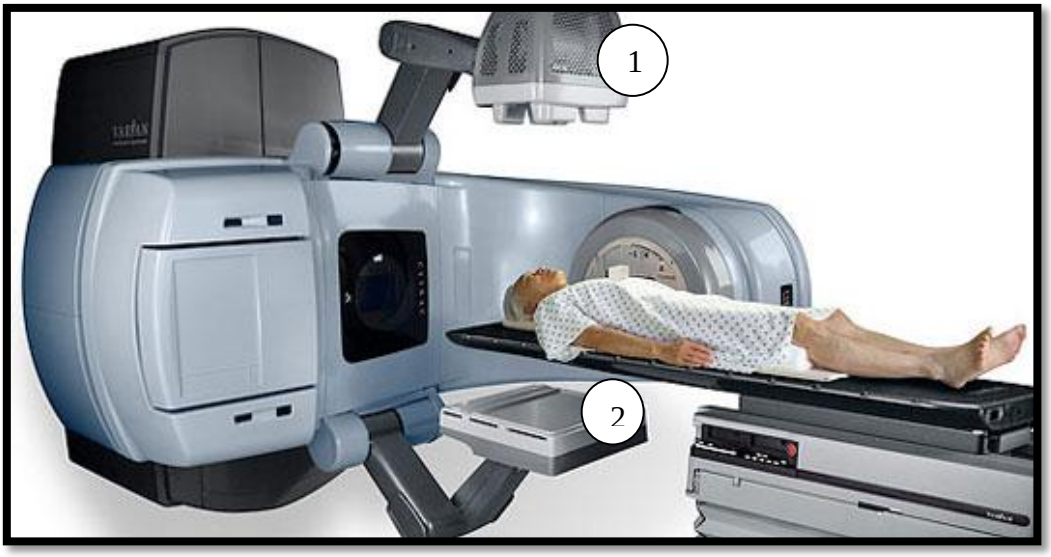

Figure 3: Varian's CBCT system. 1- x-ray source and 2- flat panel detector, (Varian, 2008).

The current question surrounding the use of CBCT is whether to acquire images of the tumour deformation prior to delivering the first treatment, in the middle of the treatment course or on a daily basis. It is also uncertain whether CBCT in different mode setting can be used for treatment planning. The aim of this project was therefore to answer the aforementioned questions regarding the usage of CBCT in radiotherapy treatment planning. In order to achieve this, the study included a comparison of the doses measured following daily CBCT. The results of this analysis will help to

determine the feasibility of using CBCT images in the re-planning process by assessing the risk of such daily imaging using the secondary cancer induction models. Following this, the ways in which CBCT could be used directly in treatment planning is assessed. The assessment will form the basis of a comprehensive set of guidelines for the use of On-Board CBCT imaging during treatment planning using IGRT in a hospital setting.

1.2 Cone Beam Computed Tomography

One of the three imaging modes of the Varian medical system with an On-Board Imager (OBI; On-Board Imager®, Varian Medical Systems, Inc., Palo Alto, CA), is cone-beam computed tomography (CBCT). The other two modes, 2D radiographic and fluoroscopic imaging, are not the main focus of this study and are therefore only briefly discussed. The radiographic mode is designed to reduce inter-fractional motion and setup errors, whereas the fluoroscopic mode is used to verify the gating thresholds of the respiratory system to account for respiratory intra-fraction motion (Yoo, et al., 2006). CBCT, on the other hand, produces a 3D representation of patient position on the treatment couch to assist in matching the planned position with the current treatment position.

The Varian OBI adds two, laterally mounted arms, for the X-ray source, and flat panel detector on the clinical linear accelerator. This is in addition to the megavoltage (MV) source and the PortalVision (PV) imager, Figure 4. The left arm (i.e. 90^{o}) is an amorphous-silicon (a-Si) flat panel detector (KVD), while the right arm (i.e. 270^{o}) is a kV X-ray source (KVS). The Elekta linear accelerator has also released the X-ray Volumetric Imager (XVI) (Synergy® RP, Elekta Oncology Systems, Crawley, UK), capable of producing a 3D CBCT image with the arms positioned the opposite way around (Song, et al., 2008). Six essential modes are available with the CBCT OBI v1.4 that can be used to acquire images. Each mode has been designed for a specific physiological site of the human body. These modes are named, standard dose head, low dose head, high quality head, pelvis, pelvis spot light, and low dose thorax. The specifications of each mode are detailed in the following sections.

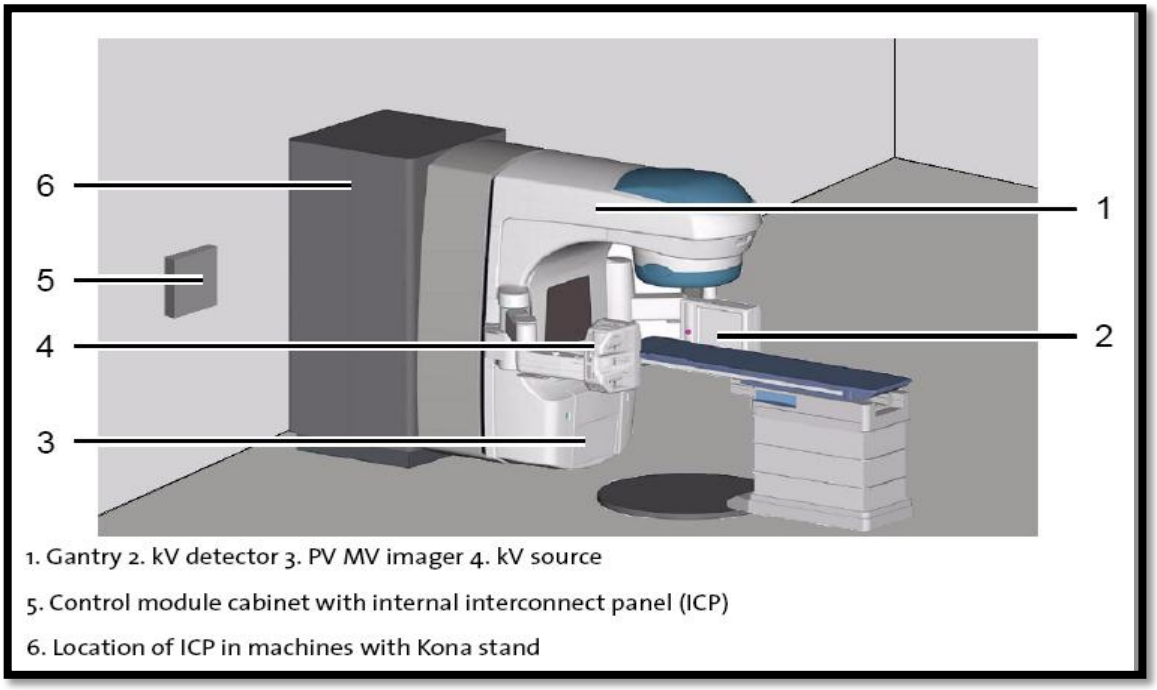

Figure 4: Clinical LINAC with OBI, Varian medical system, (Varian, 2008).

1.2.1 CBCT technology

In early 2008, Varian Medical Systems released the OBI V1.4 advanced imaging system using the new cone-beam CT scan mode setting. The main intention of this release was to reduce the imaging dose and acquisition time, while maintaining similar CBCT image quality to the previous scan protocols (OBI V1.3) (Kim, et al., 2010). The X-ray and flat panel detector components of the OBI CBCT are controlled by two arms that allow them to move in and out during imaging. The top view of the linear accelerator containing the OBI CBCT (Figure 5), shows how these two arms control the CBCT system. The construction and movement of the arms are similar to that of human arms.

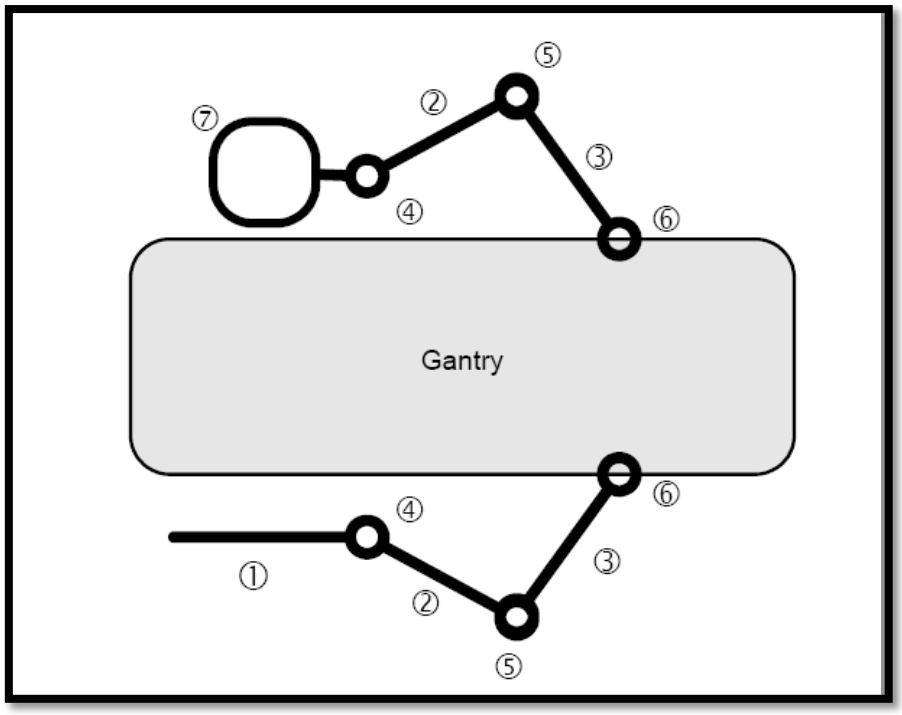

Figure 5: Top view of the OBI system. 1- kV detector, 2- Forearm, 3- Upper arm, 4- Wrist, 5- Elbow joint, 6- Shoulder joint and 7- kV source, (Varian, 2008).

The detector shown in Figure 6 is an amorphous silicon detector with an active rectangular imaging area of 397 mm x 298 mm. The X-ray source, kVS, has a target angle of 14° and two possible focal spot sizes: 0.4 mm and 0.8 mm.

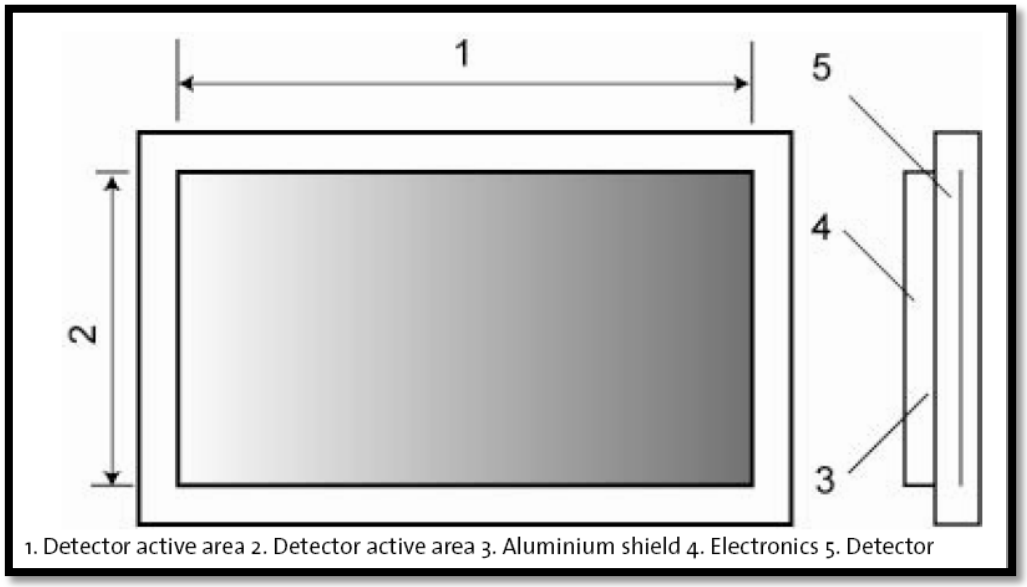

Figure 6: CBCT detector. (Varian, 2008).

To control the quality of the images, two types of filter; the full and half Bow-tie filters, are added (Figure 7). The main functions of the filters are to reduce skin dose; reduce X-ray scatter, which results in improved image quality; reduce the amount of charge trapped in the detector, and to allow higher magnitude X-ray techniques to be used without saturating the detector (Varian, 2008).

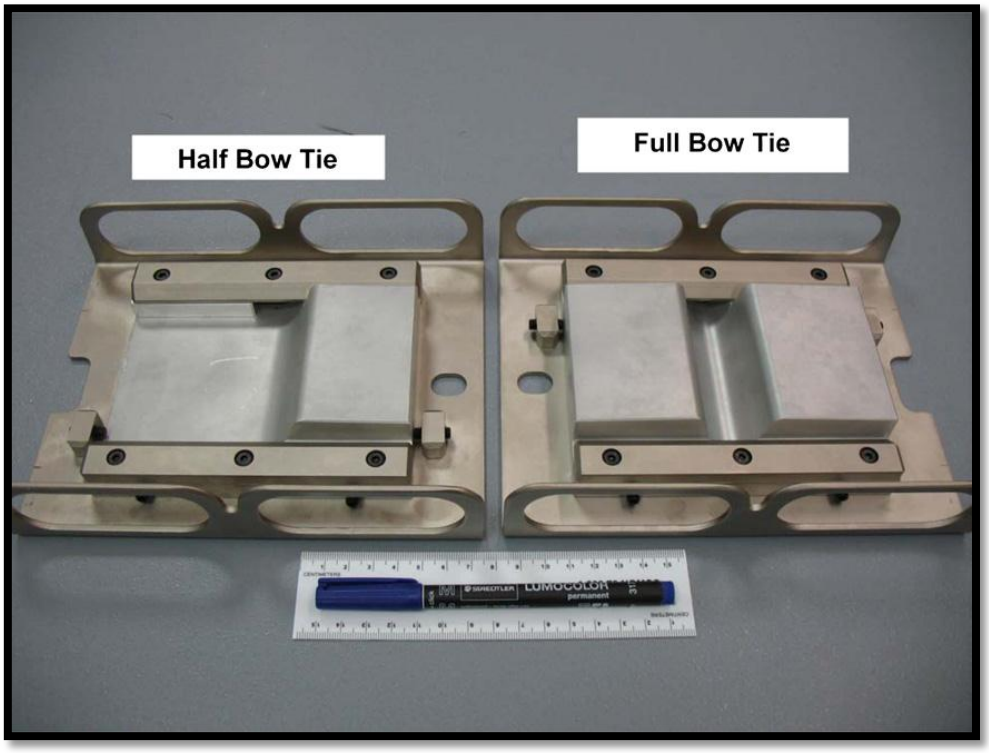

Figure 7: Full and half bow-tie filter used in the Varian OBI v1.4 (Ding et. al., 2007).

The Varian system comes with software to register and regulate the images acquired. The speed of motion in the vertical, longitudinal, and lateral directions of the arms ranges from approximately ≤3 mm/s to 40 mm/s (Varian, 2008). Following image registration, the actual position of the patient is matched with the corresponding position in the planning CT, and positional error can be corrected by remotely moving the treatment couch.

The two CBCT image acquisition categories are classified according to the dimension of the imaging site. If the imaging site diameter is ≤25 cm, the image falls into the category of head scans with full fan beam and full bow-tie filter. If the imaging site diameter is >25 cm the image is categorised as a body scan with half fan beam and

half bow-tie filter. Subsequently, there are six modes of CBCT, as named above that are classified under these two main categories (Varian, 2008). The reconstructed volume in the head scans is 25 cm diameter and a maximum of 17 cm long and 45 cm diameter and 15 cm long for body scans. A representation of each scan type is shown in Figure 8. In the case of the body scan, the flat panel detector is shifted laterally by 14.8 cm towards the gantry head. The CBCT mode settings of the old and the new Varian versions (1.3 and 1.4 respectively) are detailed in Table 1.

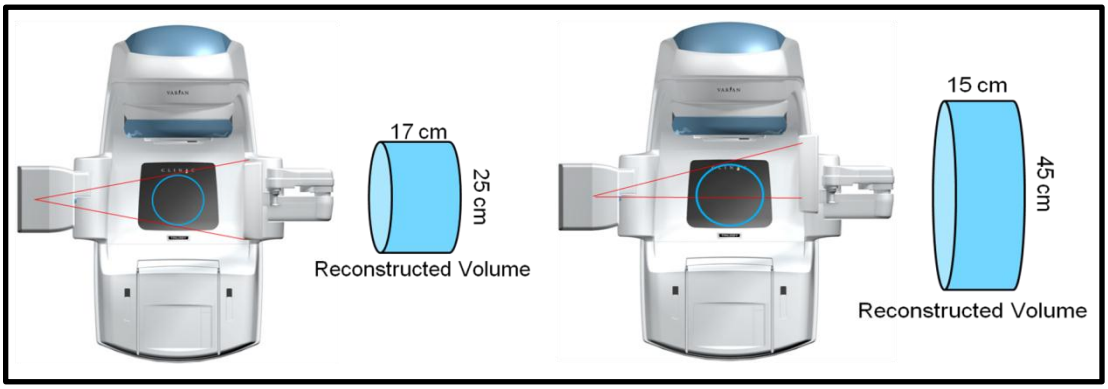

Figure 8: Full fan and bow-tie filter. Head scan, left. Half fan and half bow-tie filter, Body scan, right.

In version 1.4 of the Varian OBI, the X-ray rotates 204^{o} under the couch in the standard dose head mode, to form the CBCT image. The X-ray can start in one of two possible positions; 292^{o} or 88^{o}, with the final position always being opposite to the start position (i.e. start at 292^{o} and finish at 88^{o}). This is slightly larger rotation in practice compared with the stated 200^{o} rotation. In the mode used for pelvic examination, the X-ray rotates 364^{o} (starts at 178^{o} and ends at 180^{o}), moving in a clockwise direction around the imaging site to form the CBCT image (Figure 9).

Table 1: Parameters and the correlation between versions 1.3 and 1.4) of the CBCT modes

Old version 1.3						
Protocol name	Low dose 150 cm Bow-tie	n/a	Standard dose 150 cm Bow-tie	Standard dose 150 cm Bow-tie	n/a	Low dose 150 cm Bow-tie
X-ray voltage [kVp]	125		125	125		125
X-ray current [mA]	40		80	80		40
Exposure time [ms]	25		25	25		25
Exposure [mAs]	1340		1340	1340		1340
Stated acquisition angle [deg]	360		360	360		360
Number of Projections	650 - 700		650 - 700	650 - 700		650 - 700
Fan type	Head		head	Body		Body
Bow-tie filter	Full		full	Half		Half

New version 1.4						
Protocol name	Standard dose head	Low dose head	High quality head	Pelvis	Pelvis spot light	Low dose thorax
X-ray voltage [kVp]	100	100	100	125	125	110
X-ray current [mA]	20	10	80	80	80	20

Table 1: Parameters and the correlation between versions 1.3 and 1.4 of the CBCT modes (continued)

Protocol name	Standard dose head	Low dose head	High quality head	Pelvis	Pelvis spot light	Low dose thorax
Exposure time [ms]*	20	20	25	13	25	20
Exposure [mAs]	150.8	75.2	754	706.2	752	270.8
Stated acquisition angle [deg]	200	200	200	360	200	360
Number of Projections	360	360	360	655	360	655
Fan type	full fan	full fan	full fan	half fan	full fan	half fan
Bow-tie filter	Full	full	full	Half	half	Half

* Exposure time is for planner imager per fraction.

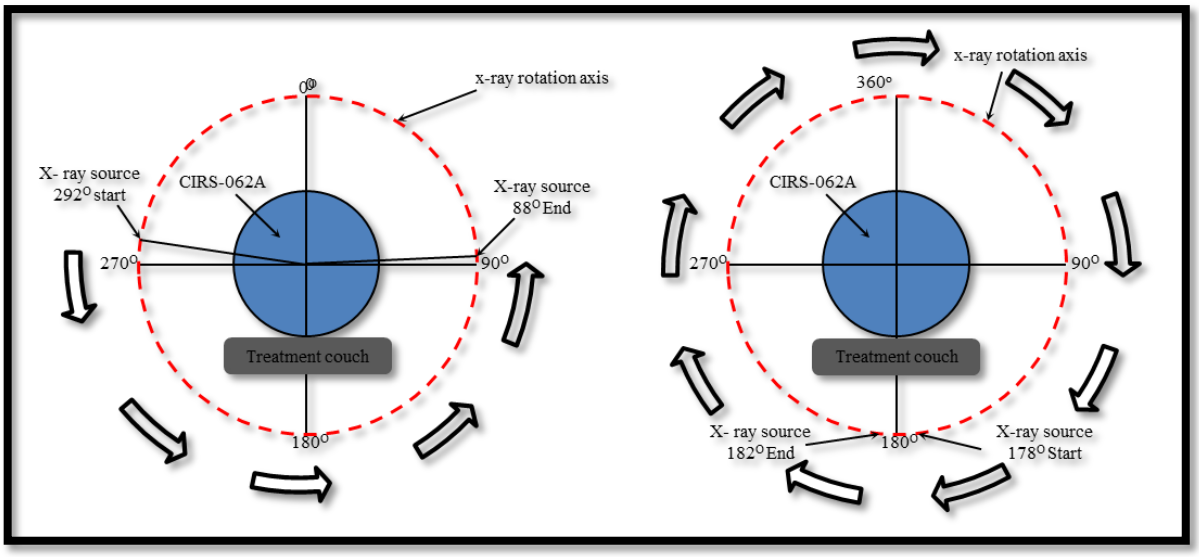

Figure 9: Standard dose mode as an example of CBCT 204° rotation around the CIRS-062A (left). The arrows show the direction of rotation of the X-ray source. Pelvis mode as an example of 364° rotation around the CIRS-062A is shown on the right.

1.2.2 Current usage of CBCT

Several published papers have attempted to investigate the use of this technology in assisting the treatment planning and adaptive radiotherapy (Yoo & Yin, 2006, Ding, et al., 2007, Nijkamp, et al., 2008 and Guan & Dong, 2009). Others have investigated the use of CBCT for treatment fraction check-up (Zijtveld, et al., 2007). The basic principle of CBCT is to set the patient on the treatment couch for the normal fraction delivery. Prior to applying the treatment beam, the attached CBCT device images the current position of the patient. This 3D image produced is then matched to the original treatment planning position, and any positional disagreements are corrected by an automatic adjustment mediated by the CBCT technology, alternatively the treatment may re-planned.

Four main areas of interest regarding the use of CBCT technology in radiotherapy exist. The first area is quality assurance, where the image quality, parameters affecting the image, and performance of the machine are assessed (Yoo, et al., 2006). The second area examines the actual uses of CBCT for IGRT. In this area, efforts are on-going to find the optimum way to utilise CBCT for patient positioning, and checking

and confirming that the patient actually receives the planned treatment dose in the correct bodily location (Marchant, et al., 2008). The third area concerns the ability to adapt the treatment plan based on daily CBCT imaging to match tumour deformation during the treatment fractions; this is known as adaptive radiotherapy (Paquina, et al., 2008 and Ho, et al., 2011). The last area of interest underway is the utilization of the CBCT data set for dose calculation. This involves determining the dose that should be delivered to the patient on the treatment day (Zijtveld, et al., 2007) and basing the longer-term treatment plan on this data set (Richter, et al., 2008, Rong, et al., 2010 and Sriram, et al., 2011).

1.3 Literature review of the scope of CBCT

1.3.1 CBCT doses

As mentioned previously, the practice of IGRT entered the field of radiotherapy to help reduce some of the uncertainties in the treatment planning process. The current trend of enthusiasm for IGRT is largely due to the advent of on-line imaging devices. Broadly stated, IGRT involves any use of imaging to aid the decisions made in the radiotherapy process, such as decisions of whether/how to treat the patient. Imaging can also aid the delineation of structures of interest; patient positioning; verification, and monitoring of doses; and the assessment of treatment progression and outcome prognosis (Greco & Clifton, 2008). As CBCT is one of the IGRT modalities, the scope of this literature review will focus on this particular mode and not the alternative functions.

A number of papers published in the last decade have examined the CBCT imaging dose delivered to patients. These publications have established the main methods that may be used to determine concomitant dose; either by simulating the dose using a Monte Carlo (MC) code together with detailed CBCT geometry (Ding & Munro, 2011 and Ding & Coffey, 2009) or by using phantoms to acquire the data experimentally (Hyer, et al., 2010 and Kan, et al., 2008). The results obtained from the use of two types of CBCT system have been reported in the literature; the X-ray Volumetric Imager (XVI) from Elekta Synergy (XVI, Elekta Oncology Systems, Crawley, UK) (Amer, et al., 2007) and version 1.3/1.4 of the Varian OBI (OBI, Varian Medical Systems, Palo Alto, CA). The CBCT doses calculated using these two imagers are not the same. In addition, even when using the same system and acquiring mode, rotation of the X-ray source may start and end at different positions, which changes the concomitant dose (Ding & Coffey, 2009 and Amer, et al., 2007). Moreover, scan parameters may be specific to institutional protocols (Kim, et al., 2008, L'etourneau, et al., 2005 and Hyer, et al., 2010). There have also been some limited studies suggesting that the concomitant dose may be affected by differences in patient size ((Hyer, et al., 2010) (L'etourneau, et al., 2005) (Wen, et al., 2007)). In fact, no accepted dose metric currently exists for CBCT, which is a knowledge gap that needs to be

filled if the large scale application of this technology is to be optimised (Kim, et al., 2010).

The work presented in the literature is a natural extension of previously published works regarding the CT Dose Index (CTDI) in Multi Detector CT (MDCT) (Kim, et al., 2010). In the following paragraphs, details of CBCT dose measurements extracted from the literature between 2005 and 2012 are discussed, in reverse chronological order.

In June (2011) Ding and Munro used MC BEAMnrc and DOSXYZnrc to simulate the CBCT dose for the new version 1.4 OBI-CBCT. Two modes of the CBCT were used; standard dose head, and pelvis mode. For a head scan the dose to eye, brain, brain stem, and spinal cord are 0.14, 0.15, 0.13 and 0.13 cGy which are approximately 38% lower compared to standard Head scan in OBI version 1.3. For pelvic mode the dose to prostate, rectum, bladder, and femoral heads are 0.8, 0.86, 0.87 and 1.5 cGy, which are approximately 43% lower compared to the pelvis scan in OBI version 1.3. This study concluded that the newly designed x-ray source is able to reduce CBCT image dose to the patient without compromising image quality (Ding & Munro, 2011).

Feng et al., (2011) also used MC BEAMnrc and DOSXYZnrc to simulate and measure the CBCT dose from the new version 1.4 OBI-CBCT. They found that Monte Carlo dose calculation for a RANDO head phantom indicated that the posterior right side of the head receives a higher dose, due to the posterior KV scan from the gantry in going from 290^{o} to 90^{o} (Feng, et al., 2011).

Hyer et al., (2010) used the two CBCT systems currently available on medical linear accelerators, namely the XVI and the OBI to measure patient organ doses from such images (Hyer, et al., 2010). The dose measurements were performed using a fibre-optic coupled (FOC) dosimetry system along with an adult anthropomorphic phantom for three different clinically relevant scan sites: head, chest, and pelvis. The results indicated that for the XVI, the dose to the lens of the eye (1.07 mGy) was highest in a head scan; thyroid dose (19.24 mGy) was highest in a chest scan; and gonad dose (29 mGy) was highest in a pelvis scan, as one would expect. For the OBI, brain dose (3.01

mGy) was highest in a head scan; breast dose (5.34 mGy) was highest in a chest scan; and gonad dose (34.61 mGy) was highest in a pelvis scan. Measurements of image quality using CATPhan 440 demonstrated that the OBI provided superior image quality for all protocol mode settings, with better spatial resolution and low-contrast detectability (Hyer, et al., 2010).

Ding et al., (2009), used the Vanderbilt-Monte-Carlo-Beam-Calibration (VMCBC), to simulate Varian OBI dose. This was performed to determine the magnitude of additional imaging doses to patients' radiosensitive organs from CBCT. Five adult and three paediatric patients were included in this analysis. Doses calculated in adult patients' eyes, spinal cord, brain and cervical vertebrae were 7, 5, 5, and 18 cGy, respectively. Doses were higher in paediatric patients at all of the same bodily sites; 8, 6, 6, and 23 cGy, respectively. This provides reason for a precautionary approach when treating paediatric patients. Using version 1.3 of the Varian OBI, this group also found that at a total skin dose of 1.5-2 Gy, the patient may also receive a bone dose of 4.5-8.4 Gy from IGRT in roughly 25-35 treatment fractions. These findings provide required data for clinicians to make informed decisions concerning additional imaging doses. The dose to bone is two- to four-times greater than dose to soft tissue for kV X-rays, caused by increased mass-energy absorption coefficients associated with high atomic number materials resulting from photoelectric effect interactions within bone. This is a potential concern, especially for paediatric patients. In addition, these patients, due to age-based selection, represent extremes of patient size and show that the range of radiation doses resulting from an imaging guidance procedure is highly size dependent (Ding & Coffey, 2009).

Kan et al., (2008) used an anthropomorphic phantom to perform a comprehensive study that determined the effective dose to 26 organs. The measurements were repeated for three different scan sites: head and neck, chest, and pelvis. This group utilised the Lithium Fluoride thermoluminescent response of Harshaw micro-cube dosimeters (TLD-100), and placed at least two TLDs at each organ site. CBCT images were obtained using the Varian OBI version 1.3 at two acquisition settings: 125 kV, 80 mA, 25 ms (standard mode) and 125 kV, 40 mA, 10 ms (low-dose mode), both with 150 cm source-to-image distance. When using the standard dose mode, the

following doses were calculated; 6.6, 6.22, 4.8, 4.08, 11.08 and 5.34 cGy, to the skin surface, eye, brain, spinal cord, thyroid, and lung, respectively. The low dose mode gave approximately one fifth of the dose from the standard mode. In conclusion, the research group calculated an approximate range of dose, ~1.5 to 2 Gy from CBCT at various organs when exposed to 35 fractions during the radiotherapy treatment. This dose was estimated to lead to an additional secondary cancer risk of 3% to 4% (Kan, et al., 2008). Following the research of Kan and colleagues (2008), Hyer et al., (2010) repeated the study using the same anthropomorphic phantom and CBCT OBI Varian system but with software version 1.4 instead of 1.3 . For ease of interpretation, a comparison table has been generated (Table 2, below) to emphasise the dose differences measured in these two studies. It can be seen clearly how the dose is reduced significantly when the new version is used.

Table 2: Comparison between old and new CBCT dose.

organ	Kan et. al. (2008)	Hyer et. al. (2010)
	cGy	
brain	4.800	0.301
thyroid	11.080	0.238
esophegus	3.810	0.001
breast	4.690	0.534
lens	6.220	0.059

Song et al.. (2008) made a comparison between the two old CBCT image systems, the XVI and OBI version 1.3. For this comparison, Song and colleagues used two phantoms to represent the head and body, with diameters 18cm and 30cm respectively. These two uniform density cylindrical acrylic phantoms allow dose measurements at the centre and periphery, 2cm below the surface. The XVI used 100 and 120 kVp and estimated an average dose range of 0.1 to 3.5 cGy, with the highest dose measured using the prostate protocol with the body phantom. The OBI, on the other hand, used 125 kVp and estimated average doses from 1.1 to 8.3 cGy, with the highest dose measured using the full-fan protocol with the head phantom. These

values clearly indicate that version 1.3 of the OBI delivered higher radiation doses than the XVI at all body sites.

Kim et al., (2008) employed the point-dose measurement method to assess the radiation doses delivered by CBCT and MDCT. The doses were measured using TLDs inserted into head and body CT phantoms. The results from this group showed that the weighted CT dose index for CBCT and MDCT were 89.7±4.0 mGy and 137.0±7.4 mGy respectively, at the head phantom. For the body phantom, results were 37.9±1.4 mGy and 74.3±5.3 mGy respectively. In summary, these results show that CBCT for the head scan delivered a 35% lower dose than MDCT, and a 49% lower dose in the body scan (Kim, et al., 2008).

Wen et al., (2007) measured the daily pelvic scan dose using the Varian system v1.3. In this measurement, TLD capsules were placed on the patient's skin at the central axis of three beams, namely the anterior posterior (AP), left lateral (Lt Lat) and right lateral (Rt Lat). For all scans, a setting of 125 kV, 80 mA and 25 ms was used. CBCT scans were acquired in half-fan mode using a half bow tie filter. They concluded that, the larger the patient size the less the AP skin dose. Lateral doses did not change much with patient size; however, the Lt Lat dose was ~40% higher than the Rt Lat dose (Wen, et al., 2007).

Islam et al., (2006) used the Elekta system to measure the doses received by two water phantoms, a 30 cm diameter cylindrical shaped phantom to represent the body, and a 16 cm diameter phantom to represent the head. Doses were measured using an ion chamber and complete rotation of x-ray source with different fields of view (FOV). Depending on the FOV, the maximum dose received by the body phantom varied from 1.8 to 2.3 cGy with a 120 kVp beam, and from 2.8 to 3.5 cGy with a 140 kVp beam. For the body phantom, central and periphery doses of 1.6 cGy and 2.3 cGy, respectively were measured using the largest FOV of 26 x 26 cm^2 with the 120 kVp beam. As would be expected, doses were higher and measured to be 2.4 cGy and 3.5 cGy, respectively, when using the 140 kVp beam. For the head phantom, the doses at the centrel and periphery were 1.7 cGy and 1.8 cGy respectively, using a FOV of 15 x 26 cm^2 with a 100 kVp beam. Higher doses of 2.9 cGy and 3.0 cGy were measured

using the 120 kVp beam at the same locations (Islam, et al., 2006). These results showed that the CBCT dose is directly proportional to the tube voltage if measured on the same phantom.

L´etourneaua et al., (2005) measured the isocentre and surface doses administered by the XVI Elekta system to phantoms. Doses measured were benchmarked with helical CT doses. The XVI scans were acquired on an in-house XVI system and two water phantoms were used to represent the head (16cm in diameter) and body (32cm diameter). To the body phantom, the XVI delivered doses of 4.4 cGy and 2.8 cGy to the surface and isocentre respectively. The helical CT on the other hand, delivered doses of 2.5 cGy and 1.5 cGy to the surface and isocentre respectively, for the same phantom. To the head phantom, the XVI surface and isocentre doses were 2.7 cGy and 1.9 cGy respectively. In addition to dose measurement, the same research group studied the effect of increasing doses on image quality. It was concluded that the choice of an acceptable trade-off between image quality and image dose would vary with treatment site and the treatment strategy (L'etourneau, et al., 2005).

In summary, the literature presented above highlights that the dose to patients from the Varian OBI System v1.3 is greater than that delivered by the Elekta XVI System. However, doses are significantly reduced with the new version of the Varian OBI (version 1.4). The radiation dose to bony structures is larger than the dose to soft tissues, due to a higher attenuation coefficient within the high-density material than in low-density material. The centre of the phantom receives less dose than the surface due to the inverse square law and attenuation. Finally, although the dose from CBCT to the patient from one treatment fraction is small compared with the therapeutic dose, the total CBCT dose from all treatment fractions may be equivalent to the therapeutic dose given in one fraction. This cumulative effect could increase the probability of inducing secondary cancer by 2-4 % (Kan, et al., 2008).

1.3.2 Cone Beam CT based treatment planning

The basic rationale behind using CBCT scan images for treatment planning relies on utilising Hounsfield unit (HU) numbers, otherwise known as CT numbers. The obtained image is utilised by the treatment planning system algorithm by the generation of a HU-to-Electron density relationship (Richter, et al., 2008, Hatton, et al., 2009 and Rong, et al., 2010). This relationship forms the basis of dose calculations based on a CBCT data set. Many factors play significant roles in generating the HU-to-Electron density relationship, such as kV source energy, the tube current of the kV source, and the acquisition mode of the image (Hatton, et al., 2009). Under some conditions, the position of the insertion inside the phantoms also affects the HU number. It is accepted that the HU numbers obtained from the CBCT scanner are not absolute values for each electron density (Richter, et al., 2008). In other words, each mode setting of the CBCT images results in a different HU-to-Electron density relationship. In addition, the human body is composed of various tissues and cavities, with different electron densities. These variations make it difficult to obtain reliable HU numbers and even more challenging to calculate an accurate HU-to-Electron density relationship.

It has been demonstrated that the relationship between the HU-to-Electron density is relatively linear, where HU numbers increase proportionally with electron density, although there are some exceptions to this relationship (Saw, et al., 2005). Normally, a specific relationship is established once for a given CT-scanner, to enable dose calculation in the treatment planning system. However, the relationship is not the same for all CBCT scanners due to differences in image quality between CT and CBCT, and the large contribution of radiation scattering (L'etourneau, et al., 2005). These factors complicate the relationship and make it difficult to generate a standardised relationship that could be applied across all radiotherapy centres. Therefore, at present, individual HU-to-Electron density relationships must be established from individual CBCT scanner parameters.

A number of papers have recently been published on the relationship between the CBCT imaging data set and HU-to-Electron density relationship. In all of the

publications, the intention was to calibrate HU numbers from CBCT scans to electron density. This was achieved using doses measured in phantoms and comparing the dose calculation results utilising the CT scan data. The very first attempt to use CBCT data set for dose calculation was made by Lo and colleagues in 2005, who developed a method to map electron density information from planning CT to CBCT for a dose verification calculation. In this publication, the method was described as 'a novel strategy for accurate dose calculation based on the CBCT' however; the authors unfortunately concluded that the CBCT data sets would yield unacceptable errors if used clinically for dose calculation. Furthermore, the authors stated that image quality required improvement if used for this purpose (Lo et al., 2005).

Since the initial attempt, a number of papers have used the CBCT data sets for the auto-delineation of tumours (Peng, et al., 2006), verification of the dose (Chi, et al., 2007), treatment planning (Rong, et al., 2010), and for direct dose calculation (Paliwal, et al., 2006). Some authors have used the data to calculate and verify the dose directly and named the technique "dose of the day" (Zijtveld, et al., 2007) while others have used it for treatment-based and adaptive radiotherapy (Richter, et al., 2008). All of these attempts were made following thorough investigation into how the HU-to-Electron density relationship can be utilised. Different authors have used different approaches to determine the HU-to-Electron density relationship, depending on the specific CBCT mode settings employed.

Recently in 2010, Rong et. al., studied the impact of changing three imaging parameters; mAs, source-image distance and cone angle, and size, on the accuracy of the HU number and HU-to-Electron density relationship using the Varian CBCT v-1.3 (Rong, et al., 2010). Three different configurations of the CIRS phantom were used to represent the head, lung and lower body (pelvis/abdomen) regions. Based on this study, it was shown that CBCT imaging is a feasible option for dose computation in adaptive radiotherapy approaches, if site-specific calibration is applied.

In 2008, Richter et al., investigated the feasibility and accuracy of dose calculation using CBCT data sets. In this study, two systems were used; the Elekta XVI, and the conventional multi-slice CT as a reference image (Richter, et al., 2008). Two types of phantoms were also used in the investigation; the CATPhan (CATPhan CTP503), and

the Gammex RMI (Gammex RMI 467). The CATPhan phantom was selected to investigate the influences of scan parameters (tube voltage, filter and collimator, and rotation angle).The second phantom; Gammex, was used to generate the relationship between the density of different materials and their corresponding CT values. Depending on the CBCT acquisition parameters used, there were large variations in the CT values between the CT and CBCT. It was shown that CT values were highly influenced by specific CBCT image acquisition parameters, namely, tube voltage, filtering and collimation. The researchers concluded that a correction of CT values was necessary for dose calculation with cone beam data sets. Three HU-to-Electron density tables specific to CBCT image acquisition parameters and specific to anatomical regions including the pelvis, thorax and head and neck are now considered to be sufficient for this purpose. Once the HU-to-Electron density tables are generated correctly, direct dose calculation from CBCT datasets is possible without the need for reference to CT for pixel value calibration.

The use of a moving phantom for dose calculation was investigated by Yang et al., in 2007 (Yang, et al., 2007). Specifically, Yang and colleagues evaluated the achievable accuracy when using a kV CBCT for dose calculation using the OBI Varian system. This group obtained the relative electron density as a function of HU, for both planning CT and CBCT using a Catphan-600 calibration phantom. Their results showed a 99% agreement when using the static phantom, but a notable difference in dose distributions with the moving phantom due to the appearance of motion artefacts in CBCT images. The study concluded that CBCT can be employed directly for dose calculation for disease sites such as the head and neck and prostate, where motion artefacts are minimal, but not for more mobile tissues.

Despite the above-mentioned findings, the HU-to-Electron density relationship can be obtained using any phantom equipped with different insertions of different materials with different electron densities. Huauqun and Hang, (2009) advised against the use of the CatPhan, since it was designed mainly for quality assurance of CBCT, making the insertions too small for the attainment of correct HU numbers with less uncertainty (Guan & Dong, 2009). For instance, the insertion of the CatPhan-600 phantom is 10 mm in diameter, whereas in the CIRS-062A it is approximately three times larger (30.5 mm diameter).

1.4 Why this research and what does it contribute to the field of IGRT radiotherapy?

This research seeks to complement the published research by more fully investigating the concomitant dose received from the OBI version 1.4. This includes:

1. Measuring the CBCT for the full range of modes and treatment sites.
2. Finding the relationship between CBCT doses with the patient size.
3. Investigating more fully the induced cancer risk.

The research then investigated fully the possibility of employing directly such CBCT images from OBI version 1.4 in treatment planning. This involves:

1. Calibrating the CBCT scan images, (HU-to-ED).
2. Testing the ability of the CBCT to perform calculation for simple and complex (IMRT) dose distribution.

The aforementioned steps are considered in order to reach a claim that the CBCT scan images can be used for adaptive radiotherapy. At the beginning of this research, the published literature stated clearly that the CBCT images cannot be used for adaptive radiotherapy due to high dose per scan and that such scan images cannot be used for direct dose calculation (Peng, et al., 2006) (Wang, et al., 2006). These findings presented the challenge to investigate more deeply the new version of the OBI CBCT v 1.4. Very recent publications suggested that the new version OBI CBCT v 1.4 doses are 15 times (head), 5 times (thorax) and 2 times (Pelvis) lower than the old OBI 1.3. The data determined in this research are compared with these finding (Ding & Munro, 2011).

2 CBCT dose measurements

In this work, two methods for determining CBCT doses have been investigated. The first method of determining the CBCT dose involves the use of phantoms; herein three types of phantoms were used. Doses were measured using TLDs in a RANDO phantom, adapted cylindrical water phantoms of different sizes and a CIRS-062-A phantom. The second method of dose assessment is theoretical calculations using a 2D mathematical model and 3D Monte Carlo (MC) simulation of CBCT. The MC simulation employed Monte Carlo N-Particles MCNP-4c and BEAMnrc and DOSXYZnrc codes (Rogers, et al., 1995, Nelson, et al., 1985 and Walters, et al., 2002). A detailed report of the CBCT MC simulation using the MCNP-4c, BEAMnrc and DOSXYZnrc with dose calculation procedures and results is presented in chapter 3.

This chapter begins by providing the technical details of each phantom selected for dose measurement. This is followed by description on how TLDs were prepared for the dose measurement. Doses applied to each phantom are discussed separately from section 2.3 to 2.5. A mathematical model generated as an attempt to calculate the CBCT dose is included in this chapter. In addition, a 3D MC simulation (using MCNP-4C and BEAMnrc/DOSXYZnrc with a cylindrical water phantom) was conducted and the relationship between dose verses phantom size is presented. A risk assessment of the CBCT dose and its use on a daily basis is also considered as an aid to facilitating the use of this technology in clinical practice. Finally, in the last section of this chapter, a comparison is made between the doses received by the phantoms employed herein and literature values, in order to assess the reliability and generalizability of the data.

2.1 Phantoms used in this study

Three phantoms have been used to specifically address different aspects of CBCT dose. For example, some phantoms were selected for calibration of CBCT while others were selected for dose calculation and MC simulation. The phantoms were the RANDO phantom, the Computerized Imaging Reference Systems (CIRS) model CIRS-062A phantom, and five adapted water phantoms. Relevant details of each phantom are provided in the following sections.

2.1.1 RANDO phantom

The Alderson Radiation Therapy (ART) phantom and its early version, the Alderson RANDO phantom, have been in use for over 30 years (The RANDO phantom, The Phantom Laboratory, Salem, NY). The ART female phantom was used in this research, with measurements taken on the head phantom only, Figure 10. The female ART phantom represents a 155 cm tall and 50 kg individual, designed to represent the average female body. The phantom is transected-horizontally into 2.5 cm thick slices. Each slice contains holes for TLD insertion, except the top head slice (Figure 10). These slices are numbered and slice number 4, 7, 9 and 11 are shown in Figure 11 as examples.

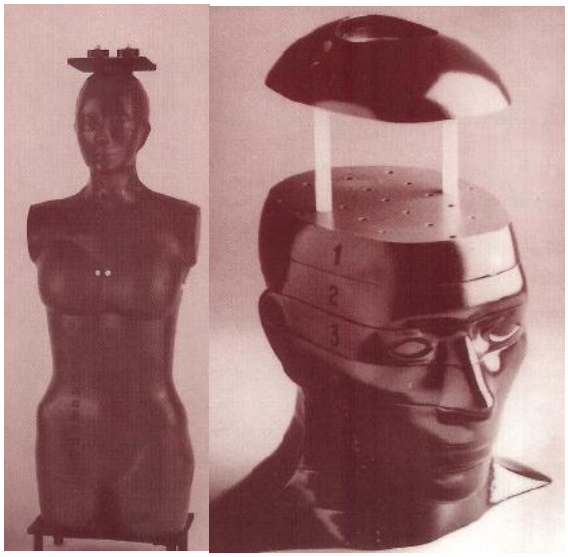

Figure 10: The ART female head phantom. The image on the right shows the top slice without a TLD insertion.

Figure 11: Side view of the ART female phantom slice. Top right and left images are slice numbers 4 and 7 respectively. Bottom right and left images are slices 9 and 11 respectively.

2.1.2 Computerized Imaging Reference System CIRS-062A

The CBCT electron density phantom CIRS-062A, manufactured by Computerized Imaging Reference System INC (Norfolk, Virginia USA) (Figure 12), is an extended version of the CIRS Model 062 electron density phantoms, specifically designed for CBCT Imaging systems (CIRS Tissue Simulation and Phantom Technology, Norfolk, VA). This phantom has 17 insertions that can be positioned anywhere in the phantom. These insertions have a variety of densities enabling the study of HU number changes and can thus be used for any calibration.

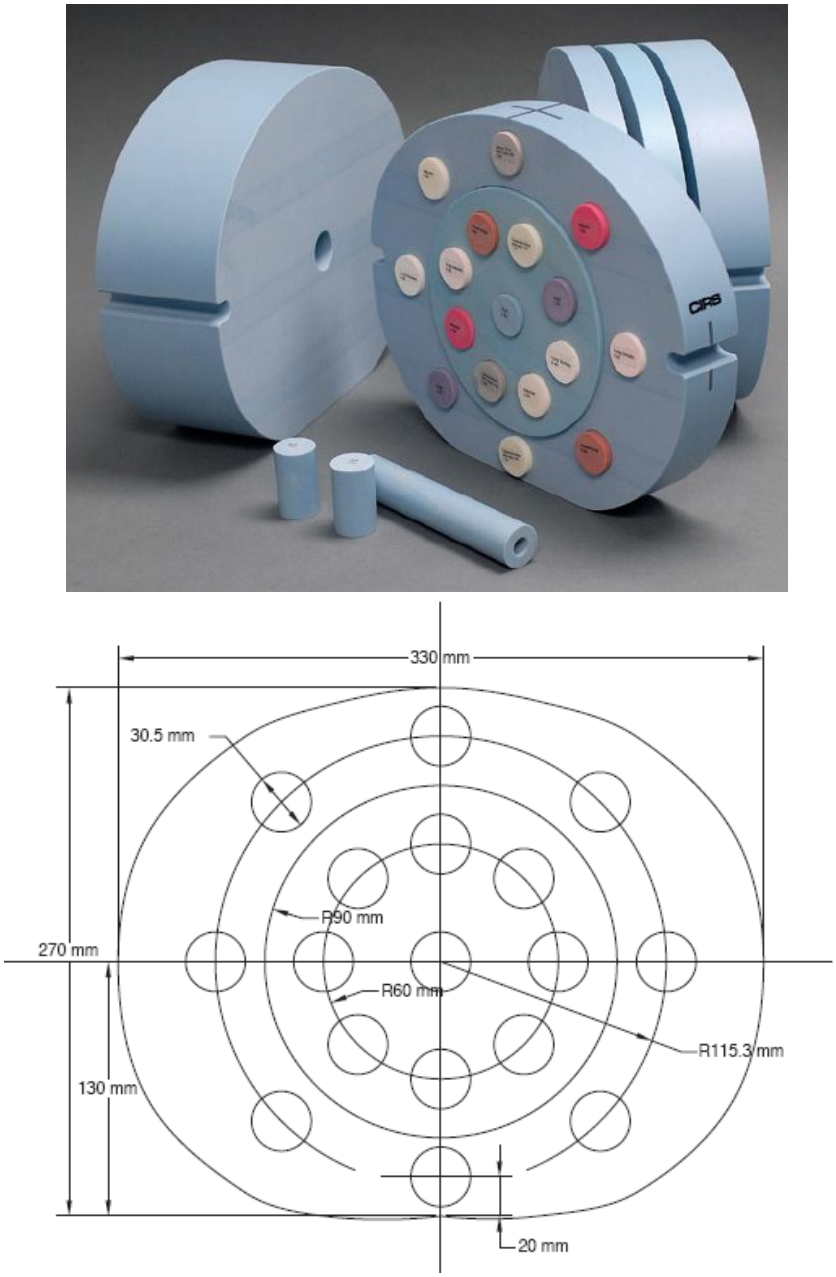

Figure 12: CIRS-062A phantom representation of the human body. Full phantom with insertions and slices (top). Cross sectional view of the slice, which contains the insertion positions (bottom).

The CIRS-062A phantom has the dimensions 25 cm x 33 cm x 27 cm (depth x width x height) and is composed of plastic (epoxy resin based) and water® and weighs 18.15 Kg. The insertions are made from tissue-equivalent materials of dimensions 3 cm x 5 cm; two represent the lung (inhale and exhale) and other insertions represent adipose, breast, muscle, liver and bone at 200 mg/cm^3 and 800 mg/cm^3 densities. Insert densities are summarised in Table 3.

Table 3: Physical and electron density of CIRS-062A phantom insertions (Varian, 2008).

Material		Physical Density g/cm^3	Electron density per cm^3 x 10^{23}
1	Lung (inhale)	0.20	0.634
2	Lung (exhale)	0.50	1.632
3	Adipose	0.96	3.170
4	Breast	0.99	3.261
5	H_2O syringe	1.00	3.340
6	Muscle	1.06	3.483
7	Liver	1.07	3.516
8	Trabecular bone	1.16	3.730
9	Dense bone	1.53	4.862

The CIRS-062A phantom is divided into 5 slices, as shown in Figure 12. There are two possible configurations of the phantom, which are determined by the position of the slice that contains the insertions (Figure 13). These configurations are named the central axis and offset configurations.

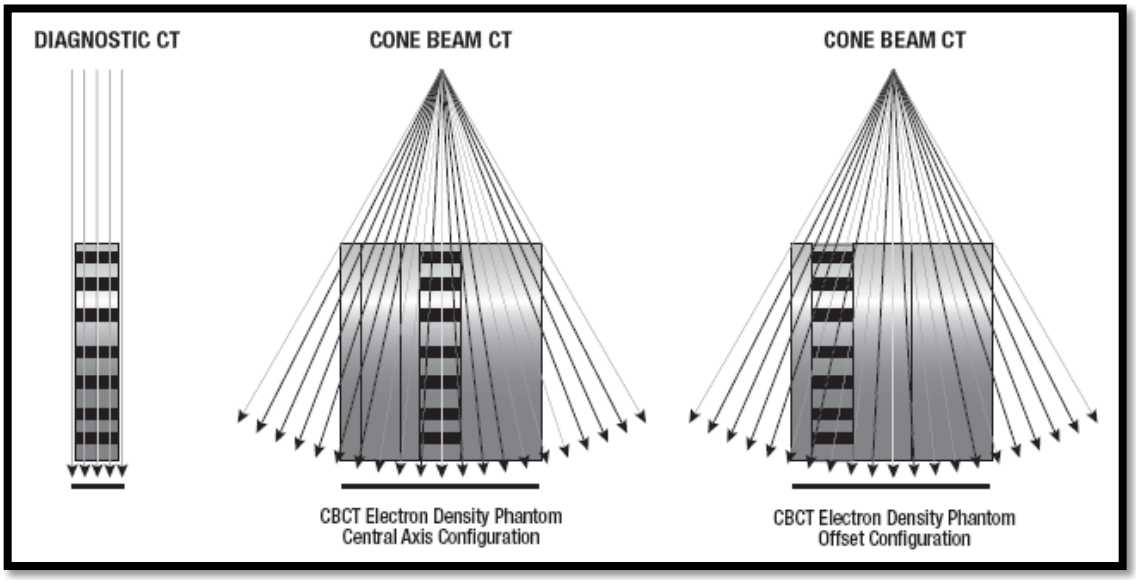

Figure 13: Possible configurations of the CIRS phantom

2.1.3 Water phantoms

Five water phantoms of radius 5.0, 5.95, 7.15, 8.6 and 10.25 cm were employed in this research. Each phantom is designed to allow measurement of the CBCT imaging dose in the centre of the phantom (C) and at the surface on the left (L), right (R), anterior (A) and posterior (P) positions. These phantoms were manufactured at the Royal Surrey County Hospital (RSCH) workshop, Figure 14.

Figure 14: Manufactured phantoms at RSCH.

Figure 14 shows how the phantom has been adapted by the generation of a hole to allow TLD insertion for dose measurements inside the water phantom. The dose at each of the above-named locations were measured using three TLDs in each position. TLDs were inserted into a small, light, opaque container and then placed on the phantom with a positional uncertainty of ± 0.5 cm. Later, the phantom was placed at the centre of the treatment couch. This arrangement is depicted in Figure 15.

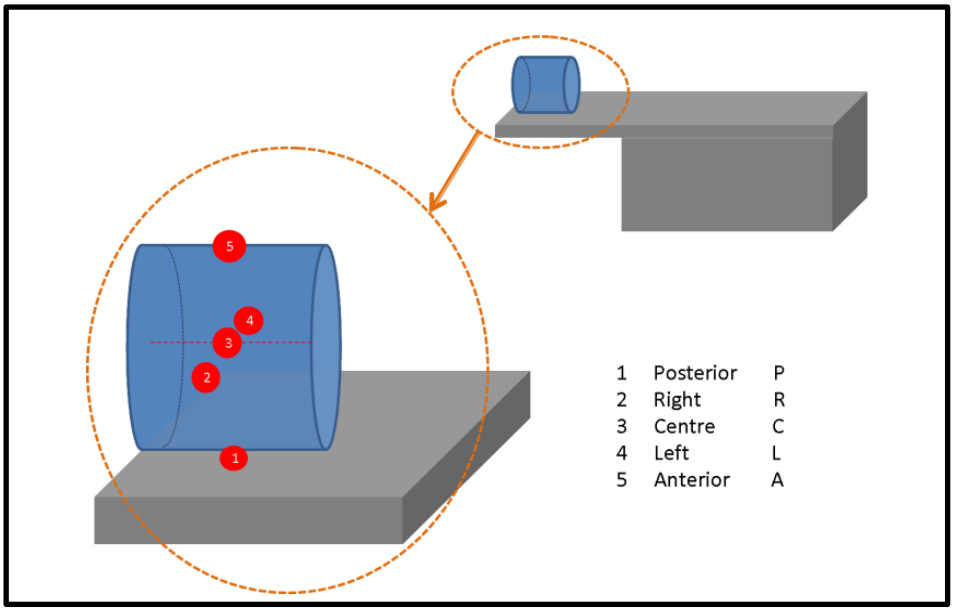

Figure 15: Positions of the TLDs on/in the water phantom.

2.2 TLD preparation and calibration

Preparing the phantoms and TLDs correctly is a critical part of the CBCT dose measurement process, to ensure that the dose is measured and readout accurately. It has been suggested by Kan and colleagues that the best way to calibrate the TLDs is through the use of a radiotherapy superficial X-ray unit, the PANTAK DXT 300 (Kan, et al., 2008). TLD calibration by this method is more consistent and results are expected to be more accurate and reliable. Beam calibration is generally maintained within tight tolerance, whereas diagnostic beams have a much more variable output. Calibrations were carried out twice to observe the sensitivity of each TLD.

2.2.1 TLD Calibration using the PANTAK DXT300

In this study calibration was performed using the radiotherapy superficial X-ray unit (PANTAK DXT 300) which as stated is more accurate and reliable since the unit is calibrated with a much lower uncertainty in the Radiotherapy Department than the units employed within the Radiology Department. The Farmer Dosimeter (model no. NE 2570) was used to measure the dose from the X-ray source in Gy. A total of 50 TLDs (3.2 x 3.2 x 0.9-mm) were placed side by side on medium density fibre board (MDF) where the ion chamber were setting in the surface of the MDF. The X-ray beams, 90 kV with half value layer (HVL) of 2.5 mm Al, filter of 1.65 mm Al and 20 mA, were directed perpendicularly to the MDF at a 60 cm source-to-MDF distance.

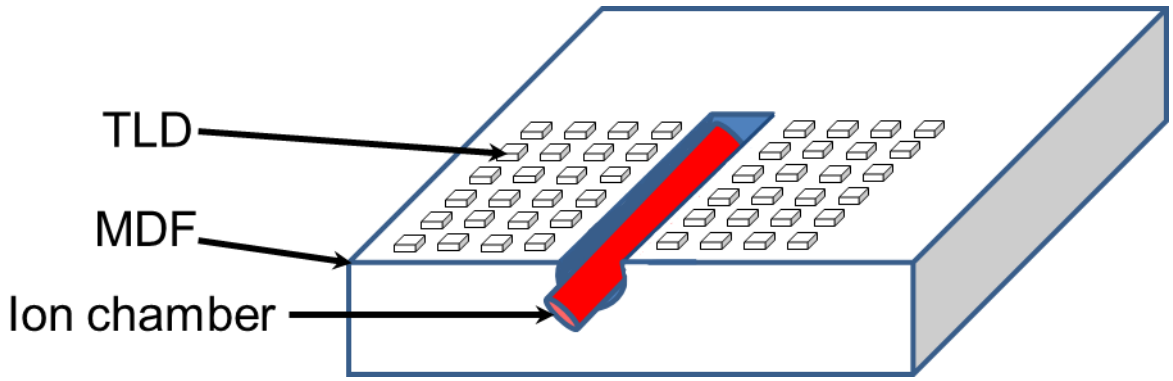

Figure 16: Illustration of TLD placement with the Ion-chamber on the surface of the medium density fiber bord (MDF).

To calculate the absorbed dose obtained by each TLD, the Institute of Physics and Engineering in Medicine and Biology (IPEMB) 1996 protocol for low energy X-rays was used to measure the ion chamber reading (Klevenhagen, et al., 1996) based on the following formula:

$$D_{W,Q} = M_Q \times N_{K,Q} \times \left[\left(\frac{\mu}{\rho} \right)_{W,air} \right]_Q$$

Where; Q is the user's energy measured in terms of HVL; M_Q is the corrected electrometer reading in Coulomb (C) for the ion chamber at the user's energy Q, with a particular treatment cone. $N_{k,Q}$ in Gy/C is the air kerma calibration factor for the ion chamber at the user's energy Q. Finally, $[(\mu/\rho)_{w,\ air}]_{\ Q}$ is the ratio of mass energy absorption coefficient of water to air at the user's energy Q.

The temperature and pressure (T/P) correction is applied to the standard temperature and pressure (STP) of 20^0C and 760mmHg. The calibration using the PANTAK was performed twice and the data for both measurements are shown in Table 4.

Table 4: Setup parameters and results for the PANTAK-300 measurements.

	First calibration	Second calibration
Beam & applicator	90kV, Filter 1, C8/30	90kV, Filter 1, C8/30
Calibration factor (N_k)	0.887	0.887
Energy absorption factor (μ/ρ)	1.019	1.019
Room temperature ^{0}C	21	20
Pressure mmHg	750.7	735.25
T/P Correction	1.016	1.034
Set dose (MU)	8	8
Ion chamber reading	2.2	2.13
Measured output (cGy/MU)	2.02	1.99

The TLDs were then inserted into the Harshaw 4500 reader (Harshaw Thermo Electron, Solon, USA) and reading in nC were obtained. Then the reading from the

ion chamber value in each calibration was divided by the TLD reading in nC and the total dose measurement using TLD, ion chamber and water measurement was calculated using the following expression:

$$TLD\ dose\ in\ cGy = \frac{D(IC)\_MDF}{R(TLD)\_MDF} \times R(TLD)\_water$$

Where D(IC) is the dose to ion chamber, R(TLD)_MDF and R(TLD)_water in the TLD reading during the MDF calibration and water measurement respectively. Following this, individual calibration factors (CF) were calculated by dividing the measured output value in Gy/MU by the TLD reading in nC. The percentage difference between the two measurements was calculated using the expression below. The differences between the obtained calibration factors in both cases are shown in Figure 17.

$$Percentage\ \ difference = \left(\frac{CF_{1n}}{CF_{2n}} \times 100 \right) - 100$$

Where CF is the calibration factor and n is the number of the selected TLDs. TLD numbers range from 1 to 58, but numbers 5, 11 and14 are missing.

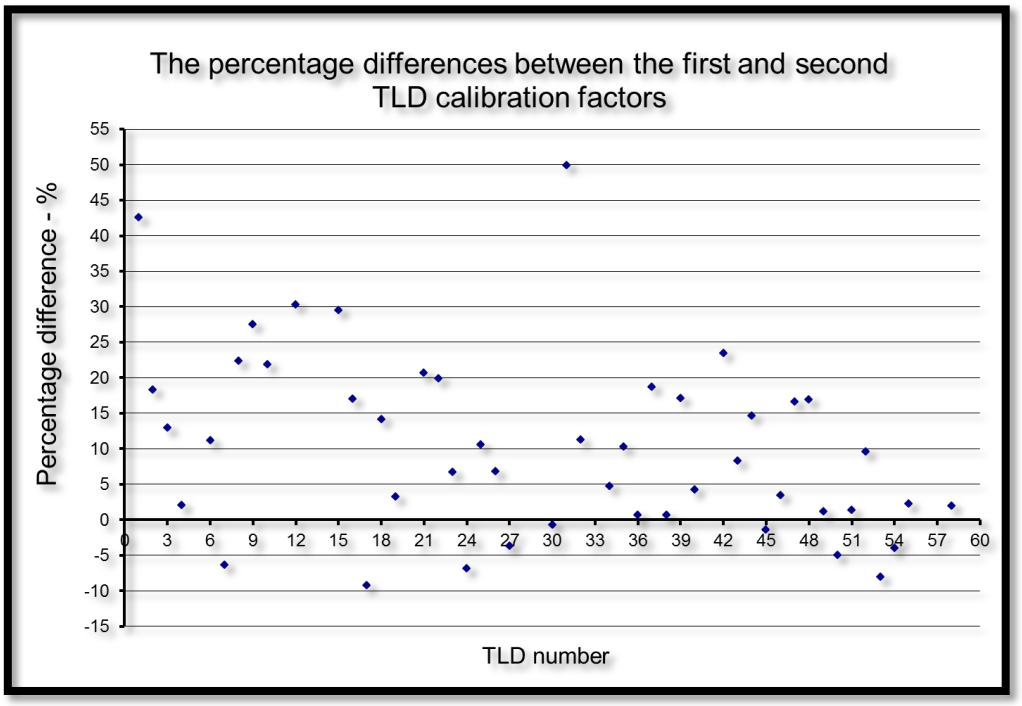

Figure 17: The percentage difference in the TLD calibration factor in both measurements

TLDs with percentage differences of more than 10% were eliminated from future use whereas those with less than a 10% difference were accepted and used for dose measurements. The mean values for the latter TLDs were used as calibration factors whenever each TLD was used for a CBCT measurement.

2.2.2 Discussions of TLD calibration

Measurements using TLDs always involve some degree of uncertainty. Measurements were repeated several times to reduce the effects of these fluctuations on the estimated dose measurements. Using the presented methodology uncertainty introduced during the calibration stage, the setup procedure when TLDs were placed on MDF, and when reading the nC result from the TLD reader. Uncertainty is also generated from the radiotherapy superficial X-ray unit beam output and contributes to the overall uncertainty.

RANDO CBCT dose measurements, were repeated twice and average results are presented in the next section, 2.3. Each CBCT dose measurement, involved averaging the readings from three TLDs. If the reading gave an anomalous value, the measurement was repeated using different TLDs. The reason for such unexpected results may be a consequence of practical necessity. For example, moving TLDs from a low-radiation location to a high-radiation location may result in background TLD. Water contamination, when TLDs are inserted into the centre of the water phantom, can also contribute to erroneous readings.

The total uncertainty associated with the TLD measurements was calculated based on the estimated uncertainty of the radiotherapy superficial x-ray beam calibrations (± 1.5%), the positional uncertainty in placing the TLDS (±5 mm leading to ± 0.5% dose uncertainty), and the TLD calibration factor uncertainty (±10%). Therefore, the total estimated uncertainty is ~10% based on the following equation:

$$Total\ uncertainty = \sqrt{\left(\frac{1.5}{100}\right)^2 + \left(\frac{0.5}{100}\right)^2 + \left(\frac{10}{100}\right)^2} = 10.1\%$$

2.3 RANDO Phantom dose measurements

In this phantom, TLDs were inserted in slices numbered 2, 3, 4, 7 and 8 as explained in section 2.1.1. The exact positions of the TLDs are shown in Figure 18.

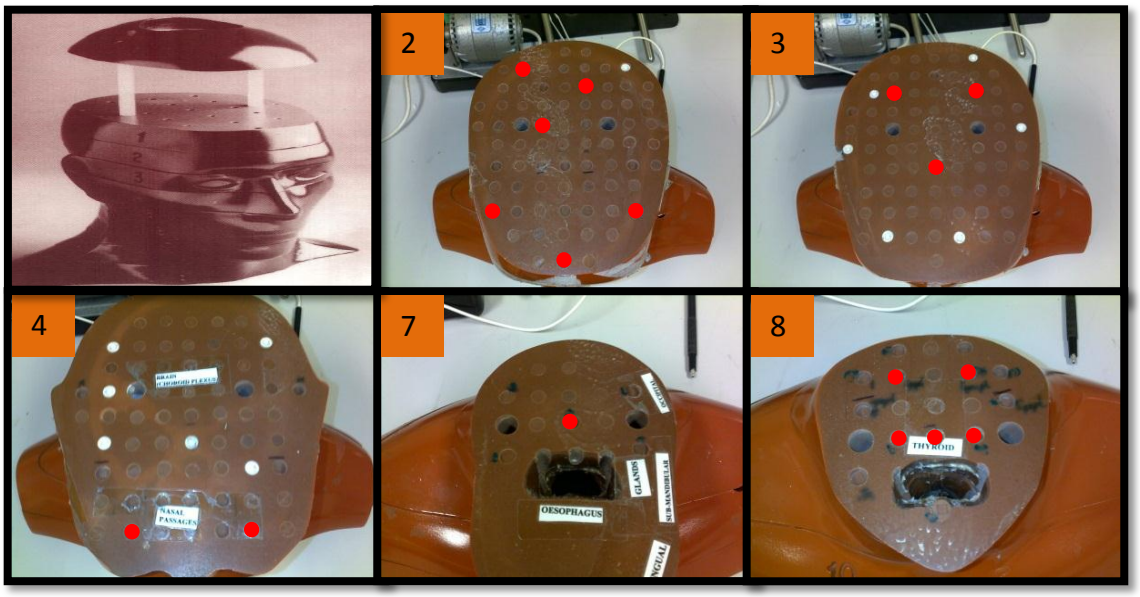

Figure 18: TLD positions in slices numbered 2, 3, 4, 7 and 8 of the RANDO head phantom.

The critical organs selected for measurement in the standard dose head mode were the eyes, thyroid, oesophagus, brain and skull bone. Slice number 4 represents the eyes; slice 7 the oesophagus; 2 and 3 the brain; 2 the skull; and 8 the thyroid (Table 5). The standard dose head mode parameters used herein were 100 kV, 20 mA and 20 ms. Kan et al., (2008) investigated the CBCT dose applied in the standard dose mode of Varian OBI version 1.3 with the following parameters: 125 kV 80 mA and 25 ms (Kan, et al., 2008). The same dosing scenario as employed by Kan et al., was used in this study, with the exception that the X-ray tube rotates 370^{o} in version 1.3 and 204^{o} in version 1.4. A similar study by Ding et al., (2009) employed a MC simulation to find CBCT doses, using version 1.3 (Ding & Coffey, 2009). Table 5 summarises the results from the two CBCT versions and demonstrates a significant reduction in concomitant dose for each organ with version 1.4.

Table 5: CBCT doses on RANDO phantom at organs with TLDs slice numbers.

	slice number	TLD no.	Current study , v-1.4		Kan et. al. v-1.3	Ding et. al. v-1.3
			cGy			
right eye	4	49	0.17 ± 0.02		6.22 ± 0.49	6
left eye	4	53	0.13 ± 0.01		6.22 ± 0.49	6
oesophagus	7	27	0.50 ± 0.05		3.81 ± 4.43	n. a.
thyroid	8	38	0.517	0.51 ± 0.05	11.08 ± 1.19	8
		30	0.478			
		45	0.508			
		25	0.417			
		4	0.614			
Brain	2	35	0.261	0.3 ± 0.03	4.80 ± 0.69	5.4
	2	17	0.285			
	3	52	0.233			
	3	58	0.364			
	3	36	0.357			
bone skull	2	7	0.304	0.176 ± 0.02	n. a.	n. a.
		51	0.199			
		40	0.078			
		34	0.122			
n. a. = not applicable						

2.4 Water phantom dose measurements

Two CBCT modes were selected for this calculation regardless of the size of the phantom; the standard dose mode and the pelvis mode as they are the two most frequently used clinical settings in radiotherapy practice. Both modes also encompass the X-ray tube voltages employed in all other settings at: 100 and 125 kV. As mentioned previously, five water phantoms of radius 5.0, 5.95, 7.15, 8.6 and 10.25 cm were used. For a larger phantom size, the CIRS-062A phantom was used, which has a radius of 16.5 cm and is composed of 5 slices of tissue-equivalent material. Therefore in total 6 phantoms of different sizes were used to investigate the relationship between the CBCT dose and phantom size for two modes.

2.4.1 Standard dose head mode

In standard dose head mode, the X-ray source rotates anti-clockwise for all measurements, starting from an angle of 292^{o} and stopping at an angle of 88^{o}. This gives a 204^{o} rotation instead of 200^{o}, as stated in the user manual (Table 1) and an additional 20^{o} arc of direct exposure to the R-position compared with the L- position. The experimental results showing the relationship between the CBCT dose at each position on the phantom and the phantom size using the standard dose head mode are shown in Figure 19. The trend lines are power fitting functions, which have been added using Origin v8 to ease the interpretation of the data points.

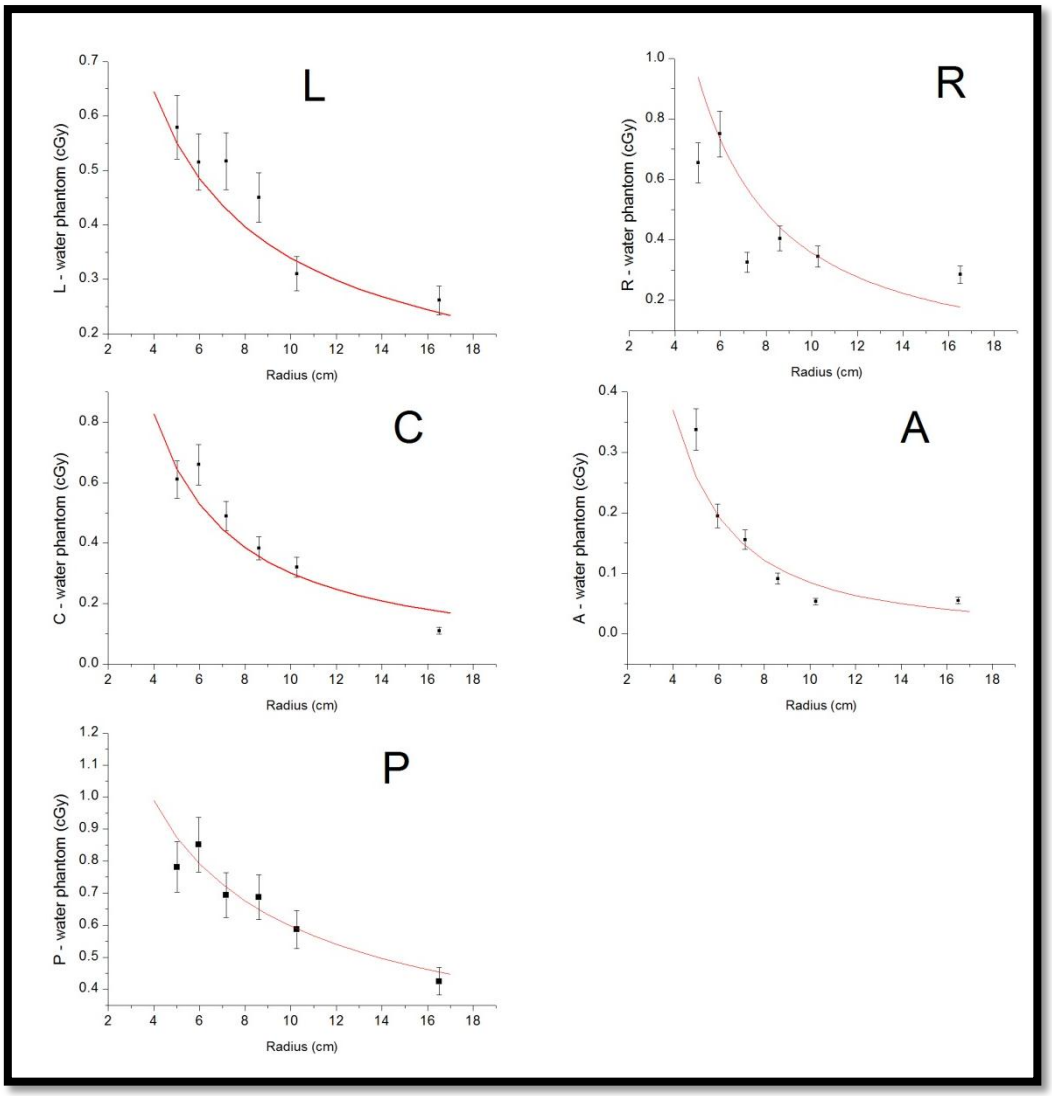

Figure 19: Relationship between phantom size and CBCT v 1.4 concomitant dose using the standard dose head mode. L = left, P = posterior, R = right, C = centre and A = anterior.

2.4.2 Pelvis mode

In the pelvis mode, the X-ray source moves clockwise from 178^{o} and stops at 182^{o}, which gives a total rotation of 364^{o}. The pelvis mode has been designed so that both the start and end positions of the X-ray source are beneath the treatment couch. The experimental measurements determining the relationship between the CBCT dose at each position on the phantom and phantom size using the pelvis mode are shown in Figure 20.

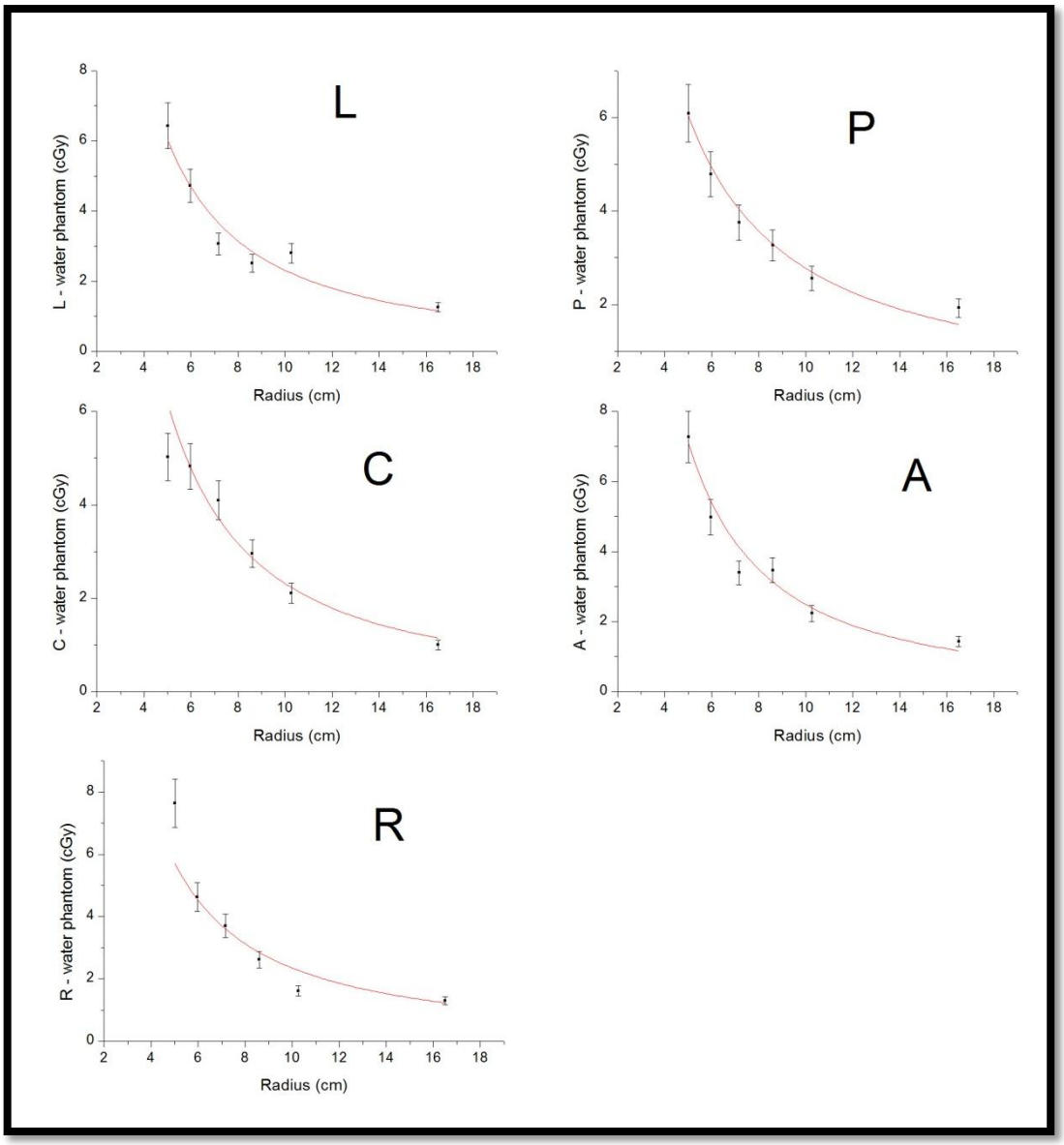

Figure 20: Relationship between phantom size and CBCT v1.4 dose using the Pelvis mode. L = left, P = posterior, R = right, C = centre and A = anterior.

The relationships shown in Figure 19 and Figure 20 were modelled by fitting a power curve in the form Y=ax^b, where Y represents dose in cGy, x represents the phantom radius, a is the magnitude of the dose, and b controls the degree of the exponential. The values of a, and b are shown in Table 6. These power curves are in good agreement with measurements presented herein, with the exception of position R (R Sqr. = 0.541) for the standard dose mode. It is assumed that this disagreement may be due to the proximity of position R to the start of the X-ray source rotation position and instabilities in X-ray output at beam switch on.

Table 6: Factor a and b values from the fitted exponential curve equation

	a	B	R Sqr.	a	B	R Sqr.
	Standard dose mode			Pelvis mode		
P	2.1	-0.6	0.950	37.1	-1.1	0.990
A	3.4	-1.6	0.973	81.9	-1.5	0.967
L	1.7	-0.7	0.910	55.6	-1.4	0.956
R	3.9	-0.9	0.541	44.9	-1.3	0.855
C	3.8	-1.1	0.897	59.9	-1.4	0.981

2.5 2D mathematical approach to CBCT dose measurement on water phantoms

2.5.1 Methods

A 2-D mathematical model was simulated in Microsoft EXCEL to see the accumulated transmitted radiation from a point source that rotates around a central water phantom, see Figure 21. To calculate the accumulated relative dose, the point source rotates by an increment of one degree per simulation. The start and end position of the point source was matched to the setting modes of the CBCT Varian v1.4, (Table 1). Two factors were considered when calculating the dose received from each position of the point source: the inverse square law (based on the start position of the X-ray tube as a reference point) and the attenuation coefficient of water and air.

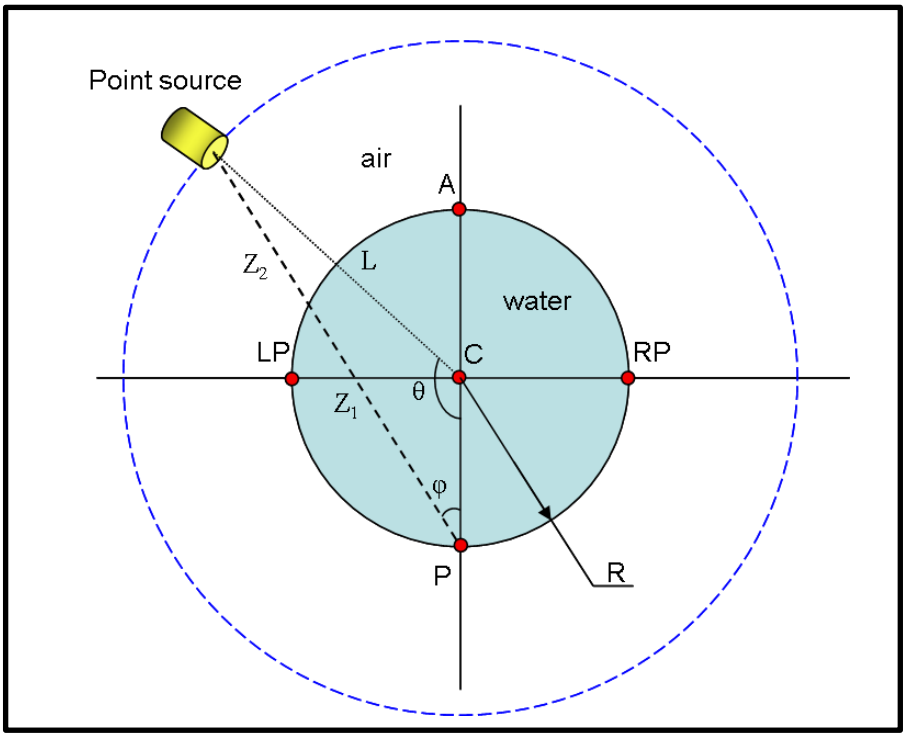

Figure 21: Illustration diagram to show the 2D mathematical approach to determine the CBCT dose.

The expressions required to combine the aforementioned factors are equations 1 and 2 as follows:

$$D(P,R,Z_1,Z_2)=\int_{\theta_1}^{\theta_2} e^{-Td(\theta)}\times\left(\frac{L}{Z_1 d(\theta)+Z_2 d(\theta)}\right)^2 d\theta \qquad \textbf{(1)}$$

$$T=Z_1(\theta)*\mu_{water}+Z_2(\theta)*\mu_{air} \qquad \textbf{(2)}$$

Where, D is the intensity of the radiation reaching position P. θ_1 and θ_2 are the start and end positions of the X-ray tube rotation. R is the radius of the phantom, and Z_1 and Z_2 are the thicknesses of the pathway of radiation in water and air, respectively.

The effect of air attenuation is negligible compared to water. The selected linear attenuation coefficients μ are 0.167 cm^{-1} and 1.95x10^{-4} cm^{-1} for water and air, at 100 keV and 0.157 cm^{-1} and 1.83x10^{-4} cm^{-1} at 125 keV respectively (Cember, 1996). Z is the initial distance between the point source and the measured dose point, where L is a fixed distance between the point source and the centre of the phantom. The value of L is assumed to be 76.75 cm (based on 153.5 cm between the source and detector surface, (Varian, 2008)) and is fixed at this value for all measurements. Z is the summation of Z_1 and Z_2 and can be calculated based on the Cosine function as shown in equation 3:

$$Z=\sqrt{R^2+L^2-2LR\cos(\theta)} \qquad \textbf{(3)}$$

Following this, the value of Z_1 can be found based on the value of φ. These two values can be found using equations 4 and 5:

$$Z_1=2\times R\cos(\varphi) \qquad \textbf{(4)}$$

$$\varphi=\arccos\left(\frac{R^2+Z^2-L^2}{2RZ}\right) \qquad \textbf{(5)}$$

The first portion of equation 1 takes into account the attenuation caused by the air and water inside the phantom. This part calculates the amount of attenuated radiation resulting from this interaction using the cross-sectional property. Thus, the probability of scattering has been ignored in the mathematical approach. The second portion in Equation 1 takes into account the inverse square law. In order to calibrate the data to the dose measurements at the hospital, a dose value of the standard dose head and pelvis mode measurement to the centre of 10 cm in radius was used.

2.5.2 Results

Figure 22 shows the transmitted radiation, and the radiation intensity from a point source that rotates around the phantom in the standard dose mode setting of CBCT. Doses at points L, A, R, and C are all decrease as the phantom size increases. Since position A is located at the top of the phantom, in the standard dose mode, the rotation of the X-ray source is underneath the treatment couch. Therefore, the radiation intensity reaching point A is decreased as the phantom size increases and almost approaches zero for very large phantoms. This is similar to the effect observed at the C position.

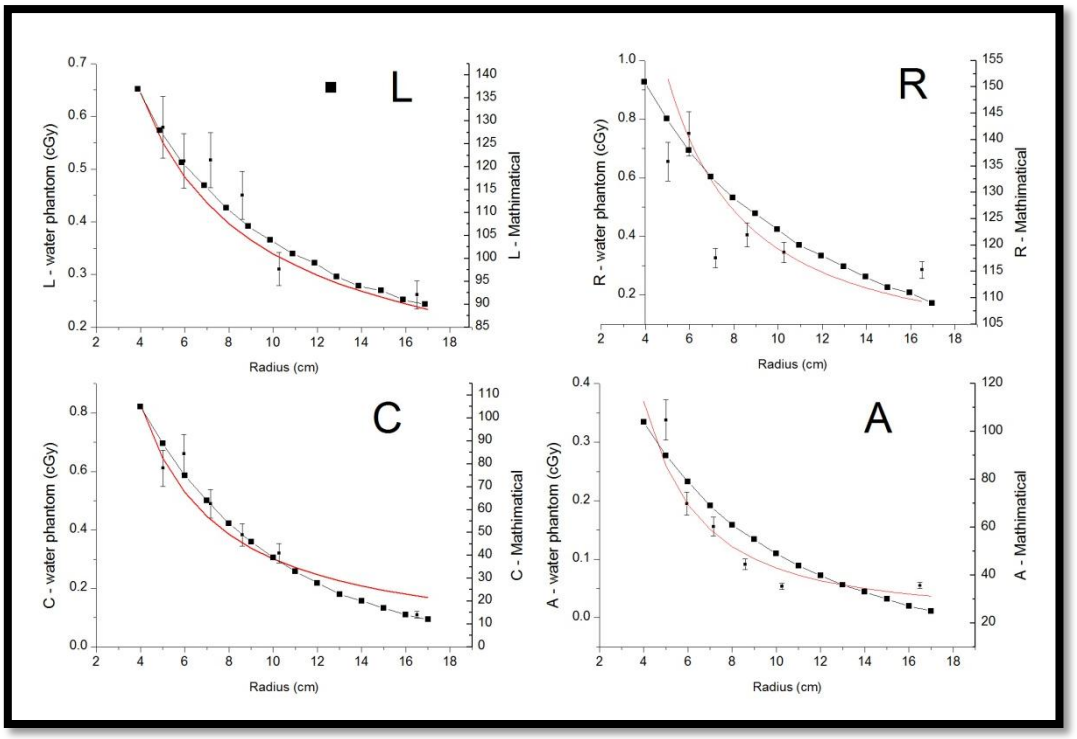

Figure 22: CBCT doses using 2D mathematical model (black) and hospital measurement (red) of the standard dose head mode. L = left, P = posterior, R = right, C = centre and A = anterior.

Figure 23 shows the transmitted radiation, and the radiation intensity from a point source that rotates around the phantom in the pelvis mode setting of CBCT. Similar results were observed in this mode to those measured in the standard dose mode. For small phantom size, radiation intensity measured in all locations decreased as the phantom size increased, including at point P. The reason for this is because the rotation of the X-ray source in the pelvis mode is 364^{o} instead of the 204^{o} rotation in the standard dose mode (Table 1; Figure 9).

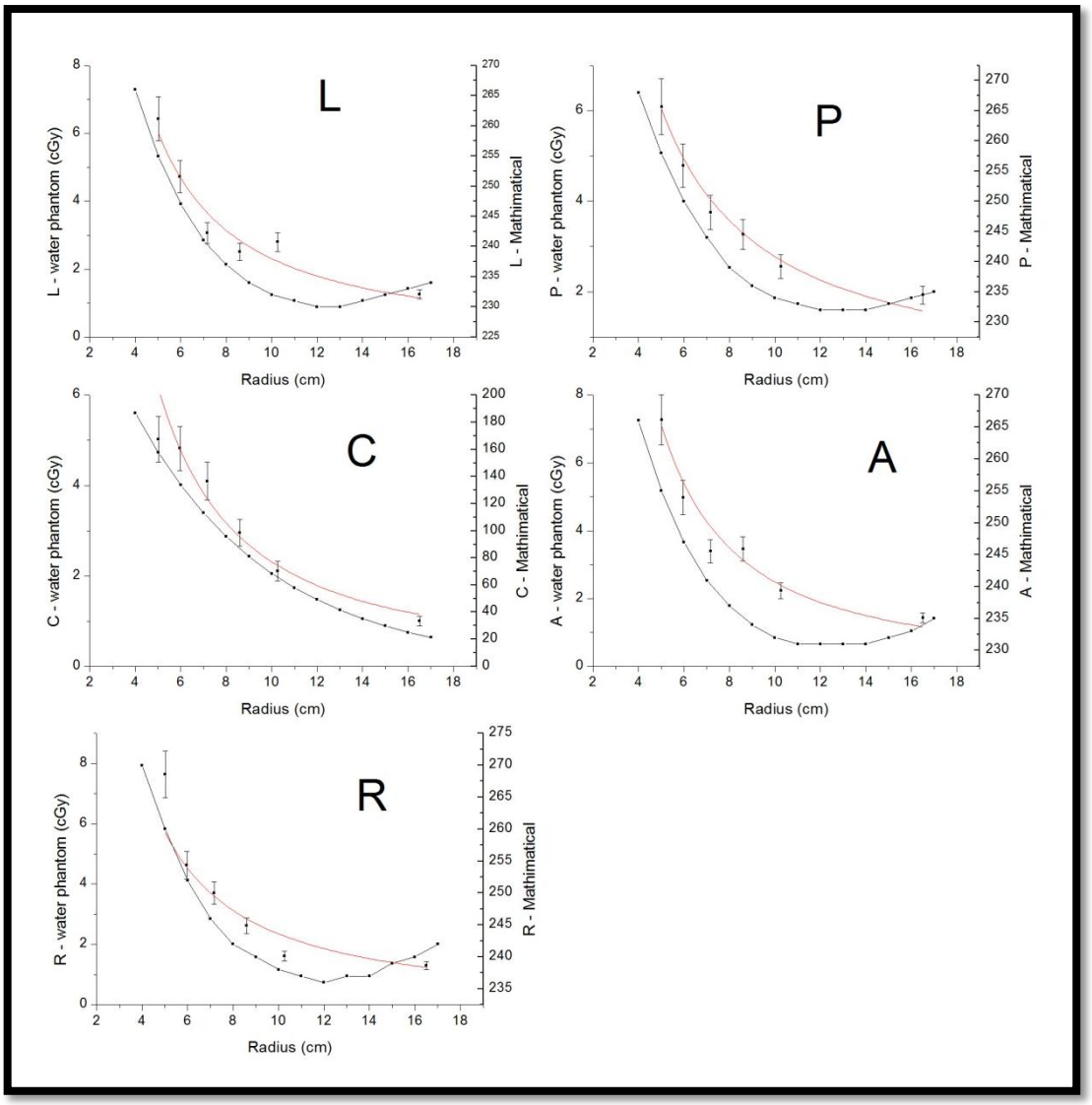

Figure 23: CBCT doses using 2D mathematical model (black) and hospital measurement (red) of the pelvis mode. L = left, P = posterior, R = right, C = centre and A = anterior.

2.5.3 Discussion and Conclusions

The 2D mathematical model is not the ideal method to represent the cone beam CT simulation, especially as the simulated beam in the 2D mathematical model is a pencil beam source hitting a 1mm thick disk with a different radius from 4 to 17 cm. This model has been used to illustrate the effect of the scattered radiation and its effect on the adjacent slices especially on position P.

The centre dose in both modes decreases as the phantom size increases. This is true of any radiation interaction and attenuation. The only difference between the two modes is that the pelvis mode yields a higher radiation dose due to the larger rotation (364^{o} instead of 204^{o}) resulting in greater exposure. These findings are in agreement within ~ ±8% and ±11% in the standard head dose and pelvis mode measurements on the water phantoms used in the RSCH (Figure 19 and Figure 20), respectively.

It was initially expected that in the standard dose mode, the R and L positions would receive the same proportion of the dose as the phantom size changed. However, following measurement, it was apparent that the R position received a higher dose than the L position since there is 20^{o} more rotation on the right than the left. The trends of the dose reduction, however, were the same for both locations and modes. The R and L positions in the pelvis mode received the same dose. Hospital dose measurements matched, within the measured uncertainty, the water phantom measurements, see Figure 19 and Figure 20. For practical reasons, the maximum phantom size used at the hospital was 32cm in diameter; therefore no dose information for larger phantoms is available. More details are provided in conclusions section 2.7.

2.6 Risk assessment of CBCT dose

Risk models based on atomic bomb survivors are valid for low dose but cannot be easily related to the higher doses received by OARs (DASU, et al., 2005). The CBCT effective dose falls into the low dose range where there are more than one possibility for calculating the risk of secondary induced cancer, this can be explained by looking at Figure 24, (Hall, 2006).

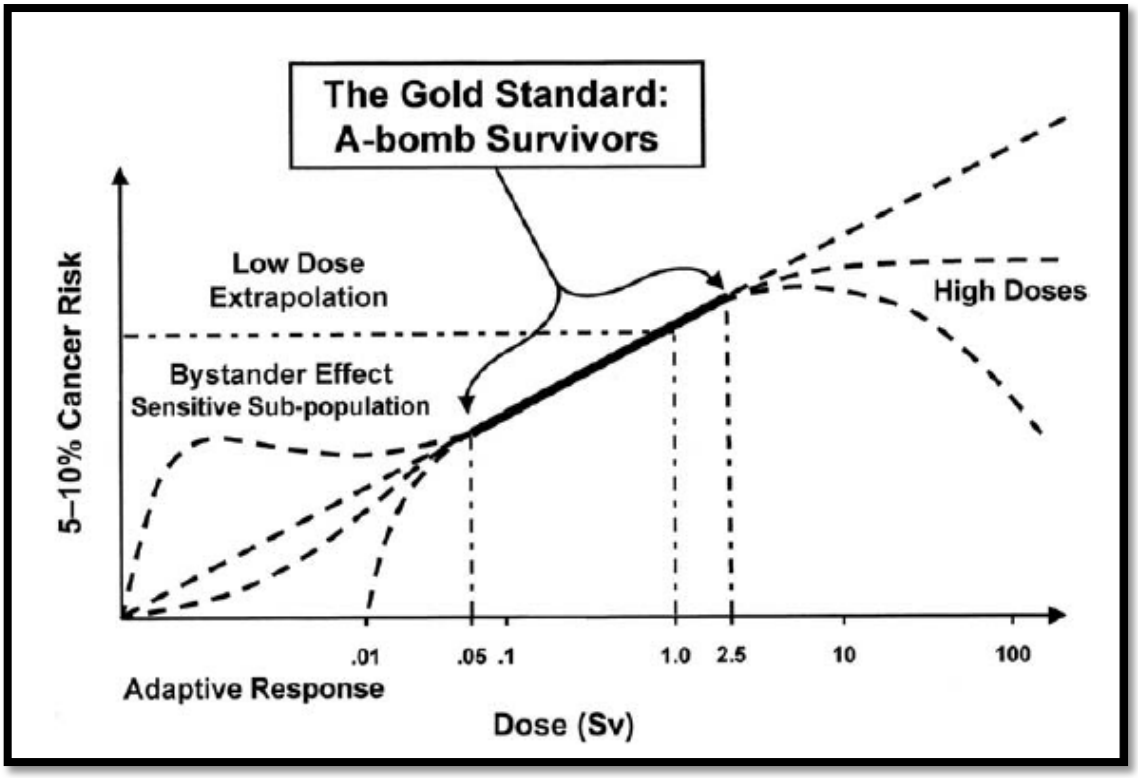

Figure 24: Illustration of the dose–response relationship for radiation induced carcinogenesis in humans. The atomic-bomb data represents the "gold standard," that is, the best quantitative data over a dose range from about 0.1 to 2.5 Gy, (Hall, 2006).

Figure 24 shows a wide range, from zero to 100 Sv, of the dose response relationship for induced cancer. It shows that the relationship is linear from 0.05 to 2.5 Sv based on atomic-bomb survivor data. At low doses, risks may be slightly higher, but they are not statistically significant and the shape of the dose response curve is uncertain (Hall, 2006). There are many possibilities for the risk below this range. At low doses, incorporating the Bystander effect in the secondary induced cancer risk model suggested that the risk increases dramatically for the very low dose and reaches a

plateau response until 0.05 Sv. Other possibilities suggest either a linear relationship between the dose and the risk or Adaptive response model suggest a polynomial response between zero dose to 0.05 Sv. Another possibility suggests that there is no secondary induced cancer risk for dose below 0.01 Sv and dramatically increase after that. At doses above 2.5 Sv, the shape of the dose response curve is also in doubt. The secondary induced cancer risk in this range falls into three possibilities as shown in Figure 24. Dr Elaine Ron from the National Cancer Institute in Washington D.C. compiled data for three tissues namely breast, bladder and stomach and concluded that the cancer incidence as a function of dose rises rapidly at low doses and then plateaus; it does not fall rapidly at high doses, because of cell killing, Figure 25 .

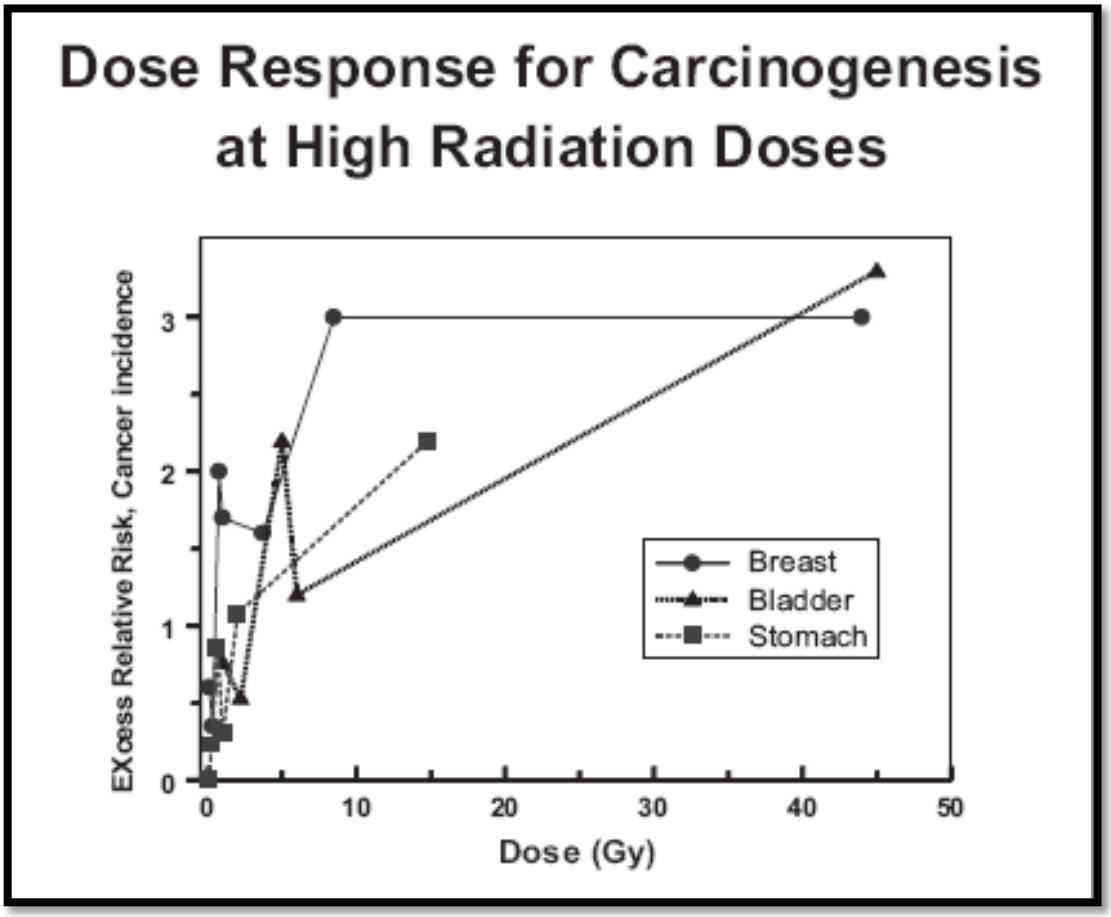

Figure 25: The dose response relationship for radiation-induced carcinogenesis for 3 types of cancer, for which data are available over a wide range of doses. The low-dose data are from the atomic bomb survivors, and the high-dose data are from radiotherapy patients. The figure was compiled by Dr. Elaine Ron, National Cancer Institute (Hall, 2006).

Calculations of the risk of secondary induced cancer herein are based on the risk coefficients from the ICRP Report no.103 (ICRP, 2007) (Table 7). Radiation weighting factor from this report were used to convert radiation specific dose from Gy to Sv. The risk of secondary-induced malignancy in specific organs was calculated using risk coefficients, which are given in % per cGy. The risk coefficients are population averaged based on gender and age (age range 0 - 80 years old). In general, the risk for younger patients may be slightly higher (UNSCEAR, 1993) (Hussein, et al., 2011).

Table 7: ICRP 103 risk coefficients (%/Sv).

ICRP 103 risk coefficients (%/Sv)	
Thyroid	0.07
Lungs	0.85
Brain	0.49
Oesophagus	0.3
Stomach	1.1
Liver	0.15
Colon	0.85
Skin	0.02
RBM	0.5
Gonads	0.8
Bladder	0.3

Table 8 shows the liftime risk of secondary skin cancer, calculated by using the equation below, for the different dose modes and phantom radii as a percentage, assuming daily imaging over 30 fractions of radiotherapy.

$$\text{Risk of Secondary Cancer} = Equivalent\ Dose\ (Sv) * risk\ coefficient\ (\%/Sv) * fractions$$

The same method was used to calculate the lifetime risk of secondary cancer at the oesophagus, thyroid, and brain sites from the RANDO phantom measurements; these values are 0.0443, 0.0106 and 0.0439 % respectively for 30 fractions of head and neck treatment. Previous literature on the Varian CBCT 1.3 version suggested that the risk

of secondary cancer might reach 0.342, 0.233 and 0.705% (Kan, et al., 2008) respectively, and 0.168 and 0.794% at the thyroid and brain (Ding & Coffey, 2009). More details are provided in section 2.7.

Table 8: The risk of secondary skin cancer for the different modes and phantom radii as a percentage for 30 fractions.

	Standard head dose mode				Pelvis mode			
radius (cm)	A	R	L	P	A	R	L	P
5.01	0.002	0.004	0.003	0.005	0.044	0.046	0.039	0.037
5.97	0.001	0.005	0.003	0.005	0.030	0.028	0.028	0.029
7.16	0.001	0.002	0.003	0.004	0.020	0.022	0.018	0.022
8.59	0.001	0.003	0.003	0.004	0.021	0.016	0.015	0.020
10.27	0	0.002	0.002	0.004	0.013	0.010	0.017	0.015
16.50	0	0.002	0.002	0.003	0.009	0.008	0.008	0.012

2.7 CBCT doses: Discussion and Conclusions

In the literature, a variety of methodologies, including anthropomorphic phantoms (Kan, et al., 2008) and simulation of the linear accelerator CBCT system using a MC code (Ding & Munro, 2011) (Ding & Coffey, 2009) and (Ding, et al., 2008) have been employed for dose simulations. Others have used TLDs for both phantom and in-vivo dose measurements in patients (Hyer, et al., 2010) and (Kim, et al., 2008). In the current research, these methods of measuring the CBCT dose were also used, in addition to a mathematical model to include a phantom of larger size. MC simulation of the CBCT dose calculation was also included using two codes MCNP-4C, and BEAMnrc details are in Chapter 03.

Reports in the literature indicate that the Varian v 1.3 CBCT system results in a higher concomitant dose than the Elekta system (Song, et al., 2008) (Wen, et al., 2007) (Islam, et al., 2006). The dose to bone is reported to be much higher than to soft tissue, when taking into account the tissue density and X-ray energy (Murphy, et al., 2007). Although the dose received from one session of CBCT imaging is small compared to the dose received from one radiotherapy treatment fraction, the accumulated CBCT dose may be significant. The total accumulated CBCT dose received by the patient during the entire treatment program, using the old version of the Varian CBCT 1.3, could reach the order of a treatment fraction dose. This potentially adds a significant radiation dose to healthy tissue, raising the risk of secondary cancer and making it necessary to monitor CBCT doses (Murphy, et al., 2007).

Ding et al., (2008) used MC to investigate the integral dose from all acquisitions of the Varian OBI version 1.3. From this investigation, the researchers concluded that daily CBCT doses can reach as much as 2 to 10% of the typical daily prescription dose of 2 Gy to soft tissue and bone, respectively (Ding, et al., 2008). Kan et al., (2008), using a direct experimental method, calculated that daily CBCT in the standard mode of the Varian OBI version 1.3 could deliver a substantial dose to the critical organs close to the treatment target volume. Critical organs such as the small intestine, rectum, lens, brainstem, and spinal cord all received doses of up to 1.4, 2.2, 2, 1.7, and 1.4 Gy, respectively in 35 fractions (Kan, et al., 2008). Table 9 shows

some published results of the CBCT scan doses from one session to selected critical organs.

In older version of Varian CBCT v-1.3, Kim (2008) stated that it is possible that an IGRT patient could receive approximately 0.2 Gy from head scans over 20 fractions (Kim, et al., 2008). Furthermore, Amer (2007) stated that typical CBCT imaging protocols for the pelvis would result in a patient surface dose of 2 Gy from 40 fractions (Amer, et al., 2007). Wen et al., (2007), found that although the daily CBCT imaging dose is only 2 % of the prescription dose for the pelvis, it may deliver 1.30 Gy to the central tissue, 2 Gy to most of the peripheral tissues, and more than 4 Gy to the left hip joint region, over 42 fractions. Thus, since daily standard mode CBCT doses can reach significant levels, these should be taken into account during treatment planning (Wen, et al., 2007). The aforementioned data on CBCT dose gives a clear indication that the concomitant dose from CBCT depends on the technique used, the geometry, and the scan protocol. As a consequence, there are no standard dose values from the CBCT to human body for either the Varian and Elekta systems.

Table 9: Single fraction CBCT dose measurement studies using version 1.3 of Varian system, units are in cGy.

study	system	tool	mode	surface	eye	brain	spinal cord	thyroid	bone	Lung
Ding et al. (2009)	Varian	Vanderbilt-Monte-Carlo-Beam-Calibration, VMCBC simulation.	half fan	9	8	5.5	5.5	9	28	
			full fan	7	6	5.4	4.5	8	21	
Ding et al. (2008)	Varian	MC simulation, BEAM/DOSZX	half fan	12	8	5	5		25	
Kan et. al. (2008)	Varian	Female anthropomorphic phantom using TLD.	standard dose mode	6.6	6.22	4.8	4.08	11.08		5.34
			low-dose mode	1.34	1.3	1.01	0.875	2.1		1.17

There is an association between the doses received and the patient size. Song et al., (2008) also addressed the relationship between imaging dose and the imaging tube voltage current (mAs), for OBI and XVI systems (Song, et al., 2008). Wen et al., (2007) investigated the relationship between the AP patient separation distance and the dose of the OBI. The larger the patient size, the less the AP skin dose, but lateral doses were found not to change significantly with patient size (Wen, et al., 2007). The AP skin dose result of Wen and colleagues match exactly with the results in this research. Herein, the CBCT dose decreased as the phantom size increased in both standard dose head and pelvis scan modes.

In all of the above mentioned studies, the Varian OBI version 1.3 was employed. In the current study, the concomitant dose using the standard dose mode in Version 1.4 on the RANDO Phantom was 0.171 cGy for the right eye. It has been found that for the same mode, a dose of 6.22 cGy is delivered to the eye by version 1.3 (Ding, et al., 2008). This result shows that a 36-fold higher concomitant dose was delivered by the older Variant version compared with version 1.4. Similarly, doses delivered to the oesophagus, thyroid and brain were also higher, by factors of 8, 22 and 16 respectively (see Table 5, page 36). Varian v1.3 uses only 4 mode settings, all of which use 125kVp for the X-ray tube. Modes are classified as standard and low for both body and head, with a 40mA tube current for the low and an 80mA tube current for the standard. However, in version 1.4 there are six mode settings classified according to the human body site (Table 1, page 10). In the version 1.4 standard dose head mode, parameters were 100 kV, 20 mA and 20 ms, whereas Kan et al., (2008) and Ding et al. (2008) both applied 125 kV 80 mA and 25 ms in the standard mode. Since the CBCT imaging dose is directly proportional to the tube current and voltage, (Song, et al., 2008), the reason for dose reduction on the RANDO phantom using the CBCT v1.4 is clearly obvious. Moreover, the newer version achieves this dose reduction while maintaining a good image quality (Kim, et al., 2010). Mode settings for both versions, 1.3 and 1.4, Varian OBI are addressed in Table 1 page 10.

Table 10 shows recently published dose results for the Varian OBI version 1.4 (Hyer, et al., 2010) compared with the current study measurements and those from version v-1.3 (Kan, et al., 2008) and (Ding & Munro, 2011). This table helps to emphasise two

main points, which are the significant reduction in the dose between the old and new versions of the Varian CBCT and that there is no standard value of the CBCT dose. Despite both published authors using the same phantoms and methods to measure CBCT doses, different CBCT systems yield variable results. In conclusion, the dose reduction from CBCT with version 1.4 makes it more probable that the technology could be used on a daily basis for treatment planning. The use of this technology therefore needs to be reconsidered for future use.

Table 10: Comparison between old and new CBCT applied doses. All data are TLD measurement except Ding et. al. (simulation)

organ	Kan et. al. (2008)	Hyer et. al. (2010)	current study (2010)	Ding et. al (2011)
	v-1.3	v-1.4	v-1.4	v-1.4
	cGy			
Brain	4.8 ± 0.687	0.301	0.3 ± 0.03	0.15
Thyroid	11.08 ± 1.19	0.238	0.51 ± 0.05	-
Oesophagus	3.81 ± 4.43	0.001	0.50 ± 0.05	-
Lens	6.22 ± 0.49	0.059	0.17 ± 0.02	0.14

Two sizes of phantom, 16 cm and 30cm, are commonly used in the literature for CBCT and CT dose measurements to represent the head and body respectively (Islam, et al., 2006). Phantoms with radii of 5-16 cm (10-32 cm diameter) were used herein for the hospital measurements. Normal infant/pediatric and adult head and pelvis sizes are shown in Table 11. The measurements presented here do not necessarily assume a paediatric patient head size of 5cm radius. Rather, the range has been included to investigate the relationship between the CBCT dose and patient size using both modes; standard dose head and pelvis.

Table 11: Standard dimensions of the head and pelvis for infants, children, and adults (Yarn Standards, 2011).

	head size (cm)			Pelvis (cm)		
	infant	child	adult (man)	infant	child	adult (man)
circumference	35.5	45.5	56	48	63.5	104
radius	5.7	7.2	8.9	7.6	10.1	16.6
diameter	11.3	14.5	17.8	15.3	20.2	33.1

Dose to the eyes, in the RANDO phantom measurement, can be compared with the dose to point A using the water phantom measurements; since point A is located on the surface of the phantom and eyes are also located on the top surface of the RANDO phantom. The circumference of the RANDO phantom head measuring at eye-level is 50.5 cm, with a radius of 8.04cm. Using the values of (a) and (b) in Table 6 (page 40), which were obtained from Figure 19 (page 38) for point A, the value of the dose at the same phantom radius is calculated to be 0.12cGy, given that:

$$y = ax^b \quad \longrightarrow \quad y = 3.4 \times 8.04^{-1.6} \quad \longrightarrow \quad y = 0.12cGy$$

The measured doses to the eyes were 0.17 and 0.13 cGy to the right and left eye respectively.

In standard dose and pelvis modes many factors affect the CBCT concomitant dose to phantom size relationship. These factors include the source-surface-distance, measurement position, and X-ray source rotation. Thus, the relationship is a complex one. Of these factors, X-ray source rotation was found to be the most influential on the CBCT dose. Version 1.4 CBCT Varian manual states that the rotation angle of the standard dose head mode is 200^o, while in the pelvis mode it is 360^o. It has been found experimentally that during CBCT dose measurement in the standard dose head mode, the X-ray source rotates anti-clockwise, starting from an angle of 292^o and stopping at an angle of 88^o. This gives a 204^o rotation instead of the reported 200^o, and an additional 20^o arc of direct exposure to the R compared with the L position. This is one of the reasons for the variation of the R position in the standard dose mode, Figure 19, and a reason that the measured doses in each eye were different. This finding agrees with the result of Feng et al. (2011) where they concluded that, in the new version of CBCT v 1.4, the post right side of head receives higher dose, due to the posterior KV scan rotation from gantry 290^o to 90^o (Feng, et al., 2011).

In the pelvis mode, the X-ray source moves clockwise from 178^o and stops at 182^o, this gives a total rotation of 364^o rather than the reported 360^o, an additional 4^o . The pelvis mode has been designed to give a complete rotation so that the X-ray source both begins and ends beneath the treatment couch. As shown in Figure 19 and Figure

20, the CBCT doses in positions R, L, A, and C, decrease as phantom size increases for both standard head mode and pelvis mode. The cone beam covers the whole surface area of a small cylindrical phantom, but this is not true for larger phantoms. This size-beam distribution effect is illustrated in Figure 26.

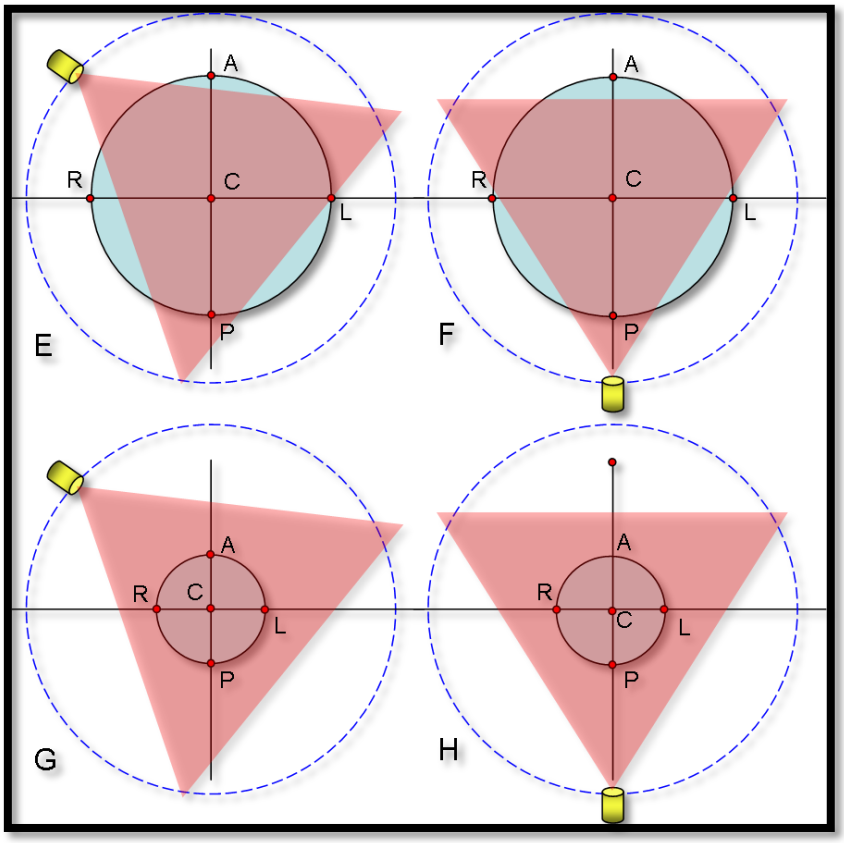

Figure 26: Illustration of the cone beam coverage at the phantom surface.

Figure 26 (E) and (F) shows that the larger the phantom is the more likely it is that the lateral sides and far end of the phantom surface are missed by the beam. Conversely, if the phantom is small enough, the chances that the beam will reach the whole surface of the phantom is high. In the latter case, the difference in the magnitude of dose received by small phantoms Figure 26 (G) and (H)) is the exposure time, i. e. the extent of X-ray rotation. As the phantom size increases, the phantom itself acts as a shield, shielding the lateral side points and far end, from the beam. Hence, this is why the total accumulated dose resulting from the CBCT rotation decreases as the phantom size increases (Figure 19 and Figure 20).

As discussed previously, the mathematical model would be improved if beam attenuation by the treatment couch was added to equation (1) as follows:

$$D(P,R,Z_1,Z_2)=\int_{\theta_1}^{\theta_2} e^{-Td(\theta)}\times\left(\frac{Z_A}{Z_1 d(\theta)+Z_2 d(\theta)}\right)^2 d\theta \quad \times \quad \int_{\theta_3}^{\theta_4} e^{-Z_3*\mu_{(couch)}} d(\theta)$$

(6)

Where Z_3 and $\mu_{(couch)}$ are the thickness and attenuation coefficient of the treatment couch, respectively. The angle θ_3 and θ_4 are the beginning and end of where the point source reach the edge of the treatment couch. The thickness of the treatment couch can be directly measured, but the attenuation coefficient, requires a simple calculation to be undertaken. If the CBCT X-ray source could be fixed above the treatment couch, and remain there without rotating throughout the run, a measurement of the initial (I_0) beam could be obtained. Secondly, an ion chamber attached underneath the treatment couch under the same circumstances could measure the attenuated beam (I). Then, by applying the following equation below, (equation 7), one could find the value of the attenuation coefficient of the treatment couch.

$$\mu_{coush} = \frac{-1}{Z_3}\times ln\left[\frac{I}{I_0}\right] \qquad (7)$$

Since it is not possible to over-ride the movement of the CBCT beam in a clinical system, this step, unfortunately, was not performed. Thus, the results achieved by the mathematical model must be interpreted with this caveat in mind.

In the standard dose mode simulation, the point P simulation deviates from the hospital dose measurement for two reasons. The first reason is that the mathematical model simulation did not account for attenuation of the treatment couch, which affected the dose distribution for the low energy gamma source. The second reason is that scattering from adjacent slices(Figure 27) cone beam would have an effect that has been ignored in the simulation. The bottom of the water phantom, position P, is where all the secondary radiation is likely to be absorbed, during the travelling and rotation through the water phantom, considering the starts and end position of the x-

ray cone beam. However, in the case of 1mm disk simulation, this effect is no longer seen and therefore the radiation intensity that reaches the bottom of the phantom is high. The mathematical equations for the simulation ignore the 3D phantom, and treatment couch attenuation effects which are the main drawbacks of the mathematical model. The relationship between radiation intensity at point P in the pelvis mode simulation was again due to rotation of the source around point P. The percentage of the beam passing directly to point P decreases as the phantom size increases: Radiation reaching point P during the rest of the beam rotation passes through the attenuation medium, Figure 26.

A recently published paper (October, 2011) by Teke et al., showed that significant differences can be observed between treatment planning system doses including the couch and those without the couch. This finding suggested an effect from the IGRT treatment couch on treatment planning doses ranging from negligible to 2.5%. Thus the kV dose, which includes the attenuation effect of the treatment couch, is best determined by using the MC BEAMnrc and DOSXYZnrc, since the treatment couch composition is provided (Teke, et al., 2011). This is suggested as future work, Chapter 6.3.

Another aspect that should have been included in the 2D mathematical approach is the scattering effect of the adjacent slices, Figure 27.

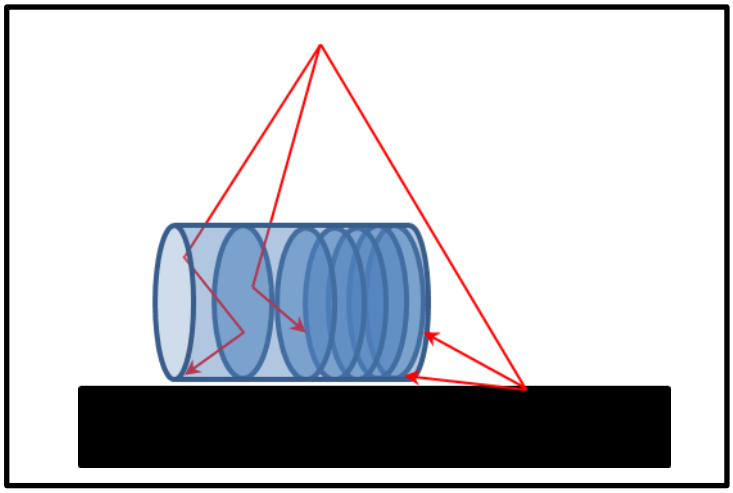

Figure 27: Illustration of the scattering radiation from the adjacent phantom slices to the calculated point.

The purpose of measuring CBCT doses in this research was to facilitate the intention to use the CBCT data set for planning radiation treatment and adapting the treatment planning process to meet individuals' needs. In order to make these decisions, the risk of using CBCT on a daily basis had initially to be considered. The concern is that the dose received by using CBCT may be sufficient to induce a secondary tumour. Although there are several published papers reporting the radiation doses delivered by CBCT, to the best of our knowledge, none has related these values with patient size. In addition, no accepted dose metric currently exists for CBCT (Kim et al., 2010). This work is therefore presented as a useful tool for considering the use of daily CBCT in paediatric and adult patients.

In summary, in both the standard dose head mode and pelvis mode, the concomitant dose at all positions decreases as the phantom size increases. It has been found that the CBCT doses from the OBI version 1.4 are significantly lower than those applied from the previous OBI version (1.3). Using a female RANDO phantom, doses were lower by factors of 36, 8, 22 and 16, for the eyes, oesophagus, thyroid and brain, respectively. The concomitant dose measured on the smallest cylindrical water phantoms resulted in a theoretical risk of secondary skin cancer of 0.005% in the standard dose mode and 0.05% in the pelvis mode, assuming a 30-fraction course of treatment with CBCT images acquired on a daily basis. Importantly, these doses are approximately 6 times greater than those measured for the larger phantoms. The data presented in this study demonstrate that the concomitant dose for different sized patients varies significantly. It is therefore recommended that patient-specific imaging protocols be considered, especially with regard to paediatric patients who can be expected to receive a higher dose. Based on these findings, it has been concluded that version 1.4 of the CBCT scanning system could be used on a daily bases to assist in adaptive radiotherapy, without a significantly increased cancer risk.

Chapter 3

3 Monte Carlo simulation of CBCT

As stated previously the MCNP-4c MC code was initially employed to simulate the CBCT. Unfortunately, it was found that this code is not sufficient to simulate the dynamic movement of the CBCT. The simulation and the results, however, were presented to show the steps followed for the simulations as well as the effect of using 2D and 3D geometrical representation of the CBCT simulations. Section 3.2 contains the BEAM/DOSXYZnrc MC simulation, which presents much better results as suggested by the hospital phantom measurements.

3.1 MCNP-4C simulation of the CBCT dose

A 3D simulation of a 100 kV spectrum gamma source rotating around a cylindrical water phantom was generated using MCNP-4c, Figure 28.

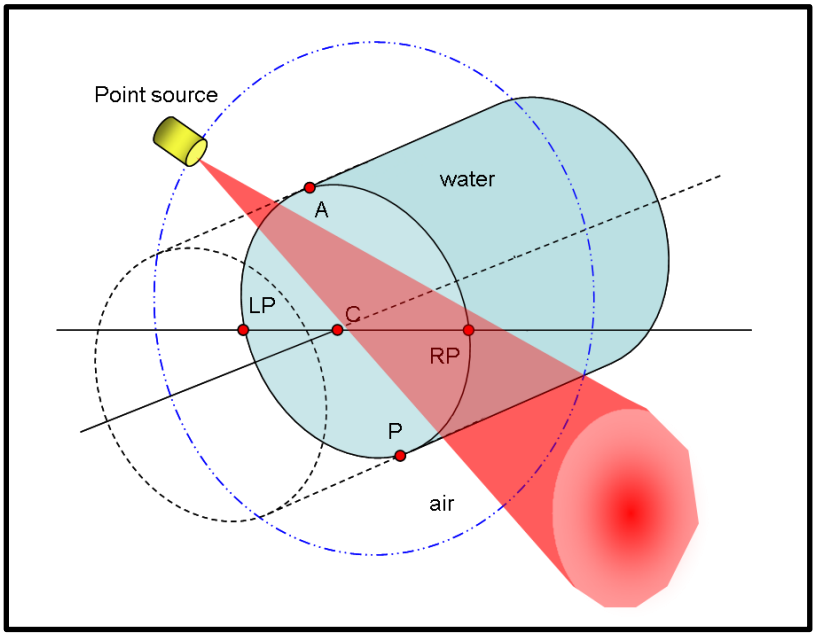

Figure 28: Illustration of the MCNP-4c simulation of the CBCT dose as the point source rotates around the cylindrical phantom.

3.1.1 Method

The MCNP-4c code is designed to simulate radiation in static environments. However, in the CBCT simulation the radiation source was moved manually from the start to the end position, (expressed as 1 to n of the CBCT rotation). The positions of the source were made to rotate with an increment of ten degree, to match the mathematical simulation and to acquire the accumulated final result (see equation below) (Figure 29).

$$D = \int_{\emptyset 1}^{\emptyset n} D(U)\, d(\phi)$$

Where, D is the total dose from a complete MC run at position U and ϕ is the rotation angle of the source and n is the number of runs.

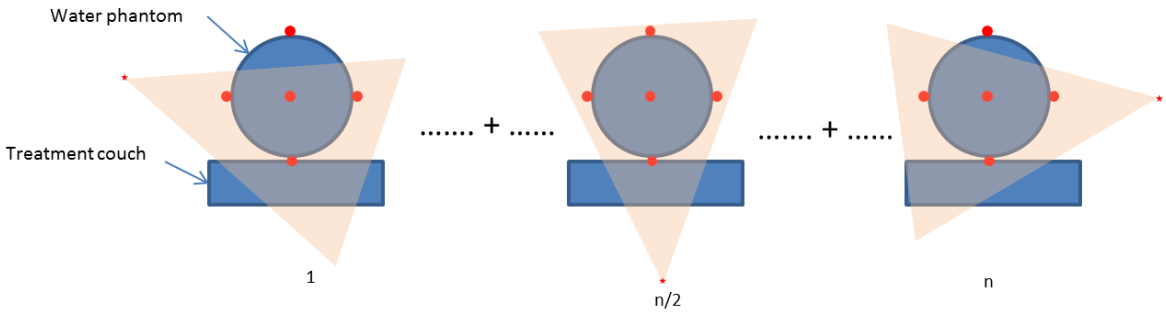

Figure 29:2D illustration of the MCNP-4c source position and accumulation of the final result.

MCNP-4c users have the ability to choose between a mono-energetic or spectral radiation sources. In the simulation for the standard dose mode, the radiation spectrum used by Ding et al., (2008) was inserted into the MCNP-4c code (Figure 30).

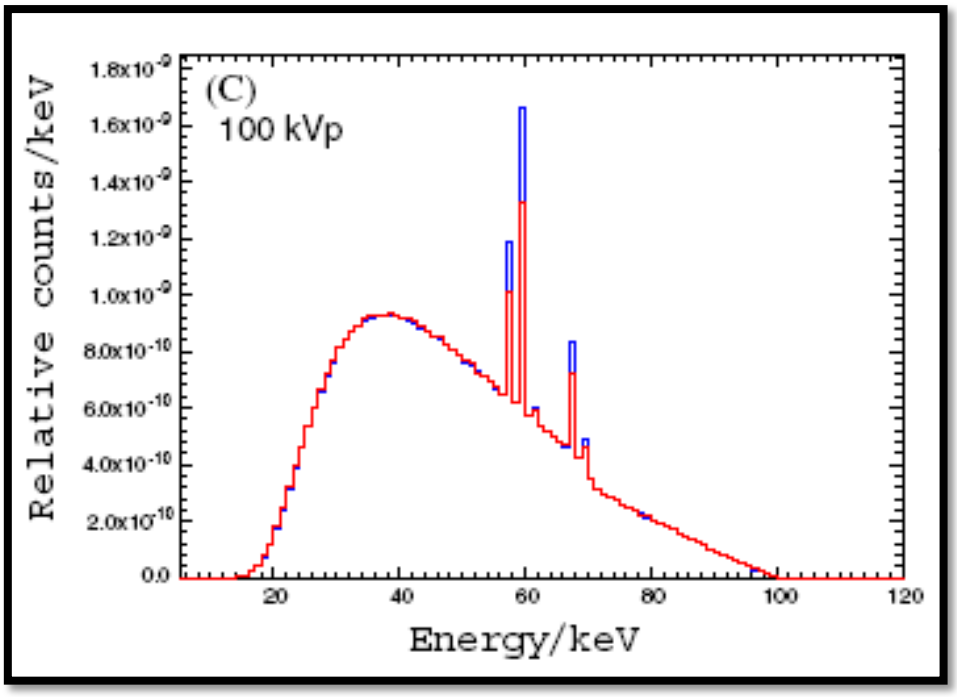

Figure 30: X-ray spectrum generated by Ding et al., (2008), which was used in the MCNP-4c simulation.

The water phantom longitudinal dimension was kept constant at 20 cm while the radii of the phantoms were varied from 2 cm to 20cm; This is similar to the radii range of the water phantoms used for dose measurement at the RSCH (5cm to 16cm radius). The source to centre distance was fixed at 100cm at all times. A detailed code script has been included in Appendix 1 for further detail. Twenty-two runs were carried out for each phantom of a different radius, where each run took an average of 6 hours. Therefore, the total running time per phantom was 5 days continuously. The history of each run was $1x10^9$ photons, which is the maximum for the MCNP-4c code if maintaining the error at less than 5% at all points. However, the error approached 20% at points A, L, R, and C, with large phantom sizes only at source positions 12, 3, 21, and 12, respectively, see Table 12 for source positions.

3.1.2 Results

One of the ways to verify the accuracy of the MCNP-4c code was written, is to calculated the delivered dose to all points (A, R, L, P and C), from all source positions for one phantom. The source rotates on x and z planes at fixed y = 0. The

coordinates of each position are presented in Table 12. Figure 31 shows the dose calculated at each point on the 2cm cylindrical water phantom from each position of the source.

The expected dose on each point was found as seen on Figure 31. As the source rotates anti-clockwise, the dose to point R decreases and increases to point L, until the source reaches its final position. In the final position, the dose to point L is at its maximum, while at its minimum to point R. The received at point A was at its highest at the beginning and end of the source rotation, and at its lowest when the source was positioned underneath the couch (position 5 to 20). Point P is closest to the source at all points and therefore received the highest dose throughout the rotation. These results are emphasised when a larger, 20 cm phantom is used (Figure 32), while keeping all other conditions constant.

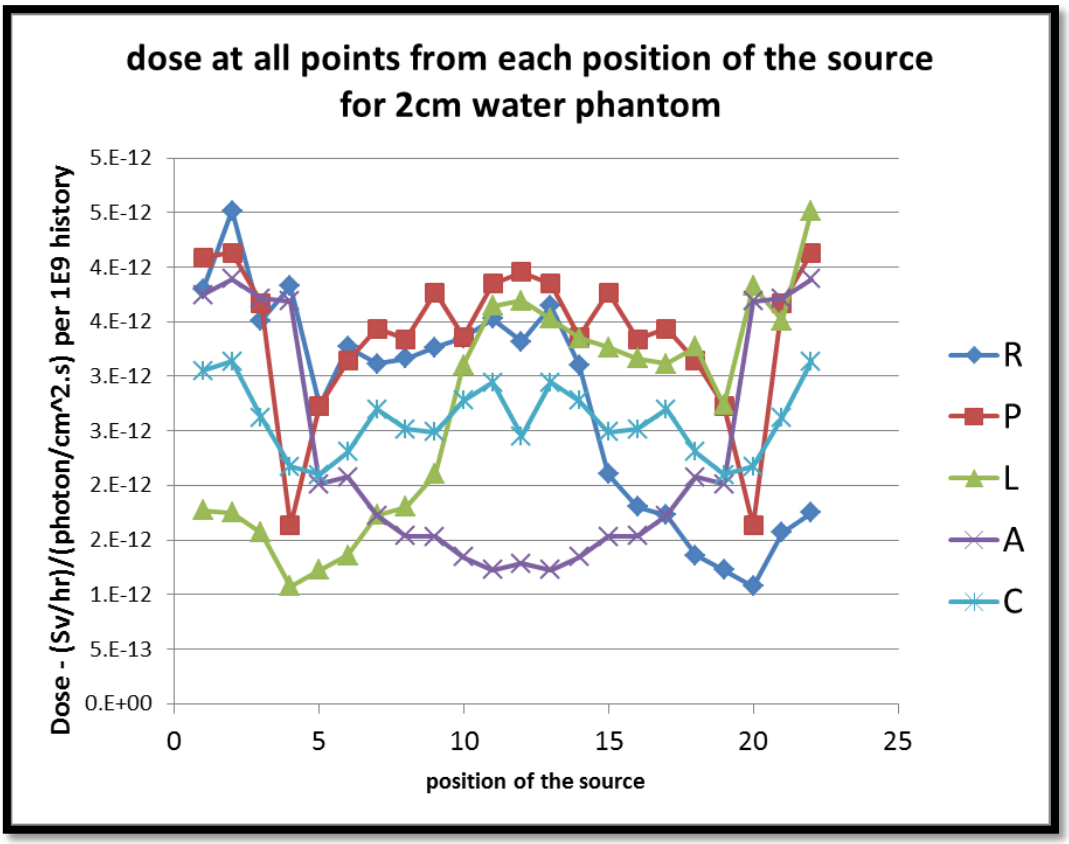

Figure 31: Dose at each source position for a 2 cm water phantom.

Table 12: Source positions used in the MCNP-4c simulation.

	x	y	z
1	-92.7	0.0	37.5
2	-98.5	0.0	17.4
3	-100.0	0.0	0.0
4	-98.5	0.0	-17.4
5	-94.0	0.0	-34.2
6	-86.6	0.0	-50.0
7	-76.6	0.0	-64.3
8	-64.3	0.0	-76.6
9	-50.0	0.0	-86.6
10	-34.2	0.0	-94.0
11	-17.4	0.0	-98.5
12	0.0	0.0	-100.0
13	17.4	0.0	-98.5
14	34.2	0.0	-94.0
15	50.0	0.0	-86.6
16	64.3	0.0	-76.6
17	76.6	0.0	-64.3
18	86.6	0.0	-50.0
19	94.0	0.0	-34.2
20	98.5	0.0	-17.4
21	100.0	0.0	0.0
22	98.5	0.0	17.4

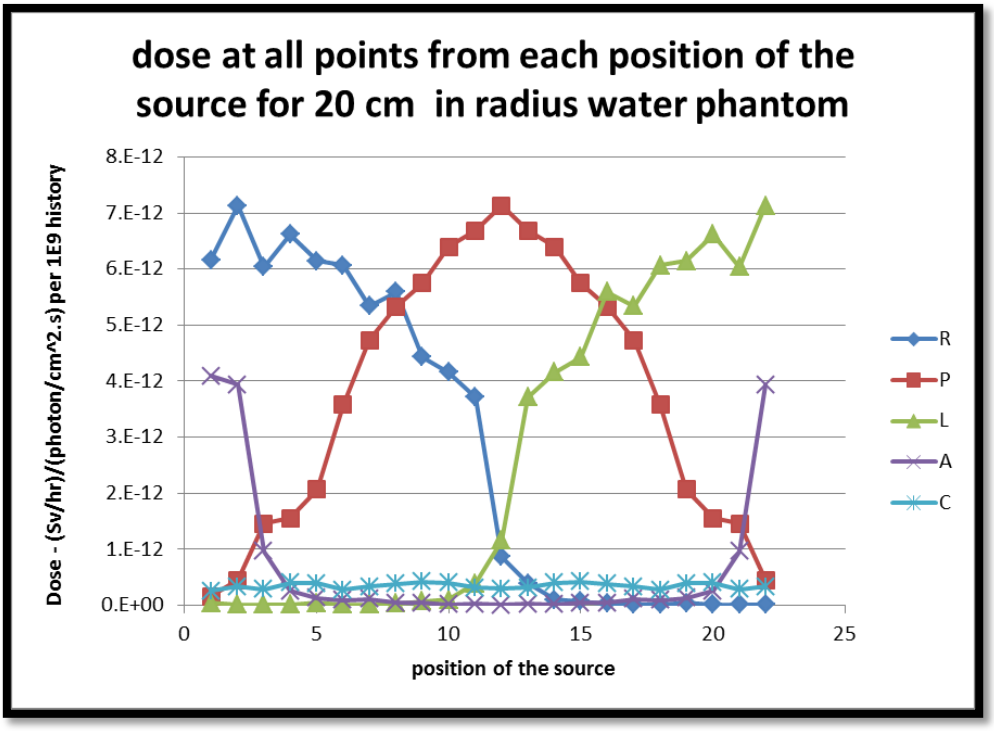

Figure 32: Dose at each source position for 20 cm water phantom.

The results of the MCNP-4c simulation of all points when using different phantom sizes are shown in Figure 33. The doses to the centre and top, C and A points respectively, in terms of trend of the dose reduction, were found to be as suggested by the hospital dose simulations and in the mathematical model. At these two points, doses decreased as the phantom size increased.

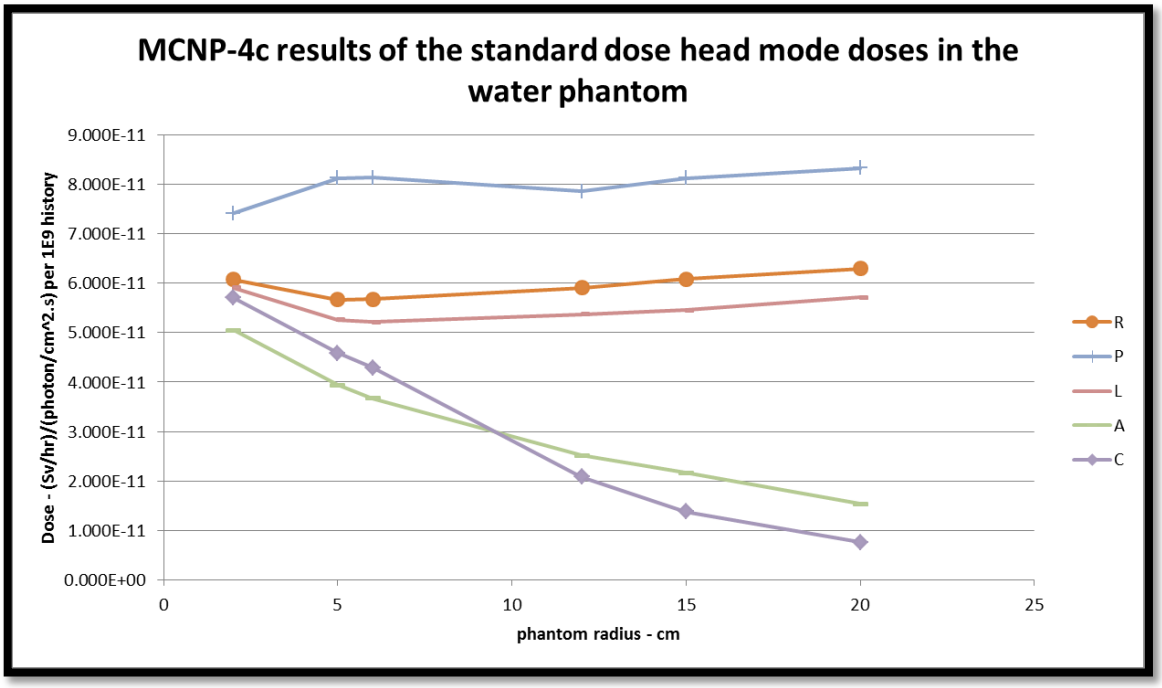

Figure 33: MCNP-4c simulation of the CBCT dose received at all positions by water phantoms of different radii in the standard dose mode.

3.1.3 Discussion

The dose at lateral positions, R and L, remained relatively constant up to approximately 7 cm in radius and then gradually increased as the phantom size increased beyond this point. The R position received a higher dose than the L position for the same reason previously discussed for the mathematical model: the start and end rotation position of the X-ray source. The doses measured at the two lateral positions were not the same as those predicted by the mathematical model

The dose to point A is high when a small phantom size of 2 cm radius are used. When the phantom radius increases to 20cm diameter, the dose to the head region is reduced

by almost 70%. This is because the rotation of the standard head mode has been designed to avoid any exposure to the eyes. For the P position, the dose is higher compared with the dose received at the A position and increases with the size of the phantom or patient, in a real scenario.

It can be seen clearly from the MCNP-4c dose result, Figure 33, that the dose at all points seems to have one value for the 2cm phantom, which spread as either an increase or decrease as the phantom size increased, Figure 33. In other words, the radiation source in the MCNP-4c code treats all points surrounding the small phantom as one point, from 100cm.

Using MCNP-4c the presence of the treatment couch was simulated assuming a thickness of 0.5 cm and an arbitrary carbon fibre composition (99.9% carbon-12). Rather than assuming an arbitrary composition, it would have been better to include the real composition of the treatment couch in the simulation so that more realistic results might be obtained. Unfortunately, the assumption was necessary due to the lack of information, at the time of simulation, regarding couch composition on the internet and in the manufacturers information manual. Ideally, the material of each component should be included in the MCNP-4c code in terms of its chemical formula and percentage abundance.

As highlighted above, source positions 3, 12, and 21 were prone to error simulations as high as 20% at L, A, and R. This is due to large scattering and interaction effects in the radiation path.

The MCNP-4c simulation results demonstrate that the dose to the top of the phantom is reduced as the phantom size increased. For phantoms with radii ranging between 2 cm and 7 (±2) cm, the trend and shape of the hospital measurements and MC simulation are similar and were in the accepted phenomenon that the dose decreases as the phantom size increases.

Despite obtaining some reasonable results showing good correlations between mathematical models and real measurements, the study was limited in some respects

and could be improved in future modelling efforts. For instance, it should be noted that in both simulation cases, (mathematical and MC), a lack of continuity existed during the simulations. In other words, the simulations modelled the movement of the radiation source in discrete position intervals rather than as one continuous movement, as it is in reality (Figure 29). In addition, formulae were used to consider the effect of the inverse square law. Moreover, the scattering effect was ignored in the mathematical simulation and Carbon-12 was arbitrarily assumed to represent the composition of the treatment couch rather than using the real composition. These factors reduced the reliability of the simulation results of MCNP-4c. However, the BEAMnrc/DOSXYZnrc MC code used herein is the best code available to account for the continuously rotating X-ray source around the water phantom. The phantom longitudinal dimension, in MCNP-4c, might also affect the dose measurements and the comparisons with the simulated results. In the hospital measurements, the phantom longitudinal dimension were varied with the radius of the phantom. However, in the mathematical model, no variation in length or scattering effects from adjacent slices were considered. Also, in the MCNP-4c model, the longitudinal dimension of the water phantom was considered, but was fixed at a value of 20 cm regardless of phantom size. Thus, the author found that the MCNP-4c is not sufficient to simulate the dynamic movement of the imaging device and here it is recommend to use BEAMnrc/DOSXYZnrc instead.

3.2 BEAMnrc and DOSXYZnrc MC simulation

The EGSnrc/BEAMnrc V4 2.3.1 Monte Carlo (MC) code ((Rogers, et al., 1995); (Nelson, et al., 1985); (Walters, et al., 2002)) was used in this research. The BEAMnrc and DOZXYZnrc codes (Rogers, et al., 1995) are MC simulation systems developed by the National Research Council (NRC; Canada) and have been extensively used to simulate the characteristics of megavoltage (MV) electron and photon beams in commercial medical accelerators, as well as kV X-ray treatment units, to measure the doses to phantoms. Recently, the BEAMnrc code has been applied to the simulation of CBCT doses (Ding, et al., 2007). The MC BEAMnrc code works sequentially, starting by defining the geometry of the simulation environment and ending with the desired result, such as dose distribution (Figure 34). The MC BEAMnrc code was installed on a personal laptop (Intel Corei7-2620M, 3.4GHz CPU, 4GB RAM) with Microsoft Windows 7 operating system. Therefore, all MC simulations were run, stored, and analysed on this PC.

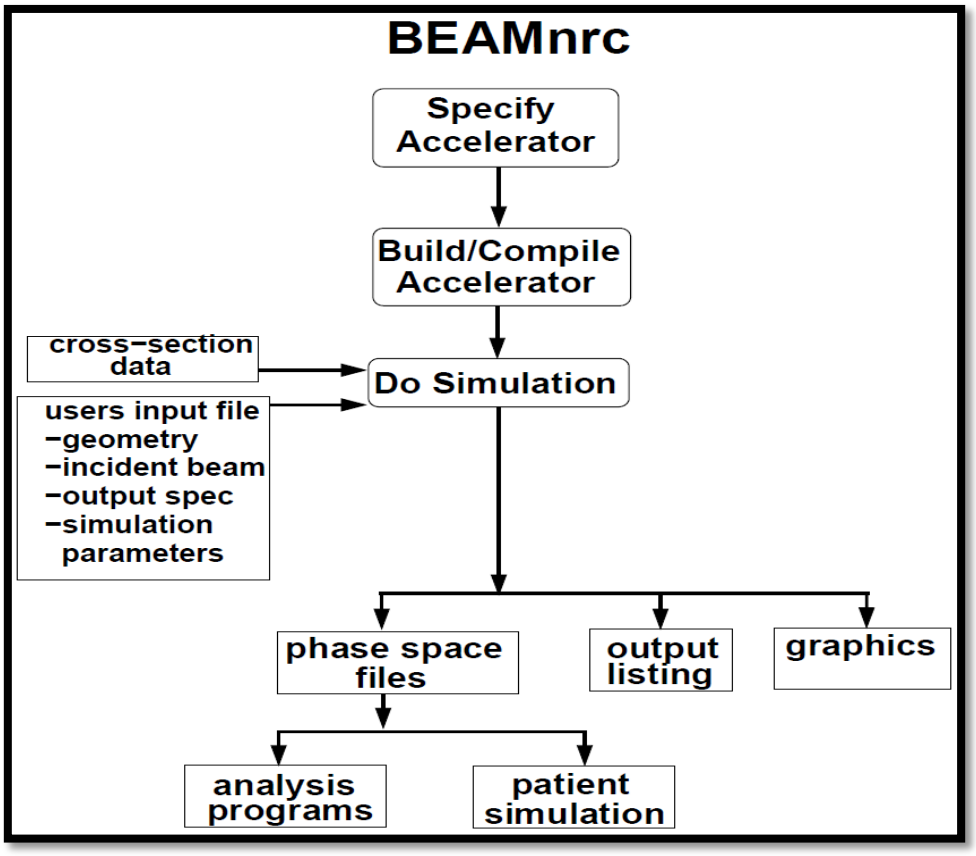

Figure 34: Steps required in BEAMnrc to perform a simulation of a radiotherapy system (Rogers et. al., 2011).

In this research, detailed geometry of the Varian-G242 X-ray tube was simulated using the BEAMnrc MC Code. X-ray tube specifications, including the rotating anode, target design, beam definition and filtration systems, and incident electron energy were obtained from the manufacturer (Varian). First, the BEAMnrc code was used to generate X-ray spectra at three different places within the X-ray tube components. Then, these X-ray spectra were analysed using the DOSXYZnrc code to simulate the dose received by water phantoms.

Many component modules (CMs), such as XTUBE, CONESTAK, SLABS etc., can be used in BEAMnrc to simulate the geometry of the CBCT X-ray tube. Each CM represents a different part of the X-ray tube. A list of the CMs used in this research is provided and described in detail in section 3.2.1. Following simulation, results such as beam profile, and percentage depth dose (PDD) were compared and discussed against literature-derived values in order to verify/benchmark the code, section 5.3. The effects of beam hardening methods and bow-tie filters on the CBCT beam are also considered. Finally, the doses received by water phantoms are presented and discussed.

3.2.1 BEAM CBCT Monte Carlo component modules

The Varian CBCT V-1.4 G-242 X-ray tube, as specified by the manufacturer, consists of a target source, an aluminium layer as a pre-filter, lead as a pre-collimator material, lead to form the upper blades, glass to support the bow-tie filter and two types of aluminium bow-tie filter; full bow-tie and half bow-tie. The CMs in the BEAM code used to simulate CBCT were ‘XTUBE’, ‘CONESTAK’, ‘SLABS’, ‘BLOCK’, ‘JAWS’, ‘PYRAMIDS’ and ‘CHAMBER’. The ‘SLABS’ CM code was used several times to represent the filter, bow-tie support, and the glass of the X-ray tube. Detailed input parameters of each CM are described in the following sections and full X-ray geometry is sketched using the BEAMnrc drawing tool. Full MC code script is provided in Appendix one.

1- XTUBE as target source:

According to the manufacturers specifications, the anode is comprised of 95% Tungsten (W) and 5% Rhodium (Rh), with a density equal to 18.68 g.cm^{-3}.The target beam angle is 14^{o} and the focal size of incident electrons ranges from 0.4 to 0.8 mm. A 0.5 mm diameter focal spot was used. A detailed schematic diagram of the X-ray tube from Varian is shown in Figure 35.

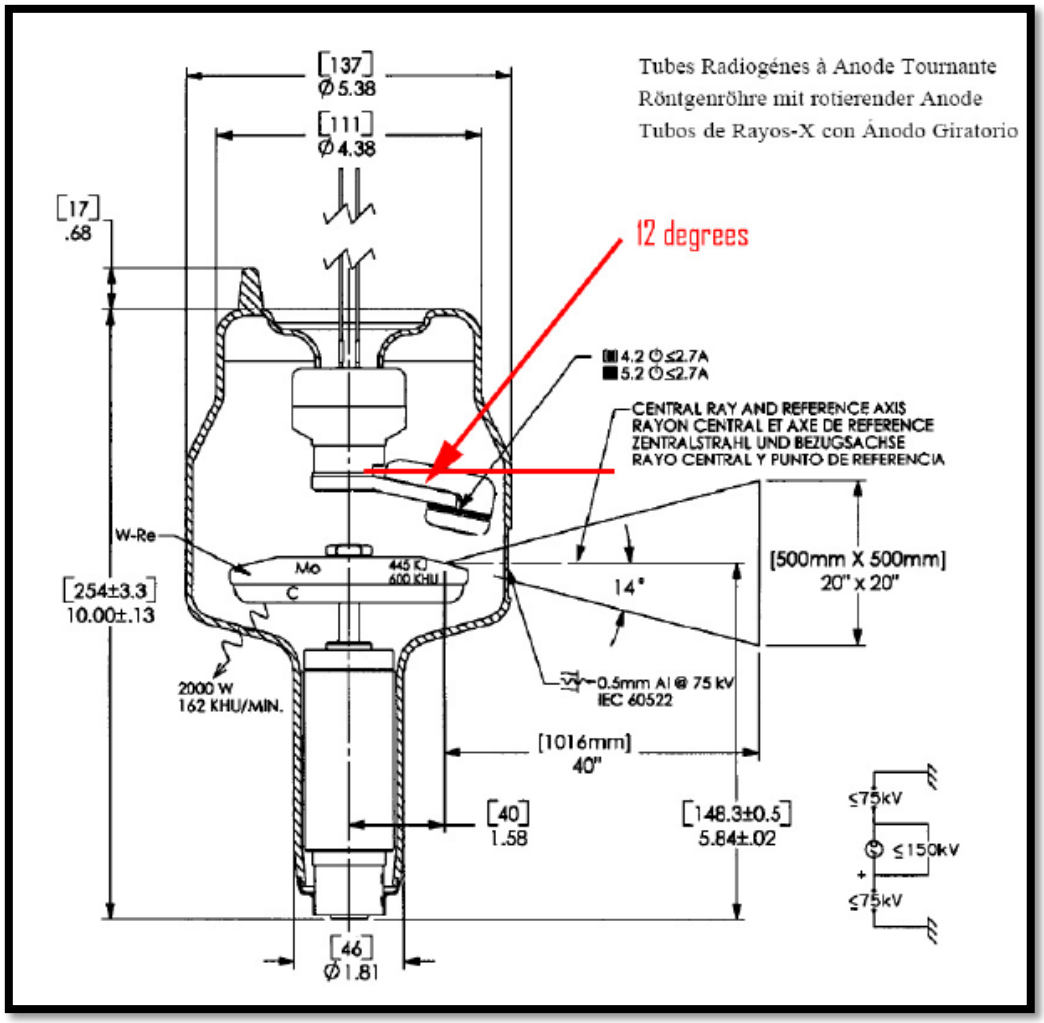

Figure 35: A detailed schematic diagram of the X-ray tube from Varian.

2- CONESTAK as exit window:

This sub-code was used to model the exit glass window. The density of the glass window was set to 2.23 g.cm^{-3} and the thickness was set to 0.9 mm. The distance between the window and the target was set to 2.8 cm and the material between the exit window and the target was set to vacuum.

3- SLABS as pre-filter:

A 2mm pre-filter, described by the manufacturer as being positioned 5.72cm away from the target source. This filter is made of 3.2315 $g.cm^{-3}$ Aluminium with a composition of 96.5% Al, 1.3% Si, 1.2% Mg and 1% Mn, Figure 35.

4- BLOCK as pre-collimator:

The 'BLOCK' code was used to simulate the pre-collimator, which was made of 2 cm thick lead and a calculated 3.2 × 3.2 cm^2 opening in the front (the closest edge to the X-ray target) and a 4.2 × 4.2 cm^2 opening in the back. The distance between the pre-collimator and the target was set at 6.52 cm.

5- JAWS as upper blades:

The 'JAWS' code was used to model the lead blade with a thickness of 3 mm and a calculated 4.72 cm opening in the front and a 4.86 cm opening at the back. The distance between the upper blades and the target was set to 9.59 cm.

6- SLABS as filter support

This code was used to model steel support with a thickness of 2 mm. The distance between this and the target was set to 11.19 cm.

7- SLABS as glass

The glass slab is a 1 mm thick sheet which carries the bow-tie filter. The distance between this and the target was set to 14.9 cm.

8- PYRAMIDS as bow-tie filter

This sub-code was used to model both full and half bow-tie filters. The filters were modeled using six layers of aluminum with the same composition as the pre-filter but with different widths at the central region which is air opening. The thicknesses of these layers are 1.5, 1.5, 7, 13, 3 and 2 mm from the front to the back, respectively. The distance between these filters and the target

was set to 15 cm. Schematic representations of these codes are all shown in Figure 36.

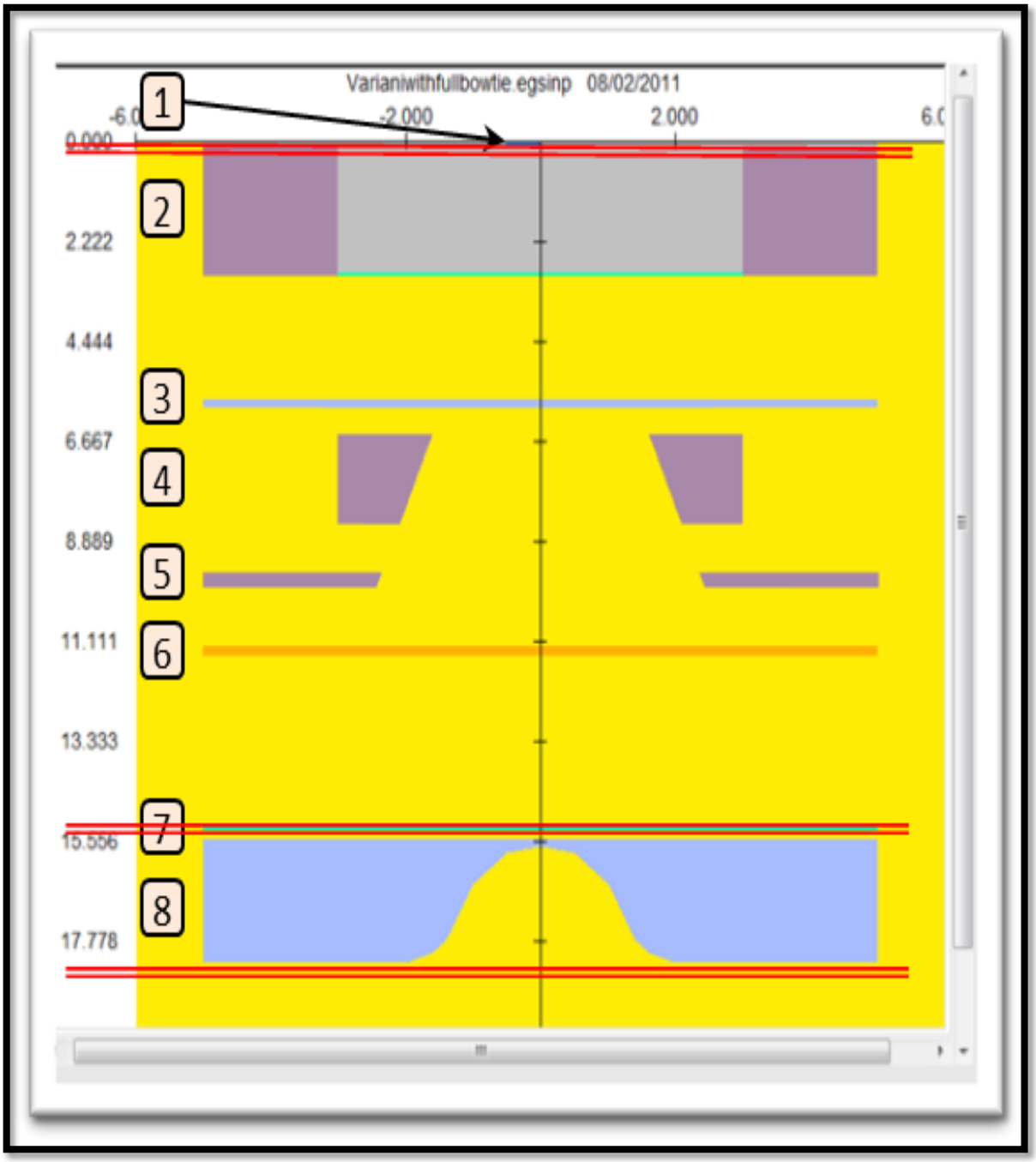

Figure 36: Schematic diagram of the simulated Varian G242 CBCT X-ray tube with full bow-tie filter. 1-XTUBE as target source; 2-CONESTAK as exit window; 3-SLABS as pre-filter; 4-BLOCK as pre-collimator; 5-JAWS as upper blades; 6-SLABS as filter support; 7-SLABS as glass; 8-PYRAMIDS as bow-tie filter. The axes are in centimetre measurement.

In the Monte Carlo simulation, the energy thresholds for secondary particle creation (AE, AP) and energy cut-off (ECUT, PCUT) for particle transport were set to AE=ECUT=0.516MeV for electrons and AP = PCUT = 0.001 MeV for photons (Ding, et al., 2007).

All simulations were run with a $2x10^9$ electrons history, giving a statistical uncertainty of less than 2.5%, which increased from 0.5% to 2.2% as the depth in water phantom measurements increased because of increased photon interaction and scattering. The average run-time for the simulations was approximately 45 hours per run for one mode setting of CBCT.

Similar simulations have been reported in the literature by Kim et al., (2010) and Ding et al., (2007) who simulated the doses from the new and old versions of Varian OBI (v1.4 and V1.3). The geometries of the OBI devices used by these authors are shown in Figure 37 and Figure 38, respectively (Kim, et al., 2010) and (Ding, et al., 2007).

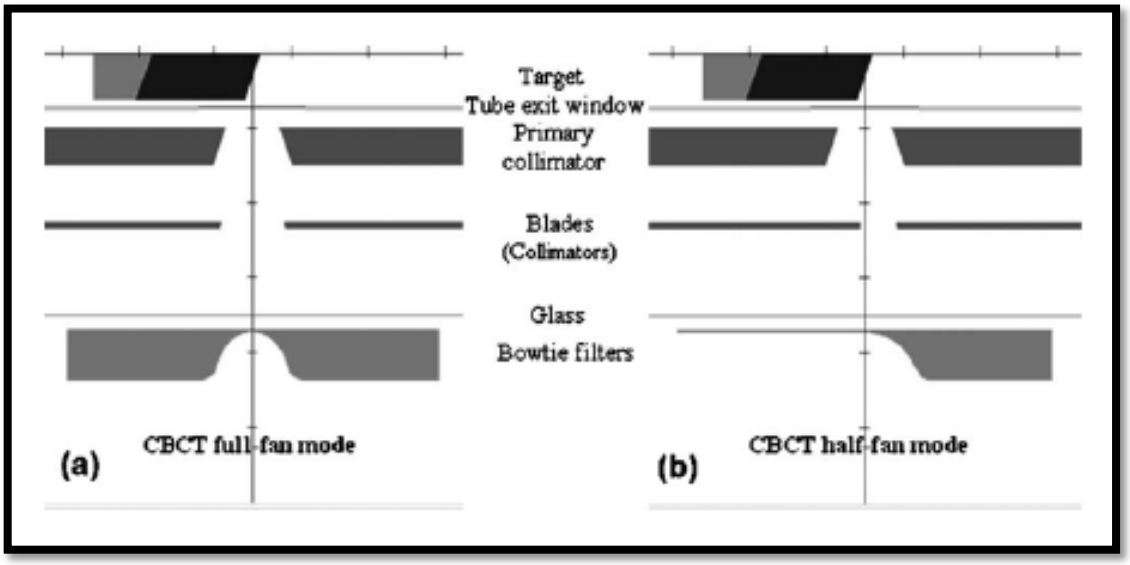

Figure 37: Varian OBI X-ray tube geometries for each full-fan mode and half-fan mode. Full-fan mode uses full-bowtie filter and half-bowtie is used for half-fan mode (Kim, et al., 2010).

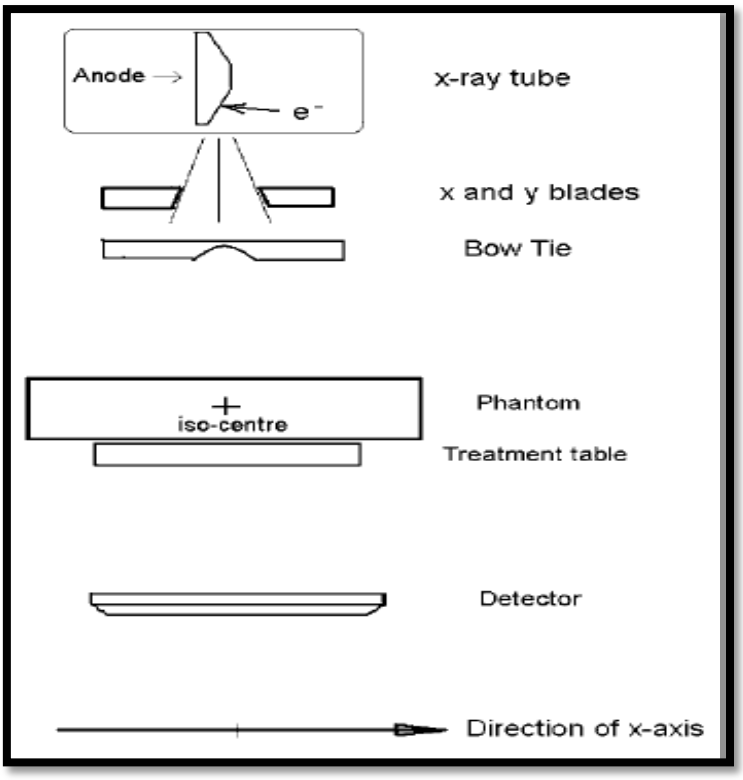

Figure 38: Schematics of the geometry of the OBI device used for Monte Carlo simulation. As shown, the x-axis is parallel to the line joining the centres of the anode and cathode. The y-axis is perpendicular to the x-axis and the beam central ray. Thus, the y-axis is perpendicular to the plane of the diagram and the x–y plane is parallel to the detector plane, (Ding, et al., 2007).

3.2.2 Results of the MC BEAM simulation

The ideal way to validate the MC CBCT simulation is by measuring the actual beam profile, PDD of the machine and comparing the results obtained against the simulation results. To measure the PDD we would have to take a measurement without rotating the gantry, which is impractical to achieve with a clinical treatment unit. Instead, recently published literature results, were used for comparison against the results obtained from the simulation.

There were three main simulations (runs), classified according to the X-ray tube voltage current used. Acceleration potential were 100kVp, 125kVp, and 110kVp for the standard dose head, low dose head, and high quality head, pelvis, and pelvis spot light, and low dose thorax respectively. In each run, three beam profiles (phase-space files), were obtained. The phase-space file is a virtual plane in the simulation, which stores all the data related to the energy, position, and direction of all the particles passing through it. These three phase-space files were added at positions just after the focal spot, before the bow-tie filter, and just after the bow-tie filter, and were named as phase-space file one, two, and three respectively (Figure 39).

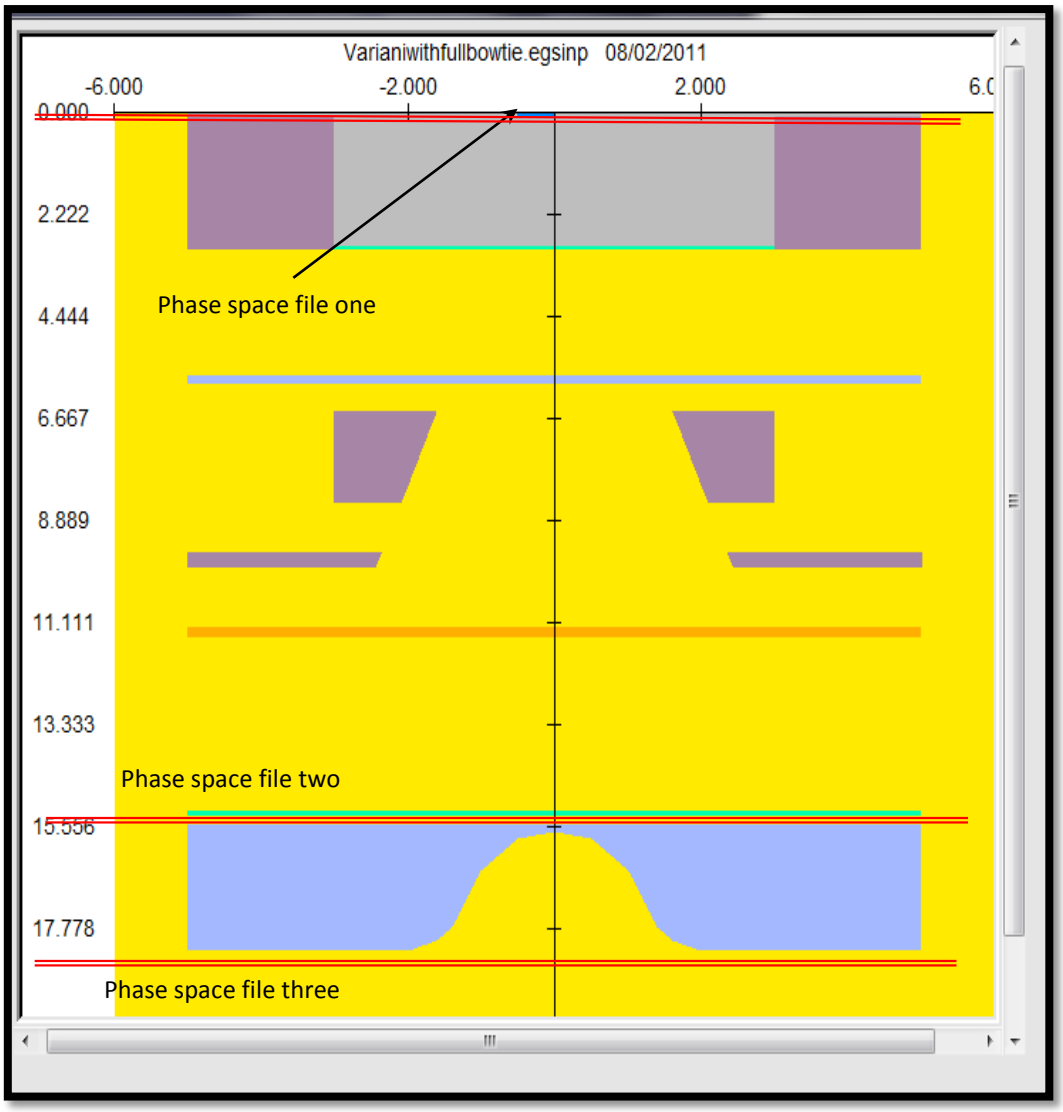

Figure 39: Phase-space files positions in the MC BEAM simulation. . The axes are in centimetre measurement.

For the first phase space file, Figure 40 shows the beam profile and the X-ray spectrum of the 100kVp electron beam. Photons are seen coming out from the source where beam filtration is absent. In this X-ray spectrum, ten characteristic peaks were observed (Table 13). These peaks arise due to the two metals that the source is composed of: 95% Tungsten (W) and 5% Rhodium (Rh). The obtained peak values were compared with values from the online edition of "Kaye and Laby: Tables of Physical & Chemical Constants", provided by the National Physical Laboratory (NPL), UK (Laboratory, 2011).

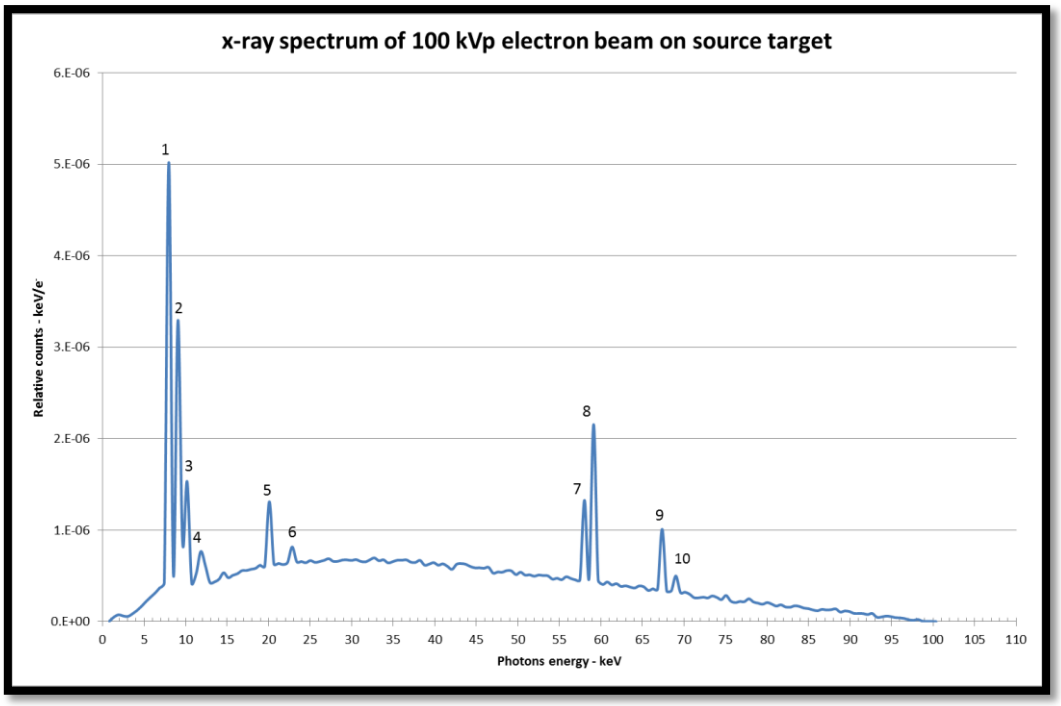

Figure 40: X-ray spectrum of 100 kVp electron beam on source target.

Table 13: The simulated and expected photon peaks using the 100kVp electron beam on the 95% W and 5% Rh source target.

peak no.	Photon Energy Peaks keV	Simulated and expected peaks – keV		
1	8	W (95%)	8.34 and 8.40	$L_{\alpha 1}$ and $L_{\alpha 2}$
2	9.1	W (95%)	9.53 and 9.67	$L_{\beta 1}$ and $L_{\beta 4}$
3	10.2	W (95%)	9.82 and 9.96	$L_{\beta 2}$ and $L_{\beta 3}$
4	11.8	W (95%)	11.28 and 11.68	$L_{\gamma 1}$ and $L_{\gamma 2}$
5	20.1	Rh (5%)	20.07 and 20.22	$K_{\alpha 1}$ and $K_{\alpha 2}$
6	22.8	Rh (5%)	22.70, 22.72 and 23.17	$K_{\beta 1}$, $K_{\beta 2}$ and $K_{\beta 3}$
7	58	W (95%)	57.98	$K_{\alpha 2}$
8	59.1	W (95%)	59.32	$K_{\alpha 1}$
9	67.4	W (95%)	67.24	$K_{\beta 3}$
10	69	W (95%)	69.10	$K_{\beta 2}$

The source spectra of the 110 kVp and 125kVp beams are similar to those measured for the 100kVp beam, in the fact that 10 peaks were also observed. However, the relative counts (keV/e$^-$) increased (integration or the area of the intensity) as the main voltage peak increased, Figure 41.

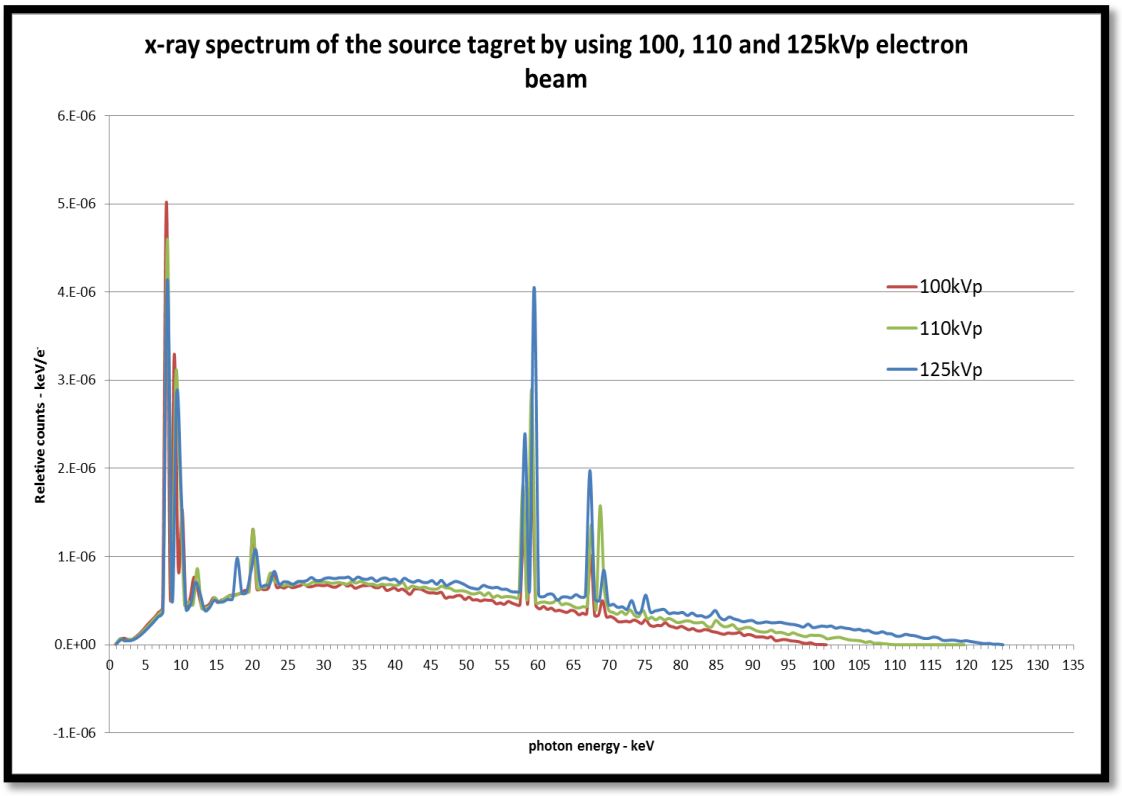

Figure 41: x-ray spectrums of the target source using 100, 110 and 125 kVp electron beam

3.2.3 The Effect of beam hardening methods and bow-tie filter on the CBCT beam

The components of the CBCT X-ray source functioned efficiently to reduce the intensity of the beam coming directly from the source (phase-space file one). The difference between phase-spaces two and three and phase-space one is very clear and can be seen in Figure 42.

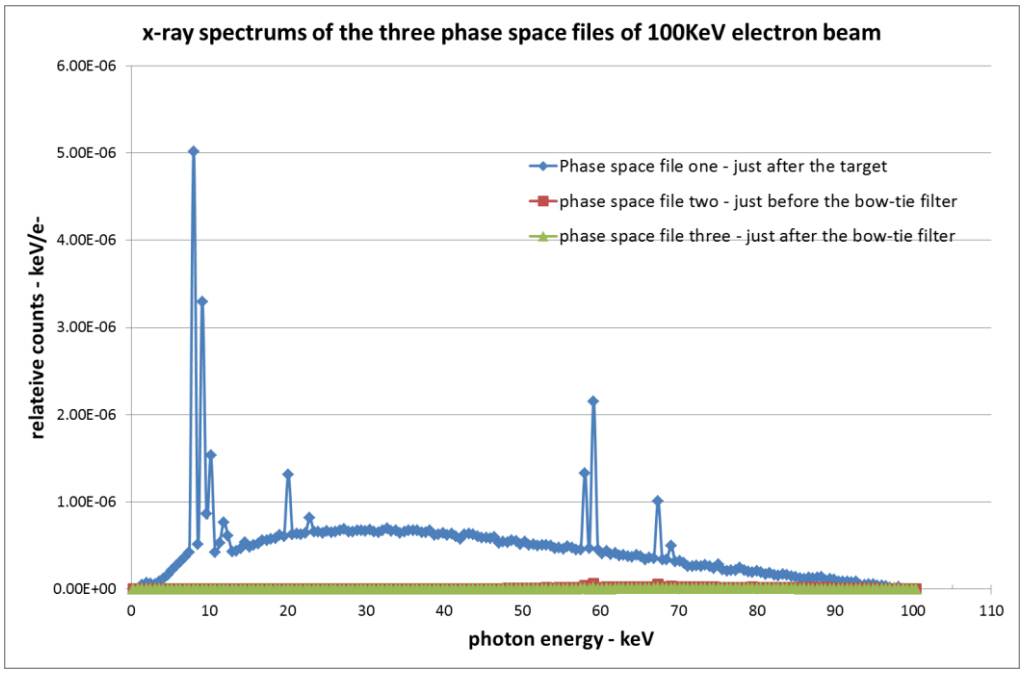

Figure 42: X-ray spectra for the three phase space files of the 100keV electron beam.

Looking at Figure 42, one can see no difference between the X-ray spectrums of phase-spaces two and three, but this is merely a consequence of scaling. When using the appropriate scale and removing phase-space one, it can be seen that the intensity of the X-ray reduces by almost half when using the bow-tie filter, as shown in Figure 43. The X-ray spectrum generated after the bow-tie filter is the beam that interacts directly with the scanned medium, whether it is patient or phantom, therefore this beam is particularly important. The phase-space file three spectrum was used to obtain the PDDs and the CBCT doses.

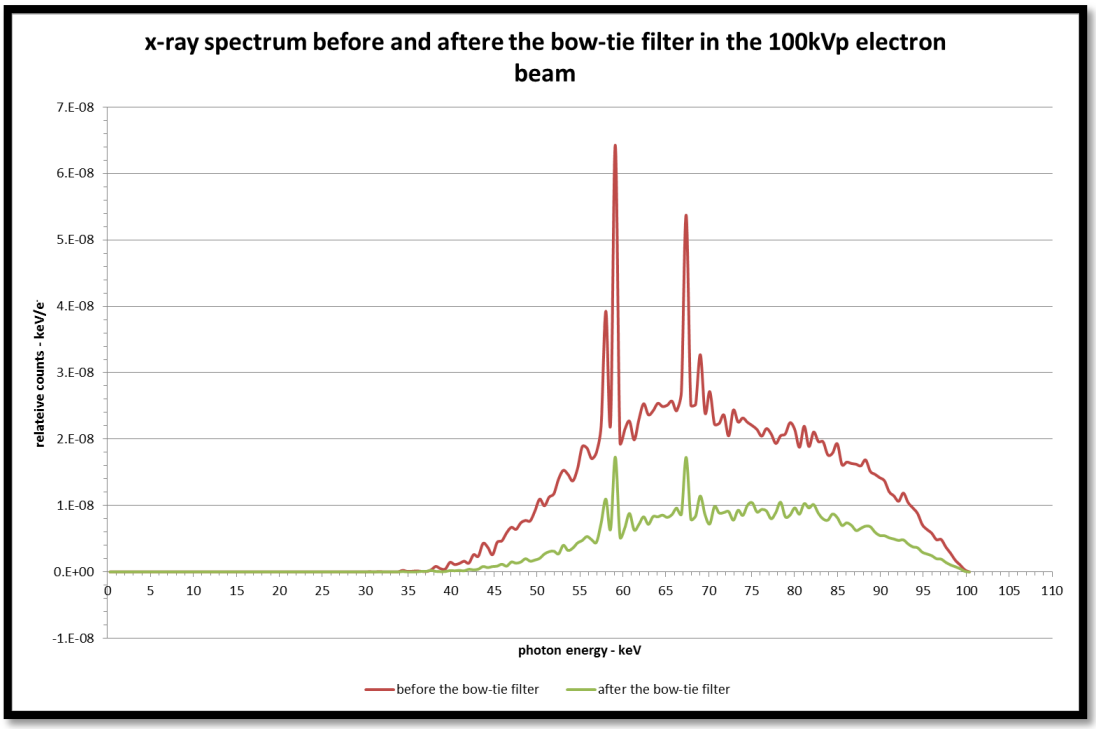

Figure 43: X-ray spectra of the 100kVp electron beam before and after the bow-tie filter.

With the exception of differences between the end energy and the intensity of the spectra themselves, the general spectra of the 110kVp, 125kVp, and 100kVp X-ray beams were similar (Figure 44). The end point energy of each spectrum is the same as the voltage peak value, for instance, the 125kVp electron beam X-ray spectrum has an endpoint of 125keV maximum photon energy.

3.2.4 Percentage Depth Dose (PDD) of the MC simulations

Figure 45 shows the PDD on a water phantom for the 100keV electron beam source. The PDD was obtained in a water tank of dimensions 20 x 20 x 30 cm^3 and the doses were measured at the central axis of the beam.

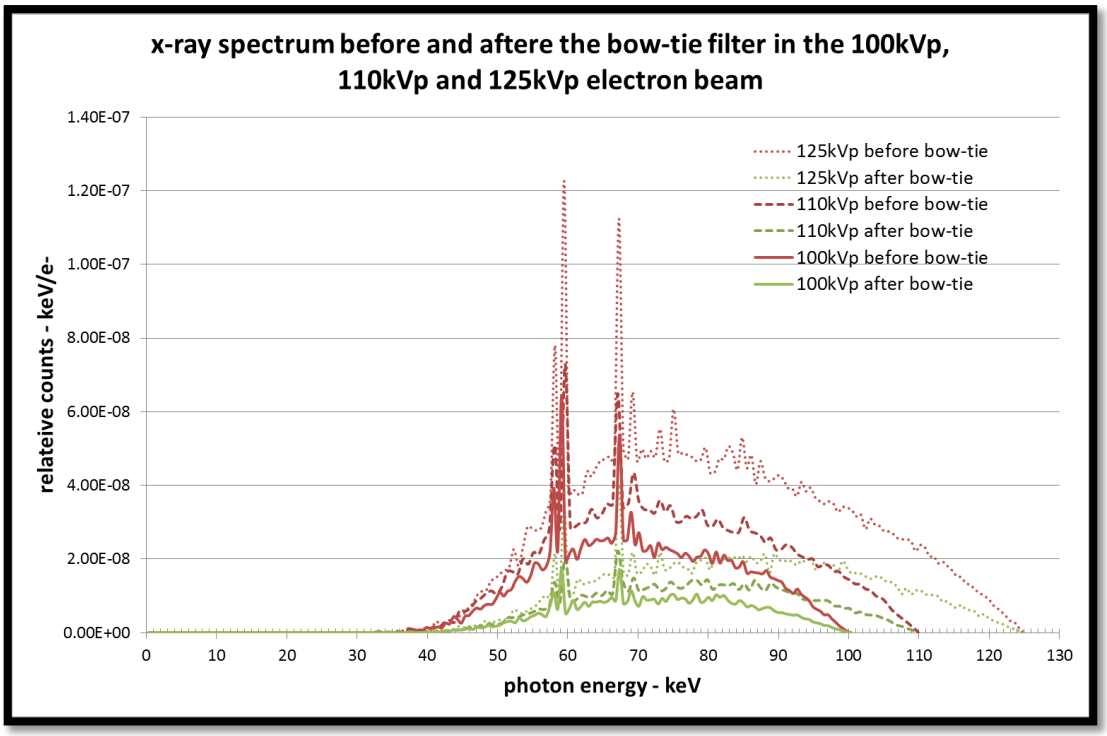

Figure 44: X-ray spectrums of the 100kVp, 110kVp, and 125kVp electron beam before and after the full bow-tie filter

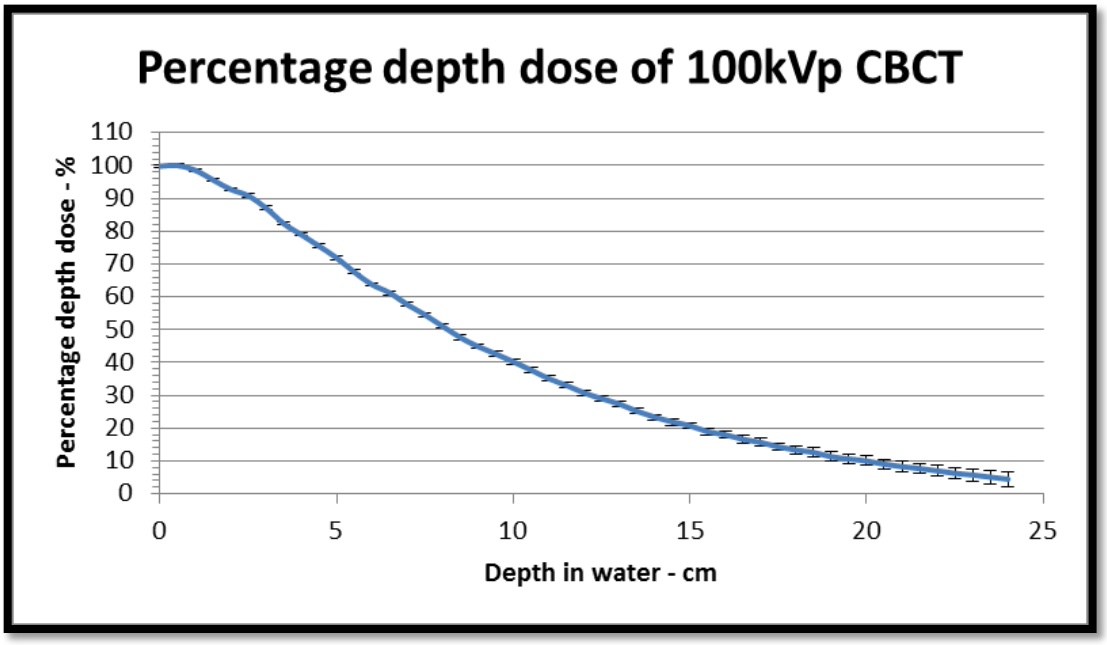

Figure 45: PDD of the photon in the water phantom for the 100kVp electron beam.

The PDD of the 110kVp and 125kVp electron sources on the water phantom are presented in Figure 46. Percentage error is increased as the beam penetrates deeper in

the phantom, since greater scattering and more interactions are involved in the calculation of the dose.

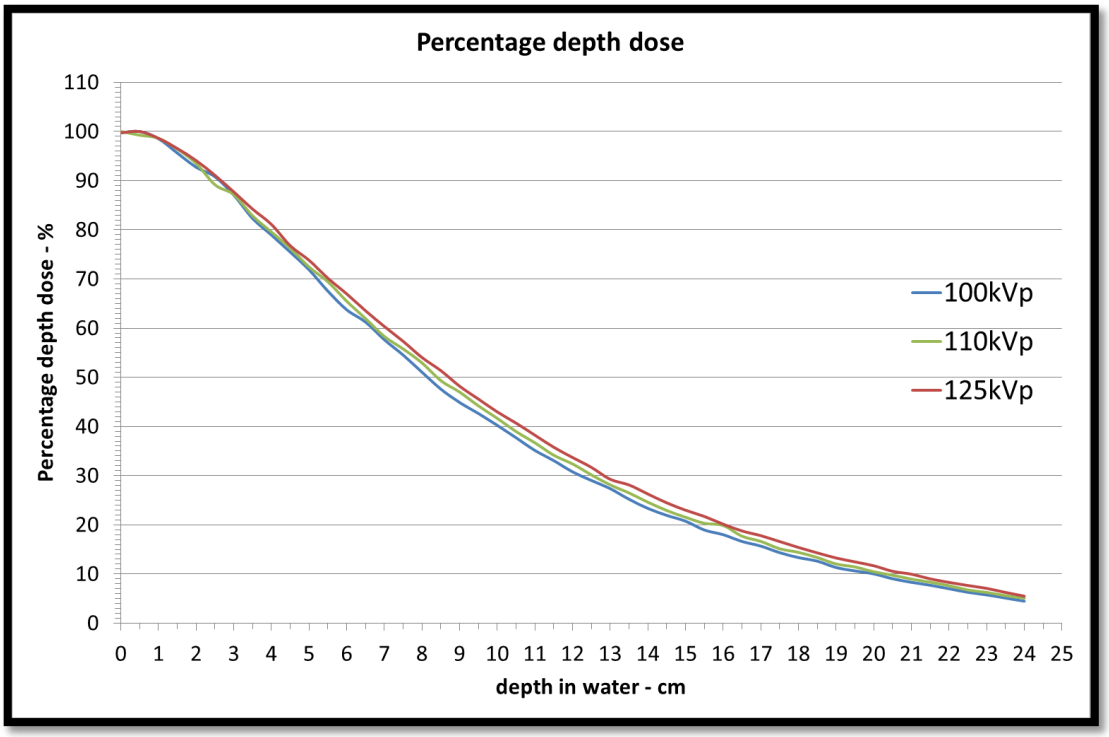

Figure 46: PDD of the MC/BEAMnrc beam on a water phantom.

3.2.5 MC DOSXYZnrc, CBCT dose measurement on water cylindrical phantoms

Following completion of the BEAMnrc simulations, the third phase-space file from BEAMnrc was used to run the DOSXYZnrc user code which is used mainly for dose calculation. In order to calculate absorbed doses in the water phantoms, a source type '8 phase-space source' was used to represent multiple directions for simulation of the rotational irradiation of CBCT scans. The rotation of the source was set to exactly mimic the rotation of the modes; for instance, standard dose mode, starting from an angle of 292^{o} and moving to an angle of 88^{o} in an anti-clockwise direction (Figure 9). The dose measurements were obtained in a cylindrical water phantom contained within a cubic air phantom with different volumes (Figure 47). The cylindrical water phantoms were selected to represent small, medium, and large size such as 4, 8, 12, and 16cm in radius. The source to phantom isocentre was set at 76.75 cm and the history of the particles was set to $9x10^{8}$ photons. Hence, the time for each simulation of each phantom took approximately 40-50hours. This gives a statistical uncertainty of less than 3%.

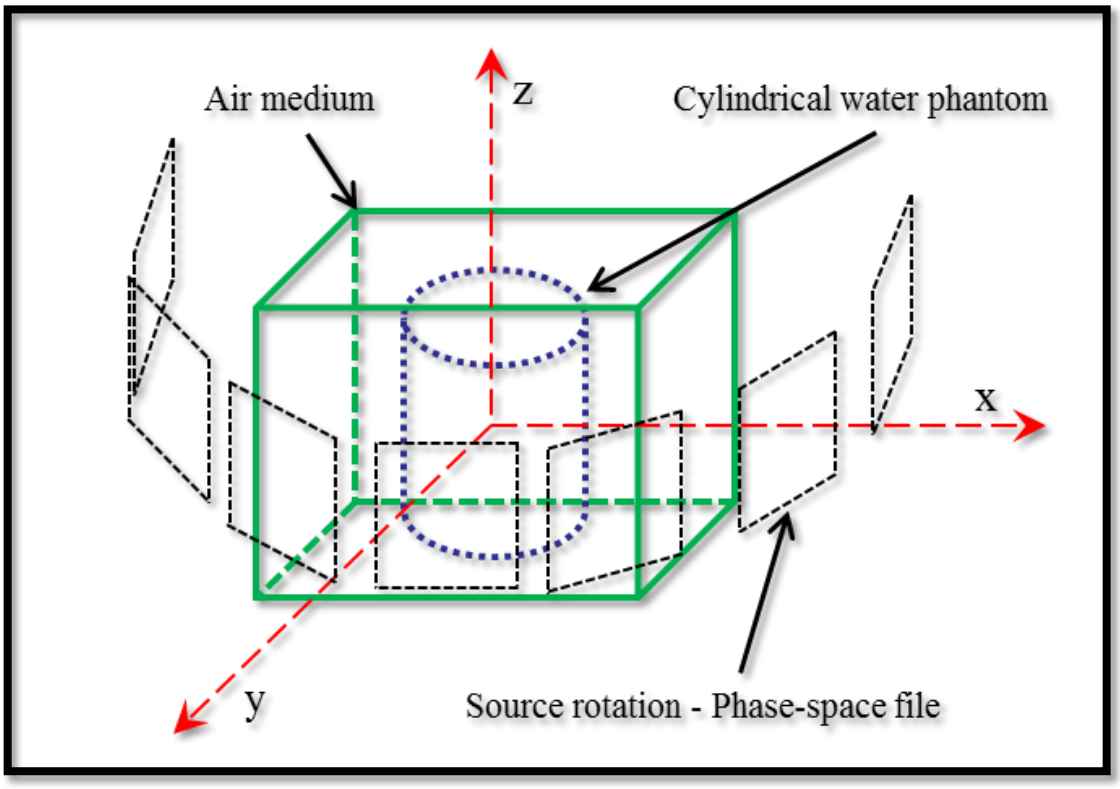

Figure 47: Geometry of the DOSXYZnrc MC code for calculating the dose distribution in the water cylindrical phantom.

Since there is no option to set a standard cylindrical shape phantom on the DOXYZnrc code, the geometry of the irradiated region consisted of voxels at volumes of 0.0156, 0.125, 0.125 and 1cm^3 for the cylindrical phantom measurements of 4, 8, 12, and 16cm respectively. Results of DOSXYZnrc are stored in a format of (*.3ddose). A MATLAB program was written to read out the DOSXYZnrc files and show the dose distribution in centre sagittal and transverse views. Dose in each phantom has been normalized so as to see the dose distribution as a percentage of a maximum of 100%, of each run separately. Figure 48 and Figure 49 show the dose distribution to the centre transverse and sagittal slices, respectively, of the water cylindrical phantoms in relation to phantom size using standard dose mode.

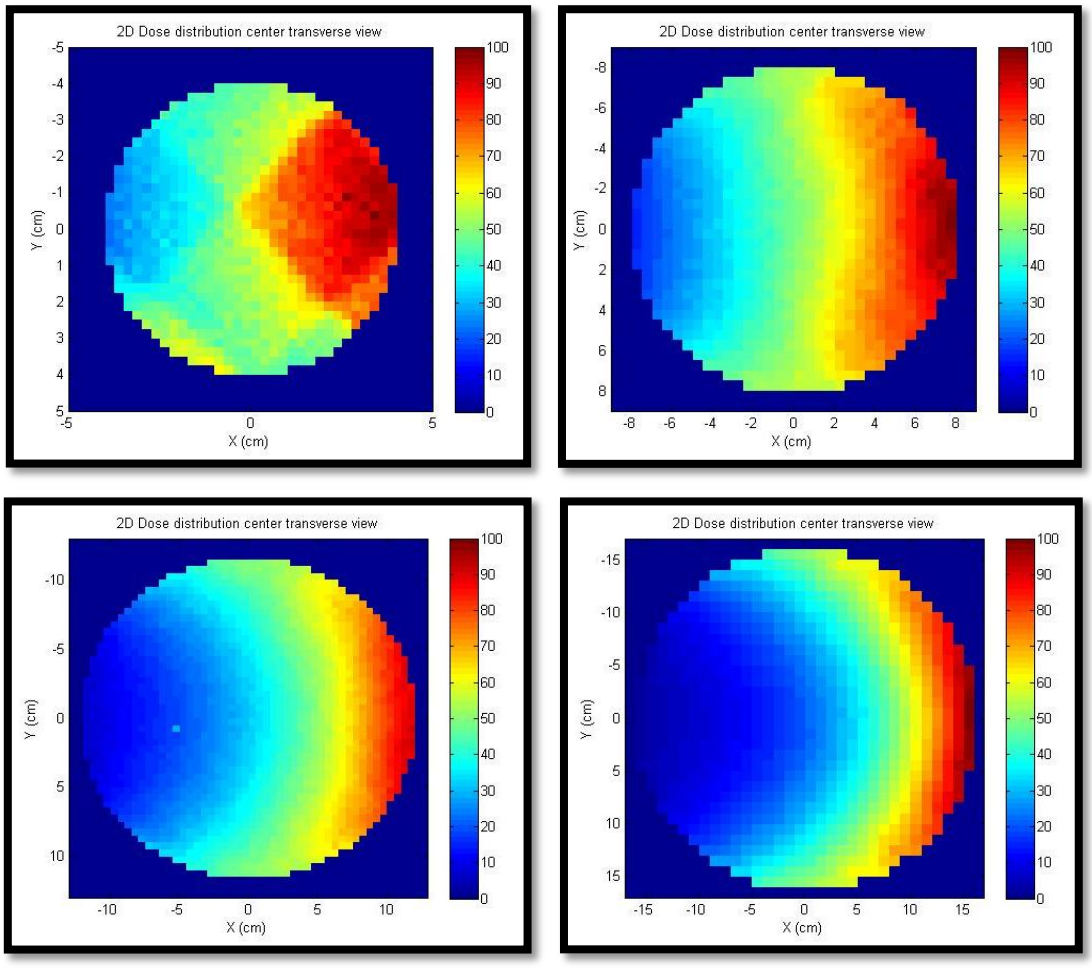

Figure 48: 2D Dose distribution at the centre transverse views of a 4, 8, 12, and 16 cm radius water cylindrical phantom (top-right, top-left, bottom-right and bottom-left) from the standard dose head mode of CBCT using the DOZXYZnrc code. Note that the colour scale is in units of as percentage of the maximum dose.

It is clearly demonstrated that as the phantom size increases the dose distribution and dose-intensity at the centre, bottom and top, and the two laterals of the phantom decreases.

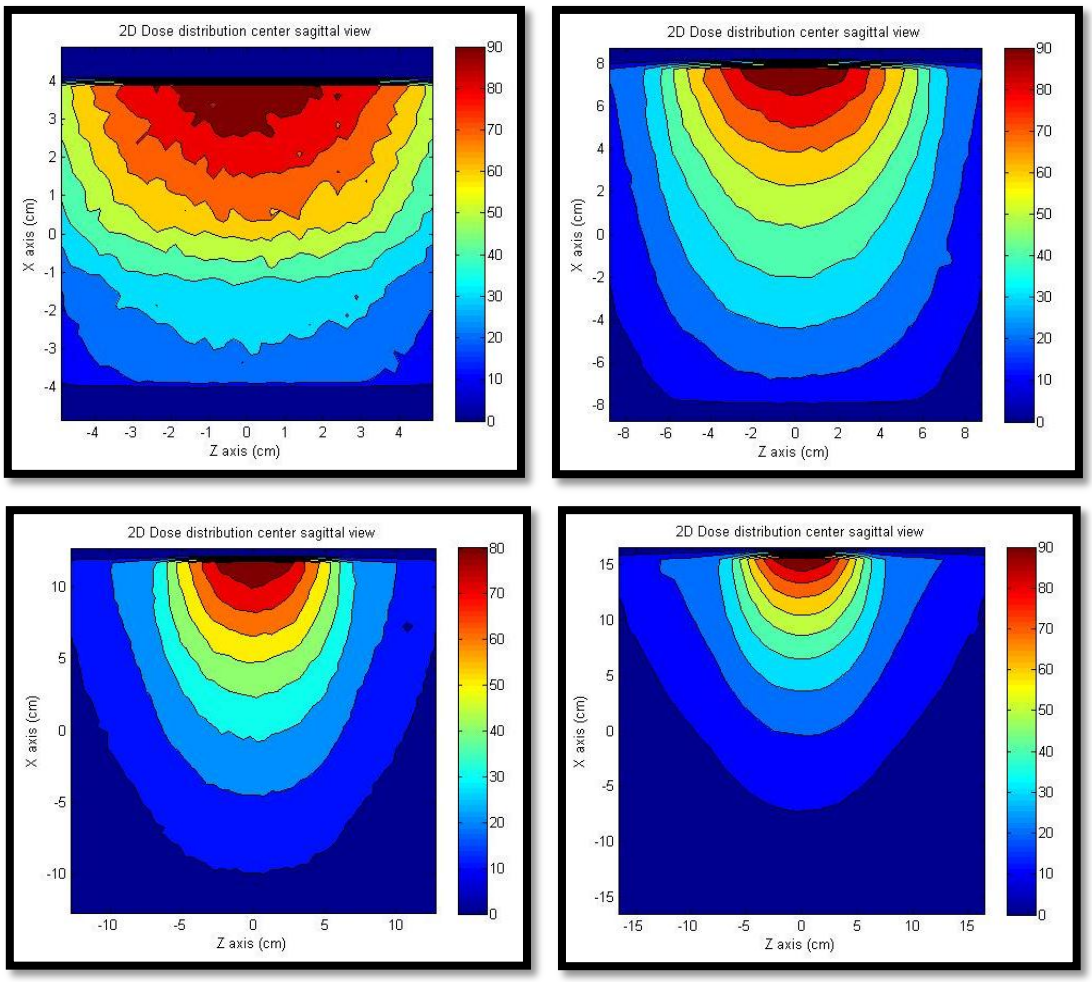

Figure 49: 2D Dose distribution at the centre sagittal view of a 4, 8, 12, and 16 cm radius water cylindrical phantom (top-right, top-left, bottom-right and bottom-left) from the standard dose head mode of CBCT using the DOZXYZnrc code. Note that colour scale is in units of percentage of the maximum dose.

The simulation was also carried out in the pelvis mode of the CBCT. The pelvis mode rotates 360^{o} around the phantom. Figure 50 and Figure 51 show the dose distribution to the centre transverse and sagittal slices, respectively, of the water cylindrical phantoms in relation to phantom size using pelvis mode. It is apparent that the dose distribution for the full rotation of the CBCT X-ray tube provides a higher dose than the half rotation at all points. In addition, doses decrease as the phantom size increase at all points as expected; top and bottom, centre, and two lateral positions.

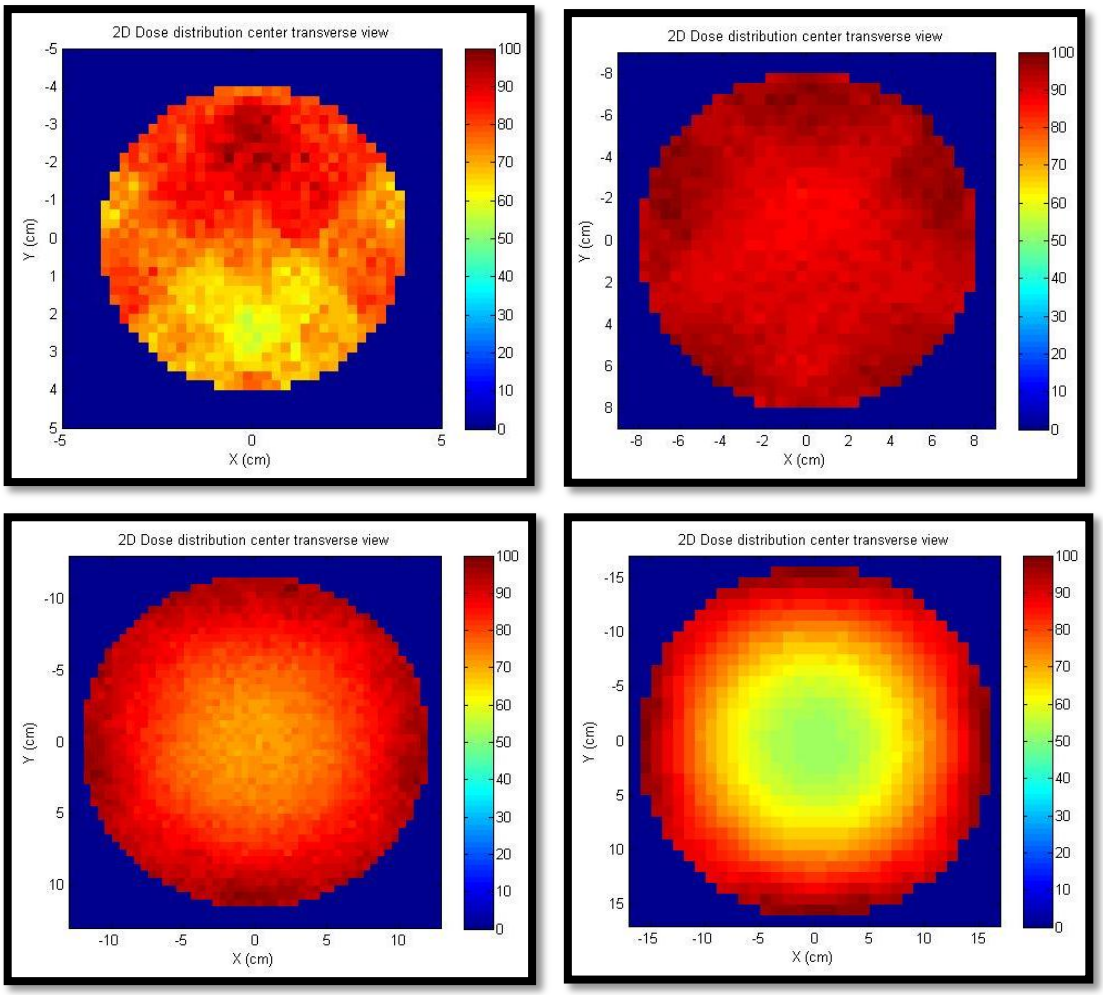

Figure 50: 2D Dose distribution at the centre transvers view of a 4, 8, 12, and 16 cm radius water cylindrical phantom (top-right, top-left, bottom-right and bottom-left) from the pelvis mode of CBCT using the DOZXYZnrc code. Note that colour scale is in units of percentage of the maximum dose.

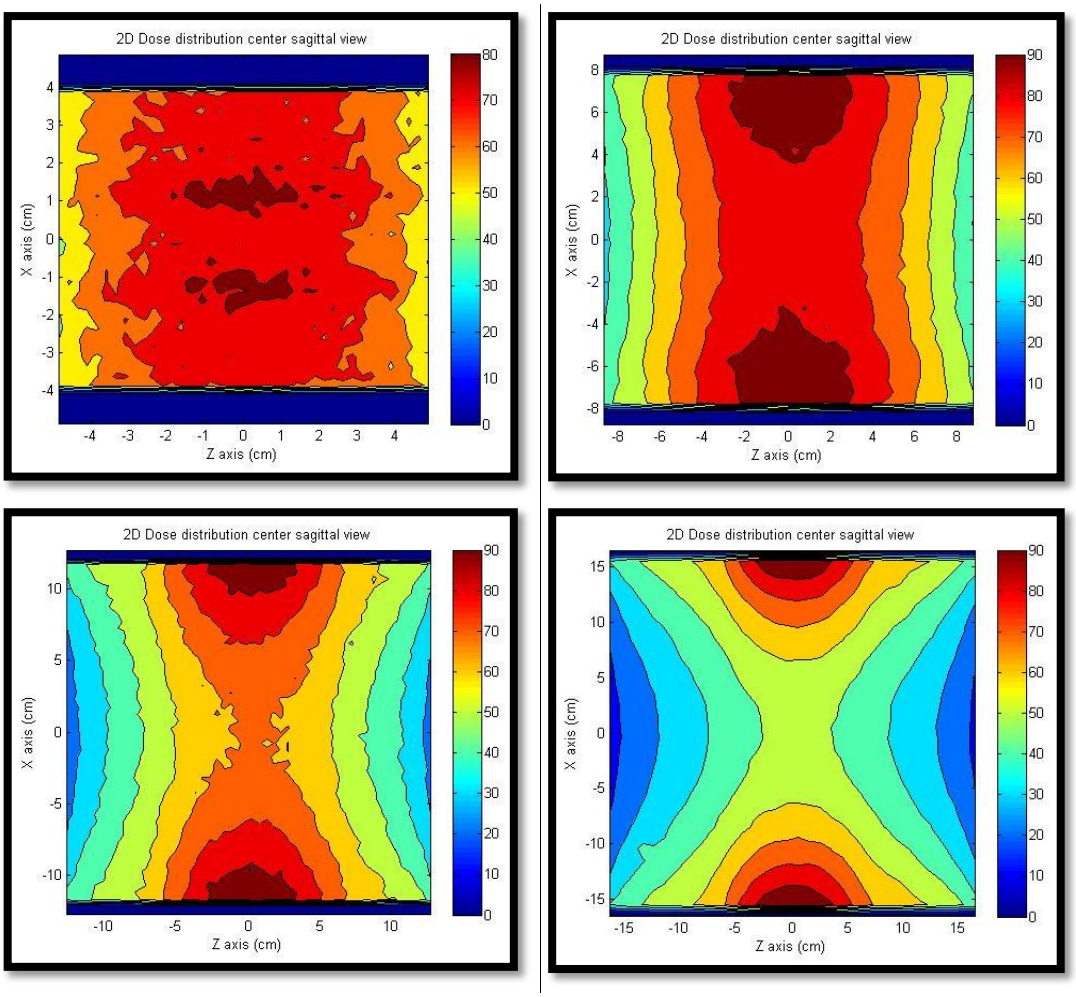

Figure 51: 2D Dose distribution at the centre sagittal view of a 4, 8, 12, and 16 cm radius water cylindrical phantom (top-right, top-left, bottom-right and bottom-left) from the pelvis mode of CBCT using the DOZXYZnrc code. Note that colour scale is in units of percentage of the maximum dose.

3.3 BEAM simulation: Discussion and conclusions

The aspects of the x-ray production and generation were clearly demonstrated in Figure 40 and Figure 41 (page 78). Figure 40 showed the full photon spectrum resulting from electrons accelerated by a 100kVp source and colliding with a target composed of 95% W and 5% Rh. The spectrum started from 1 keV and reached a maximum of 100keV, as explained above. In between the two extremes, 10 characteristic X-ray peaks were observed, which were caused by interaction with the target material (Table 13, page 78). Only two peaks resulted from the Rh component, since it only had 5% of the target composition. These are peaks 5 and 6, which correspond to k_{α} and k_{β} respectively for Rh and provide evidence that the correct beam energy and target material composition of the MC code were selected by the user.

Figure 41 showed the 110kVp and 125kVp electron beam spectra. Both ranges started at 1 keV and ended at 110keV and 125keV respectively, matching the maximum voltage applied to accelerate electrons. Similar work is reported in the literature by Ding and colleagues (2007), who simulated five tube voltages, 60, 80, 100, 120 and 125 kVp and covered more of the lower energy range (Figure 52) (Ding, et al., 2007). Similar to the current study, all these x-ray spectra ended at the maximum tube voltage. Other studies by Downes and colleagues (2009) and Spezi and colleagues (2009) presented simulations of the Elekta Synergy linac CBCT with F1 bowtie at an energy of 125kVp; Figure 53 and Figure 54 respectively for each author (Downes, et al., 2009) and (Spezi, et al., 2009). The differences seen between the beam spectra presented in Figure 53 and Figure 54 result from the use of differently shaped and sized filters, named F1, and F0, and S, M, and L respectively.

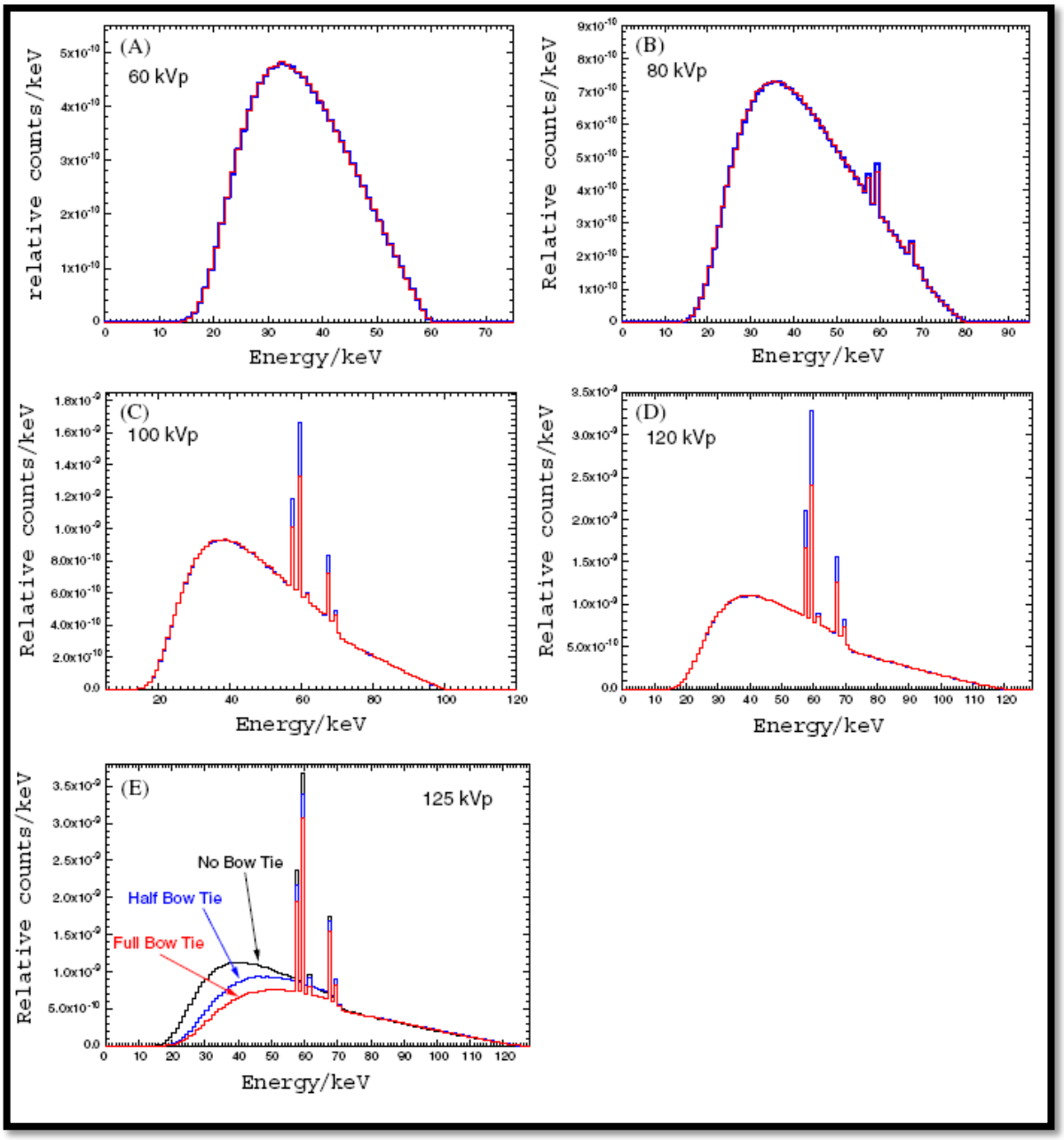

Figure 52: (A), (B), (C) and (D) show the photon energy spectra for 60 kVp, 80 kVp, 100 kVp and 120 kVp beams, respectively. (E) Photon energy spectra for a CBCT 125 kVp beam with and without bow tie filters (Ding, et al., 2007).

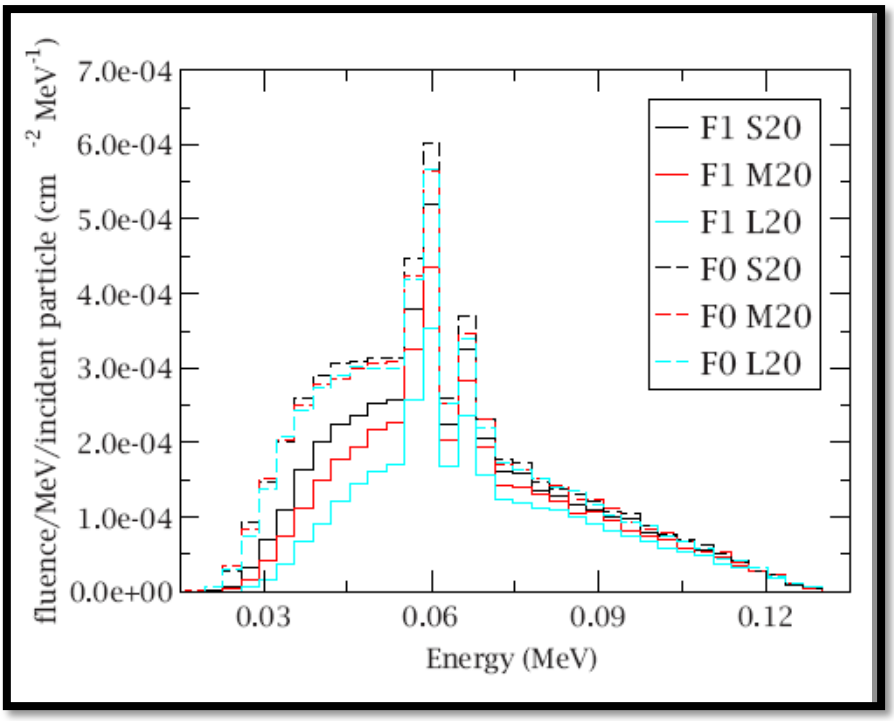

Figure 53: Energy spectra profiles of selected collimator inserts for the F1 bowtie filter (Downes, et al., 2009).

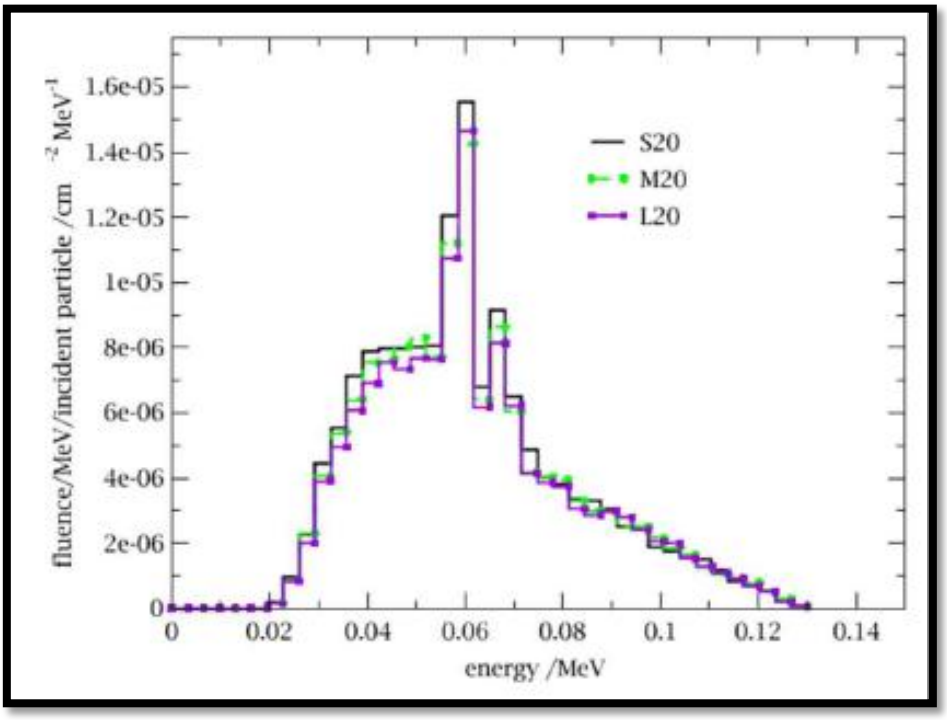

Figure 54: Spectra distributions for the radiation beams defined by a selected number of XVI collimator cassettes (Spezi, et al., 2009).

The main reason for beam hardening is to remove low energy X-rays from the spectrum to prevent them penetrating the patients' skin. Beam hardening, occurs between phase spaces one and two, in all of the tube voltage simulations. Figure 42 shows that the CBCT X-ray component removed almost all of the low energy peaks. Figure 43 (page 81), on the other hand shows the difference between spectra when using or not using the bow-tie filter. The CBCT X-ray components, composed of layers of lead and aluminium, removed all X-rays with energies below 40keV. However the bow-tie, composed of an aluminium filter, reduced only the intensity of the radiation by roughly 33% at the centre. The effects on the output spectrum in all modes, when using or not using the bow-tie filter are shown in Figure 44. Phase-space files in the BEAMnrc output spectrum were in agreement with spectra presented in the literature.

Bow-tie filters have been designed to remove low energy photons and to shape the beam to be maximal in the centre and shallow at the edges. Thus, the bow-tie filter not only affects the spectrum of the beam but also affects the shape of the beam produced on both the x- and y-axes. The beam profile follows exactly the shape of the bow-tie filter, but in reverse order. This is the basic of the radiation interaction, where the intensity of the X-ray spectrum is inversely related to filter thickness (i.e. high intensity when thin). This effect can be seen in Figure 55 where the beam is at its maximum intensity at the centre. When the bow-tie filter has a minimal thickness of 1.5mm at the centre of the beam and a maximum of 2.75cm at the edges (Figure 56), the intensity of the beam is reduced from $6x10^{-9}$ to $4x10^{-9}$ (33% reduction) at the centre and reduced to zero at the edges.

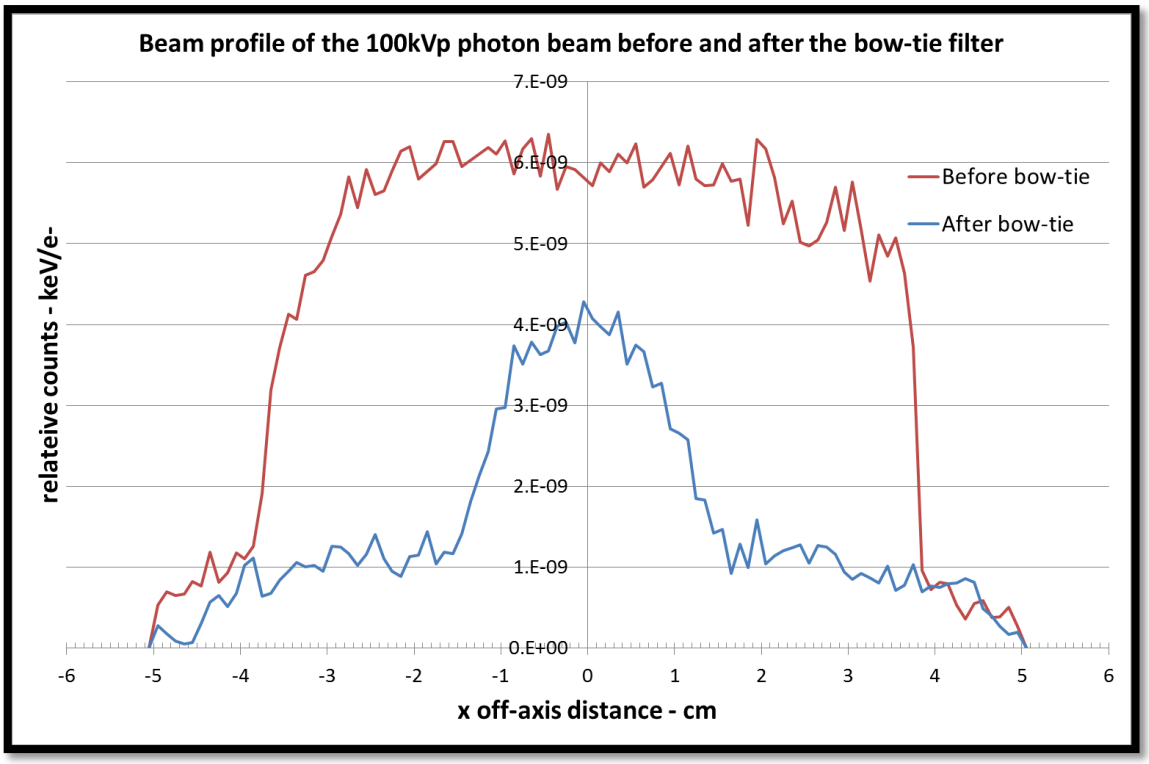

Figure 55: Beam profile on the X off-axis for the 100kVp electron beam before and after the full bow-tie filter.

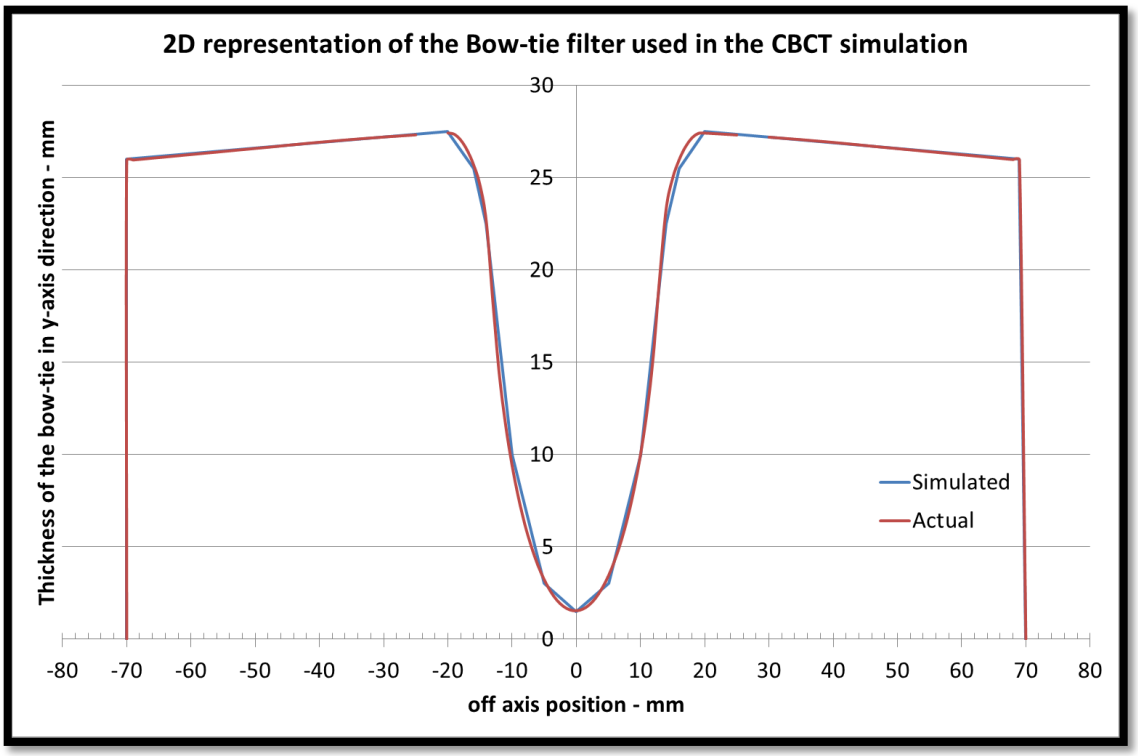

Figure 56: 2D representation of the Bow-tie filter used in the CBCT simulation.

Figure 57 shows that the beam profile on the y off-axis is flat due to the shape of the bow-tie filter (Figure 7 page 8). The only reduction of beam intensity occurs at the 1.5mm centre, which is seen at the centre of the x off-axis (Figure 57). The trend and the output of the beam profiles are the same for 110kVp and 125kVp beams (Figure 58).

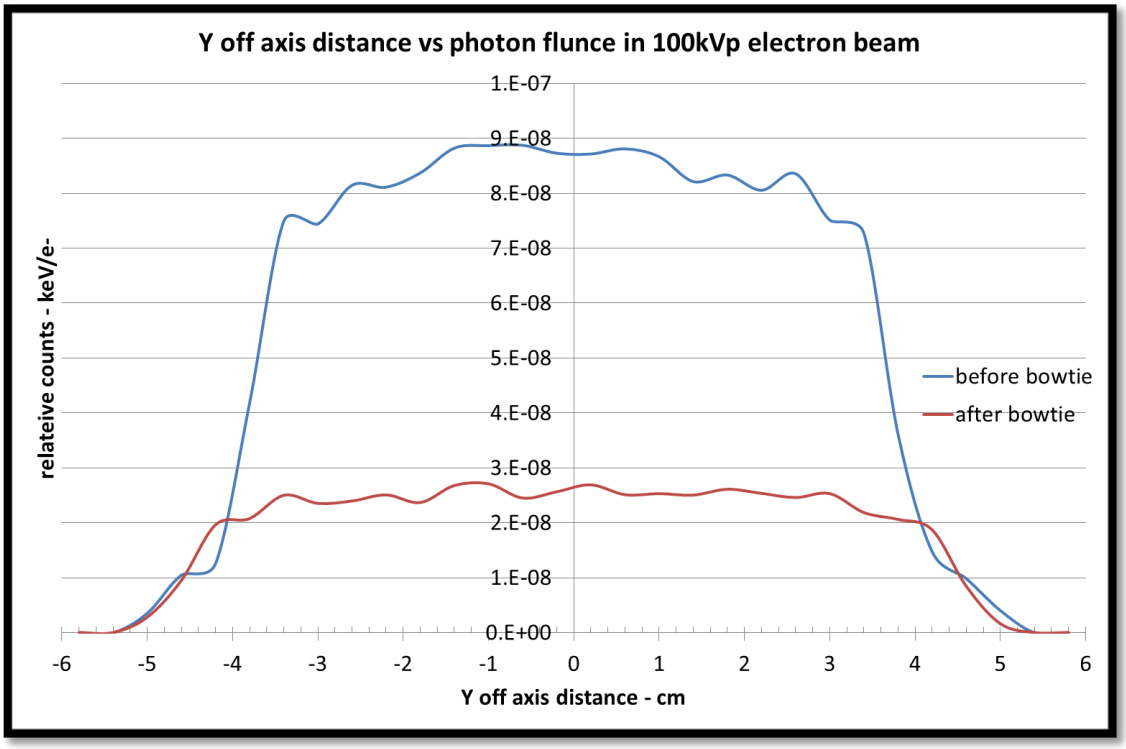

Figure 57: Beam profile on the Y off-axis for the 100kVp electron beam before and after the full bow-tie filter.

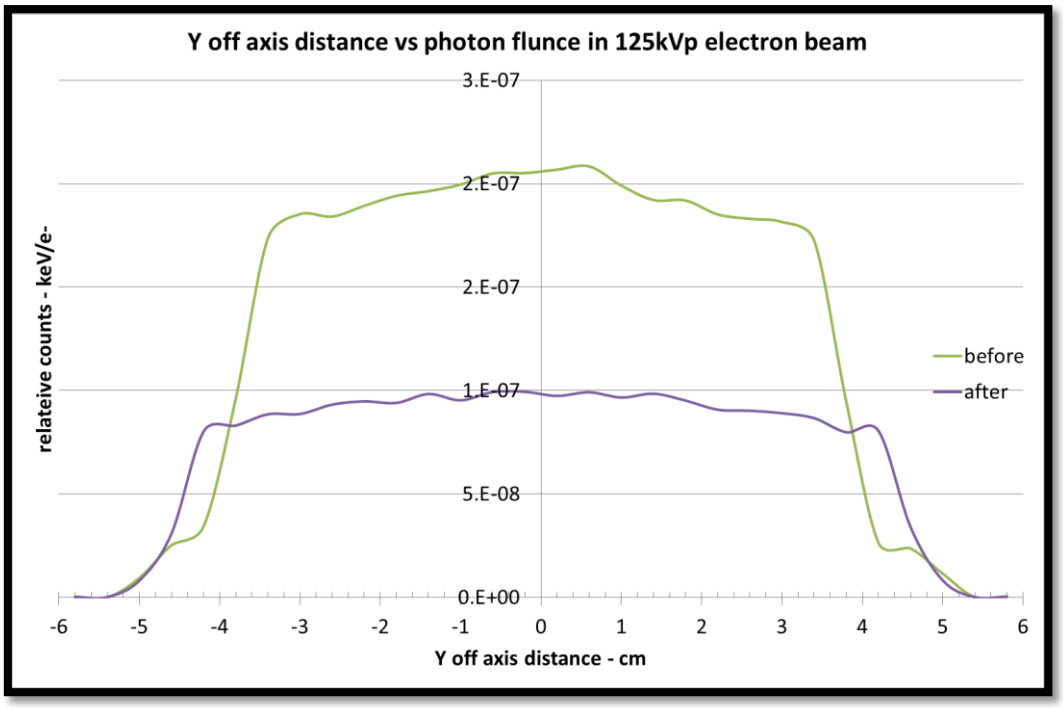

Figure 58: Beam profile on the Y off-axis for the 125kVp electron beams before and after the full bow-tie filter.

When using a half bow-tie filter, the expected beam should resemble the spectrum observed when using half of the full bow-tie filter. This is the case, as shown in Figure 59.

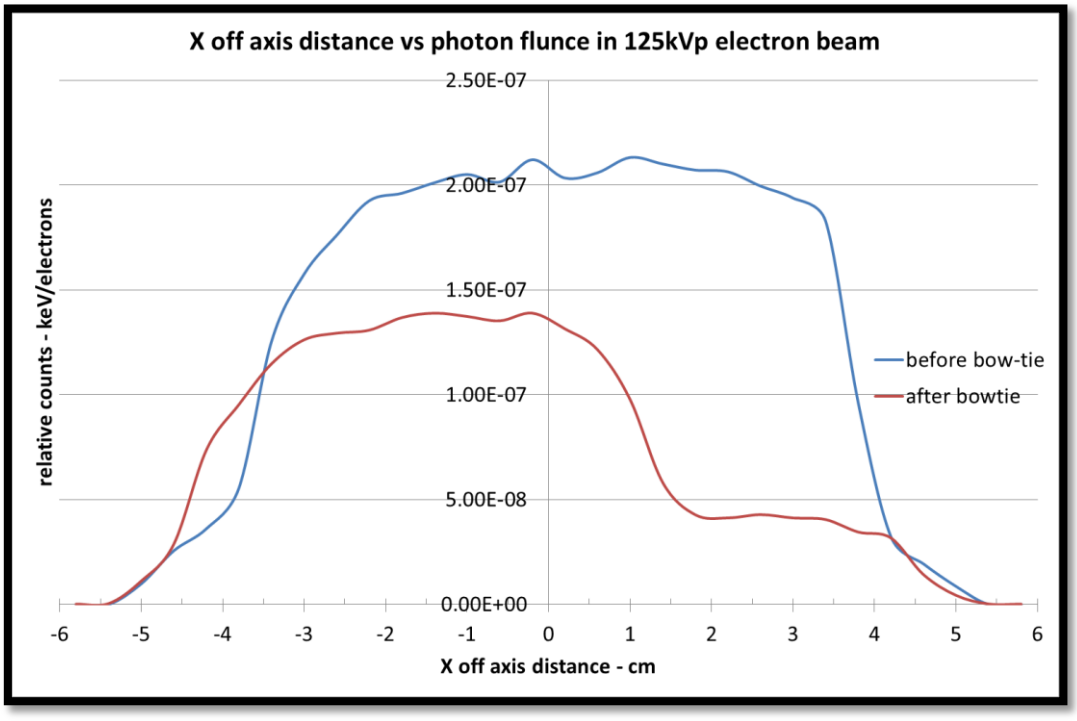

Figure 59: MC BEAM result for the X off axis versus beam flounce for the half bow-tie filter in the 125kVp electron beam.

The PDD is one of the most important components used to calculate the dose in radiotherapy treatment. The PDD is usually used to determine doses received at certain depths at a given treatment site. For the low keV energy sources, the dose is reduced as the radiation propagates through the tissue material. The degree of reduction or the behaviour of the curve depends on the composition of the materials with which the X-rays interact. Since the human body consist of 75% water, the PDD is usually measured in water. For low energy radiation, the reduction in intensity begins at the surface of the water phantom or a patient. This is not the case with the high-energy beam, where there is a so-called 'build-up region'. In the high energy beam, the maximum dose is achieved a few cm from the surface depending on the energy (Figure 60).

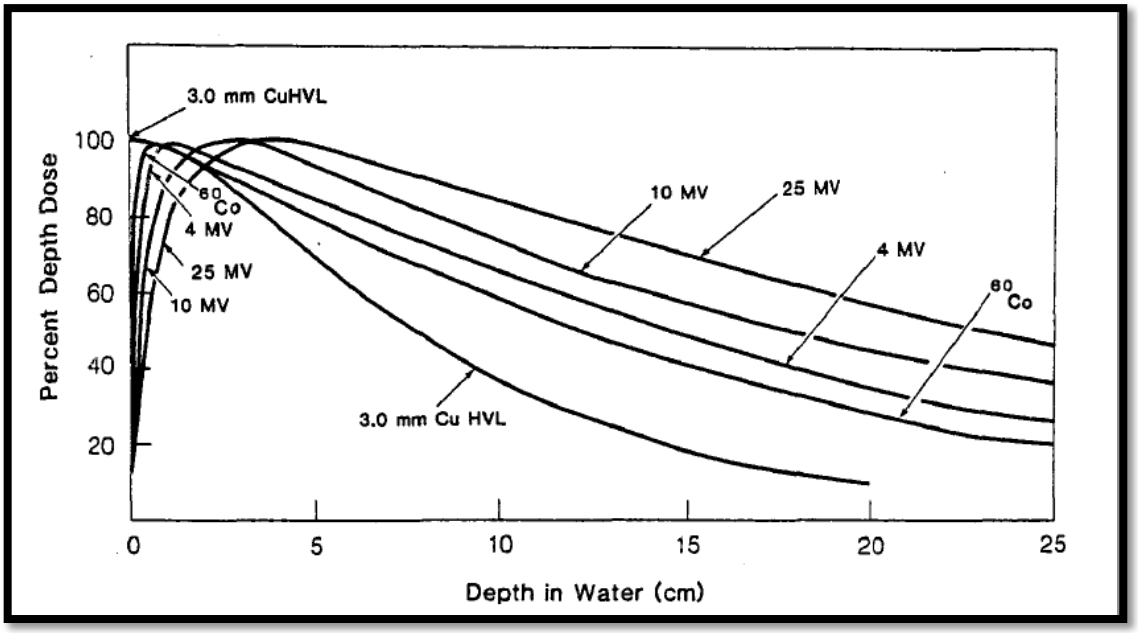

Figure 60: Central axis depth-dose distribution for different quality photon beams (Khan, 2003).

Figure 46 (page 83) shows the PDD for the low energy beams, where there is no build-up region and demonstrates that the dose increases at the beam energy increases. For the 100kVp beam, the percentage error begins at 0.5 % and increased to a maximum of 2.2 % at a water depth of 24 cm. Similarly, for the 110kVp and 125kVp beams, the errors range from 0.4% – 1.6% and 0.3% – 1.2%, respectively. The maximum PDD of the 100kVp and 125kVp beam occurs at a depth of 0.5cm whereas

it occurs at the surface for the 110kVp beam. This finding is due to experimental error, since the maximum PDD should be measured at a depth greater than that of the 100kVp beam and less than that of the 125kVp beam, to fit with the voltage-PDD relationship. Table 14 shows the PDD values and their associated errors observed at different X-ray voltages.

Table 14: PDD values at different depths for different x-ray tube voltages.

depth	PDD using x-ray source tube voltage					
cm	100kVp	statistical uncertainty %	110kVp	statistical uncertainty %	125kVp	statistical uncertainty %
1	98.53	0.5	98.62	0.4	98.61	0.3
2	92.74	0.5	93.51	0.4	94.09	0.3
3	87.06	0.5	87.14	0.4	87.71	0.3
10	40.24	0.7	41.65	0.6	42.96	0.4
15	20.75	1.0	21.54	0.8	22.98	0.6
20	10.03	1.4	10.45	1.1	11.68	0.8
24	4.48	2.2	5.09	1.6	5.50	1.2

Figure 46 showed the PDD for the water phantom only, but this research also simulated low energy sources with different phantoms. Using MC simulation, the ability to produce a PDD at any energy and using any phantom is unlimited. Figure 61 shows the PDD in muscle tissue and bone material in contrast with the PDD measured in the water phantom. The density of bone is higher than that of water and muscle tissue, and hence, the attenuation is expected to be greater. This explains why the dose decreases rapidly as the depth increases due to absorption of the radiation (Figure 61).

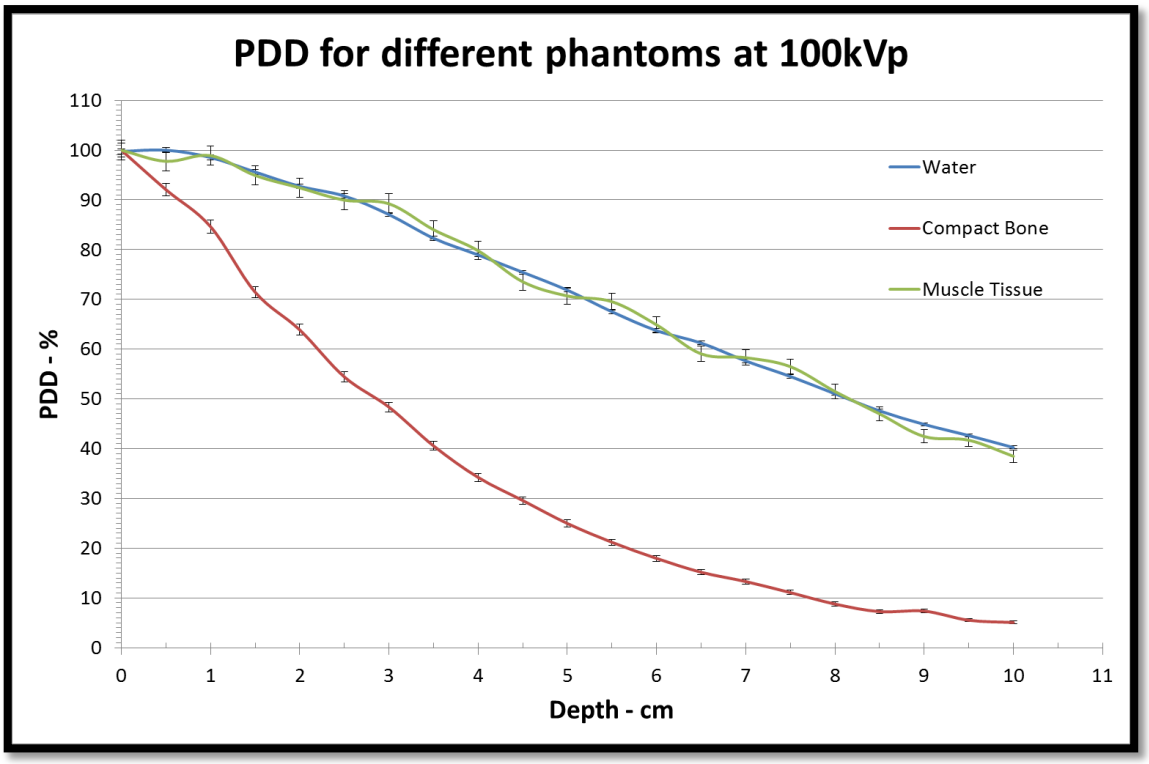

Figure 61: MC result of PDD at different phantoms for 100kVp.

As can be seen in Figure 61, only 10cm of bone is required to stop almost all of the low energy CBCT X-ray, while only 60% of the beam is stopped by an equal depth of water or muscle tissue. The PDDs at 10 cm depth were found to be 40.2± 0.3%, 38.5 ± 1.2% and 5.06 ± 0.3% in water, muscle tissue and compact bone, respectively, with a 100 kVp beam. These findings are explained by the fact that the densities of water and muscle are 1 g.cm^{-3} and 1.06 g.cm^{-3} respectively, whereas the density of compact bone is 1.85 g.cm^{-3}.

The MC results are in the magnitude of 10^{-21} incident photons from the target source. These values need to be normalized according to the DOSXYZnrc formula, which is as follows (Rogers, et al., 2001):

$$NP = NINCSRC \times \frac{NCASE + ncaseold + nsmiss + (NRCYCL + 1)}{nshist}$$

Where, **NP** is an estimate of the number of particles incident from the original, non-phase space source. **NRCYCL** is the number of times that each particle is to be recycled, **nshist** is the total number of particles in the phase space file, and

NINCSRC is the number of particles from the original, non-phase space source used to generate this phase space source. **NCASE** is the number of histories in this run, **ncaseold** is the number of histories from previous runs (if this is the first run then this will be 0) and **nsmiss** is the total number of particles from the source that missed the geometry, including in any previous runs (Rogers, et al., 2001). These values can be found in the output results of the MC code as shown in (Appendix one). The exact dose value of each point can only be found if the code has been validated using hospital measurements as a comparator, which unfortunately could not be achieved. Despite this, the MC results have been included here to show the relationship between phantom size and dose.

It is possible to CT scan the phantom and convert the DICOM image to readable format for DOSXYZnrc as an".egsphant'' file using the sub-code called CTCREATE (Kim, et al., 2010). This step is only applicable for 150 slices per scan or fewer. Kim and colleagues scanned the CATPhan phantom and converted the DICOM image into.".egsphant'' format. The next step was to use the scanned image as a phantom and measure the CBCT dose using four modes. This method is no longer applicable since the code produces many errors when converting the DICOM image to the DOSXYZnrc format (Kim, et al., 2010). The current simulation of CBCT in this study agreed with the values presented in the literature Figure 62.

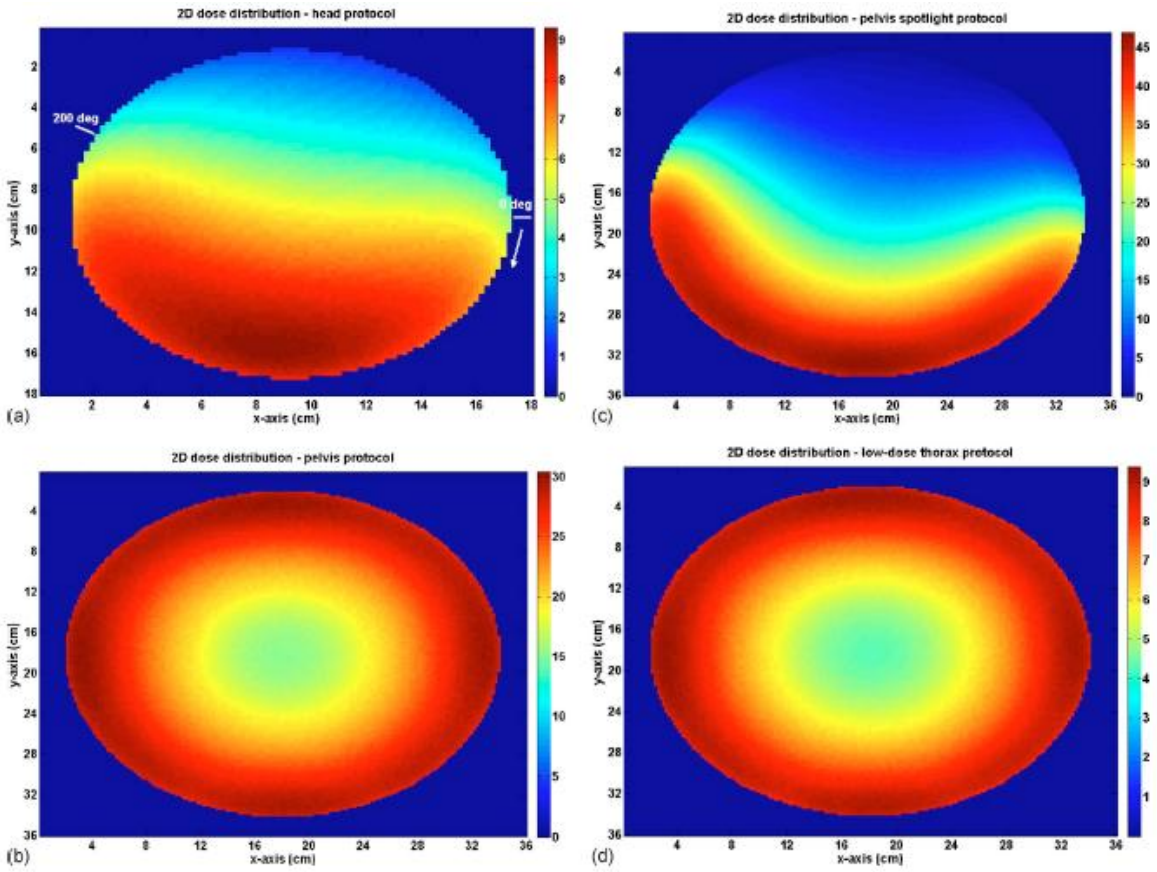

Figure 62: Visualization of the 2D dose distribution for each new CBCT scan protocol: a) Head, b) pelvis, c) pelvis spot light, and d) low-dose thorax scans. The start and end points for the partial-angle scan was marked (a). Note that the colour scale is in the unit of mGy (Kim, et al., 2010).

MC is a powerful tool that helps in working in a radiotherapy environment. The negative aspect of MC simulation is the amount of time consumed in writing and running the code. A very recent publication by Ding and Munro (2011) presented a very useful data that support the results presented herein this research where they use same MC code, BEAM/DOSXZYnrc (Ding & Munro, 2011). Their result showed that "Doses for OBI 1.3 are 15 times (head), 5 times (thorax) and 2 times (Pelvis) larger than the current OBI 1.4" and "The dose increases up to two times as the patient size decreases (Ding & Munro, 2011). In this research, doses delivered to the oesophagus, thyroid and brain were also higher compared to OBI v1.4, by factors of 8, 22 and 16 respectively (see Table 5, page 36).

4 Hounsfield number to electron density relationship

This chapter presents in some detail the changes in Hounsfield Units (HU) of the CIRS-062A phantom's inserts for each of the six acquisition modes of the Varian CBCT OBI version-1.4; and shows ways to calibrate the HU to electron density (ED) for subsequent direct use of the CBCT scans in radiotherapy treatment planning. The consistency and accuracy of the HU number should indicate the feasibility of using the CBCT images directly for treatment planning and dose calculations in place of the conventional CT scans.

The CIRS-062 phantom was scanned using all six of the different scanning modes of Varian CBCT 1.4. The phantom was also scanned using the CT (GE LightSpeed CT) at RSCH and the images obtained were used as reference images. Then both image sets, CT and CBCT, were examined in a personal computer using the imaging program, ITK-SNAP v 2.1.4-rcl. This program allows the user to extract the HU number for point or area pixels. The HU-to-ED calibration curves are then obtained using the ITK-SNAP by selecting circular area profiles of 3cm in diameter for all insertions except those representing dense bone insertions, of only 1cm, due to the size of the insertion. Later the HU-to-ED tables were used to calculate the dose volume histogram (DVH) for a single beam profile and IMRT plans.

In the following sections, comprehensive calibration curves of HU-to-ED for each mode setting and for each phantom configuration of CBCT are included. Suggestions as to which mode is suitable to be used for treatment planning for each anatomic site are also presented. The DVH for a single beam profile and for IMRT plans is addressed with percentage difference between the CT and CBCT based calculations in a separate chapter, chapter 5.

4.1 Methodology

All images were acquired using the on-board imager (OBI) system manufactured by Varian v 1.4 and CT (GE LightSpeed CT) at RSCH. The phantom configuration as well as the methods by which each image was acquired is addressed in the following sections.

4.1.1 CIRS-062A phantom configuration

The electron density phantom CIRS-062A is used in this study to give a range of electron density and representative diameter for a body and head, Figure 12 page 27. The insertions have been arranged to represent the organ positions in the body, similar to the configuration shown in Figure 63. All the CBCT scanned images have been obtained using this configuration, while the CT scanned images were obtained using a different arrangement.

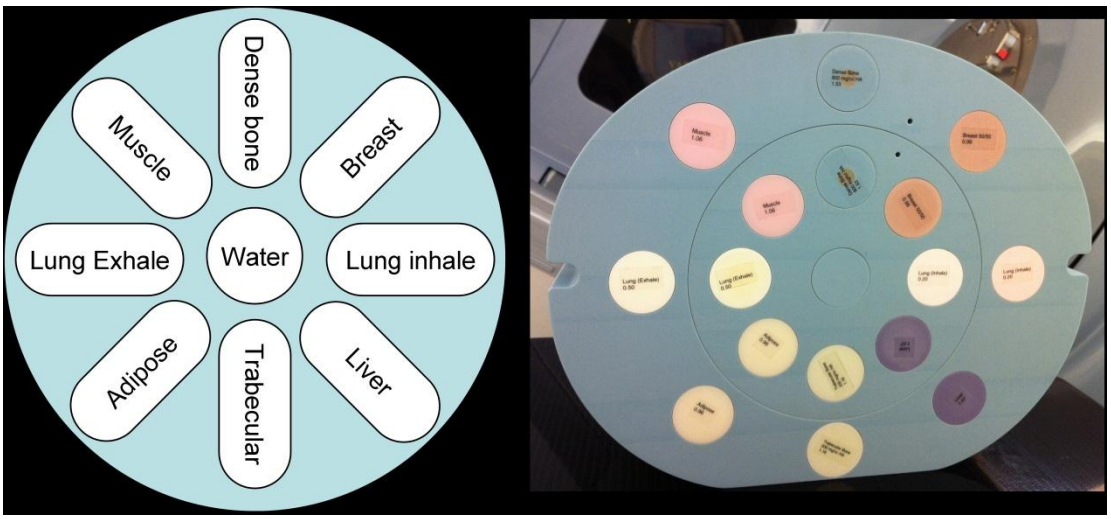

Figure 63: Insertion positions in the CIRS-062 phantom.

As it appears in Figure 63 (right), the inner circular phantom is called the head phantom and together with the outer circular phantom, the complex is called the body phantom. Many authors have agreed to use a tissue equivalent material phantom (CIRS-062 A) rather than any quality control or assurance phantom (CatPhan) in calibrating the CBCT scan images (Hatton, et al., 2009) and (Guan & Dong, 2009). This is because CatPhant, for example, was designed mainly for QA and QC. In addition, the insertions are small compared to CIRS-062A.

4.1.2 3D image acquisitions

A large number of HU readings can be obtained by placing electron density plugs in different positions, both in the central axis and offset configurations, Figure 13 page 28. More than 24 CBCT images were scanned in this study. To ease the interpretation of each image, tables are presented to give each image a specific code name. Table 15 shows each symbol used and its abbreviation making up such a code name. In addition, shows the head slice, body slice, and body phantom of the CIRS-062A phantom.

Table 15: Symbol names used to refer to scanned images

Symbol	Abbreviation
CT	Computed Tomography
CBCT	Cone Beam CT
A	Central axis configuration
B	Offset configuration
HS	Head Slice
BS	Body Slice
BP	Body phantom
M1	Standard dose head mode
M2	low dose head mode
M3	high quality head mode
M4	Pelvis mode
M5	pelvis spot light mode
M6	low dose thorax mode

The symbols shown in Table 15 have been used as combination codes to represent details about a scanned image. For instance: the code M3-B-HS means CBCT high quality head mode for the offset configuration for Head Slice. A few examples of these descriptions are shown in

Table 16. At times, the abbreviation: CT-A-BP is used twice to represent the head insertions and body insertion, herein CT-A-BP(H) is used for the Head and CT-A-BP(B) is used to denote body insertions. The ITK-SNAP 2.1.4-rc1 program was used to extract the HU numbers from all scanned images, including CT images.

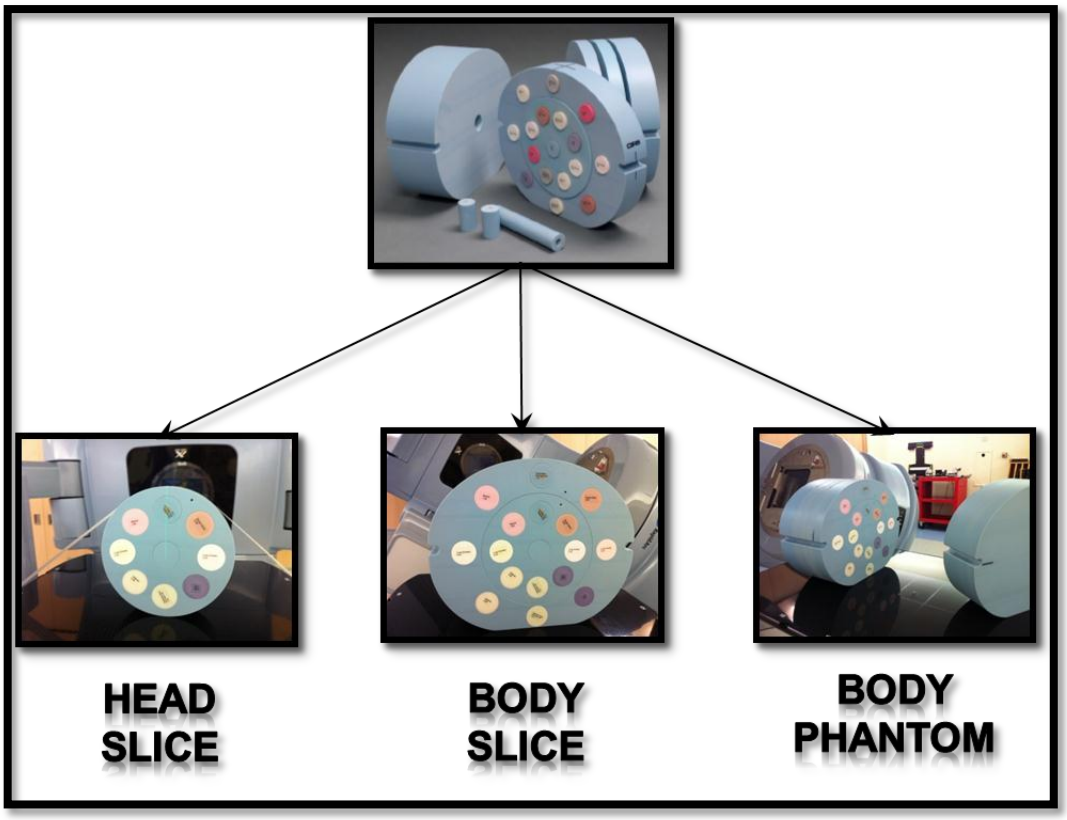

Figure 64: CIRS-062A phantom configuration during the scan and calibration of the CBCT HU-to-ED.

Table 16: Examples of image codes and their descriptions

Image name	Description
CT - A - HS	CT image of the central axis configuration for the Head Slice
M1 - A - HS	CBCT standard dose head mode for the central axis configuration for Head Slice
M3 - B - HS	CBCT high quality head mode for the offset configuration for Head Slice
M4 - B - BP	CBCT pelvis mode for the offset configuration for body phantom
M5 - B - HS	CBCT pelvis spot light mode for the offset configuration for Head Slice
M6 - A - BP	CBCT low dose thorax mode for the central axis configuration for body phantom

4.2 HU-to-ED Calibration curve results

All results presented herein are expressed as calibration curves of the HU number acquired form the scan against the electronic density of the insertions. These HU-to-electron density calibration curves have been classified into three categories, based on the scan and phantom configurations. The first category contains HU numbers for the CT scan where five curves are obtained. These scans are as follows: CT-A-HS, CT-A-BS(H), CT-A-BP(H), CT-A-BS(B) and CT-A-BP(B) as shown in Figure 65. In general, results of each calibration are almost identical, except when electron density is $\geq$ 3.8 per x 10^{23} cm^3 or when HU extends above +300 HU and below -600 HU respectively. Average HU values for all insertions and for all CT scans have been used as the reference values in all other comparisons with CBCT scans. These HU values are shown in Table 17.

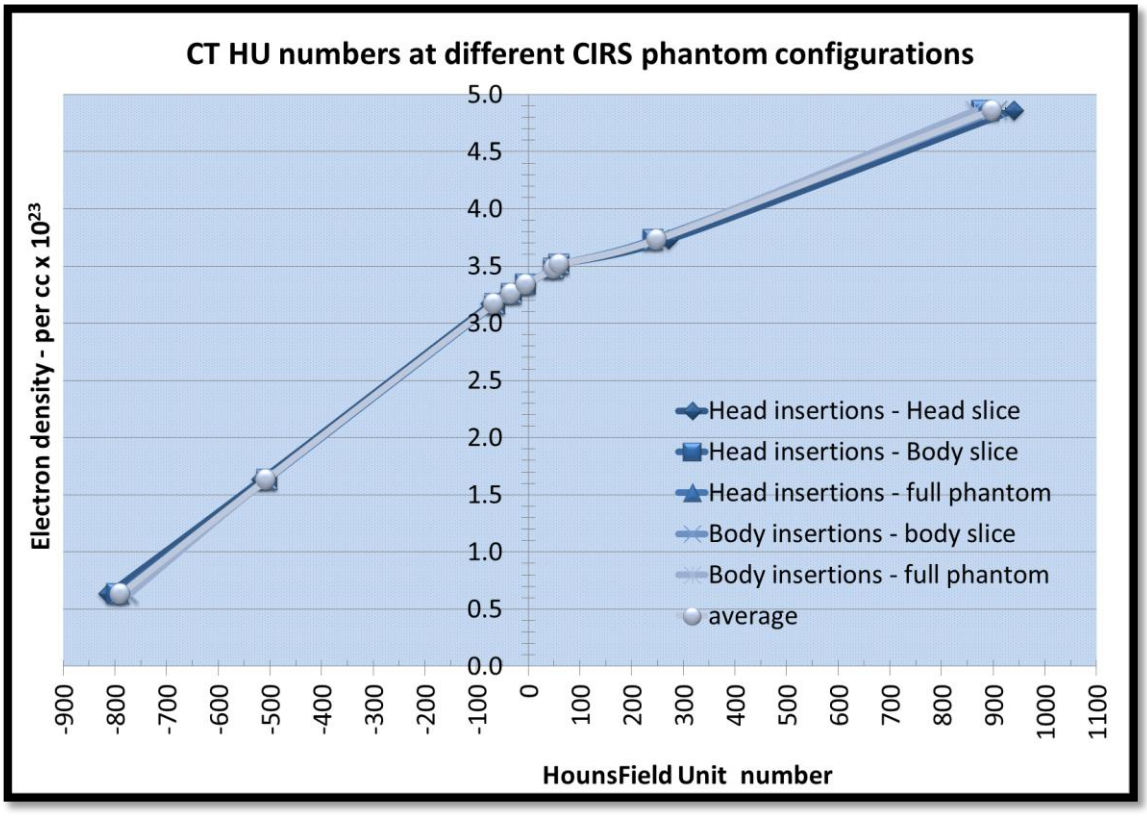

Figure 65: HU-to- Electron density relationship for the CT scans when using different phantom configurations

The second category of results contains the HU numbers for the head insertions only, which are summarised by Figure 66 to Figure 68. The first figure (Figure 66) shows the HU number in the head slice at different modes of the CBCT, where the slice is in position A,; the central axis position. Figure 67 shows the HU number for body scan at position A, while Figure 68 shows the same as Figure 67 but for position B; the offset configuration position. The acceptable tolerance in the HU number during the calibration is ±40 HU (Yoo, et al., 2006).

Table 17: The average HU number of all the CT scans. (Reference HU numbers)

Materials	Electron Density per cm^3 x 10^{23}	HU values of CT scans	
		Average	S.D
Lung inhale	0.634	-788.9	15.0
Lung exhale	1.632	-508.0	4.5
Adipose	3.170	-66.4	3.3
Breast	3.261	-33.2	2.7
Water	3.340	-4.7	1.3
Muscle	3.483	49.7	0.9
Liver	3.516	59.5	1.3
Trabecular	3.730	248.8	11.8
Dense bone	4.862	897.3	26.0

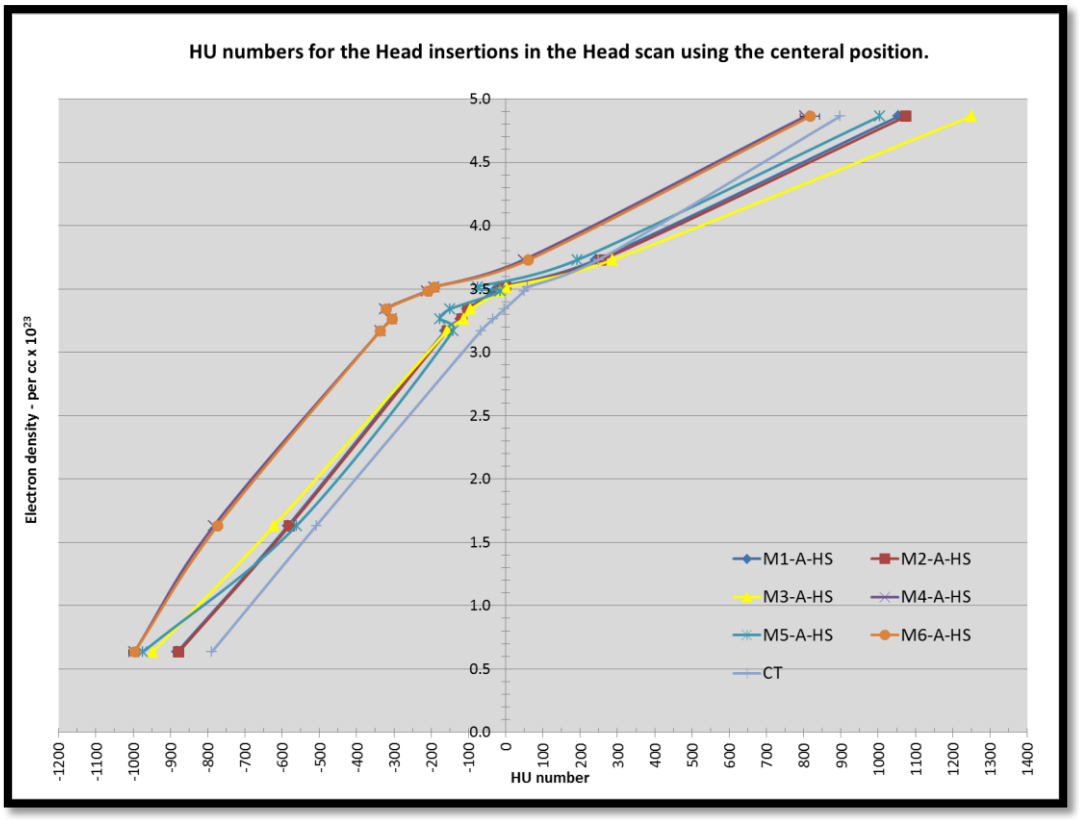

Figure 66: HU-to-Electron density relationship for head insertions in the head slice scan at position A and different modes.

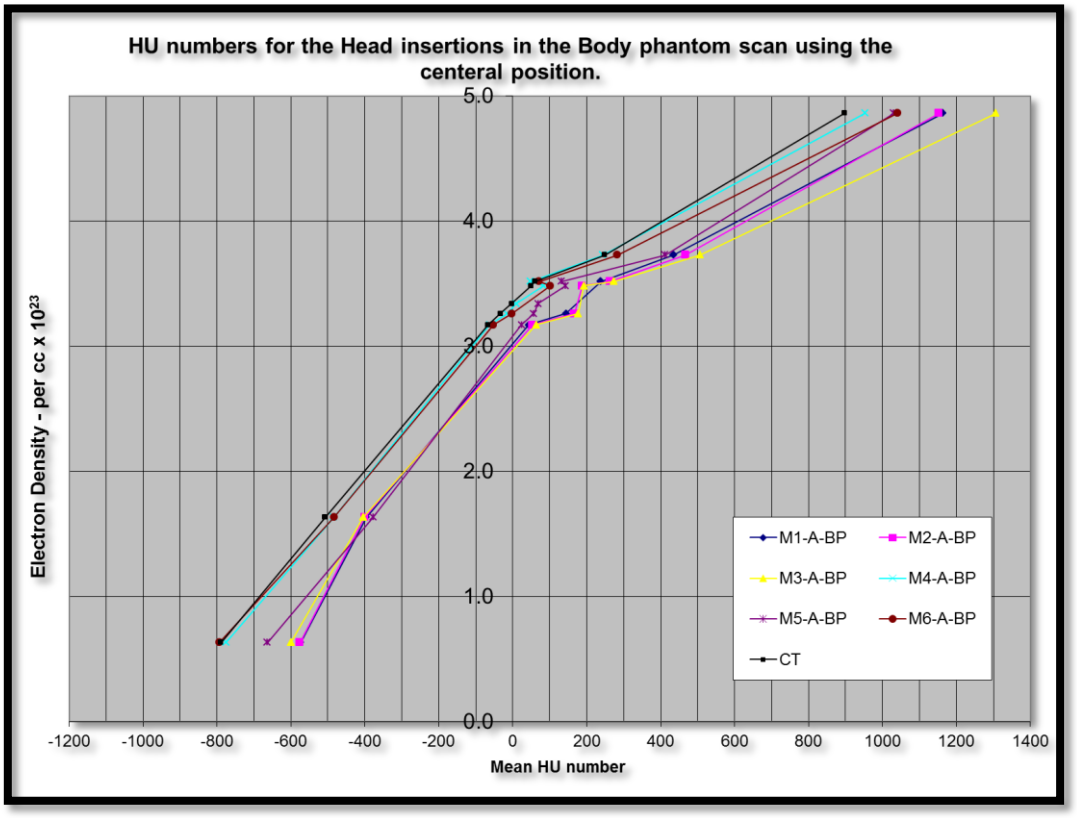

Figure 67: HU-to-Electron density relationship for head insertions for the body phantom at position A.

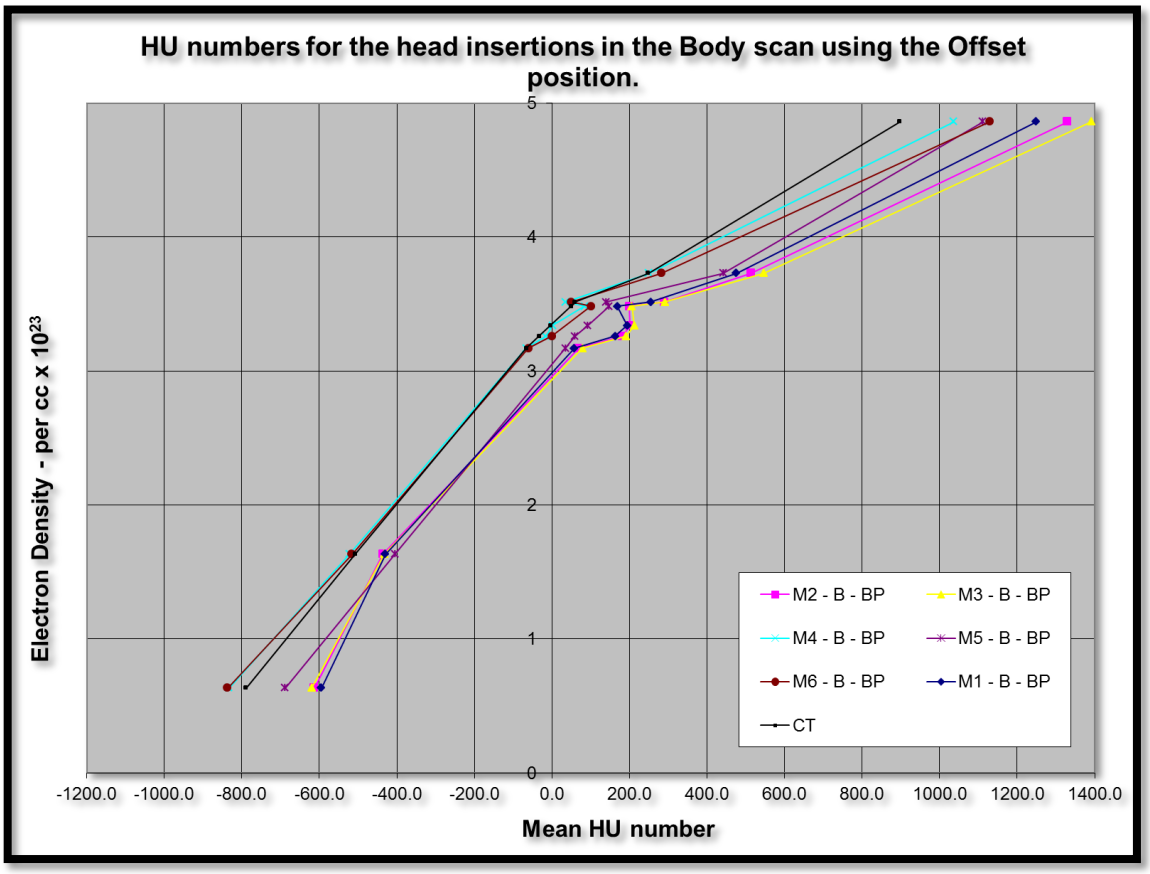

Figure 68: HU-to-Electron density relationship for head insertions in the body phantom at position B.

The third category of results contains HU number changes for body insertions only. Figure 69 and Figure 70 summarise the results of HU number changes for the body scans using positions A and B, respectively. It should be pointed out that M1, M2 and M3 are designed for small phantom size which is demonstrated from the inconsistency of the HU numbers for the body insertions. In addition, HU numbers for muscle and breast are invisible for the body insertion when M1 is used.

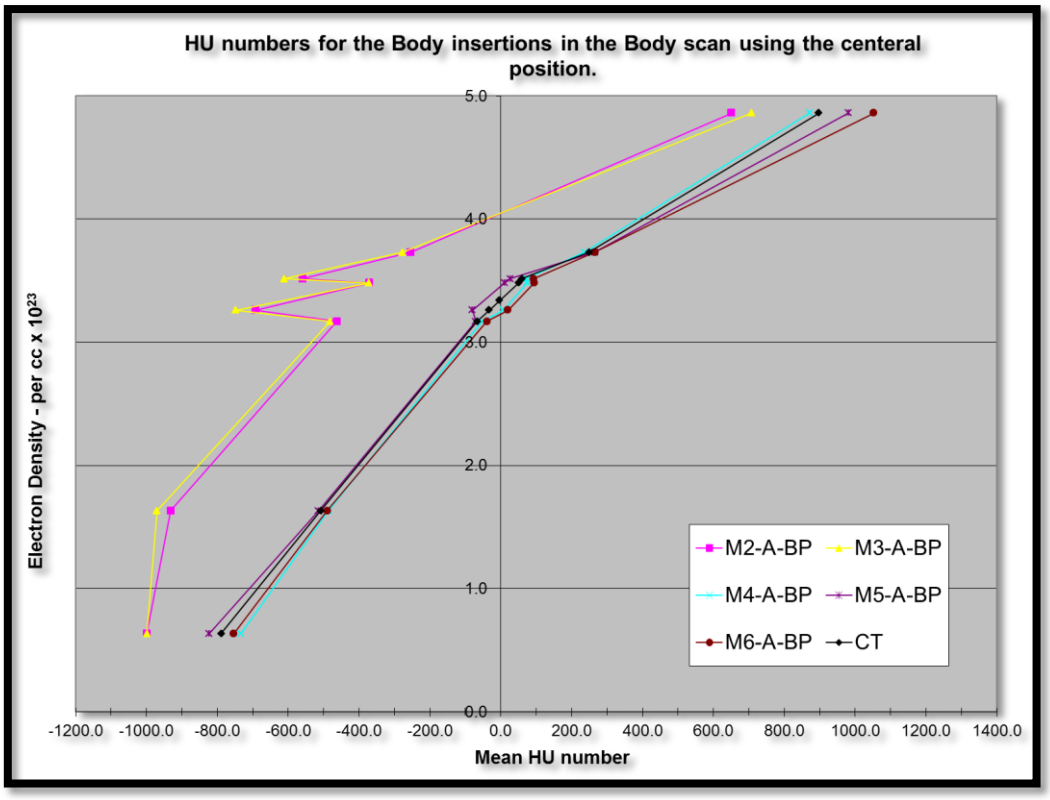

Figure 69: HU-to- Electron density relationship for the body insertions in the body phantom scan at position A

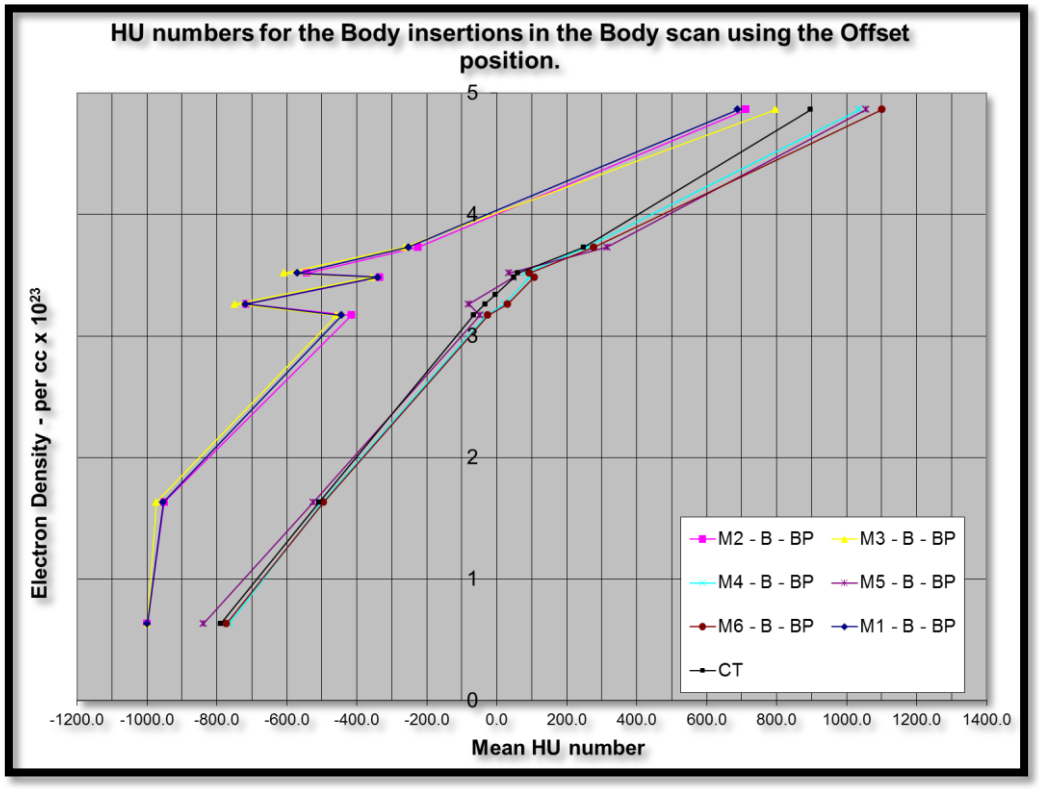

Figure 70: HU-to- Electron density relationship for the body insertions in the body phantom scan at position B

4.3 HU-to-ED calibration curves: Discussion and Conclusions

For each CT scanner, the HU-to-Electron density relationship is stable with respect to the CT acquisition parameters, with the exception of the tube voltage (Rong, et al., 2010). Here, Figure 65 (page 105), with fixed CT parameters, the consistency and accuracy of the HU number in the CT scans can be seen clearly despite the altered phantom configuration in each scan. Each mode for the CBCT, on the other hand, gives a range of values for the same materials at different phantom configurations. For instance, the HU number for the trabecular bone when scanned by CT in different configurations were 272.7, 242.9, 239.4, 244.9, and 244.5 at CT-A-HS, CT-A-BS(H), CT-A-BP(H), CT-A-BP(B) and CT-A-BP(H) respectively with an average of 248.8±11 HU. However, for the standard dose mode, M1, the values of trabecular bone on the head insertions were 242.8±30, 434.1±202 and 475.8±115 for the HS-A, BP(H)-A and BP(H)-B, respectively. This variation is due to the large contribution of beam scattering at the CBCT, which leads to inaccuracy in calculating the HU-to-Electron density relationship.

For the CT scanner, results at all phantom configurations are shown in Figure 65, this reveals that individual HU numbers are very close to the average values shown in Table 17. The maximum difference between the values was of 5% with the exception of the CT-A-HS scans. There were 9, 15, 9 and 5% differences from the average values at adipose, breast, trabecular bone and dense bone sites respectively. This is due to the size of the scan object under investigation. Since these objects are small, less attenuation of the X-ray occurred which led to larger values of these insertions than the average HU numbers. The effect of adding a body slice on the head slice insertions can be found by making a comparison between CT-A-HS(H) and CT-A-BS(H), where both results are for the head insertions, Table 18. For the dense materials such as dense bone and trabecular bone, the predominant interaction is the photoelectric effect, where the probability of this interaction increases at low energy. In this situation, the outer-phantom worked as an absorber and divider of the X-ray energy which is called beam hardening. In addition, the scattered radiation that lost its energy in the first collision, then interacted with the highly dense materials and was absorbed into it. This explains why in CT-A-HS insertions HU values are larger than those found from the CT-A-BS(H) insertion. The effect of insertion position can be found by making a comparison between CT-A-HS and CT-A-BS. (Table 18).

Table 18: The differences in HU for different phantom configurations.

insertion	Average HU of CT	(CT-A-HS) - (CT-A-BS)	(CT-A-BS(H)) - (CT-A-BS(B))	(CT-A-HS) - (CT-A-BP(H))	(CT-A-BS(B)) - (CT-A-BP(B))
Lung inhale	-788.9 ± 15	-16.6	-20.8	-22.1	-4.0
Lung exhale	-508.0 ± 4.5	-11.4	2.0	-12.0	-1.8
Adipose	-66.4 ± 3.3	-8.9	1.6	-8.7	0.8
Breast	-33.2 ± 2.7	-6.5	-1.2	-4.2	1.3
water centre	-4.7 ± 1.3	1.2	Nil	3.1	Nil
Muscle	49.7 ± 0.9	-0.8	-1.0	0.6	2.4
Liver	59.5 ± 1.3	-0.9	-0.7	2.3	1.1
Trabecular	248.8 ± 11.8	29.2	-1.5	32.7	-0.5
Dense bone	897.3 ± 26	61.0	-30.7	47.6	44.5

No obvious distinction can be made at different configurations of the phantom on the CT scan results, except when using water. The water insertion is positioned in the middle/centre of the phantom where there is a high probability of scattering radiation. However, since there are no noticeable differences between the CT-A-BS(H) and CT-A-BS(B), CT-A-HS and CT-A-BP(H) and CT-A-BS(B) and CT-A-BP(B) it can be concluded that the CT scanner is capable of recognising values of the insertion in the slice at any depth without being affected by the surrounding medium or the position of the insertions. Overall, the CT HU-to-Electron density calibration gives a good agreement at different configurations and can therefore be used as a reference to compare all of the CBCT HU-to-Electron density calibration results.

Attenuation of the CBCT X-ray by CIRS-062A is caused by three major types of interaction which are; Rayleigh scattering (coherent scattering), the photoelectric effect and Compton scattering. The probability Rayleigh scatter occurring is high for low energy X-rays and when atoms with a high atomic number are encountered. The probability of photoelectric effect is inversely proportional to the energy of the incident X-ray and directly proportional to the atomic number of the interaction medium, (i.e pe α Z^3/E^3). The probability of Compton scattering depends on X-ray energy and is independent of atomic number, Z. This is because a Compton interaction involves essentially free electrons in the absorbed medium. In fact, the probability of a Compton interaction depends on the number of electrons per gram i.e. electron density. The effective Z values for fat, muscle, water, air and bone are 5.92, 7.42, 7.42, 7.64 and 13.8 respectively. However, the number of electrons per gram of these tissues/materials are 3.48, 3.36, 3.34, 3.01 and 3.00×10^{23} respectively meaning that the probability of the Compton scattering is nearly the same for all of these materials (Khan, 2003).

The photon energy spectrum of a CBCT which was simulated by Ding et. al., (2007) and represents the minimum and maximum energy of 120keV and 125keV that the CBCT standard dose and pelvis mode produce. In this energy range, the predominant interactions for water are Rayleigh scattering, the photoelectric effect and Compton scattering (Ding, et al., 2007). However, the photoelectric effect and Rayleigh scattering are most important in bone tissue where materials of high atomic numbers

exist. In general, for the few 10keV energies, the interactions are mainly the result of Rayleigh scattering and the photoelectric effect, whereas Compton scattering is involved for the few X-ray energies at 100keV.

The HU numbers in the CBCT scan are different from one mode to another, in addition to being different in the same mode but at different phantom configurations. The main reason for the inconsistency in the HU numbers in the CBCT is the large contribution of the scattering artefact from the cone-beam of X-rays. The problem of scattering in a CT scanner has been somewhat solved by the positioning of grids next to the detector, (i.e. between the detector and the scanned object), which allow only transmitted radiation to pass through and to register at the detector. This technology has worked to reduce some of the scattering effect, (Yoo & Yin, 2006) and (Siewerdsena & Jaffray, 2000). X-ray scattering is increased if the phantom consists of more dense materials. This effect can be seen in the CT scan in Figure 65, when high dense bone 4.862 per cm^3 x 10^{23} is imaged. It would be difficult to record all of the X-rays coming from the cone beam as it has been recognised in the literature that the scattering artefact is considered as a fundamental limitation of the CBCT image quality (Zhu, et al., 2009).

In the CBCT head slice scans shown in Figure 66, the modes that matched the reference values most closely were M1 and M2: standard dose head and low dose head respectively. The HU values of the trabacular bone in M1, M2 and M3 are close to the reference values (242, 256, 287 and 248 HU, respectively). The reasons behind this are the position of the insertion and the angular rotation of the CBCT X-ray source around the phantom in these modes. The trabacular bone is positioned on the bottom of the phantom, see Figure 63, where it is less likely to be affected by the secondary scatter radiation. Furthermore, in these modes, the angular rotation of the X-ray source is 204^o, underneath the treatment couch. This is also a clear explanation for the differences between this and the dense bone as the latter is positioned in the top of the phantom, where no primary radiation passes through it, Figure 63. M4 and M6 at a 360^o rotation, where primary radiation passes through the top insertions. The HU values of the dense bone in these modes are within 10% difference to the reference values; 803 and 817 HU respectively with the reference value being 897HU.

In the body phantom scan, the HU values of the head insertions are all increased on average by 226HU (Figure 67, page 107). This shift of 226 HU, made both M4 and M6 modes almost identical to the reference values. It should be noted that, in the body phantom scan, muscle as well as water in the head insertion where invisible when M1 was used due to the setting of the mode as well as the position and density value. Muscle in the head insertion is positioned on the upper right corner, (Figure 63), therefore the insertion was made invisible due to the angular rotation of the X-ray source in addition to the effect of the body phantom on the head slice. Moreover, all insertions, in the body slice, may block primary radiation from reaching the insertion in the upper right and left corners in the modes with a setting of 204^{o} angular rotation. This may affect the selection of the 204^{o} rotation mode in the pelvic or thorax treatment areas.

Figure 68 shows the HU numbers for the head insertions in the body phantom scan using the offset configuration. The difference between HU at different phantom positions; central and offset, can be seen by comparing Figure 67 and Figure 68. Figure 71 shows that the lung exhale, lung inhale, muscle, trabacular and dense bone recorded a maximum difference between the central and offset position of 9%. The difference reaches as much as 30% in the liver and adipose tissues.

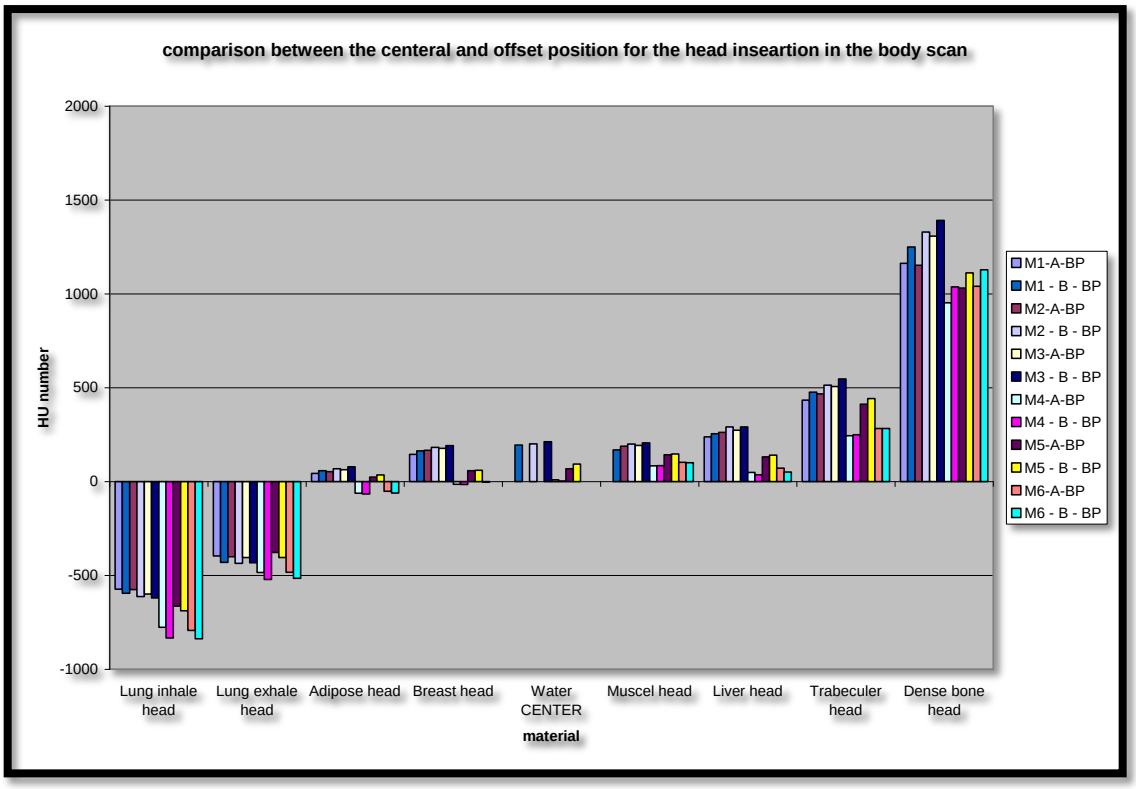

Figure 71: HU comparison between central and offset positions of the body insertions.

Figure 69 and Figure 70 show the HU number values for the body insertions in the whole body scan using different modes at central and offset positions, respectively. M1, M2 and M3 are designed for small sites, but if these modes are used for the large phantom as in the case of a body scan, Figure 69 and Figure 70, the resulting HU numbers are completely wrong and cannot be used for diagnostic nor for therapeutic applications. The zigzag behaviour shown in Figure 69 and Figure 70 are from the ring artefact on the image. The main reason for the ring artefact is detector non-uniformities (Dendy and Heaton, 1999). The result was the same when HU numbers were obtained from another slice with a 1 cm difference, see Figure 72.

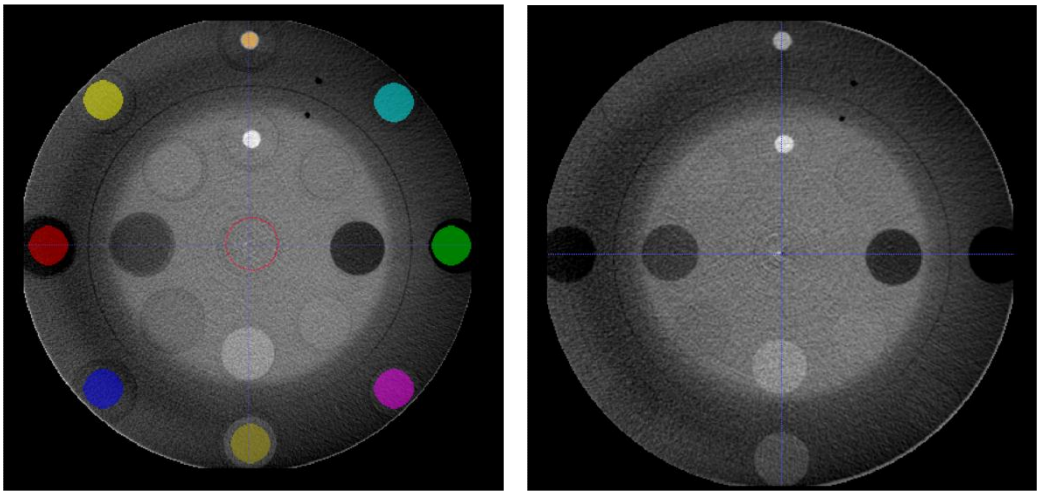

(A) (B)

Figure 72: (A) Standard dose head mode calibration for the offset positions of the insertions and full body scan. (B) Low dose head mode for central positions of the insertions and full body scan.

The previous comparison was between the CT value and modes at a fixed phantom configuration. One should also consider the comparison of the CT and each mode at different phantom configurations to confirm which mode is suitable for body site scanning. The results of these comparisons between CT and M1 to M6 are shown in Figure 73. In general, when looking at figures of CT verses each mode, one can see clearly that the closest results to the CT value out of all phantom configurations are M4 and M6. However, these modes should not be matched with the small phantom, as they have been designed for large ones. Figure 73 (A) shows that M1 is in good agreement when used for small phantoms at a central position but it is not to be used for large phantoms. Similarly, M2 and M3 should be used for small phantoms as is shown in Figure 73 (B) and (C) respectively. Among the three modes, M1, M2 and M3, M1 is the best mode to be used for treatment planning on the small phantom size, head, where it is the closest to the CT values, see Figure 74. The M5 results shown in Figure 73 (E) have good agreement with the CT for all phantom configurations with few range of variations.

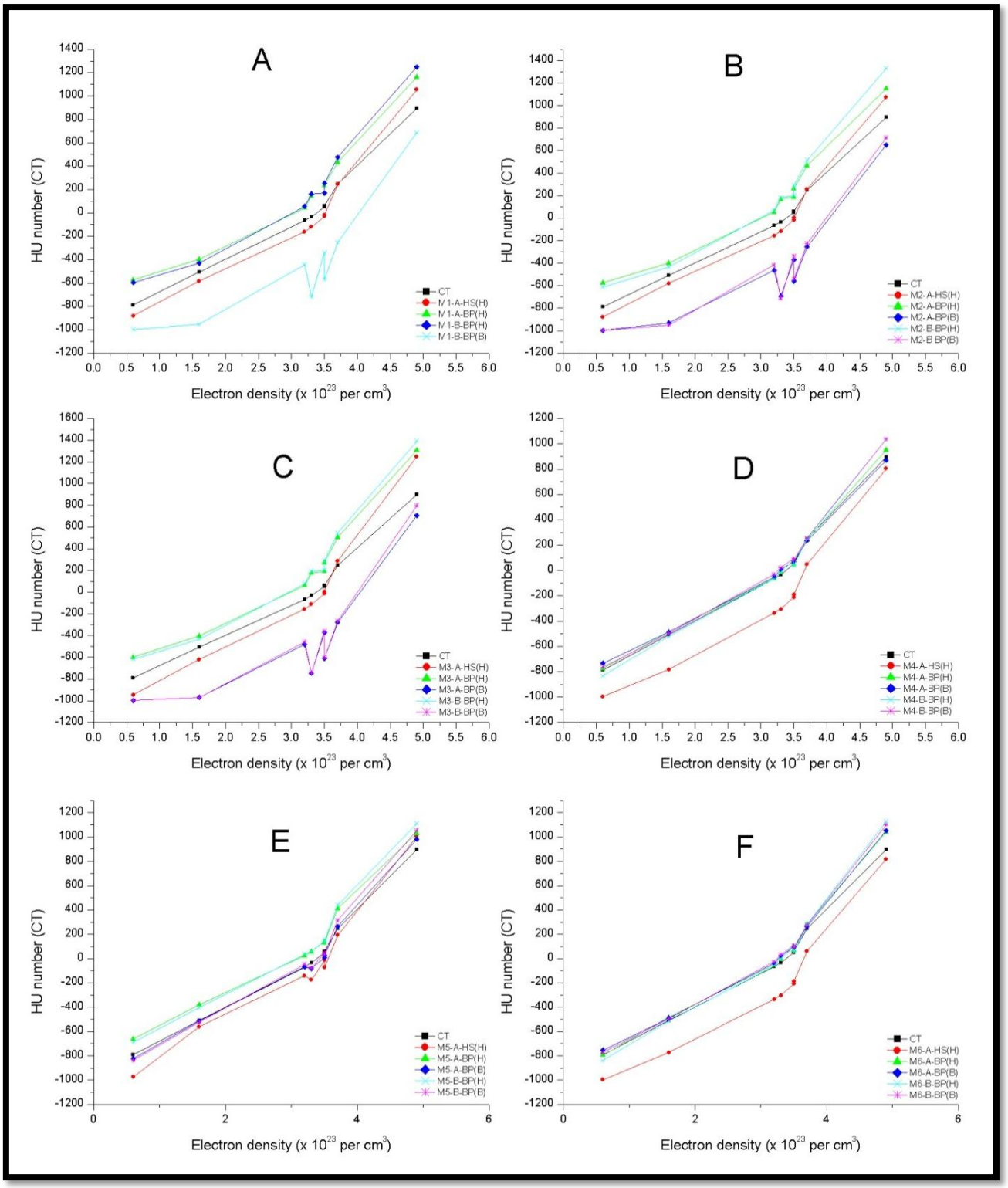

Figure 73: CT versus CBCT modes. (A) Standard dose head mode (B) Low dose head (C) High quality head (D) Pelvis (E) Pelvis spot light and (F) low dose thorax.

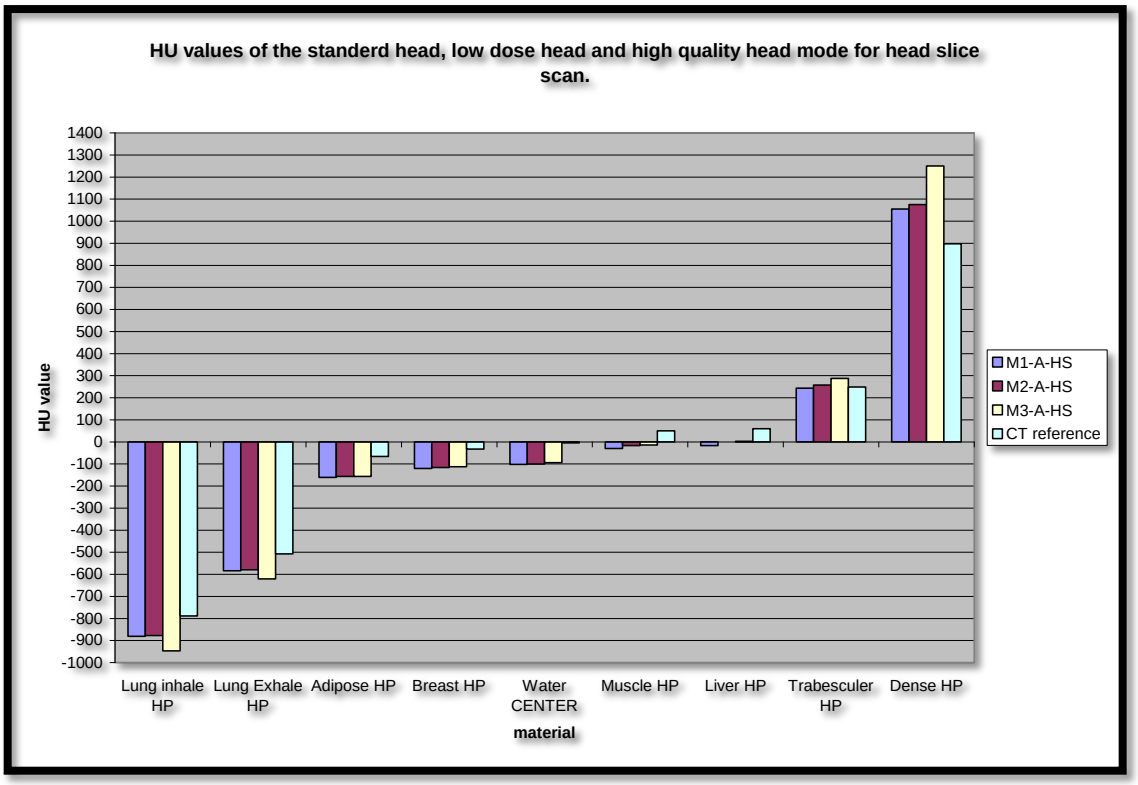

Figure 74: HU values of the head insertions using the standard head, low dose head and high quality head modes at the central position.

4.4 Suggestions and conclusions on suitable mode

In conclusion, M1 and M2 modes are suitable for small anatomical sites such as the head, and their respective calibration tables have the potential to be used for direct treatment planning. M3 mode is also acceptable for small anatomical sites but not for materials exceeding an electron density of > 4 per cc x 10^{23}. M4 is almost as good with all materials but not for small size phantoms. For the offset configuration, or when more than one organ is concerned, M5 is the most appropriate mode to be used with minor corrections to the calibration. Reviewing all the HU-to-Electron density calibrations for treatment planning it is proposes that M1, M4 and M6 have the potential to be used for the head and neck, pelvic and thorax sites respectively. These judgments of the usage of the HU-to-ED calibration curves are based on the comparison criteria on the CT calibration curve. Next, chapter 5, the judgment will be based on the calculation of dose distribution based on the two calibration curves.

5 Treatment planning based on CBCT at Royal Surrey County Hospital

Following selection of a suitable mode to assist with treatment planning, each scan mode image-type must be validated in order to be clinically useful. This chapter presents comparisons between the CT and CBCT HU-to-ED calibration curves used to validate the images for treatment planning. The methods employed to make these comparisons, and the results presented and discussed in this chapter.

5.1 Methodology

Data from the calibration curves previously obtained in Chapter 4 were put into the Varian Aria research terminal 'T-BOX' installed for research treatment planning at the RSCH. This allows the user to Varian Eclips treatment planning software independent of the actual clinical database and as one is able to upload more than one calibration curve. Comparisons can then be made between different data sets. CBCT scans of the CIRS and RANDO phantoms were imported into the T-BOX software and all of the insertions in the CIRS phantom were contoured, in addition to selected organs in the RANDO phantom. These contours were imported in preparation for the actual use of CBCT in treatment planning. Following this, single Anterior-Posterior (AP) and Intensity Modulated Radiation Therapy (IMRT) beams were applied, and dose comparisons were made between the CT and CBCT dose distribution.

5.1.1 CBCT Calibration curves

The standard CT calibration curve used for treatment planning is measured and then installed in the treatment planning (Eclipse) computer software for dose calculation. The Varian Eclipse, version 8.1 has the ability to store multiple calibration tables and allows the user to select the appropriate one prior to dose calculation (Rong, et al.,

2010). Instead, as mentioned above, the RSCH has a T-BOX computer, used mainly for research purposes. In this stand alone database calibration curves are inserted in the calibration list, for the user to select before applying the dose calculation. The calibration curves available in the T-BOX are shown in Table 19, Table 20, and Table 21, for the standard dose head mode, pelvis mode and low dose thorax mode, respectively.

The dose algorithm of Anisotropic Analytical Algorithm (AAA) was used to calculate the dose distribution on the CIRS-062A and RANDO phantoms. It is a new photon dose calculation model and has been implemented in Eclipse™ Integrated Treatment Planning. The AAA model provides a fast and accurate dose calculation for clinical photon beams even in regions of complex tissue heterogeneities such as CIRS-062A phantom. The AAA dose calculation model is a 3D pencil beam convolution-superposition algorithm that has separate modelling for primary photons, scattered extra-focal photons, and electrons scattered from the beam limiting devices. Functional forms for the fundamental physical expressions in AAA allow analytical convolution, thus reducing significantly the computation times usually required by these types of algorithms. Tissue heterogeneities are accounted for anisotropically in the full 3D neighborhood by the use of 13 lateral photon scatter kernels. The final dose distribution is obtained by superposition of the doses from the photon and electron convolutions (Sievinen, et. al, 2000).

Table 19: Calibration data for the standard dose head mode used in treatment planning at the RSCH.

	Physical density	Electron density	CT		CBCT - Head scan		
	g/cm^3	per cm^3 x 10^{23}	Average CT	SD	M1-A-HS	M1-A-BS(H)	M1-B-BP(H)
Lung inhale head	0.20	0.634	-788.9	15.0	-881.7±37	-573.9±155	-594.8±86
Lung exhale head	0.50	1.632	-508.0	4.5	-584.3±30	-396.2±178	-430.2±98
Adipose head	0.96	3.170	-66.4	3.3	-161.6±28	43.5±198	57.6±107
Breast head	0.99	3.261	-33.2	2.7	-120.8±24	144.5±160	163.4±92
Water	1.00	3.340	-4.7	1.3	-102.8±25	*	194.3±121
Muscle head	1.06	3.483	49.7	0.9	-30.4±31	**	168.5±95
Liver head	1.07	3.516	59.5	1.3	-16.9±33	237.8±193	254.6±104
Trabecular head	1.16	3.730	248.8	11.8	242.8±30	434.1±202	475.8±116
Dense bone head	1.53	4.862	897.3	25.9	1054.8±112	1162.9±218	1249.1±131
Extrapolation points [¥]	0.0				-1077.4	-692.4	-704.6
	2.20				2525.4	2525.4	2622.1

[¥] Please note that the extrapolated points in the above table have been added to cover scan images density values that are not measured directly.

* There is no water insertion in the body slices.

** The scan image was not clear to pick the muscle insertion.

Table 20: Calibration data for the pelvis mode, used for treatment planning at the RSCH

	Physical density	Electron density	CT		CBCT - Pelvis scan				
	g/cm^3	per cm^3 x 10^{23}	Average CT	SD	M4-A-HS(H)	M4-A-BP(H)	M4-A-BP(B)	M4-B-BP(H)	M4-B-BP(B)
Lung inhale head	0.2	0.634	-788.9	15.0	-996.8±9	-775.9±49	-733.4±57	-832.8±31	-764.4±41
Lung exhale head	0.5	1.632	-508.0	4.5	-782.9±17	-484.2±30	-486.6±40	-522.0±37	-498.0±38
Adipose head	0.96	3.17	-66.4	3.3	-336.5±21	-62.0±20	-51.6±27	-66.2±23	-31.1±26
Breast head	0.99	3.261	-33.2	2.7	-306.6±16	-14.5±24	7.0±23	-15.4±25	23.0±24
Water	1	3.34	-4.7	1.3	-323.5±10	9.8±25	*	2.0±26	*
Muscle head	1.06	3.483	49.7	0.9	-212.1±13	84.1±26	73.4±36	84.4±26	93.5±33
Liver head	1.07	3.516	59.5	1.3	-193.2±32	48.2±29	71.8±27	35.9±25	82.8±23
Trabecular head	1.16	3.73	248.8	11.8	47.7±42	243.8±33	236.2±26	250.0±24	257.3±26
Dense bone head	1.53	4.862	897.3	25.9	803.2±69	952.2±125	871.2±215	1037.0±76	1035.6±60
Extrapolation points ¥	0				-1206.7	-963.6	-922.5	-1035.6	-967.4
	2.2				2171.3	2176.5	3299.0	2382.6	2327.6

¥ Please note that the extrapolated points in the above table have been added to cover scan images density values that are not measured directly.

* There is no water insertion in the body slices.

Table 21: Calibration data for the low dose thorax mode used for treatment planning at the RSCH

	Physical density	Electron density	CT		CBCT - Thorax scan				
	g/cm^3	per cm^3 x 10^{23}	Average CT	SD	M6-A-HS(H)	M6-A-BP(H)	M6-A-BP(B)	M6-B-BP(H)	M6-B-BP(B)
Lung inhale head	0.2	0.634	-788.9	15.0	-996.4±12	-793.1±36	-753.4±39	-837.1±32	-772.2±39
Lung exhale head	0.5	1.632	-508.0	4.5	-773.3±19	-483.7±33	-490.3±41	-515.8±33	-495.2±43
Adipose head	0.96	3.17	-66.4	3.3	-336.2±25	-51.8±29	-39.0±29	-60.9±29	-25.6±32
Breast head	0.99	3.261	-33.2	2.7	-303.9±23	-1.8±29	20.3±28	-0.3±31	31.1±30
Water	1	3.34	-4.7	1.3	-319.9±11	*	*	*	*
Muscle head	1.06	3.483	49.7	0.9	-208.9±14	102.1±31	93.5±35	100.5±32	106.8±39
Liver head	1.07	3.516	59.5	1.3	-190.4±38	71.3±29	92.6±30	50.7±31	92.1±30
Trabecular head	1.16	3.73	248.8	11.8	61.2±37	283.1±31	265.1±29	282.4±30	277.7±30
Dense bone head	1.53	4.862	897.3	25.9	817.2±79	1040.8±94	1052.8±35	1128.9±59	1100.7±58
Extrapolation points ¥	0				-1202.5	-984.96	-949.61	-1041.3	-976.4
	2.2				2186.38	2413.86	2367.06	4456.5	4117.9

¥ Please note that the extrapolated points in the above table have been added to cover scan images density values that are not measured directly.

* There is no water insertion in the body slices.

The HU values for the liver are expected to be higher than those for the muscle, since liver is considered denser than muscle (1.07 and 1.06 g/cm^3 respectively). However, some of the HU values for muscle are greater than those for the liver; in these cases, the HU of the muscle has been ignored and not used in the calibration curve.

5.1.2 Contouring

All of the insertions are contoured to represent a total volume of 29cm^3. Figure 75 provides an example of the head slice contouring and Figure 76, provides an example of body phantom contouring.

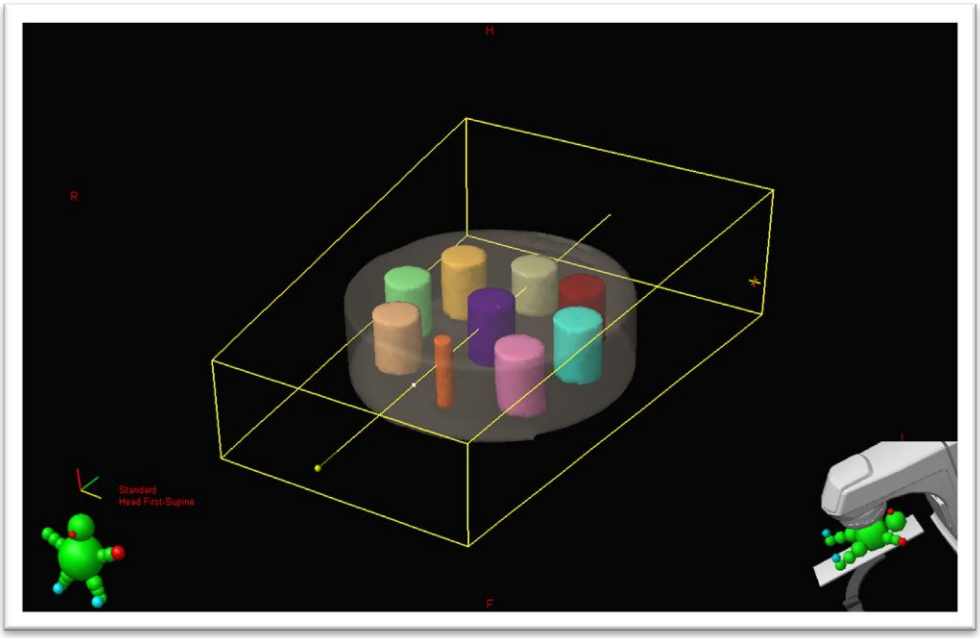

Figure 75: Head slice contouring at the RSCH.

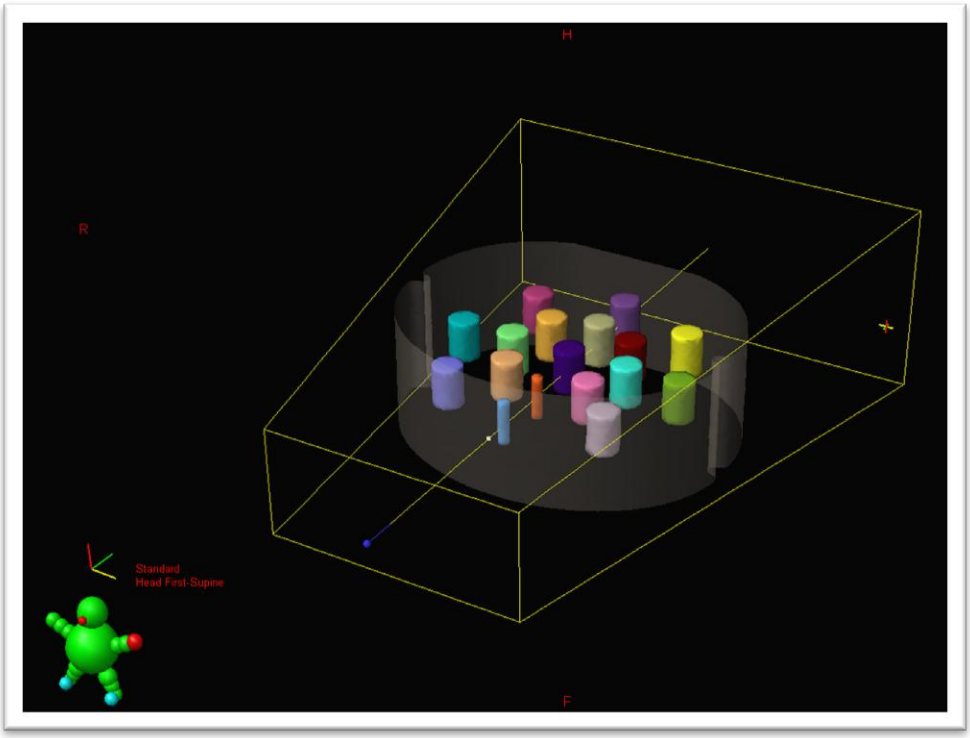

Figure 76: Body phantom contouring at the RSCH.

5.1.3 Single beam profile comparison

Two single 6MV photon beams of field size 20cm x 10cm and 35cm x 15cm (X x Y) incident in the AP direction for the head slice sites and body phantom were used respectively. The prescribed dose was 2Gy at the centre of the phantom. A summary of the steps followed in the single beam treatment plans is shown in Figure 77.

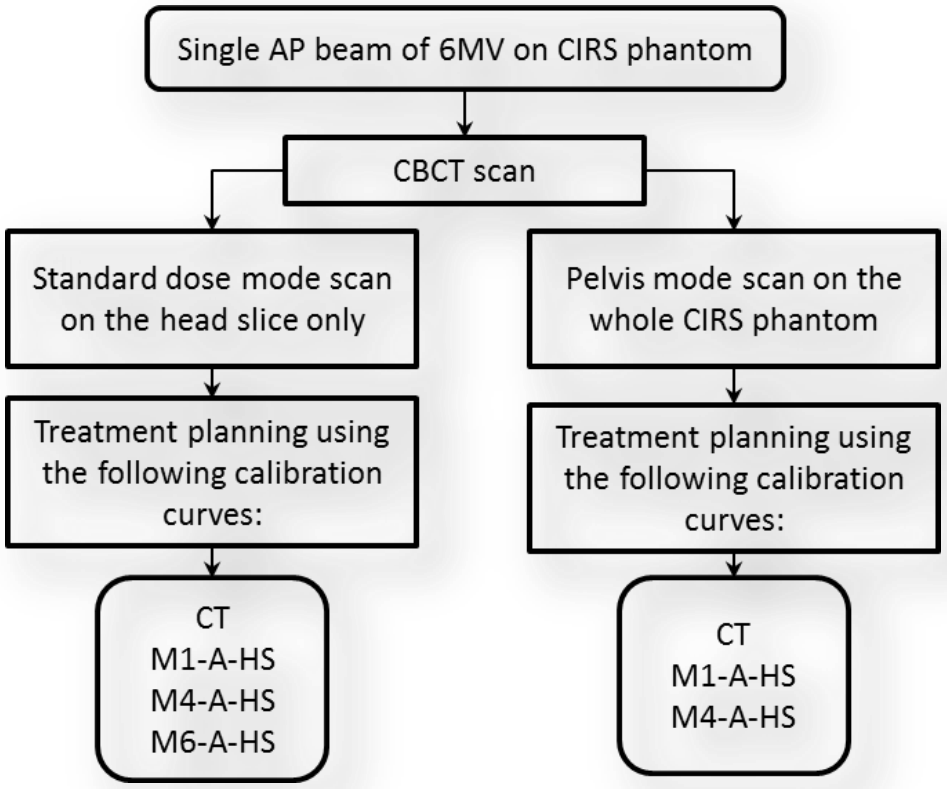

Figure 77: Summary of the steps followed in the single beam treatment plans.

5.1.4 The Intensity Modulated Radiation Therapy plan comparison

In the IMRT plan, the RANDO phantom was used. Firstly, the CBCT scan was imported into the software and then selected critical organs were contoured for calculation of the Dose Volume Histogram (DVH). The anatomical sites of the head and neck, and pelvis were included in the treatment plan. Within the head and neck region, the spinal cord, brainstem, left parotid, and right parotid were selected as critical organs. The treatment plan was programmed to deliver 65Gy in 30 fractions to PTV1 (planning treatment volume), and 54Gy in 30 fractions to PTV2. PTV1 is the primary PTV, and PTV2 was a lower dose to the neck lymph nodes of 54 Gy in 30 fractions.

Table 22: IMRT treatment plan field details for the head and neck on a RANDO phantom.

Field (name)	RPO	LPO	RAO	ANT	LAO
Energy (MV)	6	6	6	6	6
Dose rate (MU/min)	400	400	400	400	400
SSD (cm)	89	84.8	93.3	92.5	94
Gantry angle (deg)	225	135	305	0	55
Collimator rotation (deg)	342	18	340	0	20

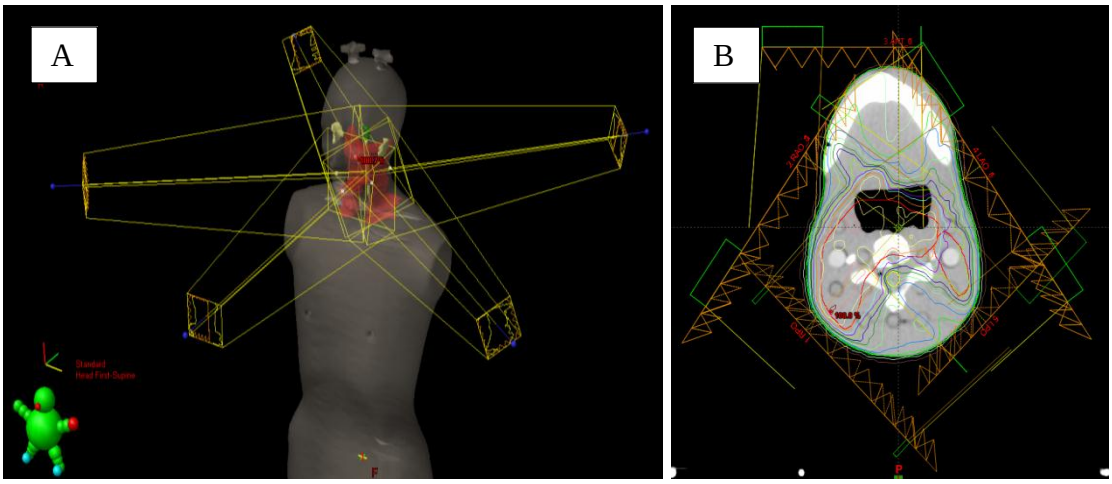

Figure 78: (A) Illustration of the five fields of the IMRT head and neck treatment plan on a RANDO phantom. (B) Calculated dose distribution from head and neck IMRT treatment plan using CBCT calibration curve (M1-A-HS).

In the pelvis region, the prostate, the bladder, Left and Right Femoral Head (LFH), (RFH) respectively and rectum were selected as critical organs. The treatment plan was programmed to deliver 74 Gy in 30 fractions to the prostate. PTV1 is defined as (prostate + seminal vesicles + 1cm) and PTV2 as (prostate + seminal vesicles + 5mm). There were five fields in the treatment, as detailed in Table 22 and Figure 78. There were five fields in the treatment, as detailed in Table 23 and Figure 79. A summary of the steps followed to generate the IMRT comparisons is shown in Figure 80.

Table 23: IMRT TP field details for the prostate plan on a RANDO phantom.

Field (name)	POST	RPO	RAO	LAO	LPO
Energy (MV)	6	6	6	6	6
Dose rate (MU/min)	400	400	400	400	400
SSD (cm)	90.7	84.1	87.6	88.4	83.9
Gantry angle (deg)	180.1	255	320	40	105
Collimator rotation (deg)	0	0	0	0	0

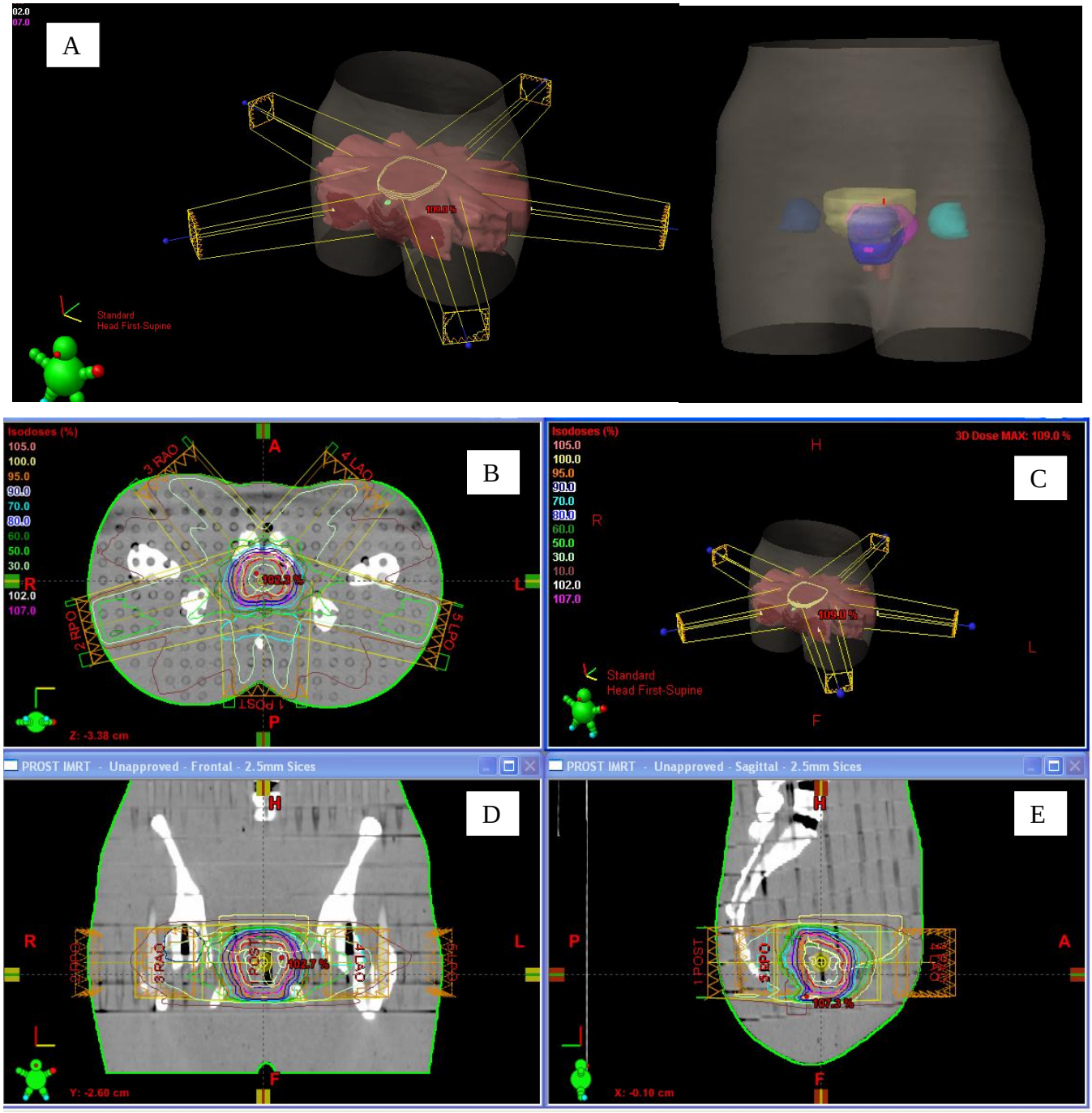

Figure 79: (A) Illustration of five fields of the IMRT prostate treatment plan on a RANDO phantom. (B, D, and E) Calculated dose distribution for the IMRT prostate treatment plan using CBCT calibration curve (M4-A-HS).

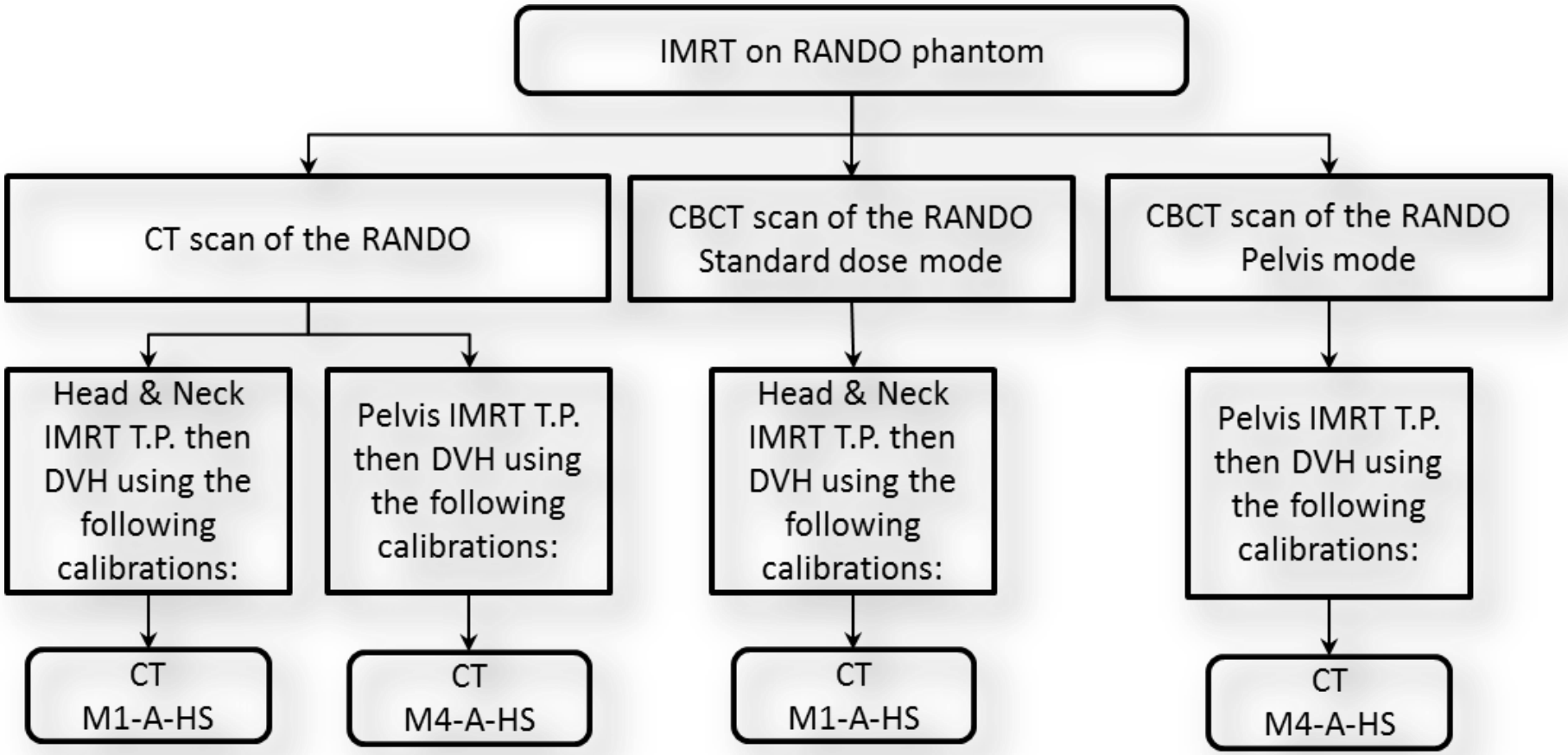

Figure 80: Summary of the steps followed in the IMRT treatment plans.

5.2 Dose calculation results

5.2.1 Single beam results

This section concerns the treatment plan for the head and pelvis sites of the body. The CIRS phantom was used in the calculation of single beam doses. The standard dose head scan of the CIRS phantom was used to test the head dosimetry using the CT and other CBCT calibrations as shown in Figure 77. The reason for selecting more than one CBCT calibration curve was to identify the curve most similar to the CT results. Similarly, the pelvis mode scan of the CIRS phantom was selected to represent the pelvis site.

All of the results presented between Figure 81 to Figure 85 are in the form of DVH. The CT calibration curve has been used as a baseline against which each comparison has been made. Figure 81 shows the DVH of a single 6 MV AP beam of 2Gy for 10 fractions at the centre of the phantom on the head slice of CIRS-062A phantom. The calculation of the dose was obtained using the CT calibration curve as the baseline. DVH values were obtained using different calibration curves. The M1-A-HS(H) calibration curve was expected to be the most similar to the CT calibration curve, given that the HU-to-ED ratios are comparable (as mentioned in chapter 3.34.3), Figure 82. Figure 82, Figure 83 and Figure 84 shows the DVH of a single 6 MV AP beam of 2Gy for 10 fractions at the centre of the phantom on the head slice of a CIRS-062A phantom using three calibration curves: M1-A-HS(H), M4-A-HS(H) and M6-A-HS(H) respectively.

It is clearly shown in Figure 82 and Figure 83that the M1-A-HS calibration is the best match to the CT calibration curve. Figure 85 shows the DVH values of the head and body insertions from a single AP beam. For the complete phantom scan, the pelvis scan mode of the CIRS phantom was used.

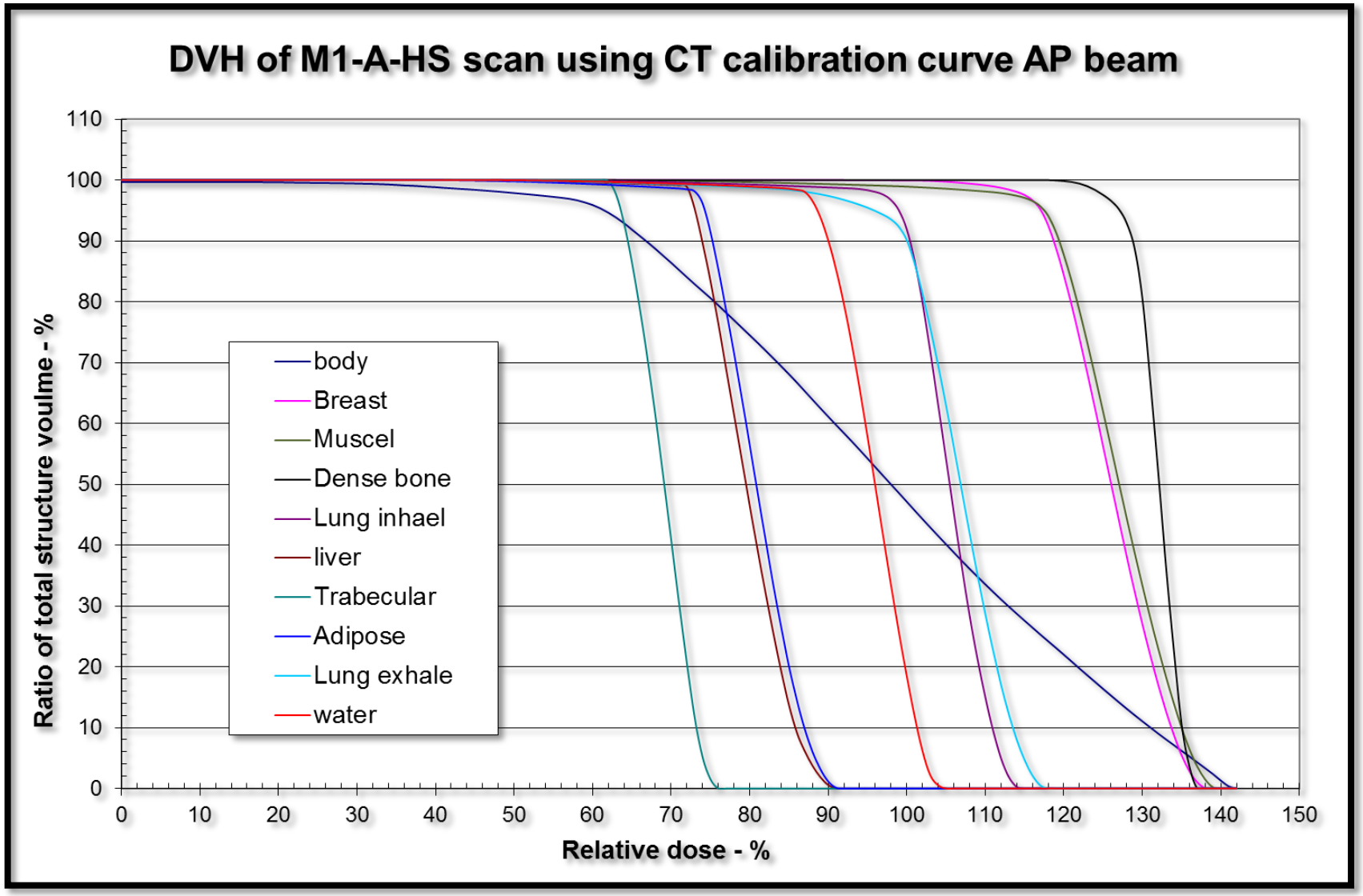

Figure 81: DVH of the CBCT image (M1-A-HS) using the CT calibration curve.

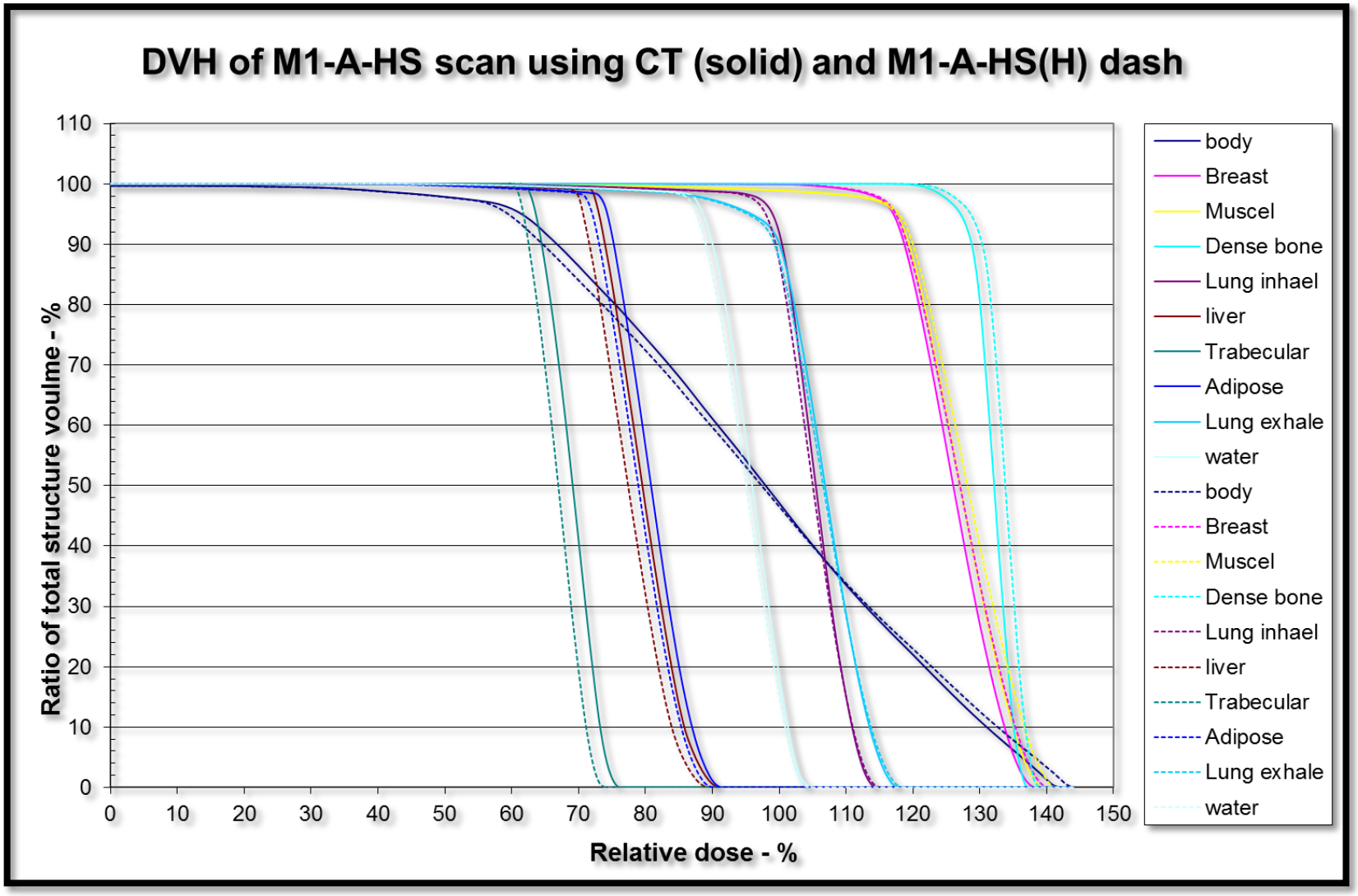

Figure 82: DVH values for a single beam directed on a CIRS phantom. Scan (M1-A-HS) using the CT(solid line) and M1-A-HS(dash line) calibration curves.

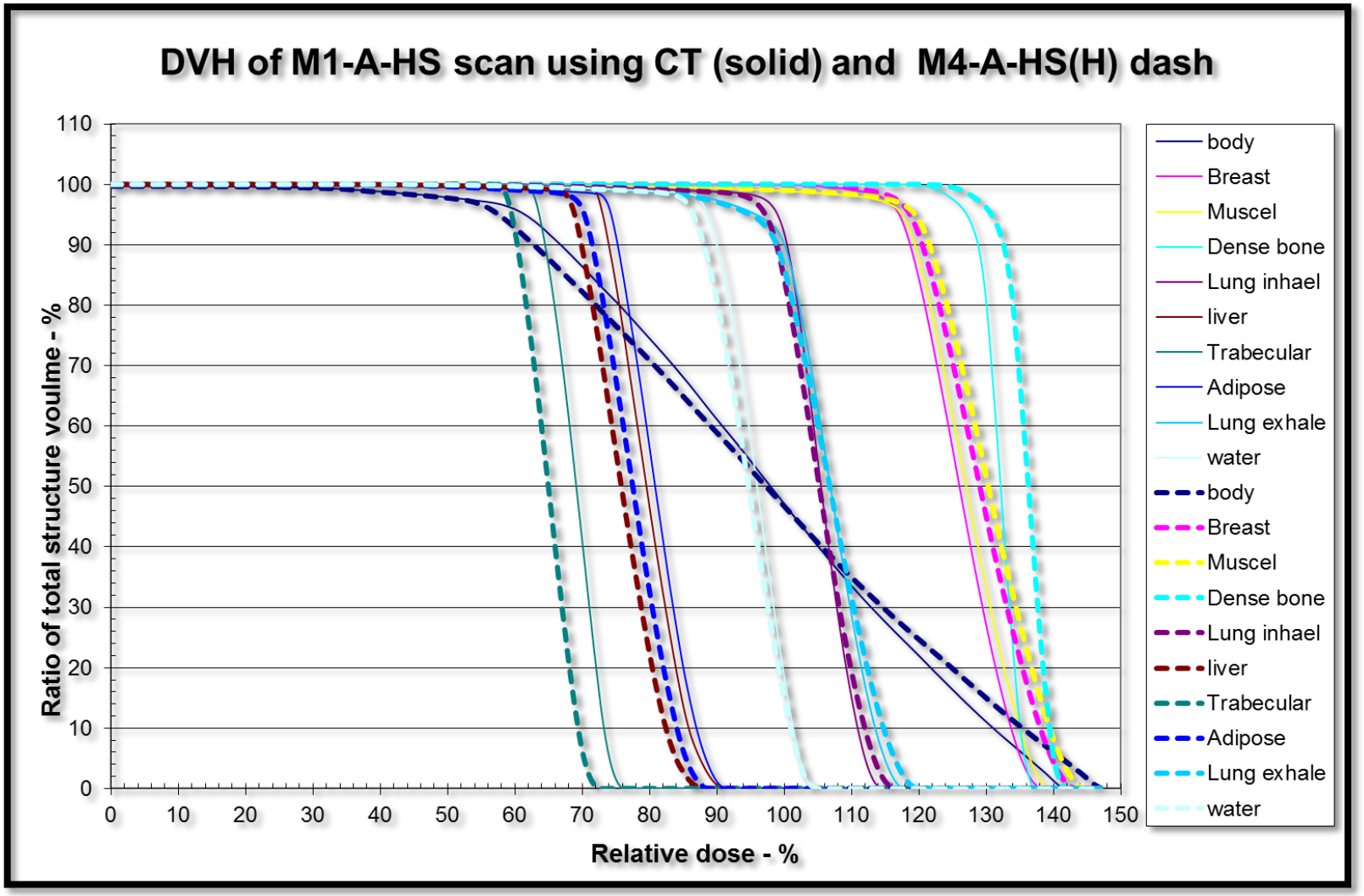

Figure 83: DVH values for a single beam directed on a CIRS phantom. Scan (M1-A-HS) using the CT(solid line) and M4-A-HS(dash line) calibration curves.

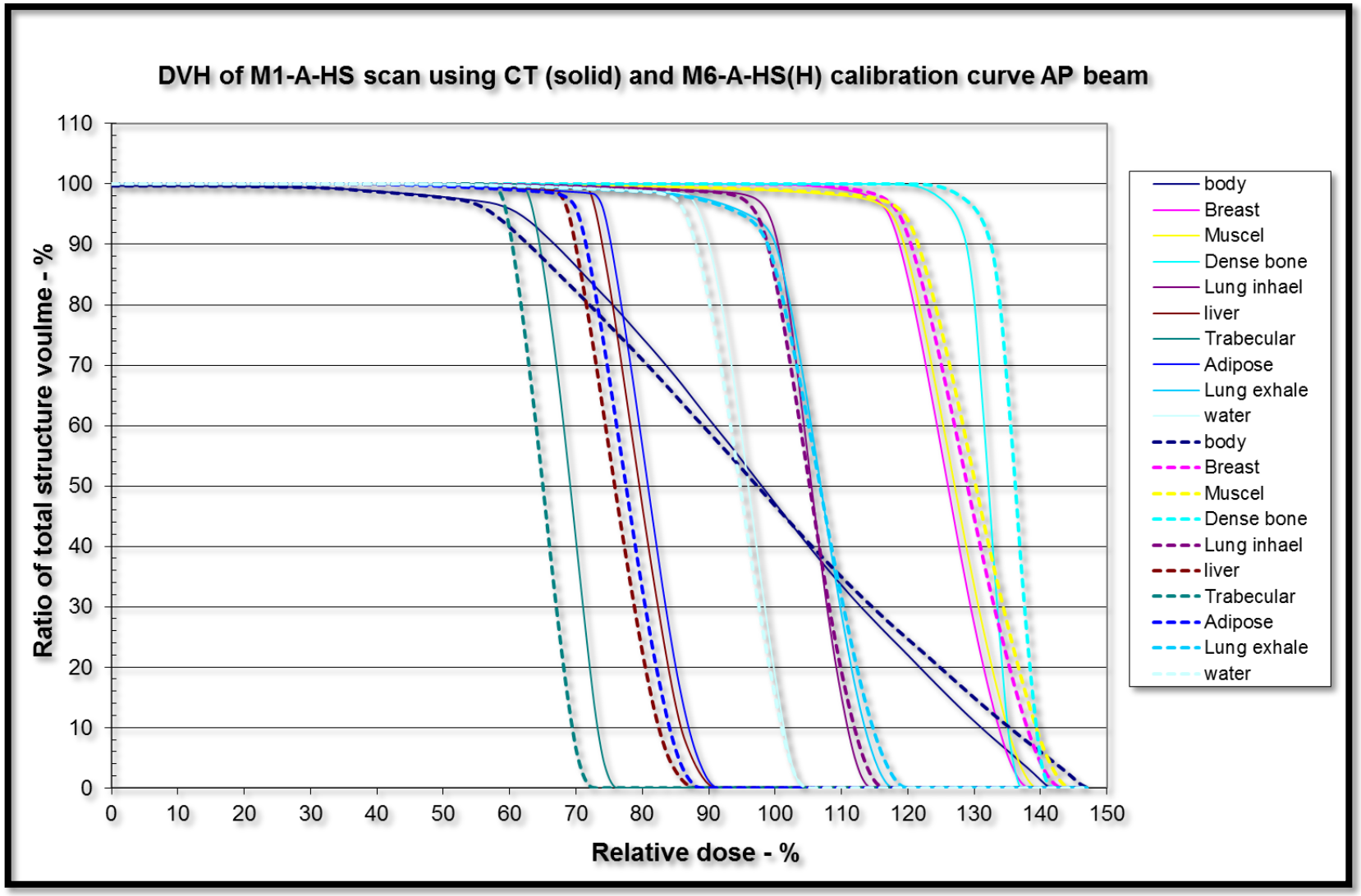

Figure 84: DVH values for a single beam directed on a CIRS phantom. Scan (M1-A-HS) using the CT(solid line) and M6-A-HS(dash line) calibration curves.

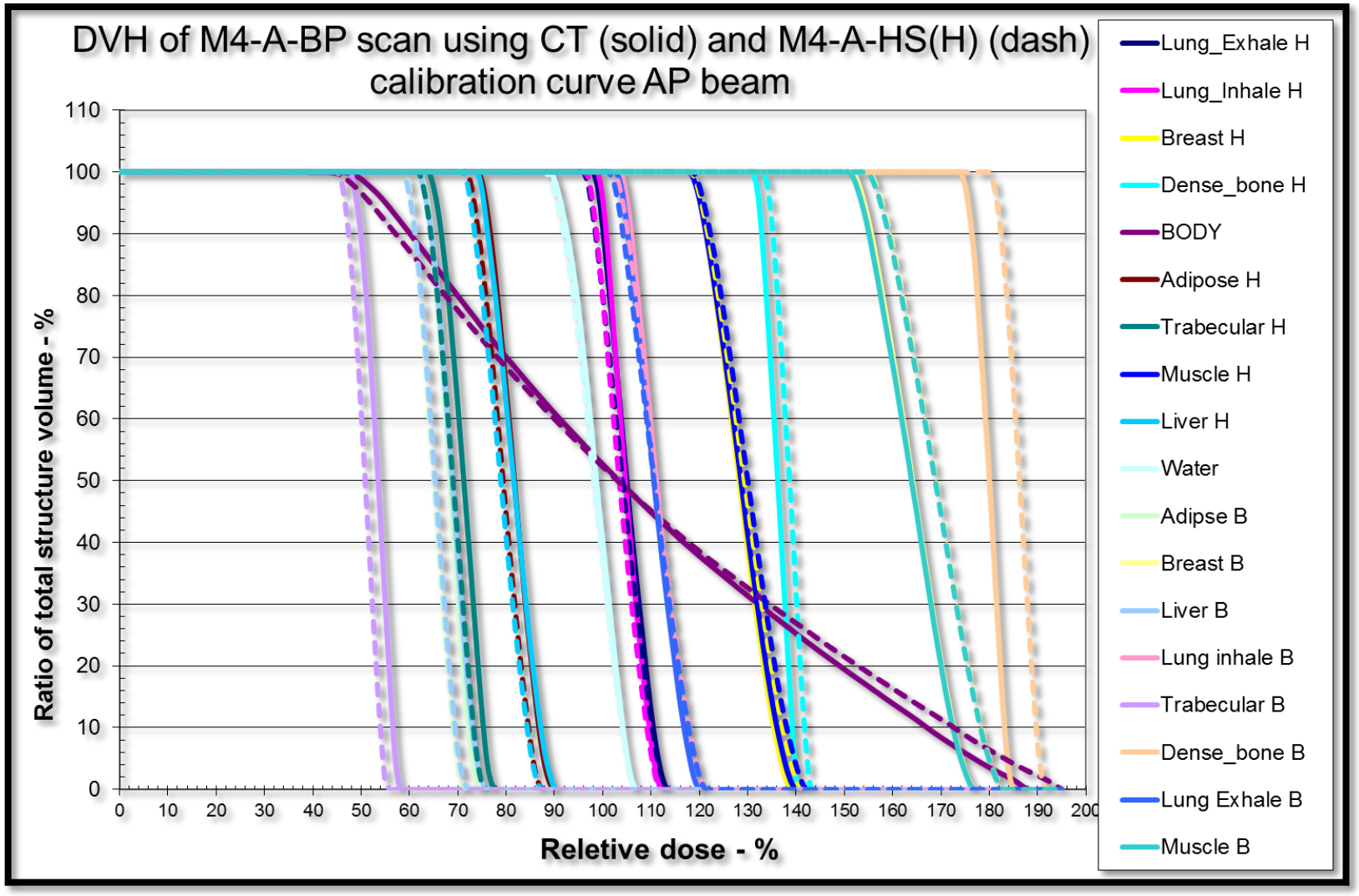

Figure 85: DVH values for the head(H) and body (B) insertions of the CIRS phantom using CT (solid) and M4-A-HS (dash) calibration curves.

5.2.2 IMRT plan results

The results shown in Figure 86 illustrate the DVH values obtained following application of the IMRT plan on CT and CBCT head scans of the RANDO phantom using CT and M1-A-HS calibration curves. Figure 87 shows the DVH values for an IMRT plan applied to CT and CBCT scan images using the CT and M4-A-HS calibration.

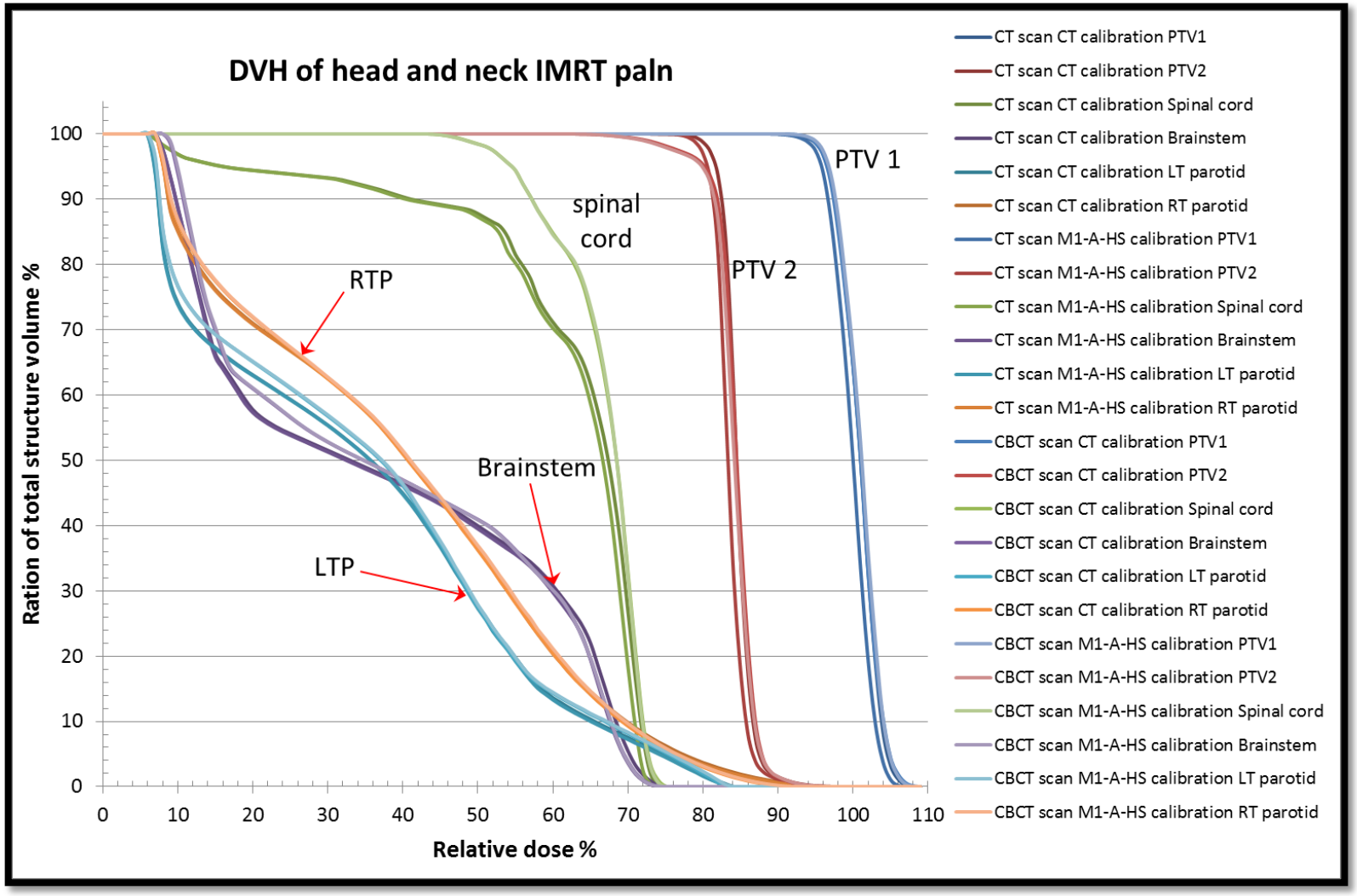

Figure 86: DVH values of the IMRT head and neck plan on CT and CBCT head scan mode using CT and M1-A-HS calibration curves.

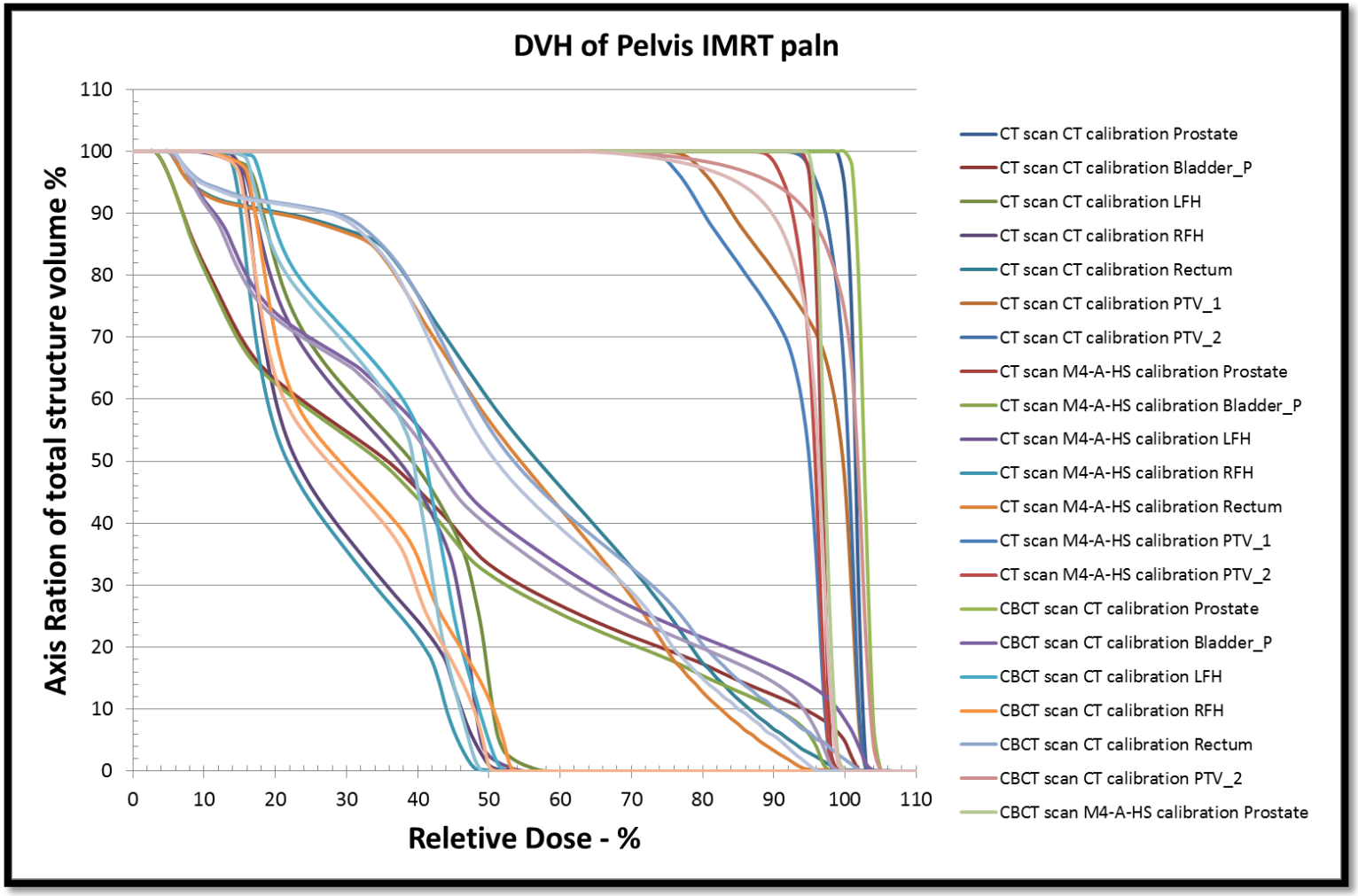

Figure 87: DVH values of the IMRT prostate plan on CT and CBCT head scan mode using CT and M4-A-HS calibration curves.

5.3 CBCT based treatment planning: Discussion and Conclusions

It has been shown that CBCT technology can be used in dose calculations for treatment planning. The calibration curves, obtained and described in Chapter 4, have been benchmarked against the CT calibration curve. In the comparisons, both CT and CBCT images were used for treatment planning, although clinically, only CT images are currently in use for treatment planning. Single beam and IMRT plans are involved and discussed in the following sections.

In the single beam comparison, the highest dose was recorded on the dense bone insertion because it is positioned in the top of the head slice and has the highest density of all the insertions. The lowest dose on the other hand, was recorded in the trabecular bone because the insertion is located at the bottom of the head slice and facing the far end of the AP beam. The breast, muscle, lung (inhale and exhale), liver and adipose insertions all received the same dose because they are positioned at the same angle (Figure 88).

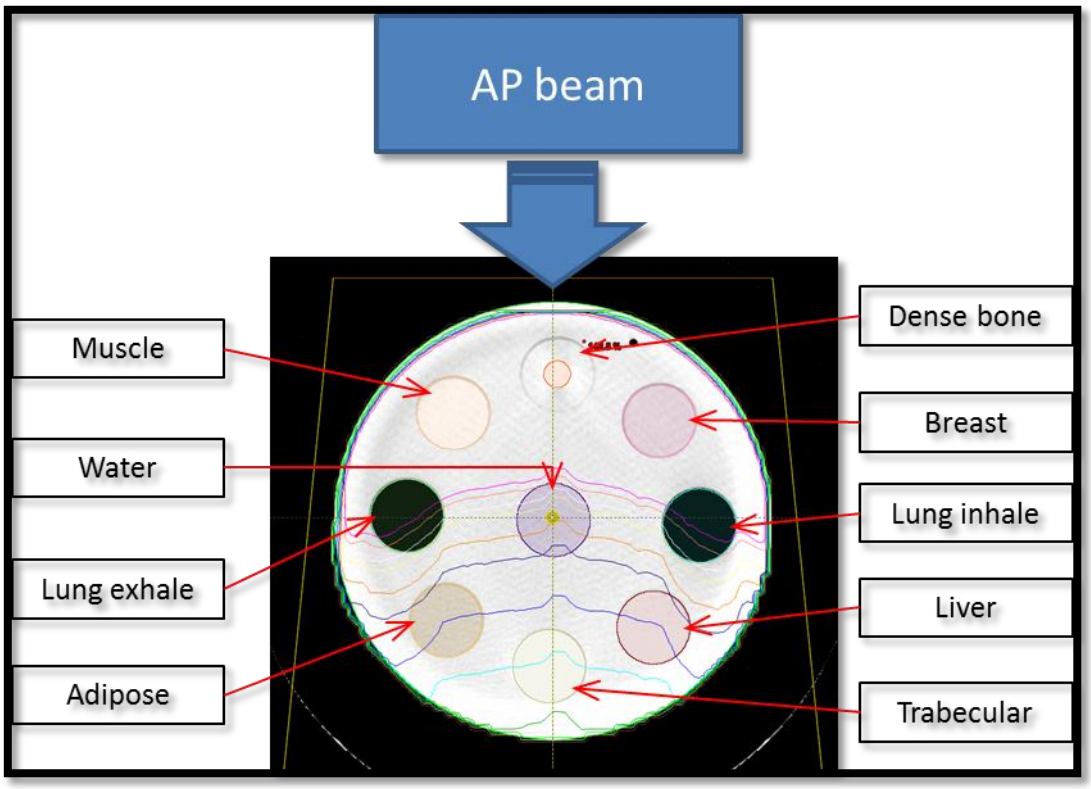

Figure 88: Insertion positions with respect to the incoming AP beam.

Since there is no prescription dose or data regarding particular organs at risk to compare the doses to, comparison of the percentage dose that each volume received when applying the various calibrations are considered below. For instance, in Figure 82 (page 134) 60% of the breast received 124.39% of the dose using the CT calibration curve, while the same volume received 123.10% using the CBCT M1-A-HS calibration curve. The differences in doses received by 60% volumes of all insertions using different calibration curves are shown in Table 24.

Table 24: The difference in relative dose at 60% volume of all insertions using different calibration curves.

60%	Calibration curve		Difference	Calibration curve	Difference	Calibration curve	Difference
Insertion	CT	M1-A-HS	%	M4-A-HS(H)	%	M6-A-HS(H)	%
Breast	124.4	123.1	1.0	124.4	0.0	124.3	0.0
Muscle	125.3	124.2	0.9	125.6	0.2	125.5	0.2
Dense bone	131.5	130.8	0.5	132.5	0.8	132.5	0.8
Lung inhale	104.4	102.2	2.1	101.8	2.4	101.8	2.4
Liver	78.2	74.9	4.2	73.5	6.1	73.5	6.0
Trabecular	68.1	65.2	4.3	63.4	7.0	63.4	6.9
Adipose	79.5	76.5	3.9	75.1	5.6	75.1	5.5
Lung exhale	104.8	103.3	1.4	103.0	1.7	103.0	1.7
Water	94.7	92.4	2.5	91.8	3.1	91.8	3.1

Table 24 supports the choice of the M1-A-HS calibration for head treatment planning over M4-A-HS(H) and M6-A-HS(H) calibrations. The differences between the CT and M1-A-HS calibration curves at most insertions are less than 2.5%, except for the insertions at the bottom of the phantom, which are the last to receive the incoming AP beam. These are the adipose, trabecular and liver insertions, yielding dose differences of 3.9%, 4.4%, and 4.2% respectively for the two calibrations.

Another way of comparing the calibration is to examine the differences in the mean dose of each insertion deposited from the single beam arrangement. These values can be seen in Table 25 and Figure 89.

Table 25: Mean dose to a CIRS phantom insertion using a single 6MV beam and two different calibrations.

Standard dose mode scan							
Insertion	Calibration						
	CT	M1-A-HS	Differences %	M4-A-HS	Differences %	M6-A-HS	Differences %
Dense bone	130.1	131.2	1.1	133.0	2.9	132.9	2.8
Muscle	124.9	125.6	0.7	127.1	2.2	127.0	2.1
Breast	124.3	124.8	0.5	126.2	1.9	126.2	1.9
Lung exhale	104.7	104.2	0.5	104.1	0.6	104.1	0.6
Lung inhale	103.8	103.1	0.7	103.0	0.8	103.0	0.8
Water	94.3	93.4	0.9	92.8	1.5	92.8	1.5
Adipose	79.7	77.8	1.9	76.4	3.3	76.4	3.3
Liver	78.6	76.4	2.2	74.9	3.7	74.9	3.7
Trabecular	68.0	66.1	1.9	64.3	3.7	64.4	3.6

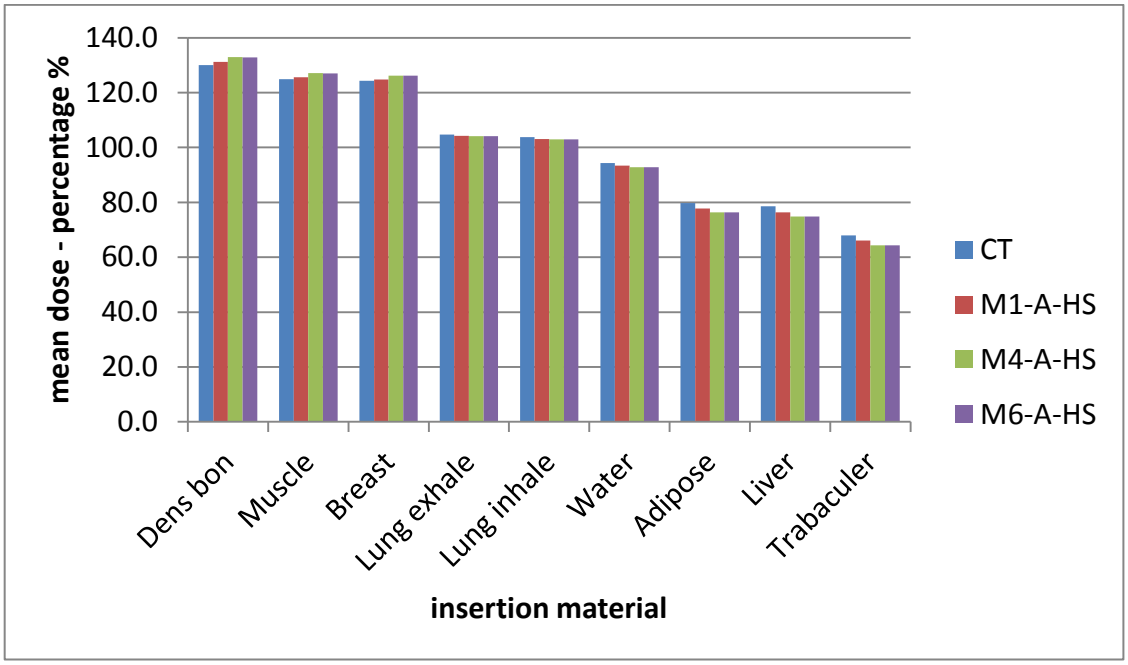

Figure 89: Distribution of the mean dose to a CIRS phantom using a 6MV single beam and different calibrations.

Figure 89 shows that for the single beam, only 1% difference in the mean dose values are received at the majority of insertions when using the CT and M1-A-HS calibration curves during CBCT for treatment planning.

When using treatment planning with a single beam on the large CIRS phantom, the head and body insertions received the same dose when CT, and M1-A-HS calibrations were applied for the head and body insertions. The dose received by the dense bone in the body insertion however was dependent on the calibration used Table 26. In all cases, the standard dose mode showed the best agreement with the CT calibration curve in the single beam plan.

Table 26: The mean doses of the dense bone insertion during the pelvis mode scan and single beam treatment.

	Mean dose %	
Calibration	Head insertion	Body insertion
CT	136.1	179.8
M1-A-HS	136.0	179.9
M4-A-HS	137.4	183.3

The IMRT treatment plan results showed very good agreement to the CT scan when the correct calibration curve was used for the dosemetric calculation. It was previously mentioned that the standard dose head, pelvis and low dose thorax scan modes are in agreement with the head and neck, pelvis and chest area modes, respectively, based on their calibration curves.

Results presented herein showed examples of the use of both correct and incorrect calibration curves during treatment planning. For the head and neck treatment plan, the standard dose head calibration curve in the IMRT plan was most similar to the CT calibration curve, Figure 86. Figure 90 (below) shows the differences in mean dose in all contoured organs.

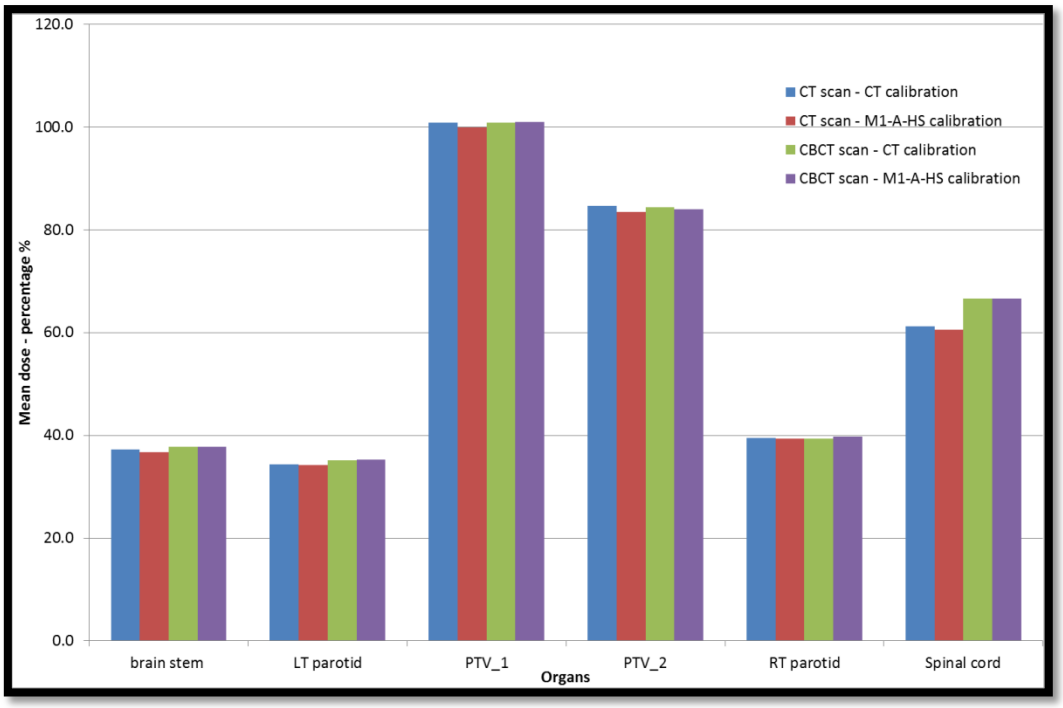

Figure 90: The mean dose differences in the head and neck IMRT plan using different calibration curves.

Figure 90 shows that when the CT scan image is used in the IMRT treatment plan, mean doses were less than 1.1% different between the CT and M1-A-HS calibration curves. However, when the CBCT scan is used, the difference was reduced to less than 0.3%, Table 27. There is however a 6% difference between the CT and CBCT scan image of the spinal cord, due to the difference between the CT and CBCT dense bone insertions, which was identified during the calibration. The HU numbers of the dense bone are 897.3±25 and 1054.8±112 when using the CT and M1-A-HS calibration curves respectively.

Table 27: The mean dose differences in the head and neck IMRT plan using different calibration curves.

	Head and Neck IMRT					
Image	CT scan			CBCT scan		
Calibration curve	CT	M1-A-HS	Differences %	CT	M1-A-HS	Differences %
brain stem	37.2	36.7	0.5	37.8	37.8	0.0
LT parotid	34.4	34.2	0.2	35.1	35.3	0.2
PTV_1	100.8	99.9	0.9	100.8	101.0	0.2
PTV_2	84.6	83.5	1.1	84.3	84.0	0.3
RT parotid	39.5	39.3	0.2	39.4	39.7	0.3
Spinal cord	61.2	60.5	0.7	66.6	66.6	0

Figure 87 provides an example of using an incorrect calibration curve (M4-A-HS) for the pelvis area. The correct calibration curve is the M4-A-BP calibration curve, as shown in (Table 20, page 123). If the incorrect calibration curve is used, the differences between the CT and CBCT calibration curves my reach as much as 4.7 and 5.5% in CT and CBCT scan images respectively (Table 28).

Table 28: The mean dose differences in the pelvis IMRT plan using different calibration curves

	Pelvis IMRT					
Image	CT scan			CBCT scan		
Calibration curve	CT	M4-A-HS	Differences %	CT	M4-A-HS	Differences %
LFH	36.0	34.2	1.8	36.8	34.9	1.9
Bladder	41.2	39.6	1.6	48.6	46.5	2.1
Prostate	101.4	96.7	4.7	102.7	97.2	5.5
RFH	28.0	26.5	1.5	31.6	29.9	1.7
Rectum	56.3	53.9	2.4	56.7	53.9	2.8

The research terminal, T-BOX computer, used in this research did not have the capacity to add the M4-A-BP calibration curve for the dose measurement of the pelvis IMRT plan. The error message displayed by the software when attempting to load the calibration can be seen in Figure 91. The error message stated that the image pixels for which the HU value is outside the scanner CT conversion curve. This suggested that, the calibration curves should accompany all the values of the HU number since

some of the pelvis mode scan as well as thorax mode scan presented some values on the scan image below the calibration curve (i.e. negative densities).

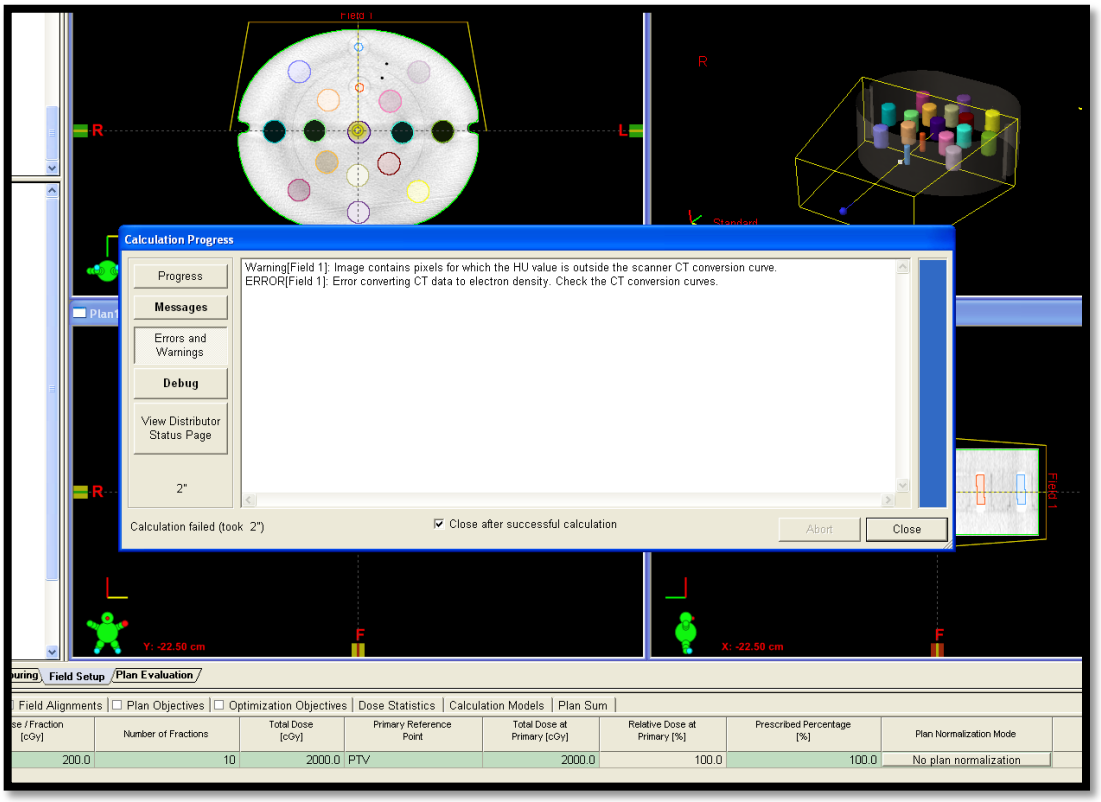

Figure 91: Error displayed when using the pelvis mode calibration curve in the T-BOX computer.

In conclusion, the single beam and the IMRT comparisons showed that the CBCT calibration curves can be used in treatment planning. The M1-A-HS calibration should be used for the head and neck site, M4-A-BP for the pelvis site, and M6-A-BP for the thorax site. Recently (2011) Sriram and colleagues used the CBCT images from OBI v1.4 for calculation of the treatment plan of single beam and IMRT plans (Sriram, et al., 2011). First they calibrated the HU-to-ED using the Catphan® 600 phantom. They found that the dose distributions calculated for a single direct 10 × 10 cm^2 6-MV photon beam for CBCT images of Catphan® 600 phantom agrees with that of CT to within 1%. In this research this comparison was used but with a more sophisticated calibration phantom CIRS-062A (Guan & Dong, 2009) and the differences was less than 1% when using M1-A-HS. In the IMRT, the head and neck site, the percentage dose difference was found to be slightly larger, although still

within ± 1% however for the thorax site, the percentage dose difference was found to be within ± 3%. In this study the head and neck IMRT the difference was found to be less than 1.1% when using the M1-A-HS calibration curve.

6 Conclusions and future work.

6.1 Conclusions

As discussed in chapter 2, CBCT doses from the OBI version 1.4 are significantly lower than those applied from the previous OBI version (1.3). Using a female RANDO phantom, doses were lower by factors of 8, 16, 22 and 36 at the eyes, thyroid, oesophagus and brain, respectively. The CBCT-to-patient dose was also measured and considered in this research. One significant finding was that the CBCT dose from the new OBI version 1.4 decreases as patient size increases. This relationship was confirmed using three methods; a hospital measurement, a mathematical approach and by simulation using MC BEAM/DOSXYZnrc code.

The concomitant radiation dose measured on the smallest of the cylindrical water phantoms resulted in a theoretical risk of secondary skin cancer of 0.005% in the standard dose mode and 0.05% in the pelvis mode. These risks were calculated assuming a 30-fraction course of treatment with CBCT images acquired on a daily basis. Importantly, these doses are approximately 6 times greater than those measured for the largest phantom. The data presented in this study demonstrate that the concomitant dose for different sized patients varies significantly. It is therefore recommended that patient-specific imaging protocols be considered, especially with regard to paediatric patients who can be expected to receive a higher dose and therefore be at greater risk of secondary cancer.

Based on these findings, it has been concluded that version 1.4 of the CBCT scanning system could be used on a daily bases to assist in adaptive radiotherapy, without a significantly increased cancer risk. However, precautionary measures are recommended to minimise the risks to paediatric patients in particular.

In chapter 3, BEAMnrc and DOSXYZnrc codes were found to be superior to the MCNP-4c code for CBCT simulation. The MCNP-4c code is designed mainly for static dosing, whereas the BEAMnrc code has been advanced to account for radiation source movement, whether in radiotherapy treatment or imaging energy. Given that some movement is inevitable during radiotherapy dosing, the dynamic code yields a much closer simulation of the real-life scenario. It has been advice in the literature that newer version of the MCNP such as MCNP5 could simulate a moving source during the simulation. This can be achieved by using a moving source tally with constant degree of rotation and probability of source intensity. This step is beyond the investigation of this research; and suggestion of BEAMnrc and DOSXYZnrc was introduced.

In chapter 4, the relationship between the Hounsfield unit and electron density was found and added to the treatment planning systems at the RSCH for dose calculation based on the CBCT scan images. Standard dose head and low dose head modes were found to be suitable for small anatomical sites such as the head, and their respective calibration tables were shown to be suitable for direct treatment planning. High quality head mode was also demonstrated to be acceptable for small anatomical sites, but not for materials exceeding an electron density of > 4 per x $10^{23}cm^3$. Pelvis mode functions consistently well with all materials but not for small size phantoms. For the offset configuration, or when more than one organ is concerned, pelvis spot light is the most appropriate mode to be used with minor corrections to the calibration.

Finally, in chapter 5, treatment planning and calculations based on CBCT calibration curves were carried out at the RSCH. For the single beam treatment plan, only 1% differences in the mean dose values were received at the majority of insertions when using the CT and M1-A-HS calibration curves during CBCT for treatment planning. In addition, it was found that when CT scan images are used in the IMRT treatment planning, mean doses are approximately 1.1% different between the CT and M1-A-HS calibration curves. However, when the CBCT scan is used, the difference was reduced to less than 0.3%. Finally, the single beam and IMRT comparisons showed that the CBCT calibration curves can be used in treatment planning. According to

these analyses, the M1-A-HS calibration should be used for the head and neck site, M4-A-BP for the pelvis site, and M6-A-BP for the thorax site.

6.2 Suggested treatment plan based on the CBCT data set

The strategy presented here for adapting the radiotherapy treatment plan is based on the Varian on-Board imager CBCT version 1.4. Any older versions may require an alternative approach due to the higher radiation doses involved.

Essentially, the suggested plan is a summary of the work conducted to meet the objectives of this research. The plan is shown schematically in Figure 92 and involves a quality assurance (QA) check, dose measurement, calibration, and treatment dose verification. Each step is explained in detail in the following sections.

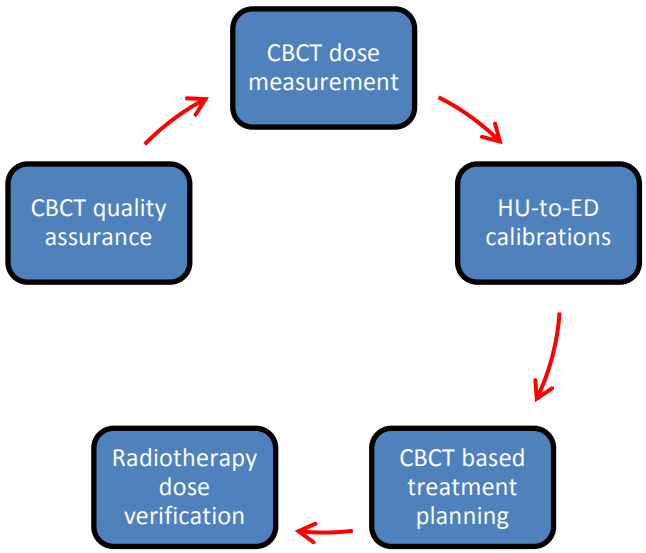

Figure 92: Suggested plan for treatment planning based on CBCT.

6.2.1 Quality assurance:

A QA step must be implemented to check the accuracy and outcome of the CBCT scan images. QA tests should be applied for all modes, although three modes are proposed for re-planning the treatment, to ensure that the CBCT is working accurately in all modes and assure its safe use during re-planning. Yoo and colleagues established some very useful tests that are based on daily and monthly QA. One of these tests involved checking the safety of CBCT devices, such as the correct functioning of tube warm-up, door interlock, warning lights, warning sounds, arm motion and overall function. The second test was to assess the isocentre and couch

movement when matching the two positions of the treatment planning with the current alignment of the patient. Further tests were to ensure image quality and involved HU reproducibility, low contrast resolutions, spatial resolution, and HU uniformity. All these tests are explained thoroughly in the publication by Yoo and colleagues (Yoo, et al., 2006) and are recommended herein as an essential component of the CBCT treatment planning protocol.

6.2.2 Dose measurement

The dose delivered from each mode should be known in order to control and limit the total dose received by the patient following a complete delivery of radiotherapy treatment, which includes IGRT. To achieve accurate dose measurement, the use of three phantoms is suggested. These phantoms are adult male, adult female, and pediatric (5 years) phantoms with the CIRS phantom model numbers 701, 702 and 705, respectively. The doses to the head and neck, chest and pelvis should be measured for all three phantoms, including the organs shown in Table 29.

Table 29: Suggested organs in the body for dose measurement.

CBCT modes		
Standard dose head	Thorax	Pelvis
Oesophagus	Lungs	Gonads (ovary)
Thyroid	Breast	Colon
Lens	Heart	Bladder
Brain	Stomach	Rectum
		LFH - RFH

Based on these measurements, it is possible to accurately determine the total accumulated dose received by any given patient undergoing a particular treatment plan.

6.2.3 Calibration

To calculate the radiation dose based on CBCT data, the system used to calculate the treatment dose fraction must have the ability to convert the CBCT image to electron density numbers. This can be achieved using HU-to-ED calibration curves, which are critical components for precise dose calculation. HU-to-ED must be obtained using a CIRS-062A phantom and rather than any other phantom such as the Catphan-500 used for QA. Three calibration curves must be added to the treatment planning system; these are M1-A-HS, M4-A-BP(B) and M6-A-BP(B) for the head and neck, pelvis and thorax respectively. Some of the values obtained from both the pelvis (M4) and thorax (M6) modes give negative HU numbers, which must be normalised to fit within the range of the calibration. To achieve this, a physical density of zero is set for HU numbers ≤1000HU. Calibration of the CBCT HU-to-ED relationship for the thorax site should be carried out using a moving phantom followed by a comparison to the M6-A-BP calibration curve.

6.2.4 Dose verification

An IMRT plan for head and neck, pelvis or thorax for both adult and paediatric phantoms should include a step to generate a calibration curve. The calibrations and the treatment plan obtained should be compared to the CT as a verification step.

6.3 Future work

Many issues should be considered when applying adaptive radiotherapy using CBCT. One of these is the amount of time required to generate a new plan based on each new scan image. Since one IMRT plan takes 2-3 hours to generate, the application of adaptive radiotherapy requires more resources and staff within the department to allocate their time and expertise to it. Therefore, these aspects should be taken into account when applying the adaptive radiotherapy using CBCT technology.

The Monte Carlo codes, BEAMnrc and DOSXYZnrc, are powerful tools for the accurate calculation of dose, and as such would be very useful for treatment planning. Since these two codes can work in parallel, the simulation of the linac head together with CBCT would make it possible to generate a full treatment plan, aid in treatment delivery and calculate the dose using the CBCT data set. Dose modification can also be studied as a consequence of the possibility to adapt the treatment plan based on the CBCT data set.

As future work I would carefully consider the following steps:

1. Comprehensive measurements of the CBCT scan dose using the full six modes and determination of the dose value in the whole body should be involved.
2. Full MC simulation and calibration of the CBCT x-ray source and detector. The simulation should include the treatment couch. The recommended MC code is BEAM/DOSXYZnrc version V42.3.2 released on 18th MAY 2011 or earlier.
3. Converting the RANDO phantom to “RANDO.egsphant” file format for dose calculation should be managed.
4. CBCT dose relationship with phantom size should be investigated using the six modes.
5. Solving the problems with the range of the pelvis mode HU-to-ED calibration and employing the calibration to RANDO phantom IMRT treatment plans.

References

Amer, A. et al., 2007. Imaging doses from the Elekta synergy X-ray cone beam CT system. Brit. J. Radiol., Volume 80, pp. 476-482.

Cember, H., 1996. Introduction to Health Physics. United States of America: McGraw-Hill.

Chi, Y., Wu, Q. & Yan, D., 2007. Dose Calculation On Cone Beam CT (CBCT). Medical Physics, Volume 34, p. 2438.

Dasu, A., Dasu, I.-T., Olofsson, J. & Karlsson, M., 2005. The use of risk estimation models for the induction of secondary cancers following radiotherapy. Acta Oncologica, Volume 44, pp. 339-347.

Ding, G. & Coffey, C., 2009. Radiation dose from kilovoltage cone beam computed tomography in an image-guided radiotherapy procedure. Int. J. Rad. Oncol. Biol. Phys, Volume 73, pp. 610-617.

Ding, G., Duggan , D. & Coffe, C., 2007. Characteristics of kilovoltage x-ray beams used for cone-beam computed tomography in radiation therapy. Physics in Medicine and Biology, Volume 52, p. 1595–1615.

Ding, G., Duggan, D. & Coffey, C., 2008. Accurate patient dosimetry of kilovoltage cone-beam CT in radiation therapy. Med. Phys, Volume 35, pp. 1135-44.

Ding, G. et al., 2007. A study on adaptive IMRT treatment planning using kV cone-beam CT. Radiotherapy and Oncology, Volume 85, pp. 116-125.

Ding, G. & Munro, P., 2011. Reduced CBCT Imaging Dose Due to the New X-Ray Source in. Medical Physics, June.38(6).

Dominguez, E., 1904. The Alderson Radiation Therapy Phantom, Long Beach, Canada: Radiology Support Devices INC..

Downes, P. et al., 2009. Monte Carlo simulation and patient dosimetry for a kilovoltage cone-beam CT unit. Am. Assoc. Phys. Med., 36(9), pp. 4156-4167.

Feng, W., Guan, H. & Bakalyar, D., 2011. Monte Carlo Simulation of Varian OBI Cone Beam CT (CBCT) and Dose Distribution in Head Phantom in 125kVp and 100kVp. Medical Physics, 38(6).

Greco, C. & Clifton, C., 2008. Broadening the scope of Image-Guided Radiotherapy (IGRT). Acta Oncologica, pp. 1193-1200.

Guan, H. & Dong, H., 2009. Dose calculation accuracy using cone-beam CT (CBCT) for pelvic adaptive radiotherapy. Phys. Med. Biol., Volume 54, pp. 6239-6250.

Hall, E., 2006. Intensity-modulated radiation therapy, protons, and the risk of Second cancers. International Journal of Radiaiton Oncology biology physics, Volume 65, p. 1–7.

Hatton, J., McCurdy, B. & Greer, P., 2009. Cone beam computerized tomography: the effect of calibration of the Hounsfield unit number to electron density on dose calculation accuracy for adaptive radiation therapy. Physics in Medicine And Biology, Volume 54, pp. 329-346.

Ho, K. F. H. et al., 2011. Monitoring Dosimetric Impact of Weight Loss With Kilovoltage (KV) Cone Beam CT (CBCT) During Parotid-Sparing IMRT and Concurrent Chemotherapy. International Journal of Radiaiton Oncology biology physics, p. e376.

Hussein, M., Aldridge, S., Guerrero-Urbano, T. & Nisbet, A., 2011. The effect of 6 and 15 MV on IMRT prostate cancer treatment: plan evaluation, TCP & NTCP analysis and the theoretical risk of secondary induced malignancies. Brit. J. Radiol, p. In press.

Hyer, D. et al., 2010. An organ and effective dose study of XVI and OBI cone-beam CT systems. Journal of Applied Clinical Medical Physics, Volume 11, pp. 181-197.

ICRP, 2007. ICRP 103: The 2007 Recommendations of the International Commission on Radiological Protection, Oxford: ICRP.

Islam, M. et al., 2006. Patient dose from kilovoltage cone beam computed tomography imaging in radiation therapy. Med. Phys., Volume 33, pp. 1573-82.

Kan, M., Leung, L. H., Wong, W. & Lam, N., 2008. Radiation dose from cone beam computed tomography for image-guided radiation therapy. Int. J. Radiation Oncology Biol. Phys.,, 70(1), p. 272–279.

Khan, F., 2003. The physics of radiation therapy. Philadelphia: Lippincott williams & wilkins.

Kim, S. et al., 2008. Comparison of radiation doses between cone beam ct and multi detector ct: tld measurements. Radiation Protection Dosimetry, 132(3), p. 339–345.

Kim, S. et al., 2010. Kilovoltage cone-beam CT: Comparative dose and image quality evaluations in partial and full-angle scan protocols. Am. Assoc. Phys. Med., 37(7), pp. 3648-3659.

Klevenhagen, S. et al., 1996. The IPEMB code of practice for the determination of absorbed dose for x-rays below 300 kV generating potential (0.035 mm Al–4 mm Cu HVL; 10 - 300 kV generating potential). Phys Med Biol., Volume 41, pp. 2605-25.

Laboratory, N. P., 2011. Tables of Physical and Chemical Constants (Kaye & Laby). [Online] Available at: http://www.kayelaby.npl.co.uk/atomic_and_nuclear_physics.html [Accessed 10 August 2011].

L'etourneau, D. et al., 2005. Cone-beam-CT guided radiation therapy: technical implementation. Radiother. Oncol., Volume 75, p. 279–286.

Marchant, T. et al., 2008. Shading correction algorithm for improvement of cone-beam CT images in radiotherapy. Physics in medicine and Biology, Volume 53, pp. 5179-5733.

Mayles, P., Nahum, A. & Rosenwald, J.-C., 2007. Handbook of Radiotherapy Physics: Theory and Practice. London: Taylor & Francis Group,.

Mayles, W. et al., 2000. Physics Aspects of Quality Control in Radiotherapy (Report No. 81). Physics in Medicine and Biology, Volume 45, p. 815.

Murphy, M. et al., 2007. The management of imaging dose during image-guided radiotherapy: Report of the AAPM Task Group 75. American Association of Physicists in Medicine, Volume 34, pp. 4041-4063.

Nelson, R., Hirayama, H. & Rogers, D., 1985. The EGS4 code system Report SLAC-265. Stanford, CA: SLAC.

Neville, S., 1995. Cancer – A family affair. London: Sheldon Press.

Nijkamp, J. et al., 2008. Adaptive radiotherapy for prostate cancer using kilovoltage cone-beam computed tomography: first clinical results. Int. J. Radiation Oncology Biol. Phys., Issue 70, p. 75–82.

Nisbet, A. & Cocker, M., 2004. Experiences of a proactive IR(ME)R inspection in radiotherapy. The British Journal of Radiology, Volume 77, pp. 329-332.

Paliwal, B. et al., 2006. Cone Beam CT Based Treatment Planning. Medical Physics, Volume 33, p. 2029.

Paquina, D., Levyb, D. & Xing, L., 2008. Multiscale registration of planning CT and daily cone beam CT images for adaptive radiation therapy. American Association of Physicists in Medicine, Volume 36, pp. 4-11.

Peng, P. et al., 2006. Auto Contour Mapping in CBCT for Adaptive Therapy Treatment Planning. I. J. Radiation Oncology, Biology and Physics, Volume 66, p. S651.

Richter, A. et al., 2008. Investigation of the usability of conebeam CT data sets for dose calculation. BioMed Central, 3(42).

Rogers, D. et al., 1995. BEAM: A Monte Carlo to simulate radiotherapy treatment units. Med. Phys., 22(5), pp. 503-525.

Rogers, D. et al., 2001. BEAMnrc users manual Report PIRS-0509(a)F. Ottawa: NRCC.

Rong, Y. et al., 2010. Dose calculation on kv cone beam ct images: an investigation of the hu-density conversion stability and dose accuracy using the site-specific calibration. Medical Dosimetry, 35(3), pp. 195-207.

Saw, C. et al., 2005. Determination of CT-to-density conversion relationship for image based treatment planning system. Medical Dosimetry, 30(3), pp. 145-148.

Secoa, J. & Evans, P., 2006. Assessing the effect of electron density in photon dose calculations. Am. Assoc. Phys. Med, 33(2), pp. 540-552.

Siewerdsena, J. & Jaffray, D., 2000. Optimization of x-ray imaging geometry (with specific application to flat-panel cone-beam computed tomography). Am. Assoc. Phys. Med., 27(8), pp. 1903-1914.

Song, W. et al., 2008. A dose comparison study between XVI and OBI CBCT systems. Med. Phys., Volume 35, pp. 480-6.

Spezi, E., Downes, P., Radu, E. & Jarvis, R., 2009. Monte Carlo simulation of an x-ray volume imaging cone beam CT unit. Am. Assoc. Phys. Med., 36(1), pp. 127-136.

Sriram, P., Niekanandan, N. & Parbakar, S., 2011. A Study on Evaluation of kV-CBCT-Image-Based Treatment Planning using Anthropomorphic Phantom. Journal of Medical and Biological Engineering, 31(6).

Teke, T., Gill, B., Duzenli, C. & Popescu, I., 2011. A Monte Carlo model of the Varian IGRT couch top for RapidArc QA. Physics in medicine and biology, Volume 56, p. N295–N305.

UNSCEAR, 1993. Sources and Effects of Ionizing Radiation 1993 Report to the General Assembly, with annexes, New York: United Nations.

Varian, 2008. On-Board Imager (OBI) Reference Guide.

Walters, B., Kawrakow, I. & Rogers, D., 2002. History by history statistical estimators in the BEAM code system. Med. Phys, 29(12), pp. 2745-2752.

Wang, C., Yang, Y. & Xing, L., 2006. Evaluation of Cone Beam CT (CBCT)-Based Dose Calculation. Int. J. Radiation Oncology, 66(3).

Wen, N. et al., 2007. Dose delivered from Varian's CBCT to patients receiving IMRT for prostate cancer. Phys. Med. Biol, Volume 52, pp. 2267-2276.

Yang, Y. et al., 2007. Evaluation of on-board kV cone beam CT (CBCT)- based dose calculation. PHYSICS IN MEDICINE AND BIOLOGY, Volume 52, pp. 685-705.

Yarn Standard, 2011. Standard Body Measurements/Sizing. [Online] Available at: http://www.craftyarncouncil.com/sizing.html

Yoo, S. et al., 2006. A quality assurance program for the on-board imager. Medical Physics, Volume 33, pp. 4431-4447.

Yoo, S. & Yin, F., 2006. Dosimetric feasibility of cone-beam ct-based treatment planning compared to ct-based treatment planning. Int. J. Radiation Oncology Biol. Phys., Volume 66, pp. 1553-1561.

Zhu, L., Wang, J. & Xing, L., 2009. Noise suppression in scatter correction for cone-beam CT. Am. Assoc. Phys. Med., 36(3), pp. 741-752.

Zhu, L., Xie, Y., Wang, J. & Xing, L., 2009. Scatter correction for cone-beam CT in radiation therapy. Am. Assoc. Phys. Med., 36(6), pp. 2258-2268.

Zijtveld, M., Dirkx, M. & Heijmen, B., 2007. Correction of conebeam CT values using a planning CT for derivation of the ''dose of the day''. Radiotherapy and Oncology, Volume 85, pp. 195-200.

Appendix 1 Monte Carlo simulation codes

MCNP-4c

```
1mcnp     version 4c    ld=01/20/00                  11/14/11 19:45:30

******************************************************************************
****              probid =    11/14/11 19:45:30
 i=f1 o=f1out

   1-              << simulation CBCT using the Standard dose mode>>
   2-       c                  cell definition
   3-       c
   4-       c
   5-       c
   6-       1 10 -1.0        8 -1 -3 2              imp:p=1 $ water phantom
   7-       2 20 -1.06       -4                     imp:p=1 $ TLD RP
   8-       3 20 -1.06       -5                     imp:p=1 $ TLD P
   9-       4 20 -1.06       -6                     imp:p=1 $ TLD LP
  10-       5 20 -1.06       -7                     imp:p=1 $ TLD A
  11-       6 20 -1.06       -8                     imp:p=1 $ TLD C
  12-       9 30 -1.78       -15 10 -11 12 -14 13   imp:p=1 $ Treatment couch
  13-       7 40 -1.293e-3   -9 #1 #2 #3 #4 #5 #6 #9 imp:p=1 $ air in the medium
  14-       8 0              9                      imp:p=0
  15-
  16-       c                  surface definition
  17-       c
  18-       c
  19-       c
  20-       1 cy 15                $ radius of the cylinder
  21-       2 py -7.5
  22-       3 py 7.5
  23-       4 s -15.2 0 0 0.115
 warning.  this surface has been replaced by a surface of type sx
  24-       5 s 0 0 -15.2 0.115
 warning.  this surface has been replaced by a surface of type sz
  25-       6 s 15.2 0 0 0.115
 warning.  this surface has been replaced by a surface of type sx
  26-       7 s 0 0 15.2 0.115
 warning.  this surface has been replaced by a surface of type sz
  27-       8 so 0.115
  28-       15 pz -15.4
  29-       10 pz -15.9
  30-       11 px 15
  31-       12 px -15
  32-       13 py -8
  33-       14 py 8
```

```
34-     9 so 120
35-
36-     c                   source definition
37-     c
38-     c
39-     c
40-     mode p
41-     sdef pos=-92.7 0.0 37.5 erg=d1
42-     si1 0.0 0.020 0.025 0.030 0.035 0.040 0.045 0.050 0.055 0.060 0.065 0.070
43-        0.075 0.080 0.085 0.090 0.095 0.10 0.105 0.110
44-     sp1 0 0.091 0.455 0.818 0.955 1 0.955 0.909 0.818 0.727
45-        0.636 0.455 0.409 0.364 0.273 0.227 0.182 0.136
46-        0.091 0.045
47-     c
48-     c          the source is at 110 KeV
49-     c
50-     f4:p 2 3 4 5 6
51-     c
52-     c   dose factor and energy for the calculation of dose
53-     c
54-     c              D(F)=(rem/hr)/(photon/cm^2.s)
55-     c
56-     DE4  0.01 0.03 0.05 0.07 0.1 0.15 0.2 0.25 0.3 0.35 0.4 0.45 0.5 0.55
57-          0.6 0.65 0.7 0.8 1 1.4 1.8 2.2 2.6 2.8 3.25 3.75 4.25 4.75 5
58-          5.25 5.75 6.25 6.75 7.5 9 11 13 15
59-     DF4  3.96e-6 5.82e-7 2.9e-7 2.58e-7 2.83e-7 3.79e-7 5.01e-7
60-          6.31e-7 7.59e-7 8.78e-7 9.85e-7 1.08e-6 1.17e-6 1.27e-6
61-          1.36e-6 1.44e-6 1.52e-6 1.68e-6 1.98e-6 2.51e-6 2.99e-6
62-          3.42e-6 3.82e-6 4.01e-6 4.41e-6 4.83e-6 5.23e-6 5.6e-6
63-          5.8e-6 6.01e-6 6.37e-6 6.74e-6 7.11e-6 7.66e-6 8.77e-6
64-          1.03e-5 1.18e-5 1.33e-5
65-     c
66-     c
67-     c       m10 is water
68-     c
69-     m10 1001 1 8016 2
70-     c mt10 lwtr
71-     c
72-     c        m20 is tissue material
73-     c
74-     m20  1001 0.105 6000 0.414 7014 0.034 8016 0.436 15031 0.001
75-          16032 0.002 17000 0.002 19000 0.002 26000 0.001
76-     c
77-     c  m30 is the treatment couch its carbon Fibber and it is
78-     c  mainly 99.9% Carbon
79-     c
80-     m30 6012.35c 1
warning.  neutron table inconsistent with mode will be ignored.
81-     m40 7014 0.75 8016 0.25 gas=1
82-     c
```

```
c  m40 is air
c
c
nps 1000000000
```

BEAM

```
Varian OBI G242 X-ray tube                                    #!GUI1.0
Air
0, 0, 0, 0, 0, 2, 0,  IWATCH ETC.
1000000, 33, 97, 0.99, 2, 10000, 0, 0,  NCASE ETC.
25, 102.1, 0, 0, 0, ,  DIRECTIONAL BREM OPTIONS
-1, 10, 0.6, -0.978, 0, 0.21,  0.0, 0.0, 0.0, 0.0,  IQIN, ISOURCE + OPTIONS
0, MONOENERGETIC
0.125
0, 0, 0.512, 0.001, 0, 2, 1,  0 , ECUT,PCUT,IREJCT,ESAVE
0, , , , ,  PHOTON FORCING
1, 9,  SCORING INPUT
5, 1
0.5, 1, 1.5, 2, 2.5,
0,  DOSE COMPONENTS
0.0, Z TO FRONT FACE
********** start of CM XTUBE with identifier Source **********
5, RMAX
x-ray source
0, 1, ZMIN, ZTHICK
14, ANGLE
1, # LAYERS
0.54, 1
, , , ,
Copper
0.09, 0.12,
, , , ,
Target
, , , ,
VACUUM
, , , ,
VACUUM
********** start of CM CONESTAK with identifier exitw **********
5, RMAX
exit glass window
1, 4, ZMIN, RBN
2, NUMBER OF LAYERS
5, 3, 3,
0.1, 3, 3,
, , , , OUTER WALL
Lead
, , , ,
VACUUM
, , , ,
Lead
, , , ,
Glass2.23
, , , ,
```

```
Lead
********** start of CM SLABS with identifier filter **********
5, RMAX
pre-filter
1, NSLABS
6.22, ZMIN
0.2, , , , , 0
ALuminum
********** start of CM BLOCK with identifier colmtor **********
5, RMAX
pre- collimator
6.52, 8.52, 0.5, ZMIN, ZMAX, ZFOCUS
1, # OF SUBREGIONS
4, NUMBER OF POINTS IN SUBREGION 1
1.6, 1.6,
1.6, -1.6,
-1.6, -1.6,
-1.6, 1.6,
3, 3, -3, -3,
, , , ,
, , , ,
Air
, , , ,
Lead
********** start of CM JAWS with identifier blade **********
5, RMAX
blade
1, # PAIRED BARS OR JAWS
X
9.59, 9.89, 2.36, 2.43, -2.36, -2.43,
, , , ,
, , , ,
Lead
********** start of CM SLABS with identifier suport **********
5, RMAX
steel support
1, NSLABS
11.19, ZMIN
0.2, , , , , 0
Steel
********** start of CM SLABS with identifier glass **********
5, RMAX
Glass window
1, NSLABS
15.29, ZMIN
0.1, , , , , 0
Glass2.23
********** start of CM PYRAMIDS with identifier bowtie **********
5, RMAX
bow-tie filter
```

```
6, 0, #LAYERS, AIR OUTSIDE
15.5, 15.65, 0.00000001, 0.00000001, -0.00000001, -0.00000001, 0.00000001,
0.00000001, -0.00000001, -0.00000001, 5, 5,
15.65, 15.8, 0.00000001, 0.5, -5, -5, 5, 5, -5, -5, 5, 5,
15.8, 16.5, 0.5, 1, -5, -5, 5, 5, -5, -5, 5, 5,
16.5, 17.75, 1, 1.4, -5, -5, 5, 5, -5, -5, 5, 5,
17.75, 18.05, 1.4, 1.6, -5, -5, 5, 5, -5, -5, 5, 5,
18.05, 18.25, 1.6, 2, -5, -5, 5, 5, -5, -5, 5, 5,
0.512, 0.001, , ,  ECUT ETC. FOR AIR
, , , ,
ALuminum
, , , ,
ALuminum
, , , ,
ALuminum
, , , ,
ALuminum
, , , ,
ALuminum
, , , ,
ALuminum
********** start of CM CHAMBER with identifier phantom **********
50, RMAX
water phantom
102.1, ZMIN
0, 50, 1, N_TOP, N_CHM, N_BOT
5, 45, 47, RADII FOR CENTRAL PART
0.5, 50, ZTHICK, FLAG FOR ALL LAYERS IN CENTRAL PART
, , , ,
Water
, , , ,  chamber wall
Water
, , , ,  gap
Glass2.4
, , , ,  container
Air
2, 47, 0, ZTHICK, RCYS, FLAG FOR LAYER 1 IN BOTTOM PART
, , , ,
Glass2.4
, , , ,
Air
0, MRNGE
**********end of all CMs**********
 ##########################
 :Start MC Transport Parameter:

 Global ECUT= 0.512
 Global PCUT= 0.001
 Global SMAX= 5
 ESTEPE= 0.25
```

```
XIMAX= 0.5
Boundary crossing algorithm= EXACT
Skin depth for BCA= 0
Electron-step algorithm= PRESTA-II
Spin effects= On
Brems angular sampling= Simple
Brems cross sections= BH
Bound Compton scattering= On
Pair angular sampling= Simple
Photoelectron angular sampling= Off
Rayleigh scattering= On
Atomic relaxations= On
Electron impact ionization= On

:Stop MC Transport Parameter:
##########################

***WARNING***
NBRSPL > $MAXBRSPLIT
NBRSPL reduced to       2000 from      10000

***WARNING IN CM    8 (PYRAMIDS):
Less than min. airgap ( 0.01000 cm) between layer    1 and layer    2
ZMIN(   2) reset to 15.66000 cm from 15.65000 cm

***WARNING IN CM    8 (PYRAMIDS):
YMAX(   2) is less than y opening, set to  5.00000 cm
from  5.00000 cm

***WARNING IN CM    8 (PYRAMIDS):
Less than min. airgap ( 0.01000 cm) between layer    2 and layer    3
ZMIN(   3) reset to 15.81000 cm from 15.80000 cm

***WARNING IN CM    8 (PYRAMIDS):
YMAX(   3) is less than y opening, set to  5.00000 cm
from  5.00000 cm

***WARNING IN CM    8 (PYRAMIDS):
Less than min. airgap ( 0.01000 cm) between layer    3 and layer    4
ZMIN(   4) reset to 16.51000 cm from 16.50000 cm

***WARNING IN CM    8 (PYRAMIDS):
YMAX(   4) is less than y opening, set to  5.00000 cm
from  5.00000 cm

***WARNING IN CM    8 (PYRAMIDS):
Less than min. airgap ( 0.01000 cm) between layer    4 and layer    5
ZMIN(   5) reset to 17.76000 cm from 17.75000 cm
```

```
 ***WARNING IN CM    8 (PYRAMIDS):
 YMAX(   5) is less than y opening, set to  5.00000 cm
 from  5.00000 cm

 ***WARNING IN CM    8 (PYRAMIDS):
 Less than min. airgap ( 0.01000 cm) between layer    5 and layer    6
 ZMIN(   6) reset to 18.06000 cm from 18.05000 cm

 ***WARNING IN CM    8 (PYRAMIDS):
 YMAX(   6) is less than y opening, set to  5.00000 cm
 from  5.00000 cm

Varian OBI G242 X-ray tube

 NRCC CALN: BEAMnrc(EGSnrc) Vnrc(Rev 1.78 of 2004-01-12 11:44:06-
05),(USER_MACROS Rev 1.5)
 ON gnu-win32 (gnu_win32)                    16:28:36 Jul 31 2011

*************************************************************************
 **                                                 **
 **                      BEAMnrc                          **
 **                                                 **
 **     Code developed at National Research Council of Canada as part of    **
 **         OMEGA collaboration with the University of Wisconsin.          **
 **                                                 **
** This is version V1 of BEAMnrc (Rev 1.78 last edited 2004-01-12 11:44:06-05**
 **                                                 **

*************************************************************************

 Max # of histories: to run  2000000000         To analyze       2000000000
              Incident charge                    -1
              Incident kinetic energy             0.125 MeV

              Bremsstrahlung splitting             DIRECTIONAL
               splitting field radius             25.000 cm
               splitting field SSD                102.150 cm
               splitting no. in field               2000
              Photon force interaction switch        OFF
              SCORING PLANES:     #          CM #
              --------------------          ----
                           1          1
                           2          7
                           3          8
              Phase space files will be output at EVERY scoring plane
              Range rejection switch               ON
              Range rejection in  95 regions
                    Fixed ECUT used
 Range rejection based on medium of region particle is traversing
 Maximum electron ranges for restricted stopping powers:
```

kinetic energy (MeV) | Range for media 1 through 7 (cm)

Air	TargetW_	Lead	Glass2.2	ALuminum	Steel	Water
0.125	22.260	0.003	0.005	0.013	0.010	0.005	0.024

Discard all electrons below energy: 1.000 MeV
if too far from closest boundary
Maximum cputime allowed 500.00 (hrs)
Initial random number seeds 33 97
LATCH_OPTION = 2: Latch values inherited, origin of secondary particles recorded.

==========

Electron/Photon transport parameter

==========

Photon cross sections	si
Compton cross sections	
Photon transport cutoff(MeV)	0.1000E-02
Pair angular sampling	SIM
Pair cross sections	BH
Triplet production	Off
Bound Compton scattering	ON
Radiative Compton corrections	Off
Rayleigh scattering	ON
Atomic relaxations	ON
Photoelectron angular sampling	OFF
Electron transport cutoff(MeV)	0.5120
Bremsstrahlung cross sections	BH
Bremsstrahlung angular sampling	SIM
Spin effects	On
Electron Impact Ionization	ON
Maxium electron step in cm (SMAX)	5.000
Maximum fractional energy loss/step (ESTEPE)	0.2500
Maximum 1st elastic moment/step (XIMAX)	0.5000
Boundary crossing algorithm	EXACT
Skin-depth for boundary crossing (MFP)	3.000
Electron-step algorithm	PRESTA-II

==========

Material summary 8 Materials used

****

#	Material	density(g/cm**3)	AE(MeV)	AP(MeV)	UE(MeV)	UP(MeV)
1	Air	1.205E-03	0.516	0.001	55.000	55.000
2	TargetW_Rh	1.886E+01	0.516	0.001	55.000	55.000

```
 3 Lead              1.135E+01       0.516     0.001      55.000    55.000
 4 Glass2.23          2.230E+00       0.516     0.001      55.000    55.000
 5 ALuminum           3.232E+00       0.516     0.001      55.000    55.000
 6 Steel             8.060E+00       0.516     0.001      55.000    55.000
 7 Water              1.000E+00       0.516     0.001      55.000    55.000
 8 Glass2.4           2.400E+00       0.516     0.001      55.000    55.000
**********************************************************************
                    SOURCE PARAMETERS

              INITIAL PARTICLES are Electrons
              PARALLEL CIRCULAR BEAM FROM SIDE, RADIUS=   0.060cm
            X,Y,Z DIRECTION COSINES = (   -0.9777    0.0000    0.2099)

              KINETIC ENERGY OF SOURCE =     0.125 MeV

REGION and RANGE REJECTION SUMMARY:
**********************************

Total number of regions, including region 1 which surrounds the geometry:  96

 Region   CM        Dose  IR_   Medium    ECUTRR res_rnge ESAVE   type
abs local  # IDENTIF   ZONE   TO_  (No.&Name)  (MeV)    (cm)    (MeV)
                (0=no)  BIT
  1   1    0 exterior   0      0    0 Vacuum
  2   1    1 Source     0     23    2 TargetW_R  0.516   0.000   1.000  DNEAR
  3   2    1 Source     0     23    0 Vacuum     0.512   0.000   1.000  DNEAR
  4   3    1 Source     0     23    0 Vacuum     0.512   0.000   1.000  DNEAR
  5   1    2 exitw      0     23    0 Vacuum     0.512   0.000   1.000  DNEAR
  6   2    2 exitw      0     23    3 Lead       0.516   0.000   1.000  DNEAR
  7   3    2 exitw      0     23    3 Lead       0.516   0.000   1.000  DNEAR
  8   4    2 exitw      0     23    4 Glass2.23  0.516   0.000   1.000  DNEAR
  9   5    2 exitw      0     23    3 Lead       0.516   0.000   1.000  DNEAR
 10   6    2 exitw      0     23    3 Lead       0.516   0.000   1.000  DNEAR
 11   1    3 filter     0     23    5 ALuminum   0.516   0.000   1.000  DNEAR
 12   2    3 filter     0     23    1 Air        0.516   0.000   1.000  DNEAR
 13   1    4 colmtor    0     23    1 Air        0.516   0.000   1.000  DNEAR
 14   2    4 colmtor    0     23    1 Air        0.516   0.000   1.000  DNEAR
 15   3    4 colmtor    0     23    3 Lead       0.516   0.000   1.000  DNEAR
 16   1    5 blade      0     23    1 Air        0.516   0.000   1.000  DNEAR
 17   2    5 blade      0     23    3 Lead       0.516   0.000   1.000  DNEAR
 18   3    5 blade      0     23    3 Lead       0.516   0.000   1.000  DNEAR
 19   1    6 suport     0     23    6 Steel      0.516   0.000   1.000  DNEAR
 20   2    6 suport     0     23    1 Air        0.516   0.000   1.000  DNEAR
 21   1    7 glass      0     23    4 Glass2.23  0.516   0.000   1.000  DNEAR
 22   2    7 glass      0     23    1 Air        0.516   0.000   1.000  DNEAR
 23   1    8 bowtie     0     23    1 Air        0.516   0.000   1.000  DNEAR
 24   2    8 bowtie     0     23    1 Air        0.516   0.000   1.000  DNEAR
 25   3    8 bowtie     0     23    5 ALuminum   0.516   0.000   1.000  DNEAR
 26   4    8 bowtie     0     23    1 Air        0.516   0.000   1.000  DNEAR
 27   5    8 bowtie     0     23    1 Air        0.516   0.000   1.000  DNEAR
```

```
28  6   8 bowtie   0   23   5 ALuminum  0.516  0.000  1.000 DNEAR
29  7   8 bowtie   0   23   1 Air       0.516  0.000  1.000 DNEAR
30  8   8 bowtie   0   23   1 Air       0.516  0.000  1.000 DNEAR
31  9   8 bowtie   0   23   5 ALuminum  0.516  0.000  1.000 DNEAR
32 10   8 bowtie   0   23   1 Air       0.516  0.000  1.000 DNEAR
33 11   8 bowtie   0   23   1 Air       0.516  0.000  1.000 DNEAR
34 12   8 bowtie   0   23   5 ALuminum  0.516  0.000  1.000 DNEAR
35 13   8 bowtie   0   23   1 Air       0.516  0.000  1.000 DNEAR
36 14   8 bowtie   0   23   1 Air       0.516  0.000  1.000 DNEAR
37 15   8 bowtie   0   23   5 ALuminum  0.516  0.000  1.000 DNEAR
38 16   8 bowtie   0   23   1 Air       0.516  0.000  1.000 DNEAR
39 17   8 bowtie   0   23   1 Air       0.516  0.000  1.000 DNEAR
40 18   8 bowtie   0   23   5 ALuminum  0.516  0.000  1.000 DNEAR
41  1   9 phantom  0   23   7 Water     0.516  0.000  1.000 DNEAR
42  2   9 phantom  1   23   7 Water     0.516  0.000  1.000 DNEAR
43  3   9 phantom  2   23   7 Water     0.516  0.000  1.000 DNEAR
44  4   9 phantom  3   23   7 Water     0.516  0.000  1.000 DNEAR
45  5   9 phantom  4   23   7 Water     0.516  0.000  1.000 DNEAR
46  6   9 phantom  5   23   7 Water     0.516  0.000  1.000 DNEAR
47  7   9 phantom  6   23   7 Water     0.516  0.000  1.000 DNEAR
48  8   9 phantom  7   23   7 Water     0.516  0.000  1.000 DNEAR
49  9   9 phantom  8   23   7 Water     0.516  0.000  1.000 DNEAR
50 10   9 phantom  9   23   7 Water     0.516  0.000  1.000 DNEAR
51 11   9 phantom 10   23   7 Water     0.516  0.000  1.000 DNEAR
52 12   9 phantom 11   23   7 Water     0.516  0.000  1.000 DNEAR
53 13   9 phantom 12   23   7 Water     0.516  0.000  1.000 DNEAR
54 14   9 phantom 13   23   7 Water     0.516  0.000  1.000 DNEAR
55 15   9 phantom 14   23   7 Water     0.516  0.000  1.000 DNEAR
56 16   9 phantom 15   23   7 Water     0.516  0.000  1.000 DNEAR
57 17   9 phantom 16   23   7 Water     0.516  0.000  1.000 DNEAR
58 18   9 phantom 17   23   7 Water     0.516  0.000  1.000 DNEAR
59 19   9 phantom 18   23   7 Water     0.516  0.000  1.000 DNEAR
60 20   9 phantom 19   23   7 Water     0.516  0.000  1.000 DNEAR
61 21   9 phantom 20   23   7 Water     0.516  0.000  1.000 DNEAR
62 22   9 phantom 21   23   7 Water     0.516  0.000  1.000 DNEAR
63 23   9 phantom 22   23   7 Water     0.516  0.000  1.000 DNEAR
64 24   9 phantom 23   23   7 Water     0.516  0.000  1.000 DNEAR
65 25   9 phantom 24   23   7 Water     0.516  0.000  1.000 DNEAR
66 26   9 phantom 25   23   7 Water     0.516  0.000  1.000 DNEAR
67 27   9 phantom 26   23   7 Water     0.516  0.000  1.000 DNEAR
68 28   9 phantom 27   23   7 Water     0.516  0.000  1.000 DNEAR
69 29   9 phantom 28   23   7 Water     0.516  0.000  1.000 DNEAR
70 30   9 phantom 29   23   7 Water     0.516  0.000  1.000 DNEAR
71 31   9 phantom 30   23   7 Water     0.516  0.000  1.000 DNEAR
72 32   9 phantom 31   23   7 Water     0.516  0.000  1.000 DNEAR
73 33   9 phantom 32   23   7 Water     0.516  0.000  1.000 DNEAR
74 34   9 phantom 33   23   7 Water     0.516  0.000  1.000 DNEAR
75 35   9 phantom 34   23   7 Water     0.516  0.000  1.000 DNEAR
76 36   9 phantom 35   23   7 Water     0.516  0.000  1.000 DNEAR
77 37   9 phantom 36   23   7 Water     0.516  0.000  1.000 DNEAR
```

```
 78  38    9 phantom   37     23    7 Water      0.516   0.000   1.000  DNEAR
 79  39    9 phantom   38     23    7 Water      0.516   0.000   1.000  DNEAR
 80  40    9 phantom   39     23    7 Water      0.516   0.000   1.000  DNEAR
 81  41    9 phantom   40     23    7 Water      0.516   0.000   1.000  DNEAR
 82  42    9 phantom   41     23    7 Water      0.516   0.000   1.000  DNEAR
 83  43    9 phantom   42     23    7 Water      0.516   0.000   1.000  DNEAR
 84  44    9 phantom   43     23    7 Water      0.516   0.000   1.000  DNEAR
 85  45    9 phantom   44     23    7 Water      0.516   0.000   1.000  DNEAR
 86  46    9 phantom   45     23    7 Water      0.516   0.000   1.000  DNEAR
 87  47    9 phantom   46     23    7 Water      0.516   0.000   1.000  DNEAR
 88  48    9 phantom   47     23    7 Water      0.516   0.000   1.000  DNEAR
 89  49    9 phantom   48     23    7 Water      0.516   0.000   1.000  DNEAR
 90  50    9 phantom   49     23    7 Water      0.516   0.000   1.000  DNEAR
 91  51    9 phantom    0     23    7 Water      0.516   0.000   1.000  DNEAR
 92  52    9 phantom    0     23    8 Glass2.4   0.516   0.000   1.000  DNEAR
 93  53    9 phantom    0     23    1 Air        0.516   0.000   1.000  DNEAR
 94  54    9 phantom    0     23    8 Glass2.4   0.516   0.000   1.000  DNEAR
 95  55    9 phantom    0     23    1 Air        0.516   0.000   1.000  DNEAR
 96  56    9 phantom    0     23    1 Air        0.516   0.000   1.000  DNEAR

 Component Module summary:
 *************************

  There are  9 Component Modules.

    COMPONENT MODULE  FIRST     BOUNDARY    DISTANCE FROM    AIR
SCORING
                  REGION  (1=cyl,2=sq) REFERENCE PLANE   GAP     PLANE
 #  TYPE  IDENTIFIERFLAG    (cm)         (cm)      (cm)   (0=none)

 1 XTUBE    Source      2     2     5.000         0.000     0.000     1
 2 CONESTAK exitw       5     1     5.000         0.120     0.000     0
 3 SLABS    filter     11     2     5.000         3.010     2.716     0
 4 BLOCK    colmtor    13     2     5.000         5.926     0.000     0
 5 JAWS     blade      16     2     5.000         8.520     0.000     0
 6 SLABS    suport     19     2     5.000         9.890     1.350     0
 7 SLABS    glass      21     2     5.000        11.440     3.800     2
 8 PYRAMIDS bowtie     23     2     5.000        15.340     0.000     3
 9 CHAMBER  phantom    41     1    50.000        18.250    83.900     0


  Component module  1 is Source (Rev 1.5)
  ---------------------------------

    Title: x-ray source

 Source geometry parameters:
 ---------------------------
 Z of front face of CM =         0.00000 cm
 Half-width of outer boundary of CM =         5.00000 cm
```

Thickness oftarget in Z direction = 0.12000 cm
Angle between the target surface and Z-axis: 14.00000 degrees

Note that since XTUBE must be the first CM, there is no airgap at the top.

slab #	thickness (cm)	coordinates XFMAX	XBMAX	XFMIN	XBMIN (cm)
1(front)	0.500	0.015	-0.015	-0.500	-0.530

Source region parameters:

local region	slab	location	electron cutoff (MeV)	photon cutoff (MeV)	range-rejection level (MeV)	dose max	zone	bit set	medium
1	1	slab	0.516	0.001	0.516	1.000	0	23	TargetW_R
2	NA	region in front	0.512	0.001	0.512	1.000	0	23	Vacuum
3	NA	holder	0.512	0.001	0.512	1.000	0	23	Vacuum

Component module 2 is stacked set of truncated cones (CONESTAK:Rev 1.8)

Title: exit glass window

exitw geometry parameters:

Distance of front of CM from reference plane = 0.12000 cm
Radius of outer boundary of CM = 5.00000 cm
Inner radius of outer wall = 4.00000 cm

layer #	Z front face (cm)	thickness (cm)	top radius (cm)	bottom radius (cm)
1	0.120	2.800	3.000	3.000
2	2.920	0.090	3.000	3.000

exitw region parameters:

local region	layer	location	electron cutoff (MeV)	photon cutoff (MeV)	range-rejection level (MeV)	dose max	zone	bit set	medium
1	1	inside	0.512	0.001	0.512	1.000	0	23	Vacuum
2	1	outside	0.516	0.001	0.516	1.000	0	23	Lead
3	1	wall	0.516	0.001	0.516	1.000	0	23	Lead
4	2	inside	0.516	0.001	0.516	1.000	0	23	Glass2.23

```
  5     2   outside    0.516    0.001   0.516    1.000     0   23  Lead
  6     2      wall    0.516    0.001   0.516    1.000     0   23  Lead



--------------------------------------------------------------------------------
 Component module  3 is one or more planar slabs  (SLABS Rev 1.6)
--------------------------------------------------------------------------------

   Title: pre-filter

filter geometry parameters:
---------------------------
Distance of front of CM from reference plane =         3.01000 cm
Half-width of outer boundary of CM =         5.00000 cm

slab #    Z front    thickness
          face
          (cm)       (cm)
airgap     3.010      2.716
  1        5.726      0.200

filter region parameters:
-------------------------
local  slab #  location  electron  photon  range-rejection  dose  bit  medium
region                   cutoff    cutoff   level     max    zone  set
          (MeV)    (MeV)   (MeV)    (MeV)
  1      1        slab     0.516    0.001   0.516    1.000    0   23  ALuminum
  2     NA        airgap   0.516    0.001   0.516    1.000    0   23  Air
              at top

--------------------------------------------------------------------------------
 Component module  4 is a BLOCK colmtor (BLOCK Rev 1.4)
--------------------------------------------------------------------------------

   Title: pre- collimator

colmtor geometry parameters:
----------------------------
Z of front face of CM =         5.92600 cm
Half-width of outer boundary of CM =         5.00000 cm
Thickness of airgap at top of BLOCK =         0.59400 cm
Z of front face of BLOCK (not incl. airgap) =         6.52000 cm
Z of back face of BLOCK =         8.52000 cm
Apertures are focused at (0, 0,         0.06000).

Outer boundary of BLOCK:
Positive X boundary =         3.00000 cm
Negative X boundary =        -3.00000 cm
Positive Y boundary =         3.00000 cm
```

Negative Y boundary = -3.00000 cm

Number of subregions = 1

Aperture #	POINT #	X at top	Y at top
1	1	-1.60000	1.60000
1	2	-1.60000	-1.60000
1	3	1.60000	-1.60000
1	4	1.60000	1.60000

colmtor region parameters:

---

local region	location	electron cutoff (MeV)	photon cutoff (MeV)	range-rejection level (MeV)	dose max (MeV)	zone	bit set	medium
1	airgap at top	0.516	0.001	0.516	1.000	0	23	Air
2	subregion + outside	0.516	0.001	0.516	1.000	0	23	Air
3	block	0.516	0.001	0.516	1.000	0	23	Lead

Component module 5 is JAWS (Rev 1.8)

Title: blade

blade geometry parameters:

Distance of front of CM from reference plane = 8.52000 cm
Half-width of outer boundary of CM = 5.00000cm

jaw #	Z front face (cm)	thickness (cm)	x or y coordinates	jawsFP	BP	FN	BN
airgap	8.520	1.070	NA	NA	NA	NA	NA
1	9.590	0.300	x	2.360	2.430	-2.360	-2.430

blade region parameters:

---

local region	jaw #	location	electron cutoff (MeV)	photon cutoff (MeV)	range-rejection level (MeV)	dose max (MeV)	zone	bit set	medium
1	1	airgap above & centre	0.516	0.001	0.516	1.000	0	23	Air
2	1	+ve jaw	0.516	0.001	0.516	1.000	0	23	Lead
3	1	-ve jaw	0.516	0.001	0.516	1.000	0	23	Lead

```
------------------------------------------------------------------------------
 Component module  6 is one or more planar slabs  (SLABS Rev 1.6)
------------------------------------------------------------------------------

   Title: steel support

suport geometry parameters:
----------------------------
Distance of front of CM from reference plane =         9.89000 cm
Half-width of outer boundary of CM =         5.00000 cm

slab #    Z front    thickness
          face
          (cm)       (cm)
airgap     9.890      1.350
  1       11.240      0.200

suport region parameters:
--------------------------
local  slab # location electron  photon  range-rejection  dose  bit  medium
region                 cutoff   cutoff   level     max   zone  set
          (MeV)    (MeV)   (MeV)    (MeV)
 1      1        slab     0.516    0.001   0.516    1.000    0   23  Steel
 2     NA        airgap     0.516    0.001   0.516    1.000    0   23  Air
              at top

------------------------------------------------------------------------------
 Component module  7 is one or more planar slabs  (SLABS Rev 1.6)
------------------------------------------------------------------------------

   Title: Glass window

glass geometry parameters:
----------------------------
Distance of front of CM from reference plane =        11.44000 cm
Half-width of outer boundary of CM =         5.00000cm

slab #    Z front    thickness
          face
          (cm)       (cm)
airgap    11.440      3.800
  1       15.240      0.100

glass region parameters:
--------------------------
local  slab # location electron  photon  range-rejection  dose  bit  medium
region                 cutoff   cutoff   level     max   zone  set
          (MeV)    (MeV)   (MeV)    (MeV)
 1      1        slab     0.516    0.001   0.516    1.000    0   23  Glass2.23
 2     NA        airgap     0.516    0.001   0.516    1.000    0   23  Air
```

at top

Component module 8 is one or more truncated pyramids (PYRAMIDS Rev 1.5)

Title: bow-tie filter

bowtie geometry parameters:

Z of front face of CM = 15.34000 cm
Half-width of outer boundary of CM = 5.00000 cm

pyr.#	Z front (cm)	thick. (cm)	coordinates XFP (cm)	XBP (cm)	XFN (cm)	XBN (cm)	YFP (cm)	YBP (cm)	YFN (cm)	YBN (cm)	XMAX (cm)	YMAX (cm)
air	15.34	0.16	NA	NA	NA	NA	NA	NA	NA	NA	NA	NA
1	15.50	0.15	0.00	0.00	0.00	0.00	0.00	0.00	0.00	0.00	5.00	5.00
air	15.65	0.01	NA	NA	NA	NA	NA	NA	NA	NA	NA	NA
2	15.66	0.14	0.00	0.50	0.00	-0.50	5.00	5.00	-5.00	-5.00	5.00	5.00
air	15.80	0.01	NA	NA	NA	NA	NA	NA	NA	NA	NA	NA
3	15.81	0.69	0.50	1.00	-0.50	-1.00	5.00	5.00	-5.00	-5.00	5.00	5.00
air	16.50	0.01	NA	NA	NA	NA	NA	NA	NA	NA	NA	NA
4	16.51	1.24	1.00	1.40	-1.00	-1.40	5.00	5.00	-5.00	-5.00	5.00	5.00
air	17.75	0.01	NA	NA	NA	NA	NA	NA	NA	NA	NA	NA
5	17.76	0.29	1.40	1.60	-1.40	-1.60	5.00	5.00	-5.00	-5.00	5.00	5.00
air	18.05	0.01	NA	NA	NA	NA	NA	NA	NA	NA	NA	NA
6	18.06	0.19	1.60	2.00	-1.60	-2.00	5.00	5.00	-5.00	-5.00	5.00	5.00

bowtie region parameters:
---
local region	pyramid	location	electron cutoff (MeV)	photon cutoff (MeV)	range-rejection level (MeV)	dose max (MeV)	zone	bit set	medium
1	1	airgap above	0.516	0.001	0.516	1.000	0	23	Air
2	1	opening	0.516	0.001	0.516	1.000	0	23	Air
3	1	layer	0.516	0.001	0.516	1.000	0	23	ALuminum
4	2	airgap above	0.516	0.001	0.516	1.000	0	23	Air
5	2	opening	0.516	0.001	0.516	1.000	0	23	Air
6	2	layer	0.516	0.001	0.516	1.000	0	23	ALuminum
7	3	airgap above	0.516	0.001	0.516	1.000	0	23	Air
8	3	opening	0.516	0.001	0.516	1.000	0	23	Air
9	3	layer	0.516	0.001	0.516	1.000	0	23	ALuminum
10	4	airgap	0.516	0.001	0.516	1.000	0	23	Air

```
            above
 11     4    opening    0.516    0.001   0.516    1.000     0   23  Air
 12     4     layer     0.516    0.001   0.516    1.000     0   23  ALuminum

 13     5     airgap    0.516    0.001   0.516    1.000     0   23  Air
            above
 14     5    opening    0.516    0.001   0.516    1.000     0   23  Air
 15     5     layer     0.516    0.001   0.516    1.000     0   23  ALuminum

 16     6     airgap    0.516    0.001   0.516    1.000     0   23  Air
            above
 17     6    opening    0.516    0.001   0.516    1.000     0   23  Air
 18     6     layer     0.516    0.001   0.516    1.000     0   23  ALuminum


--------------------------------------------------------------------------------
 Component module  9 is an ion chamberor phantom (CHAMBER Rev 1.8)
--------------------------------------------------------------------------------

   Title: water phantom

phantom region & geometry parameters:
-------------------------------------
Distance of front of CM from reference plane =        18.25000 cm
Radius of outer boundary ofCM =        50.00000 cm

   Air gap parameters:
   -------------------
local layer loc.   Z    Zthick   rad. electr photon range-reject  dose  medium
reg             front              cutoff cutoff level   max   zone
                (cm) (cm)    (cm)  (MeV)  (MeV) (MeV)  (MeV)
56   NA  airgap  18.250 83.900 50.000  0.516  0.001  0.516  1.000  0  Air
        at top

   phantom CENTRAL PART parameters:
   --------------------------------
local layer loc.   Z    Zthick  rad.  electr photon range-reject  dose  medium
reg   front              cutoff cutoff level   max   zone
                (cm)    (cm)  (cm)   (MeV)  (MeV) (MeV)  (MeV)
 1    1  layer 102.150  0.5000  5.000  0.516  0.001  0.516  1.000  0  Water
 2    2  layer 102.650  0.5000  5.000  0.516  0.001  0.516  1.000  1  Water
 3    3  layer 103.150  0.5000  5.000  0.516  0.001  0.516  1.000  2  Water
 4    4  layer 103.650  0.5000  5.000  0.516  0.001  0.516  1.000  3  Water
 5    5  layer 104.150  0.5000  5.000  0.516  0.001  0.516  1.000  4  Water
 6    6  layer 104.650  0.5000  5.000  0.516  0.001  0.516  1.000  5  Water
 7    7  layer 105.150  0.5000  5.000  0.516  0.001  0.516  1.000  6  Water
 8    8  layer 105.650  0.5000  5.000  0.516  0.001  0.516  1.000  7  Water
 9    9  layer 106.150  0.5000  5.000  0.516  0.001  0.516  1.000  8  Water
10   10  layer 106.650  0.5000  5.000  0.516  0.001  0.516  1.000  9  Water
11   11  layer 107.150  0.5000  5.000  0.516  0.001  0.516  1.000 10  Water
```

12 12 layer 107.650 0.5000 5.000 0.516 0.001 0.516 1.000 11 Water
13 13 layer 108.150 0.5000 5.000 0.516 0.001 0.516 1.000 12 Water
14 14 layer 108.650 0.5000 5.000 0.516 0.001 0.516 1.000 13 Water
15 15 layer 109.150 0.5000 5.000 0.516 0.001 0.516 1.000 14 Water
16 16 layer 109.650 0.5000 5.000 0.516 0.001 0.516 1.000 15 Water
17 17 layer 110.150 0.5000 5.000 0.516 0.001 0.516 1.000 16 Water
18 18 layer 110.650 0.5000 5.000 0.516 0.001 0.516 1.000 17 Water
19 19 layer 111.150 0.5000 5.000 0.516 0.001 0.516 1.000 18 Water
20 20 layer 111.650 0.5000 5.000 0.516 0.001 0.516 1.000 19 Water
21 21 layer 112.150 0.5000 5.000 0.516 0.001 0.516 1.000 20 Water
22 22 layer 112.650 0.5000 5.000 0.516 0.001 0.516 1.000 21 Water
23 23 layer 113.150 0.5000 5.000 0.516 0.001 0.516 1.000 22 Water
24 24 layer 113.650 0.5000 5.000 0.516 0.001 0.516 1.000 23 Water
25 25 layer 114.150 0.5000 5.000 0.516 0.001 0.516 1.000 24 Water
26 26 layer 114.650 0.5000 5.000 0.516 0.001 0.516 1.000 25 Water
27 27 layer 115.150 0.5000 5.000 0.516 0.001 0.516 1.000 26 Water
28 28 layer 115.650 0.5000 5.000 0.516 0.001 0.516 1.000 27 Water
29 29 layer 116.150 0.5000 5.000 0.516 0.001 0.516 1.000 28 Water
30 30 layer 116.650 0.5000 5.000 0.516 0.001 0.516 1.000 29 Water
31 31 layer 117.150 0.5000 5.000 0.516 0.001 0.516 1.000 30 Water
32 32 layer 117.650 0.5000 5.000 0.516 0.001 0.516 1.000 31 Water
33 33 layer 118.150 0.5000 5.000 0.516 0.001 0.516 1.000 32 Water
34 34 layer 118.650 0.5000 5.000 0.516 0.001 0.516 1.000 33 Water
35 35 layer 119.150 0.5000 5.000 0.516 0.001 0.516 1.000 34 Water
36 36 layer 119.650 0.5000 5.000 0.516 0.001 0.516 1.000 35 Water
37 37 layer 120.150 0.5000 5.000 0.516 0.001 0.516 1.000 36 Water
38 38 layer 120.650 0.5000 5.000 0.516 0.001 0.516 1.000 37 Water
39 39 layer 121.150 0.5000 5.000 0.516 0.001 0.516 1.000 38 Water
40 40 layer 121.650 0.5000 5.000 0.516 0.001 0.516 1.000 39 Water
41 41 layer 122.150 0.5000 5.000 0.516 0.001 0.516 1.000 40 Water
42 42 layer 122.650 0.5000 5.000 0.516 0.001 0.516 1.000 41 Water
43 43 layer 123.150 0.5000 5.000 0.516 0.001 0.516 1.000 42 Water
44 44 layer 123.650 0.5000 5.000 0.516 0.001 0.516 1.000 43 Water
45 45 layer 124.150 0.5000 5.000 0.516 0.001 0.516 1.000 44 Water
46 46 layer 124.650 0.5000 5.000 0.516 0.001 0.516 1.000 45 Water
47 47 layer 125.150 0.5000 5.000 0.516 0.001 0.516 1.000 46 Water
48 48 layer 125.650 0.5000 5.000 0.516 0.001 0.516 1.000 47 Water
49 49 layer 126.150 0.5000 5.000 0.516 0.001 0.516 1.000 48 Water
50 50 layer 126.650 0.5000 5.000 0.516 0.001 0.516 1.000 49 Water

phantom WALL parameters:
---

local layer loc. Z Zthick rad. electr photon range-reject dose med
reg front inner outer cutoff cutoff level max zone
(cm) (cm) (cm) (MeV) (MeV) (MeV) (MeV)
51 NA entire 102.150 25.000 5.000 45.000 0.516 0.001 0.516 1.000 0 Water
wall

phantom side air gap parameters:

```
 local layer loc.  Z    Zthick     rad.      electr photon range-reject dose med
 reg   front         inner  outer cutoff cutoff level  max   zone
              (cm)    (cm)      (cm)      (MeV)  (MeV) (MeV) (MeV)
 52  NA entire 102.150 25.000 45.000 47.000 0.516 0.001  0.516 1.000  0 Glass2.4
          gap

   phantom container wall parameters:
   ----------------------------------
 local layer loc.  Z    Zthickrad.     electr photon range-reject dose med
 reg       front         inner  outer cutoff cutoff level  max   zone
              (cm)    (cm)      (cm)      (MeV)  (MeV) (MeV) (MeV)
 53  NA entire 102.150 25.000 47.000 50.000 0.516 0.001  0.516 1.000  0 Air
         wall

   phantom BOTTOM PART parameters:
   -------------------------------
 local layer loc.   Z    Zthick  inner electr photon range-reject  dose  medium
 reg  front          rad. cutoff cutoff level   max   zone
               (cm)   (cm)    (cm)  (MeV)  (MeV) (MeV)  (MeV)
 54    1  inner 127.150  2.0000 47.000  0.516  0.001  0.516  1.000  0  Glass2.4
 55    1  outer 127.150  2.0000 47.000  0.516  0.001  0.516  1.000  0  Air


Varian OBI G242 X-ray tube

 NRCC CALN: BEAMnrc(EGSnrc) Vnrc(Rev 1.78 of 2004-01-12 11:44:06-
05),(USER_MACROS Rev 1.5)
 ON gnu-win32 (gnu_win32)                          16:28:36 Jul 31 2011

*******************************************************************************
                EXECUTION INFORMATION AND WARNING MESSAGES

*******************************************************************************

********* NEW INPUT FILE *********


 *** FINAL RANDOM NUMBER POINTERS:  ixx jxx =   48  81

 FOR THIS RUN:
 ------------
 ELAPSED& CPU TIMEs, RATIO =  150690.3  142497.2s (=  39.58HR)   1.06
 CPUTIME per history =   0.00007 sec. Number of historiesper hour =   50527313.
   On gnu-win32 (gnu_win32)

                TOTAL # CHARGED PARTICLE STEPS        1.333E+11 +/- 0.0%
       # CHARGED PARTICLE STEPS/INITIAL HISTORY        6.664E+01 +/-
0.0%
 # PRESTA-II STEPS/TOTAL # CHARGED PARTICLE STEPS           0.629 +/-
0.0%
```

NO. OF BREMSSTRAHLUNG EVENTS IN THIS RUN: 0

Maximum depth of stack= 1081

PHASE SPACE FILE OUTPUT
****

FILE #	SCORE PLANE	TOTAL PARTICLES*	TOTAL PHOTONS*	MAX. KE OF PARTICLES (MeV)	MIN. KE OF ELECTRONS (MeV)	# INCIDENT PARTICLES FROM ORIGINAL SOURCE
1	1	1904245694*********		0.1250	0.0048	2000000000.000
2	2	64853907	64852003	0.1250	0.0048	2000000000.000
3	3	28126011	28124590	0.1250	0.0050	2000000000.000

FLUENCE RESULTS
****

CM PLANE	SCORE PLANE	POSITION (cm)	TOTAL PARTICLES*	ZONE HALF-WIDTHS (cm)				
1	1	0.12	1904245694	0.5000	1.0000	1.5000	2.0000	2.5000

CM PLANE	SCORE PLANE	POSITION (cm)	TOTAL PARTICLES*	ZONE HALF-WIDTHS (cm)				
7	2	15.34	64853907	2.2361	3.1623	3.8730	4.4721	5.0000

CM PLANE	SCORE PLANE	POSITION (cm)	TOTAL PARTICLES*	ZONE HALF-WIDTHS (cm)				
8	3	18.25	28126011	2.2361	3.1623	3.8730	4.4721	5.0000

*Includes all particles of all weights

Lines with zero results are not printed

SPECTRAL-AVERAGED QUANTITIES FOR FIRST TIME CROSSINGS OF THE SCORING PLANE

NORMALIZED per INCIDENT PARTICLE

ZONE	NUMBER (/cm**2)	FLUENCE (MeV)	ENERGY (degrees)	ANGLE WRT Z-AXIS
SCORING PLANE 1, CM 1:				
ELECTRONS				

```
  1  3.058E-01+- 0.00%  8.091E-01+- 0.00%    0.098+- 0.0%    55.512+- 0.0%
  2  1.789E-02+- 0.02%  5.632E-02+- 0.02%    0.097+- 0.0%    84.130+- 0.0%
  3  5.880E-03+- 0.03%  1.340E-02+- 0.03%    0.096+- 0.0%    86.747+- 0.0%
  4  2.919E-03+- 0.04%  4.784E-03+- 0.04%    0.096+- 0.0%    87.728+- 0.0%
  5  1.742E-03+- 0.05%  2.221E-03+- 0.05%    0.096+- 0.0%    88.249+- 0.0%
  6  3.466E-03+- 0.04%  5.302E-04+- 0.04%    0.096+- 0.0%    88.834+- 0.0%
 --------------------
 Tot  3.377E-01+- 0.0%
PHOTONS
  1  6.601E-03+- 0.03%  1.661E-02+- 0.04%    0.028+- 0.0%    52.710+- 0.0%
  2  3.576E-04+- 0.12%  1.128E-03+- 0.12%    0.027+- 0.1%    84.155+- 0.0%
  3  1.190E-04+- 0.21%  2.713E-04+- 0.21%    0.027+- 0.2%    86.760+- 0.0%
  4  5.918E-05+- 0.29%  9.700E-05+- 0.29%    0.027+- 0.3%    87.734+- 0.0%
  5  3.550E-05+- 0.38%  4.525E-05+- 0.38%    0.027+- 0.3%    88.253+- 0.0%
  6  7.063E-05+- 0.27%  1.080E-05+- 0.27%    0.027+- 0.2%    88.836+- 0.0%
 --------------------
 Tot  7.243E-03+- 0.0%
POSITRONS
                SCORING PLANE 2, CM  7:
ELECTRONS
  1  1.681E-09+-51.52%  1.216E-10+-53.65%    0.057+-12.8%    36.091+-30.7%
  2  6.420E-10+-77.89%  8.075E-11+-86.99%    0.009+- 9.9%    61.929+- 9.1%
  3  5.530E-10+-90.42%  4.807E-11+-91.96%    0.042+- 5.1%    53.731+- 3.1%
  4  1.000E-12+-50.00%  6.767E-14+-50.31%    0.008+-72.6%*   40.649+-71.6%*
  5  5.005E-10+-99.90%  2.968E-11+-99.90%    0.053+-99.9%*   32.529+-99.9%*
 --------------------
 Tot  3.378E-09+-36.3%
PHOTONS
  1  9.143E-06+- 0.26%  4.777E-07+- 0.42%    0.079+- 0.1%     9.196+- 0.7%
  2  8.043E-06+- 0.39%  4.265E-07+- 0.51%    0.079+- 0.1%    13.912+- 0.5%
  3  5.940E-06+- 0.76%  3.218E-07+- 0.86%    0.079+- 0.2%    17.287+- 0.4%
  4  7.524E-07+- 2.59%  4.652E-08+- 2.88%    0.076+- 0.6%    30.629+- 0.9%
  5  4.955E-07+- 3.17%  3.170E-08+- 3.37%    0.076+- 0.7%    34.114+- 1.0%
 --------------------
 Tot  2.437E-05+- 0.3%
POSITRONS
                SCORING PLANE 3, CM  8:
ELECTRONS
  1  6.352E-10+-78.71%  4.535E-11+-79.54%    0.026+- 5.7%    43.219+- 5.3%
  2  5.615E-10+-89.05%  4.456E-11+-90.45%    0.056+- 4.8%    49.545+- 3.8%
  3  5.407E-10+-92.47%  3.145E-11+-90.73%    0.019+- 2.5%    29.347+- 1.8%
  4  5.200E-10+-96.15%  2.899E-11+-94.86%    0.049+- 2.0%    24.977+- 1.4%
  5  2.250E-12+-33.33%  2.101E-13+-37.49%    0.036+-52.6%*   47.360+-48.7%*
 --------------------
 Tot  2.260E-09+-44.3%
PHOTONS
  1  3.853E-06+- 0.56%  2.170E-07+- 0.89%    0.079+- 0.2%    12.906+- 1.4%
  2  2.434E-06+- 0.86%  1.421E-07+- 1.27%    0.080+- 0.3%    18.341+- 1.2%
  3  1.952E-06+- 1.06%  1.148E-07+- 1.52%    0.081+- 0.3%    19.728+- 1.2%
  4  1.599E-06+- 1.44%  9.429E-08+- 1.80%    0.082+- 0.4%    21.559+- 1.2%
```

```
   5  3.859E-07+- 3.71%  2.783E-08+- 4.57%     0.078+- 0.9%    34.699+- 1.9%
  ----------
 Tot  1.022E-05+- 0.4%
POSITRONS

*Covariance not included in uncertainty because no. of particles
 crossing scoring zone <    10

 SPECTRAL-AVERAGED QUANTITIES FOR MULTIPLE CROSSINGS OF THE
SCORING PLANE
                NORMALIZED per INCIDENT PARTICLE
ZONE       NUMBER          FLUENCE       ENERGY      ANGLE WRT Z-AXIS
                  (/cm**2)        (MeV)        (degrees)
---- ----------------- ----------------- --------------- ----------------
                    SCORING PLANE 1, CM  1:
ELECTRONS
   1  2.661E-03+- 0.05%  6.654E-03+- 0.06%     0.067+- 0.0%   105.290+- 0.0%
   2  6.852E-03+- 0.03%  5.725E-03+- 0.04%     0.068+- 0.0%   116.366+- 0.0%
   3  1.137E-02+- 0.02%  5.560E-03+- 0.03%     0.069+- 0.0%   120.838+- 0.0%
   4  1.654E-02+- 0.02%  5.560E-03+- 0.02%     0.070+- 0.0%   123.841+- 0.0%
   5  1.883E-02+- 0.02%  4.806E-03+- 0.02%     0.071+- 0.0%   125.854+- 0.0%
   6  1.278E-02+- 0.02%  4.959E-04+- 0.03%     0.080+- 0.0%   122.914+- 0.0%
  ----------
 Tot  6.903E-02+- 0.0%
PHOTONS
   1  3.170E-05+- 0.40%  8.118E-05+- 0.51%     0.020+- 0.5%   108.495+- 0.1%
   2  8.727E-05+- 0.24%  7.335E-05+- 0.30%     0.020+- 0.3%   117.750+- 0.1%
   3  1.571E-04+- 0.18%  7.591E-05+- 0.23%     0.020+- 0.2%   122.004+- 0.0%
   4  2.648E-04+- 0.14%  8.528E-05+- 0.17%     0.021+- 0.2%   126.111+- 0.0%
   5  3.789E-04+- 0.12%  8.815E-05+- 0.15%     0.023+- 0.1%   130.239+- 0.0%
   6  2.718E-04+- 0.14%  7.438E-06+- 0.18%     0.024+- 0.2%   131.799+- 0.0%
  ----------
 Tot  1.192E-03+- 0.1%
POSITRONS
                    SCORING PLANE 2, CM  7:
ELECTRONS
   1  5.420E-10+-92.25%  5.048E-11+-91.95%     0.039+- 5.8%   122.592+- 0.2%
   2  1.042E-09+-67.86%  6.054E-11+-65.34%     0.050+-10.4%   157.867+- 6.3%
   3  1.150E-11+-17.12%  9.805E-13+-19.14%     0.013+- 9.3%   128.724+- 3.1%
   4  1.000E-09+-70.69%  6.728E-11+-70.91%     0.057+-99.9%*  138.762+-99.9%*
  ----------
 Tot  2.596E-09+-43.1%
PHOTONS
   1  9.601E-07+- 2.54%  9.595E-08+- 3.18%     0.064+- 0.6%   130.747+- 0.5%
   2  9.148E-07+- 2.56%  8.548E-08+- 3.24%     0.064+- 0.6%   133.248+- 0.5%
   3  6.914E-07+- 2.96%  6.581E-08+- 3.83%     0.064+- 0.8%   134.098+- 0.5%
   4  3.078E-07+- 4.38%  3.131E-08+- 5.38%     0.065+- 0.9%   129.979+- 0.8%
   5  1.621E-07+- 6.17%  2.020E-08+- 7.90%     0.068+- 1.6%   125.224+- 1.1%
  ----------
 Tot  3.036E-06+- 1.4%
```

POSITRONS

SCORING PLANE 3, CM 8:

ELECTRONS

1	5.247E-10+-95.29%	3.044E-11+-90.63%	0.011+- 9.3%	153.409+- 1.0%
2	1.475E-11+-17.03%	1.612E-12+-20.27%	0.016+-15.8%	116.108+- 4.6%
3	9.750E-12+-18.67%	1.214E-12+-23.61%	0.016+-18.9%	116.106+- 5.1%
4	6.250E-12+-21.54%	5.802E-13+-23.23%	0.017+-22.9%	119.116+- 5.5%
5	1.750E-12+-42.86%	1.550E-13+-46.08%	0.026+-66.3%*	122.253+-59.5%*
6	3.700E-11+- 8.33%	5.213E-11+- 8.97%	0.034+- 4.3%	143.394+- 0.9%
Tot	5.942E-10+-84.1%			

PHOTONS

1	3.256E-09+-26.60%	2.895E-10+-49.09%	0.065+- 4.2%	149.993+- 5.5%
2	3.786E-09+-26.47%	2.062E-10+-28.10%	0.058+- 1.4%	159.841+- 1.9%
3	3.276E-09+-34.46%	1.813E-10+-38.21%	0.053+- 2.9%	144.963+- 9.6%
4	4.265E-09+-31.10%	2.245E-10+-31.74%	0.062+- 3.9%	147.873+- 8.5%
5	3.244E-09+-26.72%	1.940E-10+-33.14%	0.059+- 7.3%	150.180+- 9.3%
6	6.763E-07+- 1.32%	7.590E-07+- 1.69%	0.058+- 0.3%	157.973+- 0.1%
Tot	6.941E-07+- 1.3%			

POSITRONS

*Covariance not included in uncertainty because no. of particles crossing scoring zone < 10

MIN PARTICLE WEIGHT FOR ALL SCORING ZONES = 0.0005000
MAX PARTICLE WEIGHT FOR ALL SCORING ZONES = 1.0000000

DOSE RESULTS
****

TOTAL # CHARGED PARTICLE STEPS in DOSE REG. 1.475E+05 +/- 1.4%
CHARGED PARTICLE STEPS in DOSE REG./INITIAL HISTORY 7.377E-05 +/- 1.4%

TOTAL DOSE PER INCIDENT PARTICLE

DOSE ZONE	MASS (g)	DOSE (Gy)	ENERGY DEPOSITED (J)
1	3.927E+01	4.237E-21+/- 0.3%	1.664E-22+/- 0.3%
2	3.927E+01	4.248E-21+/- 0.3%	1.668E-22+/- 0.3%
3	3.927E+01	4.189E-21+/- 0.3%	1.645E-22+/- 0.3%
4	3.927E+01	4.101E-21+/- 0.3%	1.610E-22+/- 0.3%
5	3.927E+01	3.997E-21+/- 0.3%	1.570E-22+/- 0.3%
6	3.927E+01	3.869E-21+/- 0.3%	1.520E-22+/- 0.3%
7	3.927E+01	3.726E-21+/- 0.3%	1.463E-22+/- 0.3%
8	3.927E+01	3.577E-21+/- 0.3%	1.405E-22+/- 0.3%

9	3.927E+01	3.477E-21+/- 1.0%	1.366E-22+/- 1.0%
10	3.927E+01	3.261E-21+/- 0.3%	1.281E-22+/- 0.3%
11	3.927E+01	3.135E-21+/- 0.3%	1.231E-22+/- 0.3%
12	3.927E+01	2.980E-21+/- 0.3%	1.170E-22+/- 0.3%
13	3.927E+01	2.958E-21+/- 3.8%	1.162E-22+/- 3.8%
14	3.927E+01	2.699E-21+/- 0.4%	1.060E-22+/- 0.4%
15	3.927E+01	2.571E-21+/- 0.5%	1.010E-22+/- 0.5%
16	3.927E+01	2.554E-21+/- 4.7%	1.003E-22+/- 4.7%
17	3.927E+01	2.295E-21+/- 0.4%	9.014E-23+/- 0.4%
18	3.927E+01	2.182E-21+/- 0.4%	8.567E-23+/- 0.4%
19	3.927E+01	2.087E-21+/- 1.5%	8.197E-23+/- 1.5%
20	3.927E+01	1.955E-21+/- 1.0%	7.675E-23+/- 1.0%
21	3.927E+01	1.825E-21+/- 0.4%	7.165E-23+/- 0.4%
22	3.927E+01	1.746E-21+/- 1.1%	6.855E-23+/- 1.1%
23	3.927E+01	1.626E-21+/- 0.5%	6.386E-23+/- 0.5%
24	3.927E+01	1.520E-21+/- 0.5%	5.970E-23+/- 0.5%
25	3.927E+01	1.455E-21+/- 1.7%	5.714E-23+/- 1.7%
26	3.927E+01	1.346E-21+/- 0.5%	5.285E-23+/- 0.5%
27	3.927E+01	1.243E-21+/- 0.5%	4.880E-23+/- 0.5%
28	3.927E+01	1.194E-21+/- 0.5%	4.691E-23+/- 0.5%
29	3.927E+01	1.116E-21+/- 0.6%	4.381E-23+/- 0.6%
30	3.927E+01	1.040E-21+/- 0.6%	4.084E-23+/- 0.6%
31	3.927E+01	9.761E-22+/- 0.6%	3.833E-23+/- 0.6%
32	3.927E+01	9.223E-22+/- 0.6%	3.622E-23+/- 0.6%
33	3.927E+01	8.555E-22+/- 0.6%	3.360E-23+/- 0.6%
34	3.927E+01	7.969E-22+/- 0.7%	3.129E-23+/- 0.7%
35	3.927E+01	7.563E-22+/- 0.7%	2.970E-23+/- 0.7%
36	3.927E+01	7.054E-22+/- 0.7%	2.770E-23+/- 0.7%
37	3.927E+01	6.542E-22+/- 0.7%	2.569E-23+/- 0.7%
38	3.927E+01	6.074E-22+/- 0.7%	2.385E-23+/- 0.7%
39	3.927E+01	5.636E-22+/- 0.8%	2.213E-23+/- 0.8%
40	3.927E+01	5.297E-22+/- 0.8%	2.080E-23+/- 0.8%
41	3.927E+01	5.040E-22+/- 1.8%	1.979E-23+/- 1.8%
42	3.927E+01	4.484E-22+/- 0.9%	1.761E-23+/- 0.9%
43	3.927E+01	4.233E-22+/- 0.9%	1.662E-23+/- 0.9%
44	3.927E+01	3.828E-22+/- 0.9%	1.503E-23+/- 0.9%
45	3.927E+01	3.523E-22+/- 1.0%	1.384E-23+/- 1.0%
46	3.927E+01	3.257E-22+/- 1.0%	1.279E-23+/- 1.0%
47	3.927E+01	3.007E-22+/- 1.1%	1.181E-23+/- 1.1%
48	3.927E+01	2.678E-22+/- 1.4%	1.052E-23+/- 1.4%
49	3.927E+01	2.337E-22+/- 1.2%	9.176E-24+/- 1.2%

TOTAL DOSE EXCLUDING FAT PARTICLES PER INCIDENT PARTICLE (DBS ONLY)

DOSE ZONE	MASS (g)	DOSE (Gy)	ENERGY DEPOSITED (J)
1	3.927E+01	4.237E-21+/- 0.3%	1.664E-22+/- 0.3%
2	3.927E+01	4.248E-21+/- 0.3%	1.668E-22+/- 0.3%

3	3.927E+01	4.189E-21+/- 0.3%	1.645E-22+/- 0.3%
4	3.927E+01	4.101E-21+/- 0.3%	1.610E-22+/- 0.3%
5	3.927E+01	3.997E-21+/- 0.3%	1.570E-22+/- 0.3%
6	3.927E+01	3.869E-21+/- 0.3%	1.520E-22+/- 0.3%
7	3.927E+01	3.726E-21+/- 0.3%	1.463E-22+/- 0.3%
8	3.927E+01	3.577E-21+/- 0.3%	1.405E-22+/- 0.3%
9	3.927E+01	3.445E-21+/- 0.3%	1.353E-22+/- 0.3%
10	3.927E+01	3.261E-21+/- 0.3%	1.281E-22+/- 0.3%
11	3.927E+01	3.135E-21+/- 0.3%	1.231E-22+/- 0.3%
12	3.927E+01	2.980E-21+/- 0.3%	1.170E-22+/- 0.3%
13	3.927E+01	2.845E-21+/- 0.3%	1.117E-22+/- 0.3%
14	3.927E+01	2.699E-21+/- 0.4%	1.060E-22+/- 0.4%
15	3.927E+01	2.563E-21+/- 0.4%	1.006E-22+/- 0.4%
16	3.927E+01	2.435E-21+/- 0.4%	9.561E-23+/- 0.4%
17	3.927E+01	2.295E-21+/- 0.4%	9.014E-23+/- 0.4%
18	3.927E+01	2.182E-21+/- 0.4%	8.567E-23+/- 0.4%
19	3.927E+01	2.047E-21+/- 0.4%	8.037E-23+/- 0.4%
20	3.927E+01	1.936E-21+/- 0.4%	7.602E-23+/- 0.4%
21	3.927E+01	1.825E-21+/- 0.4%	7.165E-23+/- 0.4%
22	3.927E+01	1.728E-21+/- 0.4%	6.787E-23+/- 0.4%
23	3.927E+01	1.624E-21+/- 0.5%	6.378E-23+/- 0.5%
24	3.927E+01	1.520E-21+/- 0.5%	5.970E-23+/- 0.5%
25	3.927E+01	1.431E-21+/- 0.5%	5.619E-23+/- 0.5%
26	3.927E+01	1.346E-21+/- 0.5%	5.285E-23+/- 0.5%
27	3.927E+01	1.243E-21+/- 0.5%	4.880E-23+/- 0.5%
28	3.927E+01	1.194E-21+/- 0.5%	4.691E-23+/- 0.5%
29	3.927E+01	1.116E-21+/- 0.6%	4.381E-23+/- 0.6%
30	3.927E+01	1.040E-21+/- 0.6%	4.084E-23+/- 0.6%
31	3.927E+01	9.761E-22+/- 0.6%	3.833E-23+/- 0.6%
32	3.927E+01	9.223E-22+/- 0.6%	3.622E-23+/- 0.6%
33	3.927E+01	8.555E-22+/- 0.6%	3.360E-23+/- 0.6%
34	3.927E+01	7.969E-22+/- 0.7%	3.129E-23+/- 0.7%
35	3.927E+01	7.563E-22+/- 0.7%	2.970E-23+/- 0.7%
36	3.927E+01	7.054E-22+/- 0.7%	2.770E-23+/- 0.7%
37	3.927E+01	6.542E-22+/- 0.7%	2.569E-23+/- 0.7%
38	3.927E+01	6.074E-22+/- 0.7%	2.385E-23+/- 0.7%
39	3.927E+01	5.636E-22+/- 0.8%	2.213E-23+/- 0.8%
40	3.927E+01	5.297E-22+/- 0.8%	2.080E-23+/- 0.8%
41	3.927E+01	4.961E-22+/- 0.8%	1.948E-23+/- 0.8%
42	3.927E+01	4.484E-22+/- 0.9%	1.761E-23+/- 0.9%
43	3.927E+01	4.233E-22+/- 0.9%	1.662E-23+/- 0.9%
44	3.927E+01	3.828E-22+/- 0.9%	1.503E-23+/- 0.9%
45	3.927E+01	3.523E-22+/- 1.0%	1.384E-23+/- 1.0%
46	3.927E+01	3.257E-22+/- 1.0%	1.279E-23+/- 1.0%
47	3.927E+01	3.007E-22+/- 1.1%	1.181E-23+/- 1.1%
48	3.927E+01	2.657E-22+/- 1.1%	1.043E-23+/- 1.1%
49	3.927E+01	2.337E-22+/- 1.2%	9.176E-24+/- 1.2%

END OF RUN Aug 02 2011 10:20:06

DOSXYSnrc

```
**********************************************************************
NRCC/UW EGSnrc user-code DOSXYZnrc ($Revision: 1.44 $ last edited $Date:
2008/04/28 16:15:23 $)
 ON gnu-win32 (gnu_win32)                    11:00:54 Feb 19 2012

**********************************************************************
 **                                          **
 **                  DOSXYZnrc                    **
 **                Z pronounced zed               **
 **                                          **
 **    Code developed at the NationalResearch Council of Canada and      **
 **       University of Wisconsin as part of the OMEGA project         **
 **                                          **
 **       This is $Revision: 1.44 $ last edited $Date: 2008/04/28 16:15:23**
 **                                          **

**********************************************************************

   The following parameters may be adjusted in dosxyz_user_macros.mortran
$MXMED:    Max number of media:  7
$MXSTACK:  Max stack size:       15
$IMAX,etc: Max dose scoring regions in x,y,z directions:  128  128   56
$MAXDOSE:  Max dose scoring regions consistent with above: 917505
$DOSEZERO(=1) 1=> all doses with uncert > 50% are zeroed in .3ddose file


The following parameters may be adjusted in srcxyz.macros
$INVDIM:   number of elements in inverse CPD for input energy spectra = 1000
$NENSRC:   number of bins in input energy spectrum =  200


============================================================


 Title:  last test for water phantom doses

============================================================


 Number of media (min = 1, max =   7, 0 => CT data):              0
 Input the full name of the file containing the CT phantom created
 using ctcreate
 : C:/egsnrc_mp/dosxyznrc/Cylindrical_Phantom_8cm.egsphant

 CT Phantom summary:
```

```
 NMED =  2

 media:
 Water
 Air

 Dummy values of (ESTEPM(i),i=1,NMED)
 :      0.000     0.000

 IMAX, JMAX, KMAX :   36  36  36

 x range :     -9.00000 -      9.00000 cm
 y range :     -9.00000 -      9.00000 cm
 z range :     -9.00000 -      9.00000 cm

 Densities range from      0.00120 -      1.00000 g/cc

 ECUTIN,PCUTIN,(SMAX--DUMMY INPUT):
           0.001     0.010     0.000

 Input zeroairdose (1 to zero dose in air in .3ddosefile; 0[default]
 to not zero this dose), doseprint (1 for full dose output in .egslst;
 0[default] otherwise), MAX20 (1 to print out summary of 20 highest
 doses; 0[default] to not print this summary)
 :     1    0    0

 The material in the region outside the phantom is vacuum.
 The thickness of this region (in x, y & z direction) is:  50.000 cm


 Particles will be read from file:
C:/egsnrc_mp/dosxyznrc/Varianiwithhalfbowtie.egsphsp3

 Total number of particles in file      :     44792923
 Total number of photons                :     44790479
The rest are electrons/positrons.

 Maximum kinetic energyof the particles:            0.125 MeV
 Minimum kinetic energy ofthe electrons:            0.005 MeV
 # of particles incident fromoriginal source: 2000000000.0



NCASE,IWATCH,TIMMAX,INSEED1,INSEED2,BEAM_SIZE,ISMOOTH,IREST
ART,IDAT,
 IREJECT,ESAVE_GLOBAL,NRCYCL,IPARALLEL,PARNUM,n_split,ihowfarless
 :
  1600000000   0 500.00        33        97 100.00       1    0   0   0   0.00  10   0   0   1   0
```

****

Summary of source parameters (srcxyznrc $Revision: 1.25 $)

****

Full phase space input incident from multiple angles

x-coordinate of the isocenter, 0.0000 cm
y-coordinate of the isocenter, 0.0000 cm
z-coordinate of the isocenter, 0.0000 cm
number theta-phi groups: 1
Distance from isocenter to origin in source plane: -76.7500 cm
Source plane rotation angle, 0.0000 degrees
Total number of particlesin phase space file: 44792923

theta-phi group	theta (deg.) min.	theta (deg.) max.	phi (deg.) min.	phi (deg.) max.	no. theta-phi pairs	normalized probability
1	90.0000	90.0000	0.0000	360.0000	360	1.0000

Particles to be simulated: photon only

==========

Electron/Photon transport parameter

==========

Photon cross sections si
Compton cross sections
Photon transport cutoff(MeV) 0.1000E-01
Pair angular sampling SIM
Pair cross sections BH
Triplet production Off
Bound Compton scattering OFF
Radiative Compton corrections Off
Rayleigh scattering OFF
Atomic relaxations OFF
Photoelectron angular sampling OFF

Electron transport cutoff(MeV) 0.5160
Bremsstrahlung cross sections BH
Bremsstrahlung angular sampling SIM
Spin effects On
Electron Impact Ionization OFF
Maxium electron step in cm (SMAX) 5.000

```
 Maximum fractional energy loss/step (ESTEPE)          0.2500
 Maximum 1st elastic moment/step (XIMAX)               0.5000
 Boundary crossing algorithm                        PRESTA-I
 Skin-depth for boundary crossing (MFP)                14.10
 Electron-step algorithm                           PRESTA-II

============================================================


 Medium          AE      AP
 Water         0.516    0.001
 Air           0.516    0.001

 No range rejection.

 ************************************************************

  Histories to be simulated for this run   1600000000

  Histories to be analyzed after this run  1600000000

 ************************************************************
   Elapsed wall clock time to this point=       0.639 s


   CPU time so far for this run =       0.234 s


  BATCH #  TIME-ELAPSED  TOTAL CPUTIME  RATIO  TIME OF DAY  RNG
pointers

    1        0.0          0.0      0.00    11:00:55   ixx jxx =   97  33

 *** Warning *** Used all particles fromsource file
              Restarting from first particle infile


 *** Warning *** Used all particles fromsource file
              Restarting from first particle infile


 *** Warning *** Used all particles fromsource file
              Restarting from first particle infile

    2      1406.8        1285.0      1.09    11:24:21   ixx jxx =    2  35

 *** Warning *** Used all particles fromsource file
              Restarting from first particle infile
```

```
*** Warning *** Used all particles fromsource file
              Restarting from first particle infile


*** Warning *** Used all particles fromsource file
              Restarting from first particle infile

   3      2649.6         2526.1      1.05    11:45:04   ixx jxx =   24  57

*** Warning *** Used all particles fromsource file
              Restarting from first particle infile


*** Warning *** Used all particles fromsource file
              Restarting from first particle infile


*** Warning *** Used all particles fromsource file
              Restarting from first particle infile


*** Warning *** Used all particles fromsource file
              Restarting from first particle infile

   4      3894.5         3766.3      1.03    12:05:49   ixx jxx =    3  36

*** Warning *** Used all particles fromsource file
              Restarting from first particle infile


*** Warning *** Used all particles fromsource file
              Restarting from first particle infile


*** Warning *** Used all particles fromsource file
              Restarting from first particle infile


*** Warning *** Used all particles fromsource file
              Restarting from first particle infile

   5      5163.1         5019.8      1.03    12:26:58   ixx jxx =   48  81

*** Warning *** Used all particles fromsource file
              Restarting from first particle infile


*** Warning *** Used all particles fromsource file
              Restarting from first particle infile


*** Warning *** Used all particles fromsource file
              Restarting from first particle infile


*** Warning *** Used all particles fromsource file
              Restarting from first particle infile

   6      6485.5         6283.3      1.03    12:49:00   ixx jxx =   67   3

*** Warning *** Used all particles fromsource file
```

Restarting from first particle infile

*** Warning *** Used all particles fromsource file
Restarting from first particle infile

*** Warning *** Used all particles fromsource file
Restarting from first particle infile

7 7756.4 7535.5 1.03 13:10:11 ixx jxx = 1 34

*** Warning *** Used all particles fromsource file
Restarting from first particle infile

*** Warning *** Used all particles fromsource file
Restarting from first particle infile

*** Warning *** Used all particles fromsource file
Restarting from first particle infile

8 8998.5 8775.1 1.03 13:30:53 ixx jxx = 19 52

*** Warning *** Used all particles fromsource file
Restarting from first particle infile

*** Warning *** Used all particles fromsource file
Restarting from first particle infile

*** Warning *** Used all particles fromsource file
Restarting from first particle infile

9 10337.8 10036.4 1.03 13:53:13 ixx jxx = 35 68

*** Warning *** Used all particles fromsource file
Restarting from first particle infile

*** Warning *** Used all particles fromsource file
Restarting from first particle infile

*** Warning *** Used all particles fromsource file
Restarting from first particle infile

10 11624.3 11288.3 1.03 14:14:39 ixx jxx = 48 81

*** Warning *** Used all particles fromsource file
Restarting from first particle infile

*** Warning *** Used all particles fromsource file
Restarting from first particle infile

*** Warning *** Used all particles fromsource file
Restarting from first particle infile

Total CPU time for run = 12536.6 s = 3.482 hr => 459455865. hist/hr
On gnu-win32 (gnu_win32)

****

# of particles read from ph-sp file (N_read) = 1362288250
# of primary (non ph-sp) histories read from ph-sp file = 867725318
# of particles discarded dueto charge/LATCH/W/multiple passer = 102578966
# of particles discarded because beyond BEAM_SIZE = 0
# of photons rejected because beyond DBS splitting radius = 0
# of particles that missed geometry = -628099766
N_used/N_read = 1.174
# of times each particle in ph-sp file recycled
(last particle may be recycled less than this) = 10
# of ph-sp particles simulated (N_used) = 1600000000
# of times ph-sp file restarted in this run = 30

****

Fraction of incident energy deposited in the phantom = 0.0471

Fraction of incident energy deposited in the region surrounding
the phantom when incident particles go through it = 0.0000

Number of charged particle steps simulated, N_step = 1937338568
Number of charged particle steps/incident fluence = 2.06590E-02
No. of PRESTA-II steps/total no. of charged particle steps = 0.99564

WARNING
The ph-sp source was restarted at least once. This may lead
to an underestimate of uncertainty, especially if restarted
many times. If restarted many times, try re-running with
NRCYCL recalculated as described at topof dosxyznrc.mortran

1last test for water phantom doses
Elec/positron planar energy fluence scored in a 1cm**2 circle
centered at z-axis on the phantom surface = 0.000E+00(1/cm**2)

Photon planar energy fluence scored in a 1cm**2 circle
centered at z-axis on the phantom surface = 0.000E+00(1/cm**2)

Elec/positron planar fluence scored in a 1cm**2 circle
centered at z-axis on thephantom surface = 0.000E+00(1/cm**2)

Photon planar fluence scored in a 1cm**2 circle
centered at z-axis on the phantom surface = 0.000E+00(1/cm**2)

No. of particles incident from phase space file = 1600000000

No. of particles incident from original source =93776814080.0

DOSXYZnrc ($Revision: 1.44 $) Dose outputs
(Dose/incident particle from original source, Gy)

full dose output suppressed in this run

Total CPU time for this run = 12537.0 s = 3.482 hr

END OF RUN Feb 19 2012 14:35:45

Appendix 2 Matlab program

```
%function Read_3D_DoseXYZnrc

clc
close all
clear all

[FileName,PathName] = uigetfile('C:\Users\Fouad\Documents\PhD\BEAM
simulation\Cylindrical water phantom\*.3ddose');

fid = fopen ([PathName,FileName], 'r');

nx = cell2mat(textscan(fid, '%f', 1));
ny = cell2mat(textscan(fid, '%f', 1));
nz = cell2mat(textscan(fid, '%f', 1));

nx_2 = round(nx/2);
ny_2 = round(ny/2);
nz_2 = round(nz/2);

x_dim = nx+1;
y_dim = ny+1;
z_dim = nz+1;
no_of_voxels = nx*ny*nz;

x_cor_bndry = cell2mat(textscan(fid, '%f', x_dim));
y_cor_bndry = cell2mat(textscan(fid, '%f', y_dim));
z_cor_bndry = cell2mat(textscan(fid, '%f', z_dim));

Dose_Val = cell2mat(textscan(fid, '%f', no_of_voxels));
Error_Val = cell2mat(textscan(fid, '%f', no_of_voxels));

end_1 = ftell(fid);
eofstat_1 = feof(fid);
% if eofstat == 0;
%     beep
%     pause(0.5)
%     beep
%     warning('File format error, some data not read')
% end
rest_of_file = cell2mat(textscan(fid, '%f'));
end_2 = ftell(fid);
eofstat_2 = feof(fid);
fclose(fid);

Dose_3D_Mat = reshape(Dose_Val, nx,ny,nz);
Error_3D_Mat = reshape(Error_Val, nx,ny,nz);
a = max(max(max(Dose_3D_Mat)));
temp_3D = 100*Dose_3D_Mat/a;

A(:,:) = temp_3D (nx_2,:, :);
B(:,:) = temp_3D (:,ny_2, :);
A_e(:,:) = Error_3D_Mat (nx_2,:, :);
B_e(:,:) = Error_3D_Mat (:,ny_2, :);

% % This to make sure that reshape works in the right way
```

```
% temp_2= zeros(nx,ny,nz);
% c=0;
% for z=1:nz;
%     for y=1:ny;
%         for x=1:nx;
%             c=c+1;
%             temp_2(x,y,z)= Dose_Val(c);
%         end
%     end
% end
% temp_2 = 100*temp_2/max(max(max(temp_2)));
% A_2 = zeros(nx,nz);
% A_2(:,:) = temp_2(nx_2,:, :);
%
% TEST_0 = A-A_2;
% % end of reshape test

% xlim([min(z_cor_bndry) min(z_cor_bndry)]);
% ylim([min(x_cor_bndry) min(x_cor_bndry)]);

x_cor(1:nx)=0;
for m=1:nx;
    x_cor(m)= (x_cor_bndry(m)+x_cor_bndry(m+1))/2;
end

y_cor(1:ny)=0;
for m=1:ny;
    y_cor(m)= (y_cor_bndry(m)+y_cor_bndry(m+1))/2;
end

z_cor(1:nz)=0;
for m=1:nz;
    z_cor(m)= (z_cor_bndry(m)+z_cor_bndry(m+1))/2;
end

figure
contourf(z_cor, x_cor, A);
% axis([z_cor(1) z_cor(nz) x_cor(1) x_cor(nx)])
title('2D Dose distribution center sagittal view')
ylabel('X axis (cm)')
xlabel('Z axis (cm)')
axis equal
axis tight
colorbar


figure
contourf(z_cor, x_cor, A_e);
% axis([z_cor(1) z_cor(nz) x_cor(1) x_cor(nx)])
title('Axial Error Matrix in XZ plane')
ylabel('Field zise X (cm)')
xlabel('Depth (cm)')
axis equal
axis tight
colorbar

% axis([x_cor(1) x_cor(nx) z_cor(1) x_cor(nz)])

figure
```

```
PDD=1:nz;
PDD=PDD*0;
PDD(:)=temp_3D(nx_2,ny_2,:);
plot(z_cor,PDD)
title(['Pecentage Depth Dose']);
xlabel('Depth (cm)')
ylabel('PDD')

figure
imagesc(x_cor, y_cor, temp_3D (:,:, nz_2), ([0 100]));
title('2D Dose distribution center transverse view')
xlabel('X (cm)')
ylabel('Y (cm)')
axis equal
axis tight
colorbar
pause(1)

figure
plot(Dose_3D_Mat(ny_2,:,20))

figure
xslice = ny_2; yslice = ny_2; zslice = ny_2;
slice(temp_3D,xslice,yslice,zslice)
shading interp
colorbar

figure
xslice = ny_2; yslice = ny_2; zslice = 1;
slice(temp_3D,xslice,yslice,zslice)
shading interp
colorbar
```

Presentation arising from this work

Conferences presentations:

1- **Abolaban F.**, Jordan T., Alshanqity M., Spyrou N. and Nisbet A. "Evaluation of CBCT dose for new Varian software version". Saudi International Conference (July, 2010) at University of Manchester, Manchester. **Awarded best presentation prize**.

2- **F. Abolaban**, T. Jordan, M. Hussein, N. M. Spyrou and A. Nisbet. "Variation in Hounsfield Number with Mode Setting for a Linear Accelerator Mounted CT". European Medical Physics and Engineering Conference 2011, Trinity college, Dublin, Ireland. 1st - 3rd September 2011.

3- **F. Abolaban**, T. Jordan, M. Hussein, N. M. Spyrou and A. Nisbet. "Radiotherapy Treatment Planning using Cone Beam Computed Tomography images". Surrey Postgraduate conference, University of Surrey, Guildford, UK. January, 2012. Poster presentation.

Journal publication:

Fouad Abolaban M.Sc, Mohamad Hussein M.Sc, Tom Jordan M.Sc, Nicholas Spyrou M.Phil, MD and Andrew Nisbet PhD. "The Relationship between Concomitant Dose from a LINAC Mounted Cone Beam CT and Patient Size." Journal of Applied Clinical Medical Physics. Submitted.